

## **D2.2 Good practice criteria for multi-variable risk reduction from restoration/ESS at the Pilots, as a function of projection horizon and domain scale, as enablers to introduce risk products in coastal governance**

08/03/24

WP2

Lead beneficiary: UPC

**Author/s:** Manuel Espino, Vicente Gracia, Xavier S.-Artús, Luis Garrote, David Santillan, Ivan Federico, Salvatore Causio, Fabienne Horneman, Silvia Torresan, Elisa Furlan, Grzegorz Rozynski, Luciana Villa, Joanna Staneva, Benjamin Jacob, Wei Chen, Bas van Maren, Richard Marijnissen, Andreas Wurpts, Pushpa Dissanayake, Rosaria Ester Musumeci, Massimiliano Marino, Petya Eftimova, Nikolay Valchev, Elitsa Hineva, Nataliya Andreeva, Bogdan Prodanov, Remi Caillibotte, Christophe Briere, Soazing Mahe, Julien Fornasari & Agustín S.-Arcilla.

**REST-COAST**

**Large Scale RESToration of COASTal Ecosystems through Rivers to Sea Connectivity**



**Prepared under contract from the European Commission**

Grant agreement No. 101037097

EU Horizon 2020 Coordination and Support Action

Project acronym: **REST-COAST**  
Project full title: **Large Scale RESToration of COASTal Ecosystems through Rivers to Sea Connectivity**  
Start of the project: 01.10.2021  
Duration: 54 months  
Project coordinator: Prof. Agustín Sánchez-Arcilla, Universitat Politècnica De Catalunya (UPC)  
  
Type: Restoring biodiversity and ecosystem services  
Call: H2020-LC-GD-2020-3  
  
Deliverable title: Good practice criteria for multi-variable risk reduction from restoration/ESS at the Pilots, as a function of projection horizon and domain scale, as enablers to introduce risk products in coastal governance  
  
Deliverable n°: D2.2  
Nature of the deliverable: Report  
Dissemination level: Public  
  
WP responsible: WP2  
Lead beneficiary: UPC  
  
Citation: Espino, M., V. Gracia, X. S.-Artús, L. Garrote, D. Santillan, I. Federico, S. Causio, F. Horneman, S. Torresan, E. Furlan, G. Rozynski, L. Villa, J. Staneva, B. Jacob, W. Chen, B. van Maren, R. Marijnissen, A. Wurpts, P. Dissanayake, R. E. Musumeci, M. Marino, P. Eftimova, N. Valchev, E. Hineva, N. Andreeva, B. Prodanov, R. Caillibotte, C. Briere, S. Mahe, J. Fornasari & A. S.-Arcilla. (2024). *Good practice criteria for multi-variable risk reduction from restoration/ESS at the Pilots, as a function of projection horizon and domain scale, as enablers to introduce risk products in coastal governance*. Deliverable D2.2. EU Horizon 2020 REST-COAST Project, Grant agreement No 101037097  
  
Due date of deliverable: Month n° 27  
Actual submission date: Month n° 30

Deliverable status:

<b>Version</b>	<b>Status</b>	<b>Date</b>	<b>Author(s)</b>
1.0	Draft	09 October 2023	Manuel Espino (UPC)
1.1	Ebro Delta	30 Nov. 2023	Xavier S..Artus (UPC)
2.0	Ebro River Venice Lagoon Vistula Lagoon	12 Feb. 2024	Luis Garrote (UPM) Ivan Federico (CMCC) Grzegorz Rozynski (IBW)
2.1	Wadden Sea Sicily Lagoon	16 Feb. 2024	Luciana Villa (Hereon) Rosaria Ester Musumeci (UC)
2.2	Foros Bay Arcachon Bay	21 Feb. 2024	Petya Eftimova (BAS) Remi Caillibotte (EGIS)
3.0	Final document	29 Feb. 2024	Manuel Espino (UPC)
4.0	Final revision	04 March 2024	Agustín S.-Arcilla (UPC)

The content of this deliverable does not necessarily reflect the official opinions of the European Commission or other institutions of the European Union.

## Table of Contents

Preface .....	7
Summary .....	7
List of abbreviations .....	8
1 General introduction.....	9
2 Multi-risk projections and climate warnings with ESS in Ebro Delta Pilot (UPC, UPM) .....	10
2.1 Ebro Delta Coast.....	10
2.1.1 Criteria to define efficiency of the risk reduction .....	12
2.1.2 Risk reduction from different approaches .....	14
2.1.3 Efficiency at long-term under different climate projections .....	19
2.1.4 Conclusions .....	24
2.2 Ebro River (UPM).....	26
2.2.1 Numerical simulations on sediment transport to Ebro Delta .....	26
2.2.2 Hydrodynamic calibration of the model with controlled flood observations.....	32
2.2.3 Parameterization of hydro-morpho-eco interactions to simulate ESS .....	35
2.2.4 Assessment of current, potential and future sediment transport .....	40
2.2.5 Conclusions .....	51
3 Multi-risk projections and climate warnings with ESS in Wadden Sea Pilot (DEL, HZG, FSK). ..	53
3.1 Multi-risk projections for ESS of NBS in the Wadden Sea.....	53
3.1.1 Criteria to assess risk reduction .....	54
3.1.2 Baseline risk reduction under present day conditions and seasonal variability .....	55
3.1.3 Risk reduction under extreme weather conditions .....	55
3.1.4 Risk reduction projection for end of the century future climate conditions under the RCP 8.5 scenario ..	56
3.2 Modeling framework .....	57
3.2.1 Modeling impact of seagrass as Nature-based solution (Hereon).....	57
3.2.2 Potential application of salt marsh as a Nature-Based-Solution (NBS) for coastal protection (NLWKN) ..	65
3.2.3 Role of morphological feedbacks on the effectiveness of Nature-based solutions (Deltares).....	71
3.3 Efficiency of sea-grass in coastal protection (Hereon).....	86
3.3.1 Present day baseline .....	86
3.3.2 Seasonal variability .....	90
3.3.3 Extreme events with different return periods .....	92
3.3.4 Evaluating the benefit of sea-grass under end of the century climate conditions .....	99
3.4 Effect of saltmarsh on hydrodynamics and morphology (NLWKN) .....	105
3.4.1 Water level.....	105
3.4.2 Bed shear stress .....	106
3.4.3 Sediment transport and bed evolution.....	107
3.4.4 Conclusions .....	111
3.5 Role of morphological feedbacks on the effectiveness of Nature-based solutions (Deltares)....	113
3.5.1 Role of SLR on ecotopes and flood risk, without morphodynamic adaptation .....	113
3.5.2 Scenarios of measures .....	119
4 Multi-risk projections and climate warnings with ESS in Venice Lagoon Pilot (CMCC, COR) ..	121
4.1 Introduction .....	121



4.2	Methodological approach .....	122
4.2.1	“What-If” scenarios.....	122
4.2.2	Climate change scenarios selection and description .....	123
4.2.3	Numerical implementations .....	125
4.3	Results .....	127
4.3.1	Circulation .....	127
4.3.2	Waves .....	131
4.3.3	MOSE barriers closure .....	133
4.4	Conclusions .....	134
4.5	Annexes.....	135
5	Multi-risk projections and climate warnings with ESS in Arcachon Bay Pilot (EGIS, INR) .....	138
5.1	Introduction .....	138
5.1.1	Context.....	138
5.1.2	Objectives .....	138
5.1.3	Methodology.....	138
5.2	Socio-economic analysis .....	138
5.2.1	General situation .....	138
5.2.2	Port activities .....	139
5.2.3	Tourism and marine recreational activities .....	142
5.2.4	Oyster farming .....	144
5.2.5	Conclusion.....	145
5.3	Impact assessment.....	146
5.3.1	Method .....	146
5.3.2	Current and climatic forcing conditions.....	146
5.3.3	Sediment dynamics.....	149
5.3.4	Water quality .....	153
5.4	Sensitivity of ESS to climate forcing and multi-impact chains.....	154
5.4.1	Sediment management.....	154
5.4.2	Water quality .....	157
5.5	Conclusion.....	159
6	Multi-risk projections and climate warnings with ESS in Sicily Lagoon Pilot (UC).....	160
6.1	Case study .....	160
6.2	Materials and methods .....	161
6.2.1	Input data description.....	161
6.2.2	Modelling setup .....	165
6.2.3	Model validation .....	168
6.2.4	Simulations .....	173
6.3	Performance of the Nature-Based solutions under different climate scenarios .....	173
6.4	Conclusions .....	181
7	Multi-risk projections and climate warnings with ESS in Foros Bay Pilot (BAS) .....	182

7.1	Study framework.....	182
7.2	Data .....	183
7.2.1	Bathymetry & Topography .....	183
7.2.2	Waves and surge.....	183
7.2.3	Bottom sediments.....	184
7.2.4	Vegetation.....	184
7.3	Models and methods .....	185
7.3.1	Design of extreme hydrometeorological events.....	185
7.3.2	Modelling system.....	186
7.3.3	Ecosystem Services (ESS) assessment.....	191
7.4	Results and discussion.....	191
7.4.1	Hydrodynamic modelling .....	191
7.4.2	Morphodynamic modelling.....	195
7.4.3	Assessment of ecosystem services .....	198
7.5	Conclusions .....	199
8	Multi-risk projections and climate warnings with ESS in Vistula Lagoon (IBW) .....	201
8.1	General setting.....	201
8.2	Sea level rise.....	201
8.3	Hydrodynamic forcings .....	202
8.4	Conclusions .....	203
9	Integrated conclusions.....	204
	References.....	207

## Preface

The Rest-Coast Project (Large scale RESToration of COASTal ecosystems through rivers to sea connectivity) is an EU Horizon 2020 research project (Grant agreement No. 101037097) whose overall goal is to address with effective and innovative tools the key challenges faced by coastal ecosystem restoration across Europe. The approach chosen for this project will deliver a highly interdisciplinary contribution, with the demonstration of improved practices and techniques for hands-on ecosystem restoration across several pilot sites, supported by the co-design of innovative governance and financial arrangements, as well as an effective strategy for the dissemination of results.

## Summary

REST\_COAST / WP2 has prepared a risk assessment simulation tool based on calibrated hydro-morpho-eco coupled models with ESS parameterised as a function of restoration scale and climatic conditions. The coupled models, calibrated for present conditions and critically analysed for future climates, notably relative sea-level-rise and changes in storminess, have been used to simulate impacts across time (from storms to decades) with consistency across scales, considering the socio-economic data and projections available at the Pilots to co-design limits for alarm levels. Here the partners have agreed on future downscaled scenarios (SSP2-RCP4.5 and SSP5-RCP8.5) and horizons to be used in comparable analyses, including the return periods (5, 50 and 100 years) for assessing storm impacts. The resulting risk estimations, with explicit error intervals based on in-situ/satellite data, aim to provide warnings for present conditions (Task 2.1 / D2.1) and future scenarios (Task 2.2) with model application limits and co-designed thresholds for the dashboard being developed in WP6. This work has been the basis to prepare good practice criteria for multi-variable risk reduction from restoration/ESS at the Pilots (D2.2), as a function of projection horizon and domain scale, as enablers to introduce risk products in coastal management.

## List of abbreviations

BAS	Institute of Oceanology in Varna
BSS	Brier Skill Score
CMCC.	Centro Euro-Mediterraneo sui Cambiamenti Climatici
COR.	Consorzio coordinamento delle ricerche al Sistema lagunare di Venezia (CORILA)
CORE-PLAT.	COastal REstoration PLATform
D.	Deliverable
DEL.	Deltares
EGIS.	EGIS Water and Maritime
ESS.	Ecosystem services
EU.	European Union
FSK.	NLWKN-Forschungsstelle Küste
HZG.	Helmholtz-Zentrum Geesthacht
INR.	Institut national de recherche pour l'agriculture, l'alimentation et l'environnement INRAE
M.	Milestone
NBS.	Nature-Based Solutions
NN.	NetworkNature
RMSE	Root Mean Square Error
SLR	Sea Level Rise
T.	Task
TDV.	Tour du Valat
UC	Università degli Studi di Catania
UPC.	Universitat Politècnica de Catalunya
UPM.	Universidad Politécnica de Madrid
WP.	Work Package

## 1 General introduction

Coast is facing increasing risks of flooding and coastal erosion from extreme storms, which are becoming more frequent and intense in the context of global climate change. These risks pose a significant threat to the region's coastal communities and ecosystems, and we are committed to finding solutions to mitigate them. A unique challenge in all RESTCOAST Pilot Sites, is that the implementation of conventional hard and grey engineering solutions such as dams and breakwaters are less attractive. This reflects the need to preserve the ecological integrity and aesthetic values of the coast, and underlines the delicate balance between conservation and the need for adaptive strategies. Therefore, the need for innovative, Nature-Based Solutions has received more attention in recent years.

Restoration scenarios have been defined in WP1 for each Pilot and their analysis requires high resolution modelling suites at each site, with different levels of discretizations and suited to simulate different types of hydro-morpho-eco dynamics and interactions.

For the present deliverable report D.2.2, risk reduction in relation to flooding and erosion during future hydrodynamics and extreme wave condition at the Pilot Sites is the focus of the work developed. And with the aim to mitigate coastal risk and restore biodiversity value, a range of Nature-based Solutions (NBS) are investigated considering a current state (with actual active restoration measures) and proposed additional restoration measures.

Using their respective modelling frameworks previously described in D 2.1, the RESTCOAST partners address respectively:

- The restoration of seagrass areas as a coastal protection measure to provide ecosystem buffers and attenuate wave energy, reduce near-shore currents and stabilize the seabed (e.g. Foros Bay and Arcachon Bay);
- The development of saltmarshes which include actions such as the excavation of channels, the creation of tidal flats, re-naturalisation and seagrass transplantation (e.g. Venice Lagoon and Wadden Sea);
- And effective sediment management strategies as dune reconstruction and revegetation to stabilize the dune and improve wave dissipation capabilities of the system (e.g. Ebro Delta, Sicily Lagoons, and Vistula Lagoon);

as NBS with respect to potential improvements for different aspects of the ESS at concern.

RESTCOAST/Task 2.2 has defined (M2.3) future conditions under the commonly agreed climate scenarios and the Pilot restoration scenarios, in order to consistently forecast restoration effects on ESS delivery. Downscaled climate projections have been derived from the commonly agreed global climate scenarios (business-as-usual SSP2-RCP4.5 and pessimistic SSP5-RCP8.5, mean and upper limits) for horizons 2070 and 2100 at least. These scenarios, together with the commonly agreed return period for extreme events, define mean sea level, waves and wind projections for our Pilots, with the site to site variability introduced by the managed restoration scenarios.

## 2 Multi-risk projections and climate warnings with ESS in Ebro Delta Pilot (UPC, UPM)

### 2.1 Ebro Delta Coast

UPC is working within different mitigation strategies to reduce the impacts of storms in the Ebro Delta Coast. The approach is based on a selection from more classical interventions to more new strategies to see the efficiency of each one in present and future conditions. Specifically, they have been tested on the Trabucador Barrier beach, which has been affected with episodes of breaching during the last decades (Jiménez and Sánchez-Arcilla, 2004). The barrier beach connects the mainland with an arrow-shape end (Banya Spit), where a salt industry is located. This corridor, jointly with a high tourism rate in the barrier makes the zone important in terms of the economy of the region (Figure 2.1). Besides, the Fangar bay situated on the back of the barrier beach was designated as a RAMSAR site, with the presence of the mollusk species *Pinna nobilis* (Rodríguez-Santalla and Navarro, 2021) classified as “Critically Endangered” by IUCN Red List and as “Threatened” according to the SPA/BD Protocol Annex II under the Barcelona Convention. For all these reasons, the aim of UPC is to develop a strategy that is able to bare the storm effects in the barrier beach for present and future conditions. During the last decades, some strategies as dune systems have been tried. It has been seen that even if they work for a short amount of time, the constant hit of the waves jointly with the littoral sand transport produce a destruction of the structure at long-term. UPC is trying to be able to use a mitigation approach that can last during these long-term scenarios with few additional actions at the same time that greatly reduces the hazards on the area.

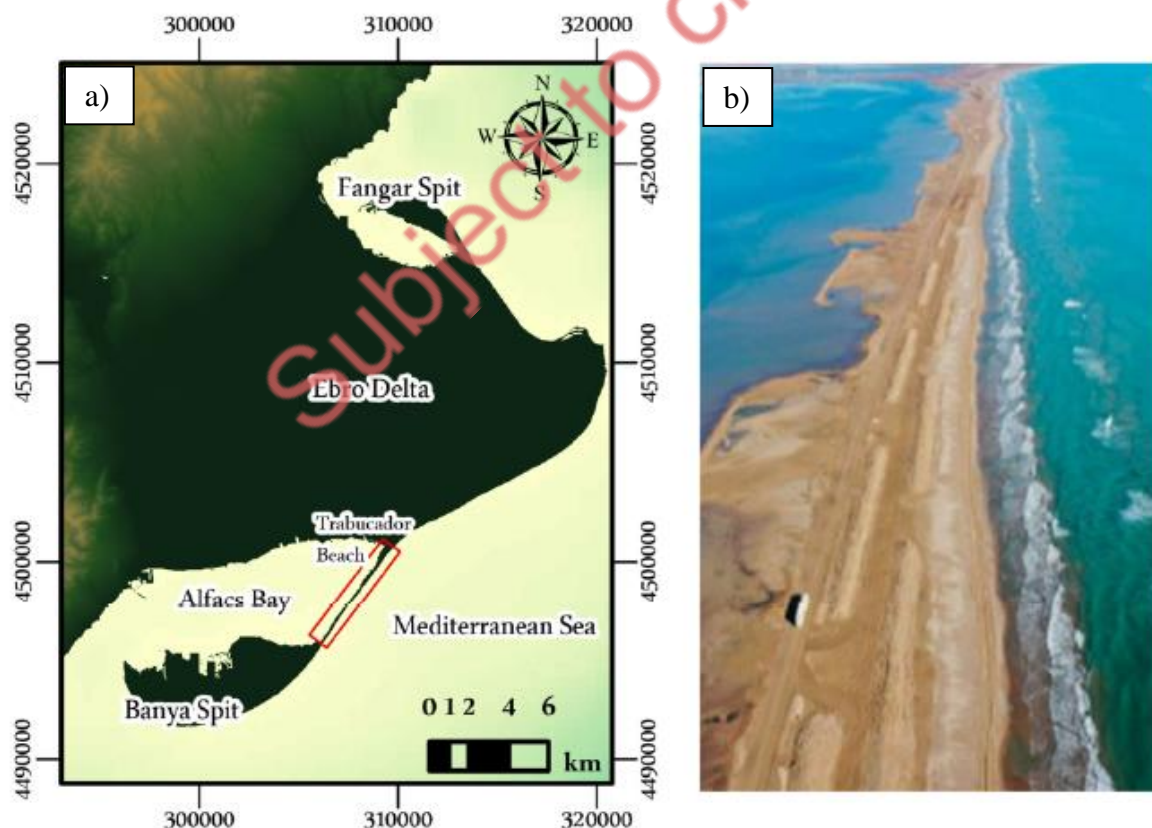
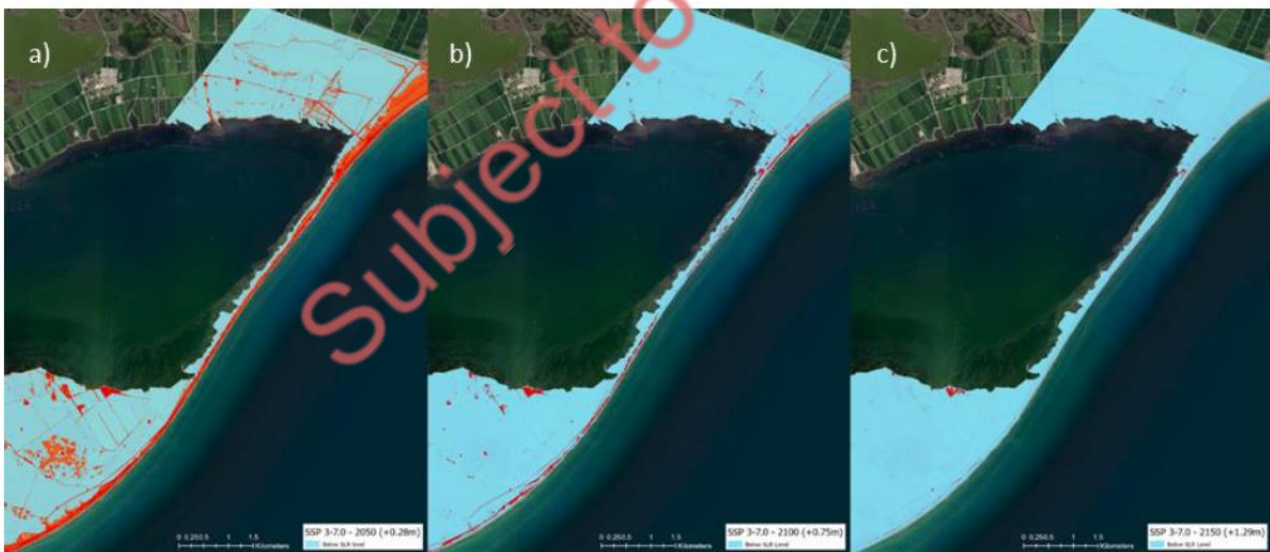


Figure 2.1. a) Ebro Delta. The red rectangle shows the study area which corresponds to the Trabucador barrier beach. b) Placement of an embryonic alternating dune system during 2023 in the Trabucador barrier beach.

Due to Ebro Delta being a low-lying environment (Grases *et al.*, 2010), sea level rise (SLR) will produce a huge impact on the area. As it can be seen in Figure 2, even without taking into account the worst scenario SSP5-8.5, the area suffers high flooding rates and within 2150, almost all the study area could be affected. Instead, it is supposed that the beach will adapt and change his equilibrium profile to bare the effects of climate change and not to be totally disappeared. Even so, to simulate or replicate these dynamics is too difficult and inexact so only the increment of SLR, without changing the topo-bathymetry of the barrier beach, has been considered in this study. Because of that, the use of SSP5-8.5 would have relied in a totally disappear of the barrier beach before the arrival of the storms when studying the horizon 2100 for example, being unable to study the efficiency of the mitigation strategies in climate change scenarios. For this reason, we decided to use SSP3-7.0 which is also an extreme scenario to see the effects of the actions on the area. While this scenario is still a negative pronostic, it allows to simulate the beach without its total flooding. In the future, some other scenarios as SSP2-4.5 or the introduction of methodologies as the Brunn rule to try to replicate the evolution of the barrier beach during the increasing of the mean water level could be discussed although the general conclusions about the efficiency of the strategies would not vary in a great extent.

In order to be able to see the effects in climate change conditions, the model has to be validated in the area as well as check that the mitigation actions work on the present conditions. Following this, Section 2.1 will talk about the validation of the model XBeach in the Trabucador barrier beach as well as about the definition of metrics to define when an action works correctly. Then, Section 2.2 will present some results of the proposed strategies for the current conditions to see if it is worth to simulate them within climate change scenarios. Finally, Section 2.3 will show the simulated efficiency of the strategies at long-term under different climate projections and discuss about possible issues that each strategy could face.



**Figure 2.2.** Flood levels proportional to SLR using SSP3-7.0 a)2050, b)2100 and c)2150 (blue represents flooded and red not flooded)



### 2.1.1 Criteria to define efficiency of the risk reduction

XBeach has to be tested and validated in the area to confirm that the model is able to reproduce the response of the beach to storm conditions. The typical calibration and validation of the beach morphodynamics use the comparison of the model results with some post-storm topobathymetries profiles or bed elevations in 1D or 2D. The most used metrics are Brier Skill Score (BSS) and Root Mean Square Error (RMSE). In this case, the work had to face one challenge derived from the lack of post storm topo-bathymetric information, being impossible to use such metrics. To be able to demonstrate the correct performance of the model, a new approach in this field has been used. The methodology is known as Mapcurves and is commonly used to classify and quantify differences between categorical maps (Hargrove *et al.*, 2006). We accommodated the strategy transforming the model outputs into polygons defining the non-breached area. Then, this can be compared with satellite data from the post-storm conditions. In this case, the observed response of the beach to storms was the breaching in the form of separated islands that could be easily assimilated into different polygons. Nevertheless, it can be also used if the continuity of the beach is maintained, taking into account one single polygon when comparing with the real response. The method uses a Goodness of fit (GOF) algorithm to quantify the spatial overlap between the categorical maps or polygons, assessing a degree of agreement. Then, a perfect fit is reached if the model output and the satellite data totally coincide. The satellite data was extracted from Sentinel-2 and also transformed into polygons using a NDWI approach, which separates land from water interface (Kriegel *et al.*, 1969). As a summary, we converted our morphodynamical results into polygons representing the area that withstand the storm (non-breaching areas) and compared them with the coastline satellite data of the post-storm conditions. Then, high GOF values relies to a better level of similarity between sources and an indicator of the well-performance of the model. Equation 2.1 describes the GOF algorithm used in this study, with A representing the area of the polygons extracted from satellite images, B being the area of the shoreline polygons from the model output, C the overlapping area of both components, all three in m<sup>2</sup>, and p the number of different polygons to compare:

$$Goodnes\ of\ fit = \sum_{n=1}^p \left( \frac{C}{B+C} * \frac{C}{A+C} \right) \quad (2.1)$$

By using this methodology, any over or underestimation in the number of polygons, in our case breached island would rely in a huge decreasing in the final performance. Consequently, enhancing the strictness of the methodology to conclude that the validation is deemed satisfactory.

In our study, the best available topo-bathymetric data belongs to the end of 2020, consisting of bathymetric information from nautical chart digitization jointly with a combination of DEM + LiDAR data provided by ICGC for the topography. We used these sources to generate a mesh to be able to simulate the Filomena storm, which hit the Trabucador barrier beach in January 2021, persisting for nearly 140 hours. The maximum wave height (Hs) registered was 5.15 m with an associated peak period (Tp) of 11 s. To calibrate and validate the response of XBeach, we started using the default parameters and a selection of parameters defined by Gracia *et al.* (2013). The obtained results were not satisfactory due to updates of the model and the incorporation of new parameters, jointly with a pass from a 1D to a 2D approach. Then, after doing a preliminary numerical exercise, a deep analysis of the performance and the GOF was done for 15 different runs. The selected calibration parameters for these tries are shown in Table 2.1. From these ones, we selected 8 runs to show in Figure 2.3 the improvements during the calibration parameters, where R1-R4 were built on default, Gracia *et al.* (2013) parameters and other runs with few changes. Then, the aim was to catch the seven different breached islands in order to achieve better GOF values. More consistent results were achieved (R10-R14), being R13 the most similar to the real response compared to the satellite images. Consequent runs trying to better catch the response did not produce better results. It has to take into account that achieving more than 50% of similarity between the model and the reality relapses in a strong performance of the model due to the strictness of the used approach. The only problem is that even though predicted polygons had a strong



overlap with the observed polygons of breached islands, it under-predicted the area thus causing a reduction in GOF.

*Table 2.1. XBeach selected calibration runs. The bold simulation (R13) corresponds to the highest GOF value achieved.*

Run	XBeach Parameters	GOF
R1	Default	0
R2	dryslp = 1.0, wetslp = 0.6, smax = 1.3 (Gracia et al., 2013)	0.11
R3	dryslp = 1.0, wetslp = 0.3	0.09
R4	wci = 1	0.1
R5	nspr = 1, turb = 0, facua = 0.225	0.08
R6	dryslp = 1.0, wetslp = 0.3, gammax = 0.5, facua = 0.2	0.15
R7	dryslp = 1.0, wetslp = 0.3, gammax = 0.4, facua = 0.5	0.09
R8	dryslp = 1.0, wetslp = 0.6, gammax = 0.4, facua = 0.5, nspr= 1	0.28
R9	dryslp = 0.6, wetslp = 0.1, dilatancy = 1, gammax = 0.4, facua = 0.15	0.26
R10	dryslp = 1, wetslp = 0.3, facua = 0.15, gammax = 0.4	0.32
R11	dryslp = 1.5, wetslp = 0.75, facua = 0.15, gammax = 0.4	0.39
R12	dryslp = 1.5, wetslp = 0.8, gammax = 0.4, dilatancy = 1, facua = 0.15	0.35
<b>R13</b>	<b>dryslp = 0.6, wetslp = 0.3, facua = 0.1, dilatancy = 1, gamma = 1.5, fallvelred=1</b>	<b>0.52</b>
R14	dryslp = 1.2, wetslp = 0.4, facua = 0.1, dilatancy = 1, gammax = 0.8, fallvelred =1	0.44
R15	dryslp = 0.3, wetslp = 0.1, gammax = 1.5, dilatancy = 1, facua = 0.1	0.48

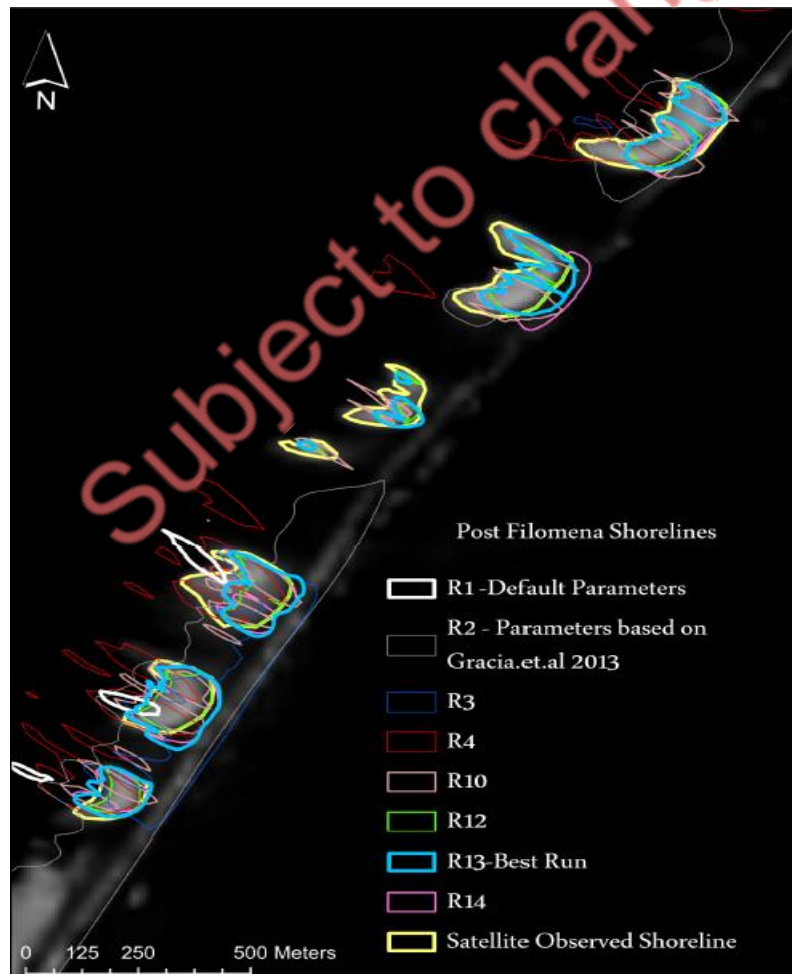


*Figure 2.3. Polygons from 8 runs compared with the Sentinel-2 extracted shoreline (yellow rectangle).*

Once the model was able to catch the response of the beach under the storm, some metrics about how to quantify the efficiency of the different mitigation strategies was discussed. First, area breached was chosen as a good metric and defined as it can be seen in Equation 2.2. This approach was chosen to give importance to the continuity of the barrier. If the breached area results on a high value, the probability that trucks are not be able to cross the barrier beach and therefore, the connection between the mainland and the arrow-end is disappeared increases. The definition relies on the quantification of number of nodes (or grids) in the model that are below 0.3m (threshold to define breaching) and then multiplied for the area of each grid which is well-know for the definition of the complete mesh.

$$\text{Breaching area} = (\text{No of grids} < 0.3\text{mBL}) \times \text{area of grid} \quad (2.2)$$

Moreover, the description of the breaching in terms of volume instead of area was also discussed. This relied in a more ecological approach since volume gives information about how much sediment is lost in the event and how difficult would be to recover the beach to its initial state. Besides, the sediment can also go to the back of the barrier affecting the normal dynamic of the bay and the whole environment. The used formula for the definition of the volume can be seen in Equation 2.3.

$$\text{Breaching volume} = \sum \begin{cases} (\text{Area of each grid} < 0.3\text{m}) * (0.3\text{m} - \text{BL}) & \text{if BL is positive} \\ (0.3\text{m} + \text{BL}) & \text{else} \end{cases} \quad (2.3)$$

Finally, although these metrics could give information about the capacity to reduce the risk of loss of sediments and the damages in the barrier beach under storm conditions, an efficiency approach will be easier to understand because it is based on percentage and not in total values. For this reason, we also defined efficiency as it can be seen in Equation 2.4 to check in % which strategy works better for each condition.

$$\text{Efficiency} = \frac{\% \text{breaching of NP} - \% \text{breaching of CP}}{\% \text{breaching of NP}} * 100 \quad (2.4)$$

where NP is no protection and CP is coastal protection.

### 2.1.2 Risk reduction from different approaches

Once the model was validated for the study area and the metrics were defined, we tested if the proposed strategies worked for present conditions. As stated at the start of Section 2, four different scenarios were simulated. First, the benchmark corresponded to the strategy where no protection was placed in the study area. Then, following an action done in the barrier during the start of 2023, an embryonic alternating dune system was placed into the mesh (Figure 2.1). Finally, the introduction of a continuous dune and a classical nourishment approaches were created to have a more general view about the response of the beach to a series of different strategies (Figure 2.4). Besides from selecting different mitigation strategies, they were also tested under three different storm conditions in order to get storm of the three highest categories defined by Mendoza *et al.* (2011) to classify a storm in the Catalan coast. Then, in addition to Filomena, used for calibration/validation, and that corresponds to a category IV out of V, also Gloria and Isaak storms were studied. Gloria was the most important storm ever recorded on Catalonia (category V/V) and Isaak was selected because was the storm hitting the barrier beach just after the placement of the alternating dunes on the field (with a category III/V).

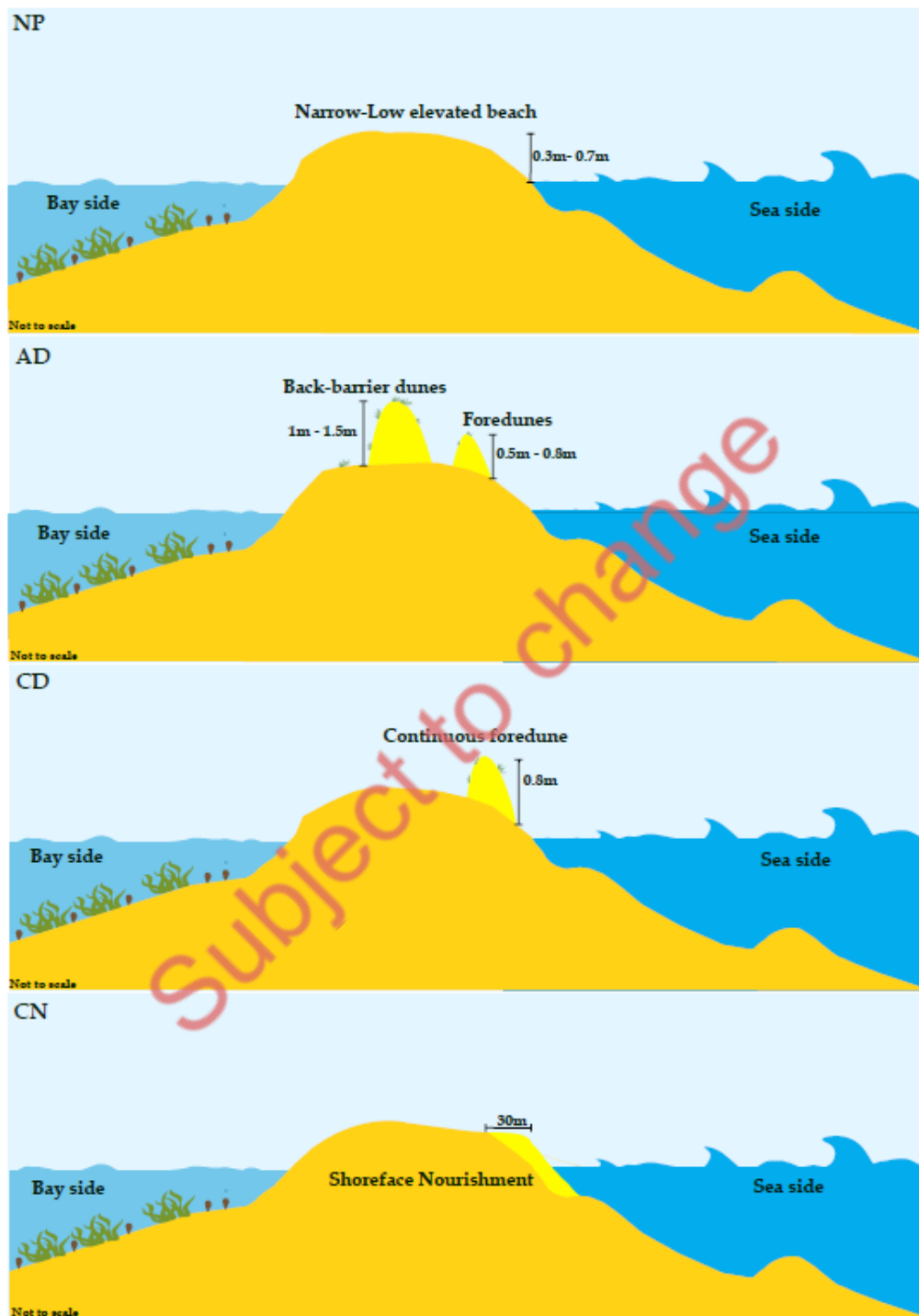
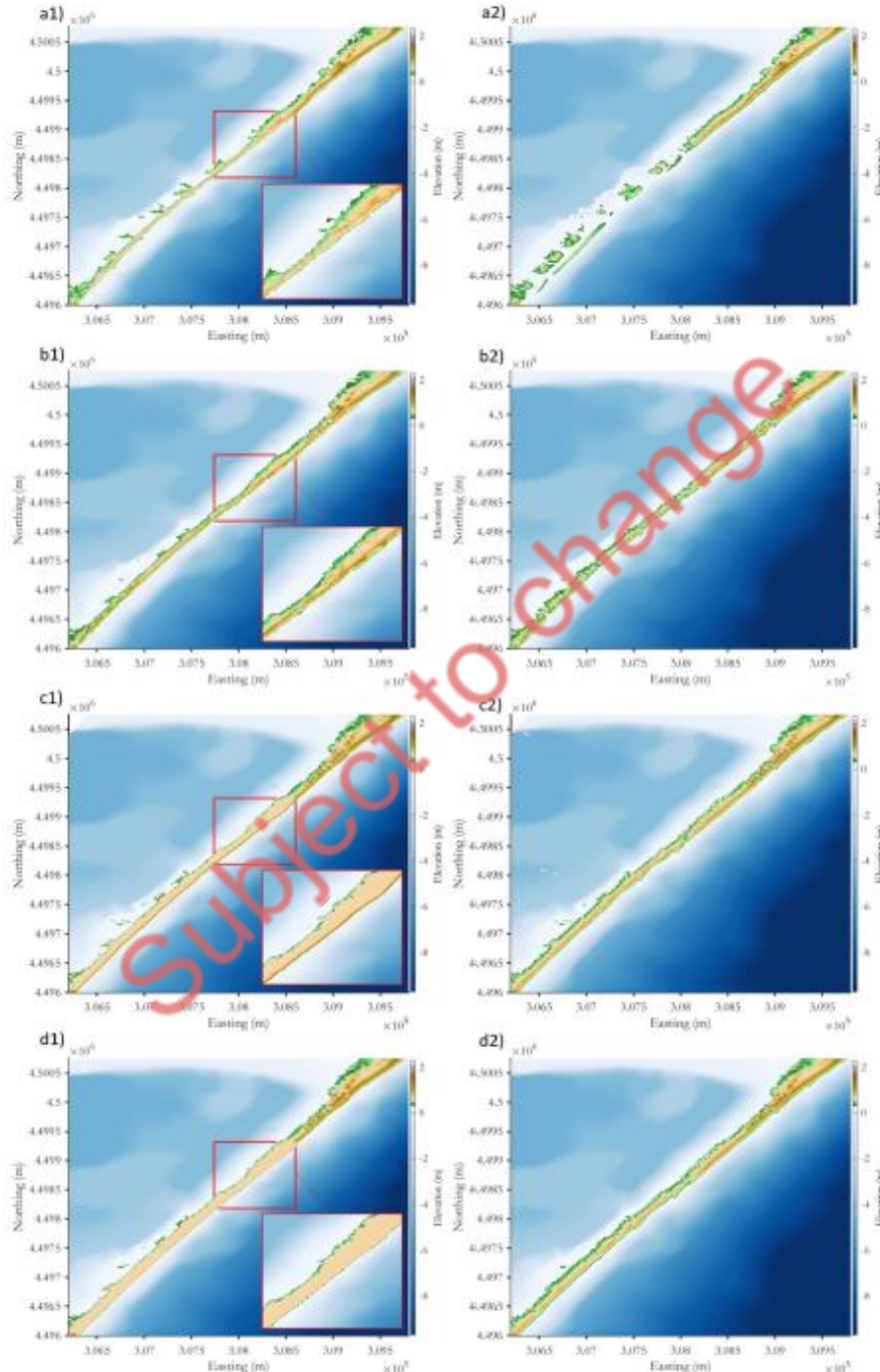


Figure 2.4. Schematisation of mitigation strategies. NP means No protection, AD alternating dunes, CD continuous dunes and CN classical nourishment.

The results of the model for each storm and within the mitigation actions for present conditions are shown in the next pages. **Error! No se encuentra el origen de la referencia.** shows the effects of Filomena (already shown in Figure 2.3 for the calibration/validation) within the benchmark test where the seven breached island can be observed. Then, it can be seen that thanks to the implementation of the three strategies, the effects could be heavily reduced, all of them completely maintaining the continuity of the barrier beach.



**Figure 2.5.** State of the barrier before (1) and after (2) storm Filomena for No protection (a), Alternating dunes (b), Continuous dunes (c) and Classical nourishment (d).

Figure 2.6 shows the response of the barrier to Storm Gloria and since this was the biggest storm recorded, it can be seen that even with the implementation of the mitigation action, the barrier beach suffers from

heavy breaching events. Classical nourishment seems to be the best strategy, but it cannot maintain the totality of the continuity on the barrier.

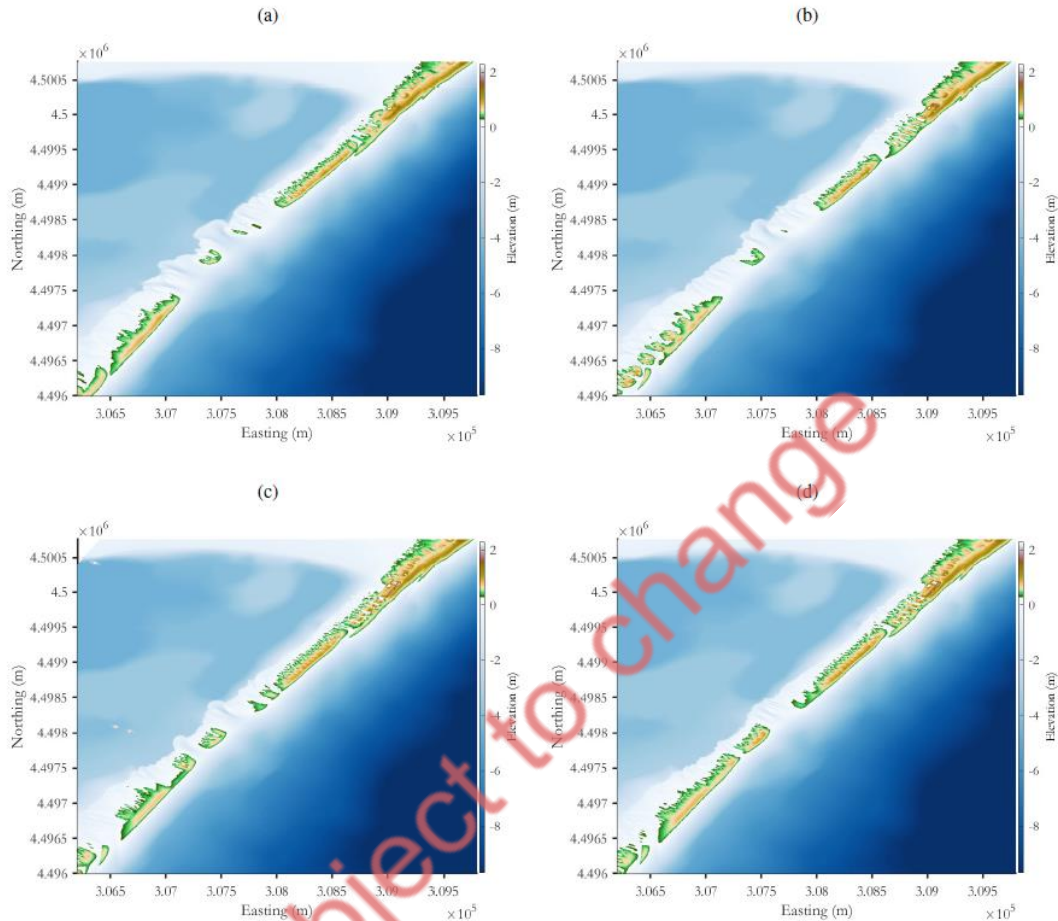


**Figure 2.6.** State of the barrier after storm Gloria for No Protection (a), Alternating dunes (b), Continuous dunes (c) and Classical nourishment (d).

Finally, Figure 2.7 shows the impacts produced by storm Isaak, being in this case the control the scenario with the placement of the alternating dunes system. It can be seen that although the other strategies also maintain the continuity of the barrier beach, if no protection action would have been done, problems could have raised from the wave impacts associated with breachings.

The results are easily to discuss in terms of numbers more than with images and thus, Figure 2.8 represents the reduction of the storm effects in terms of total volume and area breached during the event for each storm and mitigation strategy. We can observe that Isaak didn't produce breaching, neither in volume or area when mitigation actions are present while if these strategies are not placed into the model, some affectations are visible. This enhance the necessity to incorporate such actions. When studying Filomena, the response is the same where the introduction of the three mitigation actions relies in a huge reduction on the impacts produced by the storm compared to the no protection case. Even for Gloria, where no reduction can be visually observed from the figures, when computing the metrics, the volume of breaching is reduced although the area is not. This concludes that even if the continuity cannot be maintained with the mitigation strategies, the reduction in volume can ease the reconstruction of the barrier once the storm pass.



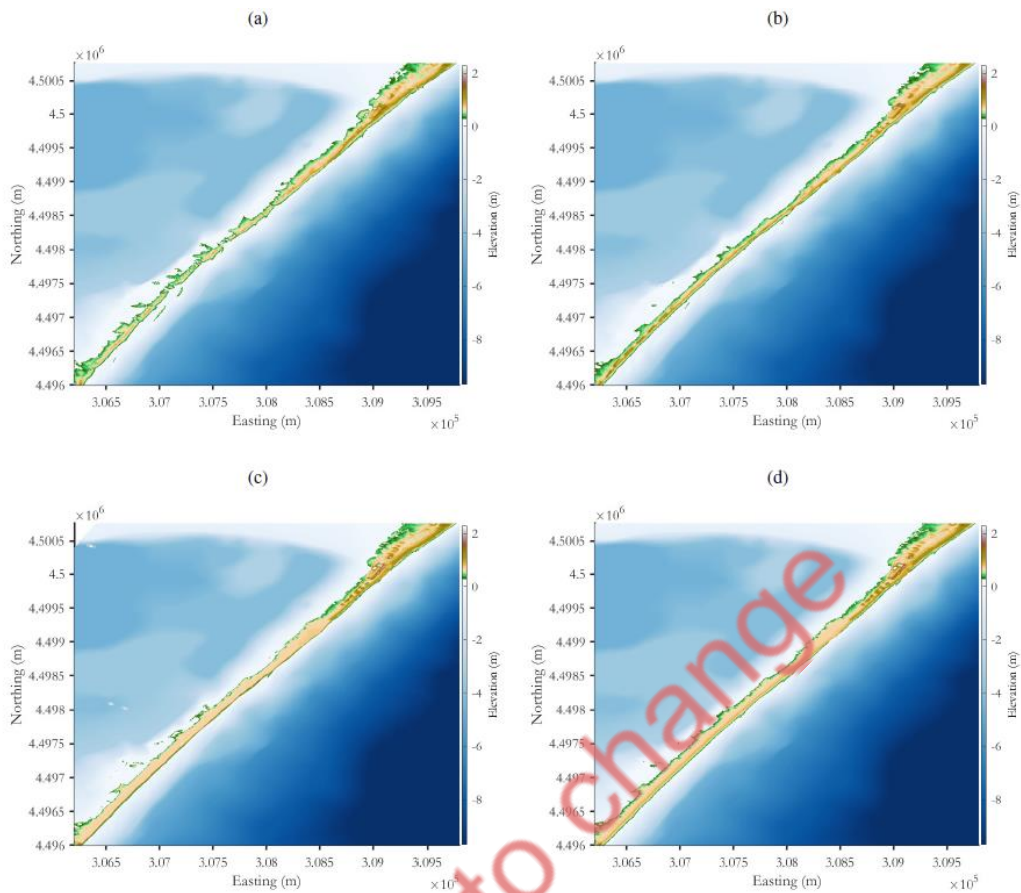


Figure 2.7. State of the barrier after storm Isaak for No protection (a), Alternating dunes (b), Continuous dunes (c) and Classical nourishment (d).

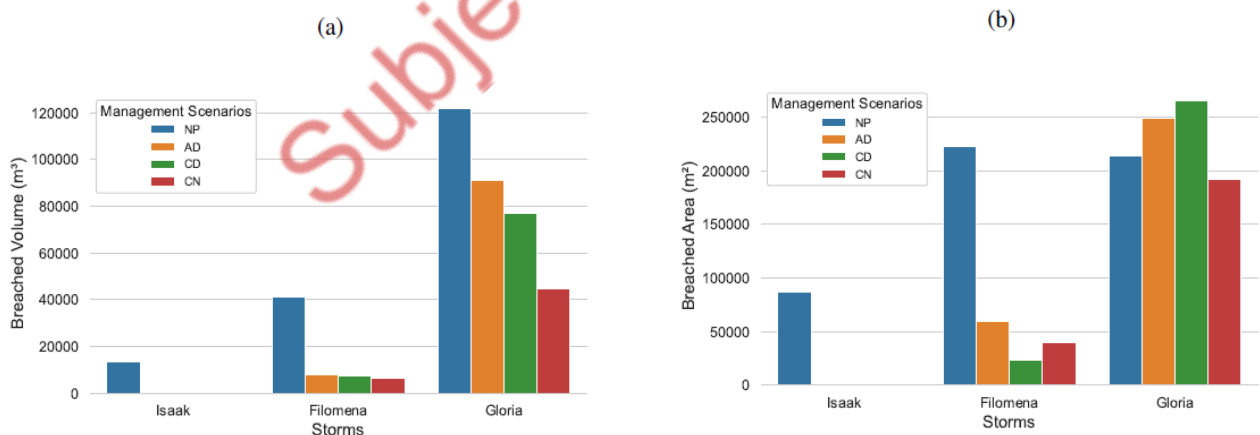
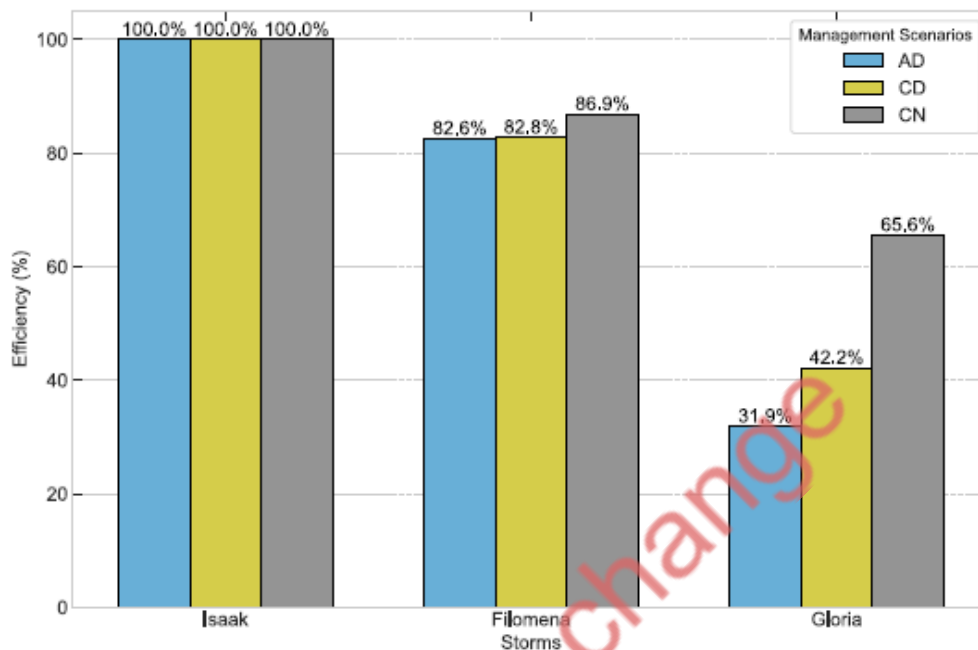


Figure 2.8. a) Breached volume for each storm condition and within the different mitigation strategies. b) Breached area for same testing scenarios.

To be able to compare the efficiency of the different strategies with the case without protection, Figure 2.9 analyses the percentage of reduction using the equation described in Section 2.1.1. For storm Isaak, the efficiency reaches 100% for all three strategies because from the breaching volume that can be observed from the no protection case we are able to reduce it completely when including the measures, fully

maintaining the continuity of the barrier. Then, with Filomena storm the reduction is also very high with more than 80%, meaning that the strategies are essential to reduce the impacts of such kind of storms. Even for Gloria, that at first look seemed that no reduction was produced when including these management actions, the reduction goes from 30% to even 65% when applying the classical nourishment approach.



*Figure 2.9. Efficiency of the different strategies compared to the benchmark (no protection)*

### 2.1.3 Efficiency at long-term under different climate projections

As stated in Section 2.1.2, the efficiency at long-term under different climate projections will be based on the IPCC AR6 SSP3-7.0 scenario since more negative scenarios as SSP5-8.5 would rely in a complete flooding of the area for the longest horizons. Then, this scenario will be simulated under 2050, 2090 and 2100 projections. Following the estimates of IPCC AR6, the increase of sea level for the area will be +0.27m, +0.57m and +0.75m respectively. Moreover, the continuous dune strategy will not be longer studied since previous results showed similar results with alternating dunes and we consider the latter better in terms of ecology and long-term persistence. In Figs. 2.10 - 2.18, the graphical results for the simulations are presented, where it can be seen the effect of each storm for all three different climate projections and within each mitigation action. It can be observed that for the period 2050 the changes are not so important although some more breaching is detected for the three storms. Then, when simulating in the 2090, the response of the beach for the Filomena storm seems like the same as Gloria in the present and Isaak is more similar to actual Filomena response. Finally, within 2100 horizon, all three storms produce heavy breaching damages and no mitigation strategy is able to sufficiently reduce the damages. Besides, all of them seems closer to Gloria's effects nowadays, concluding that within these worse-case scenarios at long-term, the proposed approaches seem inefficient.

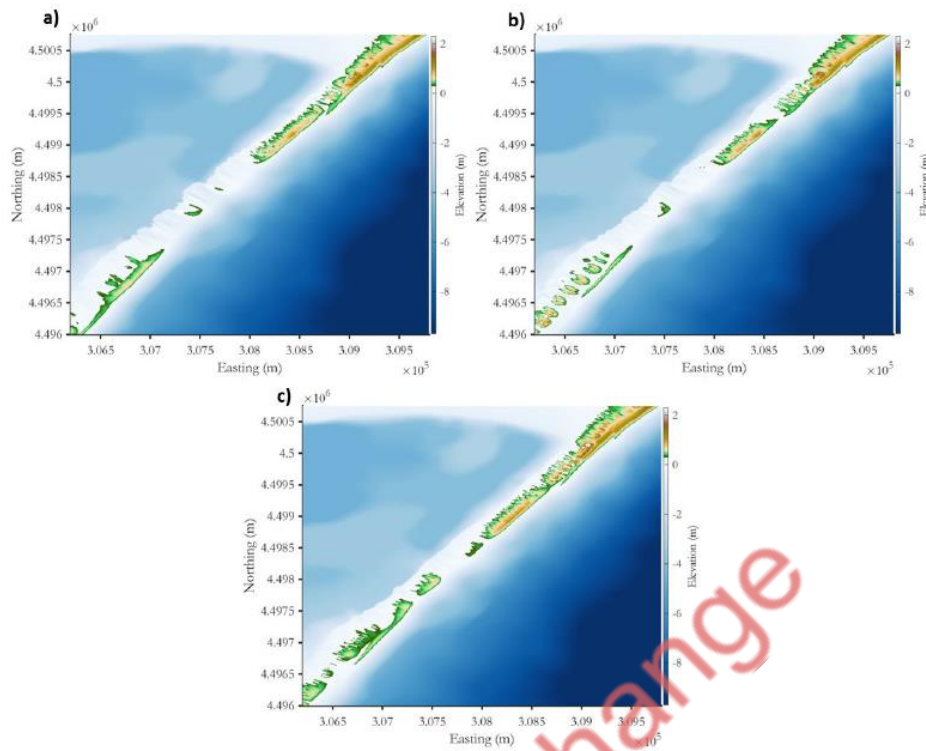


**Figure 2.10.** Final bed level after storm Filomena in +0.27 SLR conditions. a) No protection, b) Alternating dunes and c) Classical nourishment.

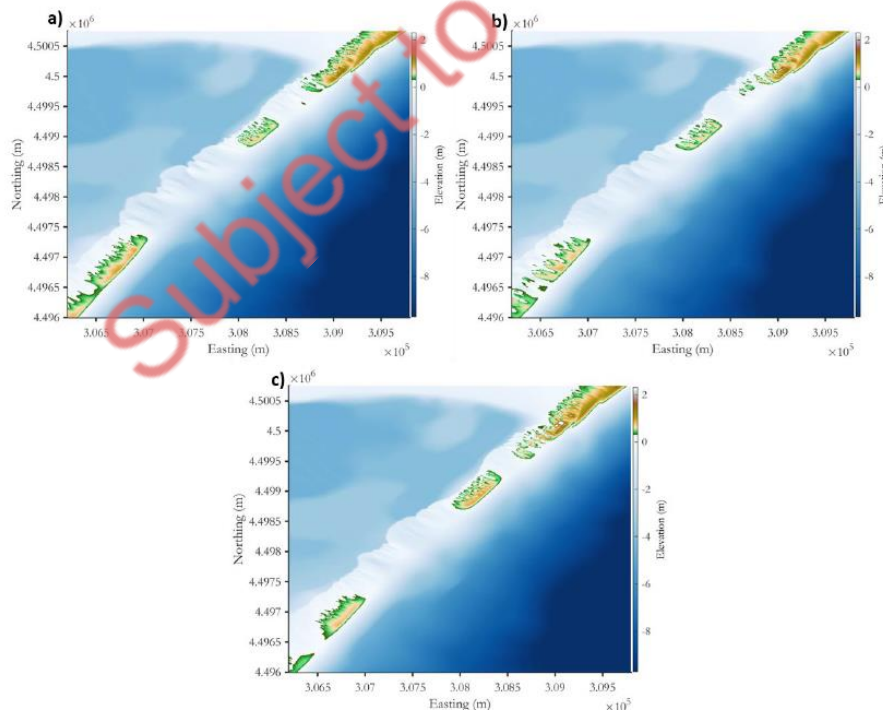


**Figure 2.11.** Final bed level after storm Gloria in +0.27 SLR conditions. a) No protection, b) Alternating dunes and c) Classical nourishment.



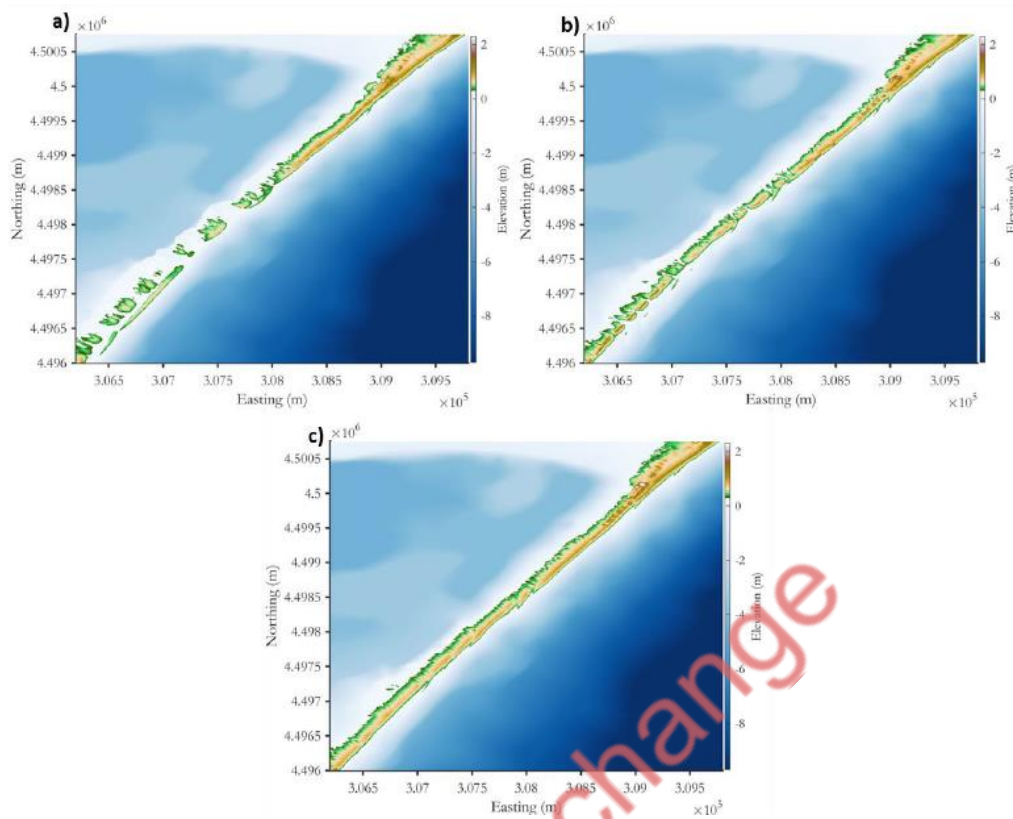


**Figure 2.12.** Final bed level after storm Isaak in +0.27 SLR conditions. a) No protection, b) Alternating dunes and c) Classical nourishment.

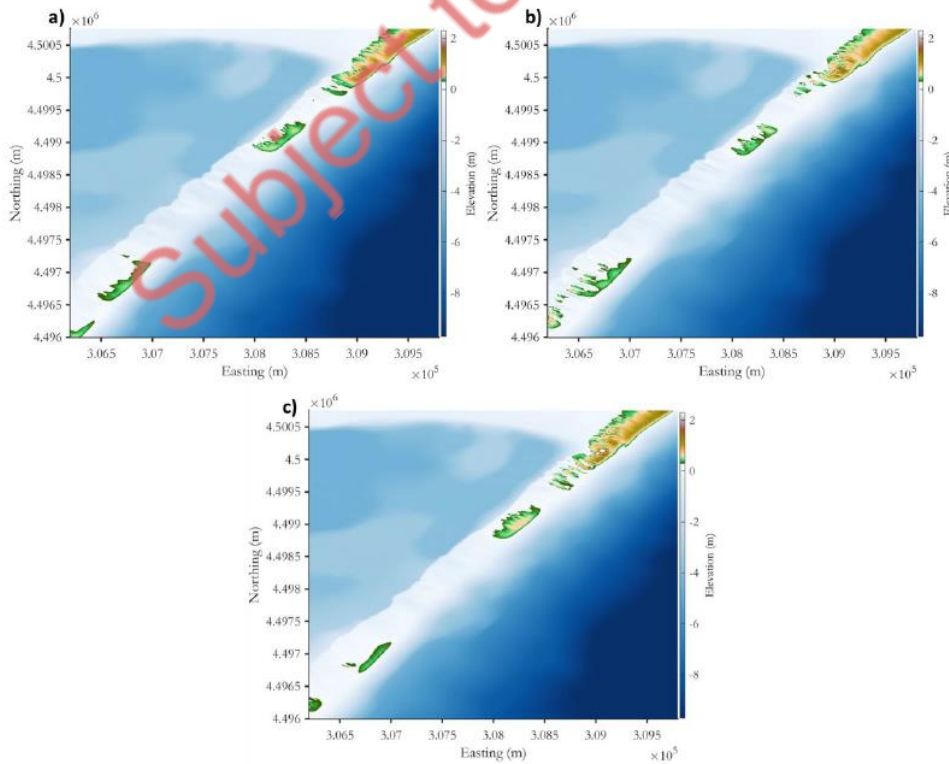


**Figure 2.13.** Final bed level after storm Filomena in +0.57 SLR conditions. a) No protection, b) Alternating dunes and c) Classical nourishment.

## D2.2 Good practice criteria Multi-variable risk projections

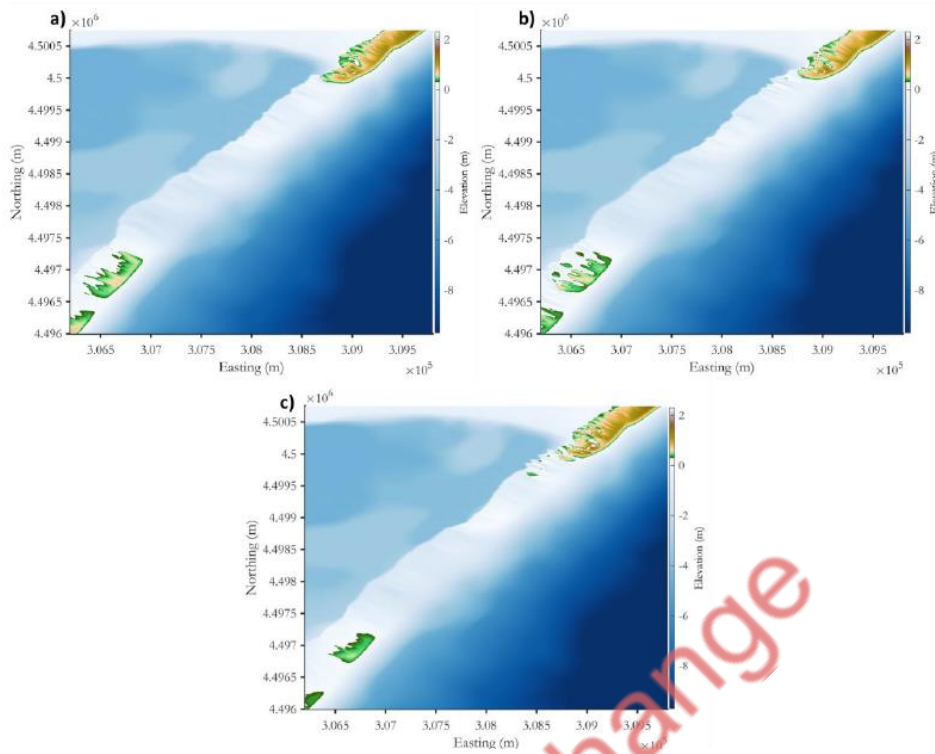


*Figure 2.14. Final bed level after storm Gloria in +0.57 SLR conditions. a) No protection, b) Alternating dunes and c) Classical nourishment.*

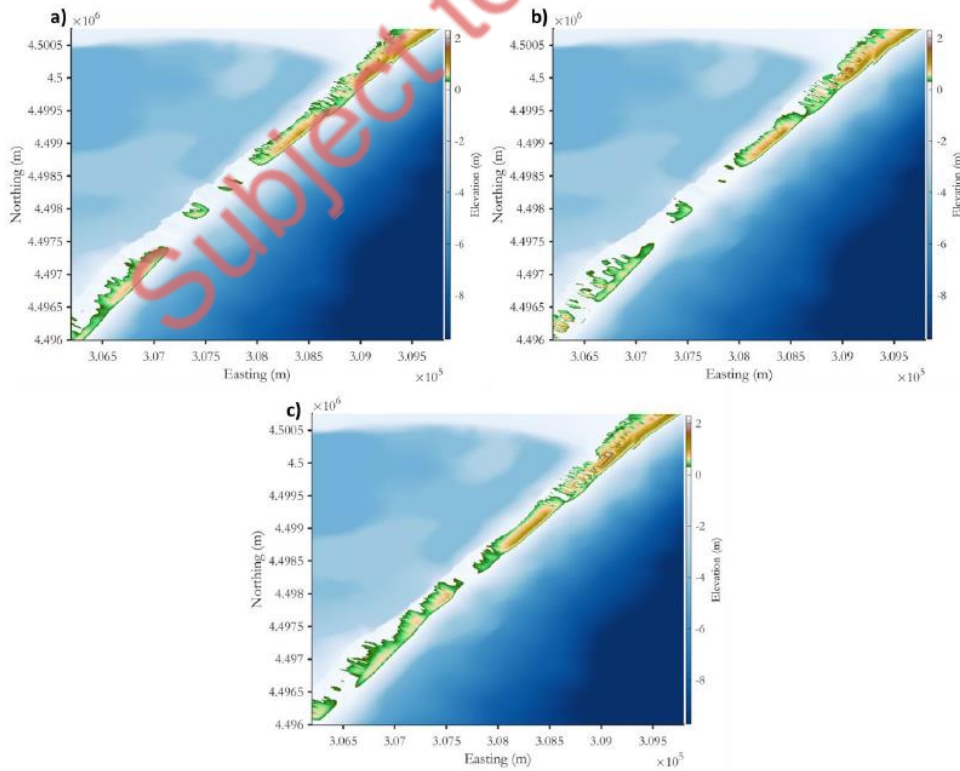


*Figure 2.15. Final bed level after storm Isaak in +0.57 SLR conditions. a) No protection, b) Alternating dunes and c) Classical nourishment.*

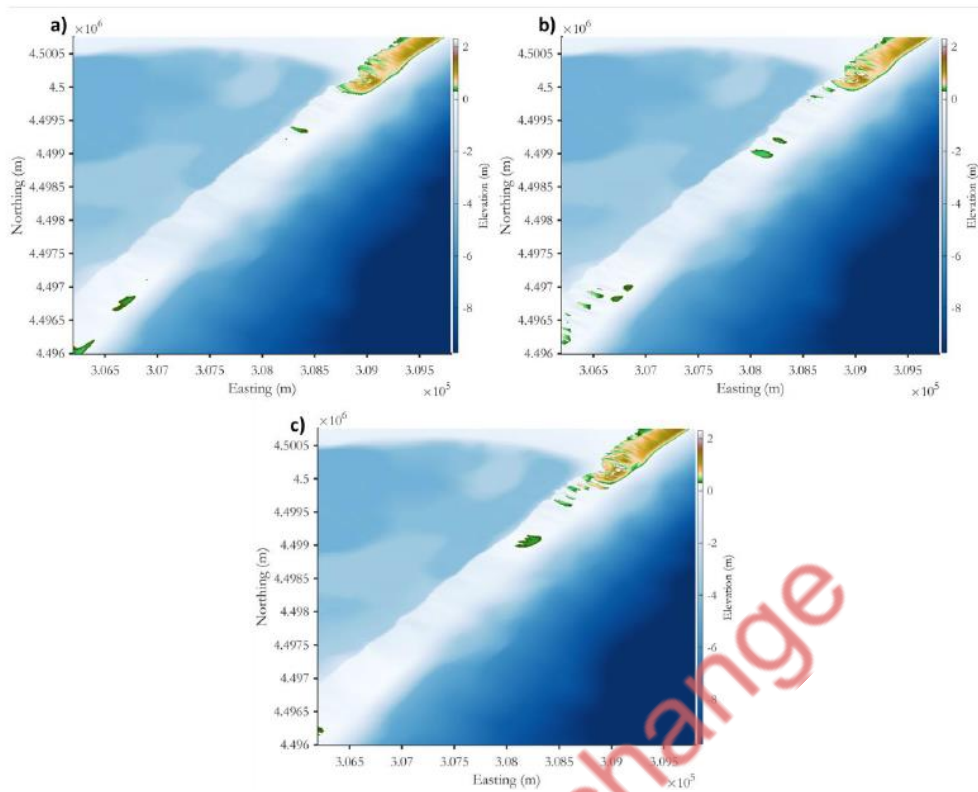


**Figure 2.16.** Final bed level after storm Filomena in +0.75 SLR conditions. a) No protection, b) Alternating dunes and c) Classical nourishment.

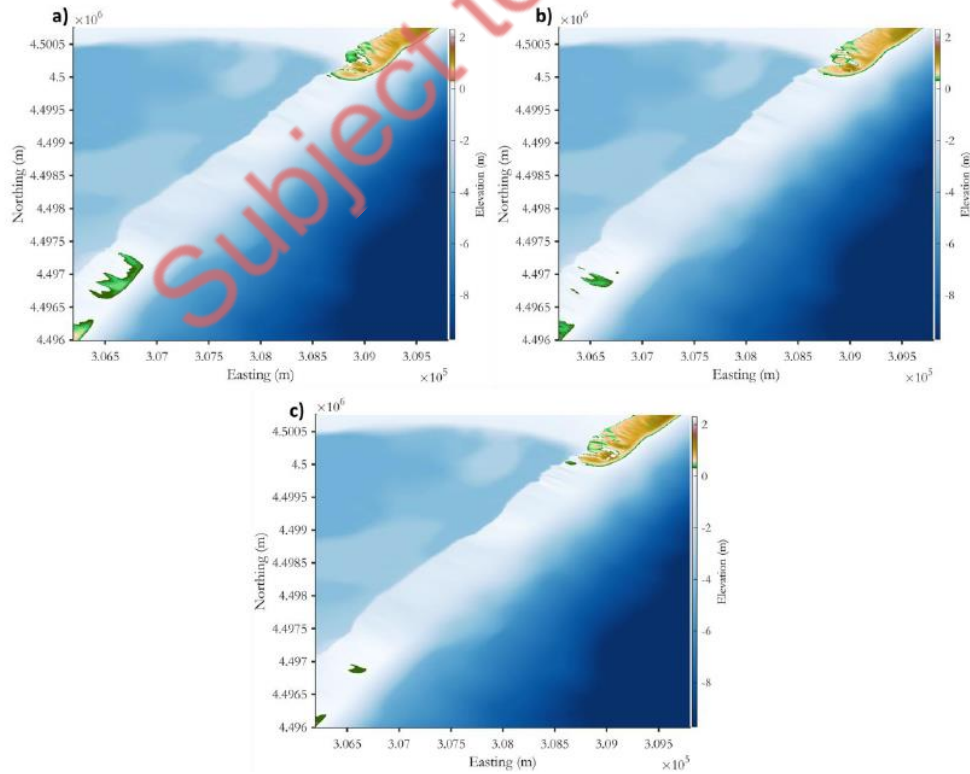


**Figure 2.17.** Final bed level after storm Gloria in +0.75 SLR conditions. a) No protection, b) Alternating dunes and c) Classical nourishment.

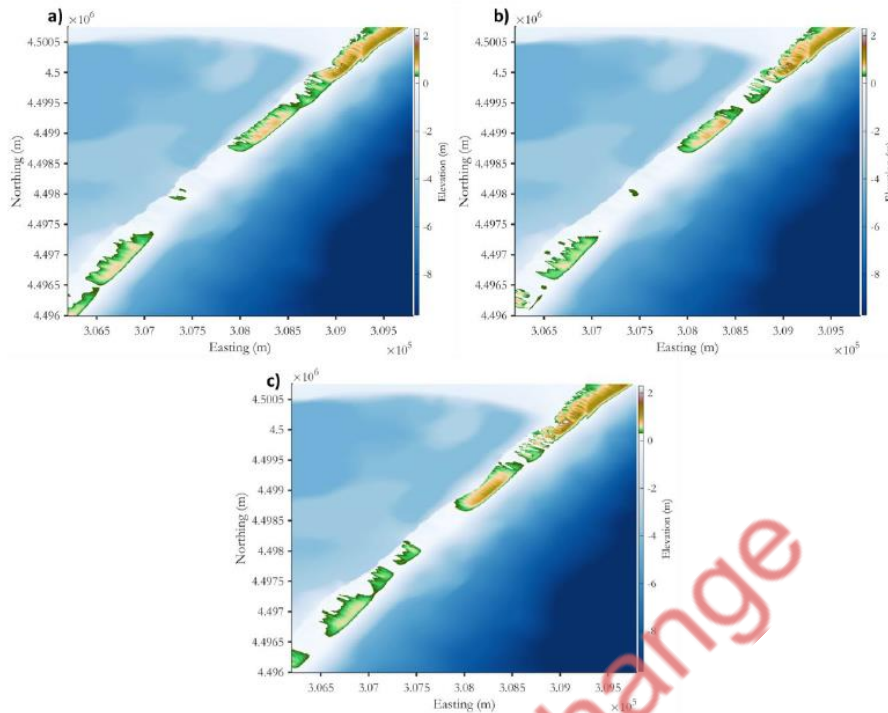


**Figure 2.18.** Final bed level after storm Isaak in +0.75 SLR conditions. a) No protection, b) Alternating dunes and c) Classical nourishment.

Again, to be able to see the real efficiency in future climate projections, it is necessary to use the metrics instead of the graphical information. In Figure 2.19, this general efficiency for all the studied case scenarios is provided. Comparing the alternating dune system with classical nourishment at the present and future conditions, we can see how the efficiency is reducing while going further into the future horizons. For the classical nourishment, under storm conditions like Gloria and Filomena the efficiency even reaches negative values because the input of sediment is also considered as breached. It can be also observed that for future projections, embryonic alternating dunes seems to work better for the higher storms meanwhile for Isaak, since the effects are not so strong, classical nourishment continues to perform better. Moreover, it can be discussed that when these thresholds are reached, the mitigation strategies would not be enough to protect the barrier beach.

#### 2.1.4 Conclusions

To conclude, in the present conditions, classical nourishment seems to be the best strategy followed by the continuous dune, with alternating dunes being the worst mitigation action although all of them heavily protect the beach from suffering damages. Nevertheless, this has to be put in a long-term view where alternating dune ends being the best strategy for several reasons. First, the simulations show that within future projections, the efficiency gap is reduced until at the end alternating dunes perform better even better than classical nourishment. Besides, classical nourishment has a huge associated problem when planned as long-term action derived from the littoral sediment transport (Dean and Yoo, 1992; Benedet *et al.*, 2016). This effect produces a known loss of sediment through time, being necessary to re-nourish the area to maintain its effectiveness. The continuous dune has been used during the last decades in different tests and although it reduces the hazard, the constant hit of waves produces the destruction of the structure at long-term. Also, the continuous dune is very weak against consecutive events for the same reason. Instead, the



embryonic alternating dune system is a more stable strategy since the waves hit the front dunes and the back ones are maintained intact, increasing their efficiency though time (Houser *et al.*, 2008; Pries *et al.*, 2008). The best strategy then would be to use alternating dune and reconstruct the front dunes if necessary and even create some small nourishments to help the structure. These small nourishments have been proved to be more ecological and stable than big nourishments (de Schipper *et al.*, 2021). Even so, when simulating future horizons with the worst climate change scenarios, the mitigation actions don't seem enough to protect the barrier beach from the combined effect of the SLR and the storms.

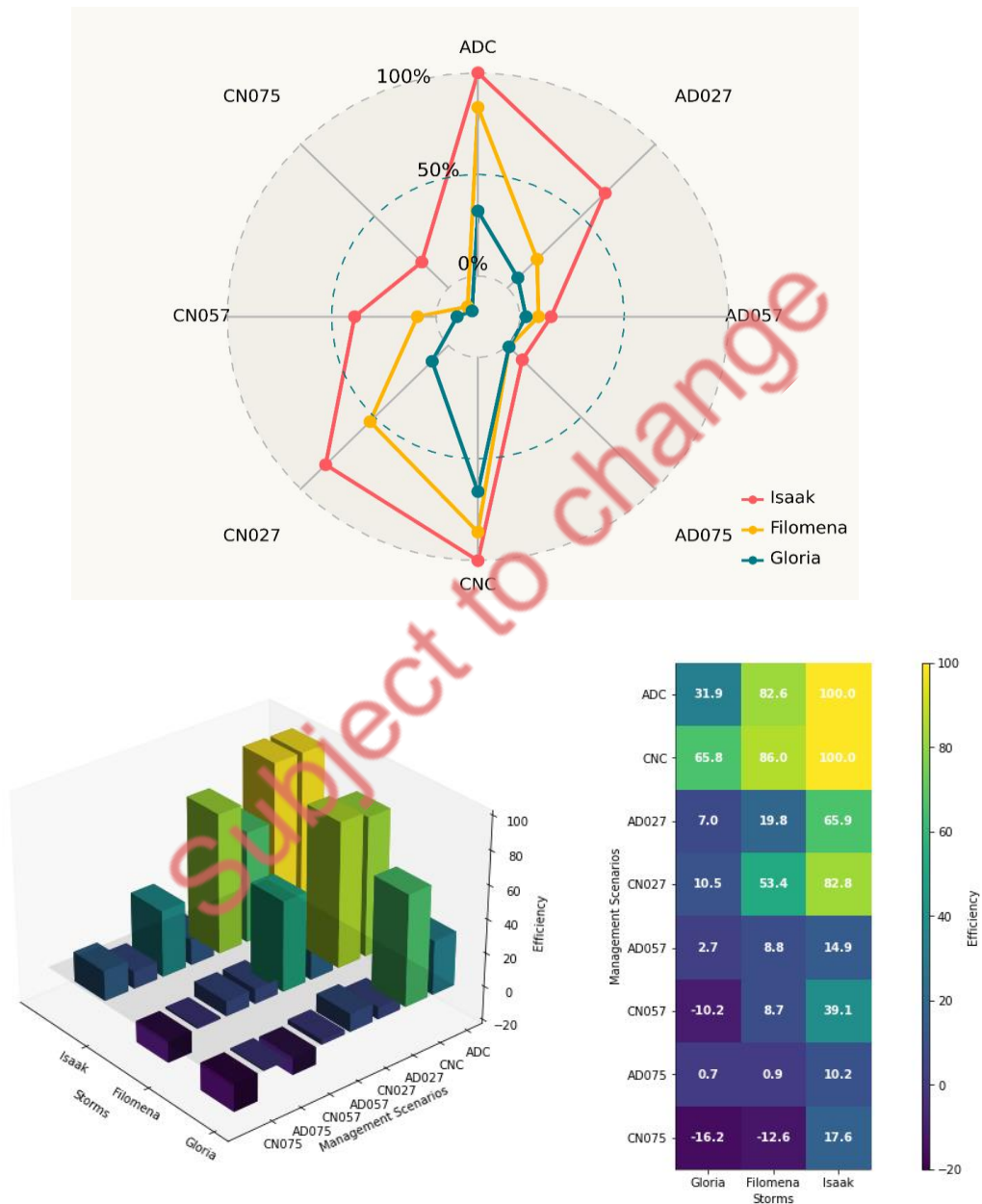


Figure 2.19. Three different representations of the efficiency of the measures Alternating dunes and Classical nourishment for present and future conditions.

## 2.2 Ebro River (UPM)

### 2.2.1 Numerical simulations on sediment transport to Ebro Delta

#### 2.2.1.1. High-resolution coupled river-coastal model

We simulated the erosion process, sediment transport, and sediment deposition in the Ebro Delta pilot case through numerical simulations. We performed the river simulations with the Iber code (Cea *et al.*, 2007; Bladé *et al.*, 2014). Iber is a two-dimensional (2-D) freely available code that solves the 2-D hydrodynamic equations coupled to the sediment transport equations, among others. In the following sections, we describe the hydrodynamic equations and the erosion model. Afterwards, we describe our pilot site, in terms of model configuration data: topography, hydrodynamic parameters, and boundary conditions. Lastly, we calibrate our hydrodynamic numerical model with controlled flood observations.

#### 2.2.1.2. Brief description of the numerical model for fluvial simulation (Iber)

Iber solves the 2-D Depth-Integrated Shallow-Water Equations (SWE) using a finite volume scheme. This scheme can handle unstructured meshes, irregular topographies, friction losses, and wet-dry fronts (Cea *et al.* 2007). The 2D SWEs are derived from the Navier–Stokes equations by assuming quasi-hydrostatic flow and incompressibility of water. The 2D mass conservation equation in a Cartesian coordinate system is given by:

$$\frac{\partial h}{\partial t} + \frac{\partial hU_x}{\partial x} + \frac{\partial hU_y}{\partial y} = 0, \quad (2.5)$$

and the momentum balance equations in conservative form with source terms in a Cartesian coordinate system are:

$$\begin{aligned} \frac{\partial}{\partial t}(hU_x) + \frac{\partial}{\partial x}\left(hU_x^2 + g\frac{h^2}{2}\right) + \frac{\partial}{\partial y}(hU_xU_y) \\ = -gh\frac{\partial z_b}{\partial x} + \frac{\tau_{s,x}}{\rho} - \frac{\tau_{b,x}}{\rho} + \frac{\partial}{\partial x}\left(v_t h \frac{\partial U_x}{\partial x}\right) + \frac{\partial}{\partial y}\left(v_t h \frac{\partial U_x}{\partial y}\right), \end{aligned} \quad (2.6)$$

and

$$\begin{aligned} \frac{\partial}{\partial t}(hU_y) + \frac{\partial}{\partial y}\left(hU_y^2 + g\frac{h^2}{2}\right) + \frac{\partial}{\partial x}(hU_yU_x) \\ = -gh\frac{\partial z_b}{\partial y} + \frac{\tau_{s,y}}{\rho} - \frac{\tau_{b,y}}{\rho} + \frac{\partial}{\partial x}\left(v_t h \frac{\partial U_y}{\partial x}\right) + \frac{\partial}{\partial y}\left(v_t h \frac{\partial U_y}{\partial y}\right). \end{aligned} \quad (2.7)$$

In the previous equations,  $h$  is the water depth,  $U_i$  is the depth average velocity along the  $i$  direction,  $\rho$  is the density of the water,  $z_b$  is the channel-bottom height,  $g$  is the acceleration of gravity,  $\tau_{b,i}$  is the bed friction along the  $i$  direction,  $\tau_{s,i}$  is the free-water surface friction along the  $i$  direction (i.e., wind traction), and  $v_t$  is the turbulent eddy viscosity. In the following simulations, we neglect molecular and eddy viscosities, wind traction, as well as Coriolis acceleration. The bed friction terms,  $\tau_{b,i}$ , read:

$$\tau_{b,i} = \rho gh \frac{n^2 U_i^2}{h^{4/3}} = 0, \quad (2.8)$$

where  $j = x, y$ , and  $n$  is the Manning's coefficient.

Iber erosion and sediment transport module solves the non-cohesive sediment transport equations with uniform granulometries, in a non-stationary regime. The hydrodynamics, sediment transport processes, and river morphology interplay at mobile-bed simulations. Iber software couples these three processes. Iber simulates sediment transport as bedload and suspended load.

The sediment transport process is simulated through the 2D Exner equation (Anderson 2002; Mudd & Furbish 2004; Paola & Voller 2005). The equation provides the bed elevation evolution in response to the erosion and sedimentation and is given in the form of bedload and suspended load. It reads:

$$(1 - \phi) \frac{\partial z_b}{\partial t} + \frac{\partial q_{b,x}}{\partial x} + \frac{\partial q_{b,y}}{\partial y} + (E - D) = 0, \quad (2.9)$$

where  $\phi$  is the porosity,  $q_{b,i}$  is the bedload discharge along the  $i$  direction,  $E$  is the entrainment deposition term of suspended sediment on the bed, and  $D$  is the deposition term of suspended sediment on the bed.

We simulate the bedload solid flow rate due to the bedload transport using the van Rijn equation (Van Rijn 1984a), as it provides satisfactory results compared with laboratory experiments (Santillan et al. 2020). The equation reads:

$$q_b^* = \frac{0.053}{D^{*0.3}} \left( \frac{\tau^*}{\tau_{crit}^*} - 1 \right)^{2.1}, \quad (2.10)$$

where  $q_b^*$  is the dimensionless bedload solid volumetric flow rate,  $D^*$  is the dimensionless diameter of solid particles,  $\tau^*$  is the dimensionless shear stress acting on the particles, and  $\tau_{crit}^*$  is the dimensionless critical shear stress. The dimensionless bedload solid volumetric flow rate,  $q_b^*$ , reads:

$$q_b^* = \frac{q_b}{\sqrt{(s - 1)gD^3}}, \quad (2.11)$$

where  $q_b$  is the bedload solid volumetric flow rate,  $s$  is the ratio between the densities of the particles and water,  $s = \rho_s / \rho$ , and  $D$  is the characteristic diameter of sediments, usually taken as the median diameter  $D = D_{50}$ .

The dimensionless diameter of solid particles is given by:

$$D^* = D \left( \frac{g(s - 1)}{\nu^2} \right)^{1/3}, \quad (2.12)$$

being  $\nu$  the kinematic viscosity of water, and the dimensionless shear stress reads:

$$\tau^* = \frac{\tau_b}{\rho(s - 1)gD}, \quad (2.13)$$

being  $\tau_b$  the bed friction shear stress, given by Eq. (2.8).

The dimensionless critical shear stress  $\tau_{crit}^*$  is given by the Soulsby-Whitehouse equation (Soulsby & Whitehouse 1997), based on the experiments of Shield (1936). It is given by:

$$\tau_{crit}^* = \frac{0.3}{1 + 1.2D^*} + 0.055(1 - e^{-0.02D^*}). \quad (2.14)$$

Iber simulates the suspended sediment transport with the depth-averaged convection-diffusion equation for the sediment concentration. The model accounts for the turbulent diffusion and the equilibrium suspended concentration, and is given by:

$$\begin{aligned} \frac{\partial hC}{\partial t} + \frac{\partial hU_x C}{\partial x} + \frac{\partial hU_y C}{\partial y} \\ = \frac{\partial}{\partial x} \left( \left( \Gamma + \frac{\nu_t}{S_c} \right) h \frac{\partial C}{\partial x} \right) + \frac{\partial}{\partial y} \left( \left( \Gamma + \frac{\nu_t}{S_c} \right) h \frac{\partial C}{\partial y} \right) + \frac{\partial D_{s,x}}{\partial x} + \frac{\partial D_{s,y}}{\partial y} + (E - D), \end{aligned} \quad (2.15)$$

where  $C$  is the depth-averaged concentration of suspended solids,  $\Gamma$  is the molecular diffusion coefficient for suspended solids,  $S_c$  is the Schmidt number, which relates the moment turbulent diffusion coefficient with the suspended turbulent diffusion coefficient, and  $D_{s,i}$  is the suspended sediment dispersion along the  $i$  direction due to the non-homogeneous vertical velocity profile and sediment concentration.

The Entrainment/ Deposition term,  $(E - D)$ , models the bedload grains that become suspended (entrainment) and deposited from suspended sediments to the bed layer. We simulate the Entrainment/ Deposition term with the Van Rijn formula (van Rijn, 1987), given by:

$$E - D = \alpha \omega_s (C^* - C), \quad (2.16)$$

where  $\alpha$  is a coefficient that relates the mean suspended particle concentration and the river bedload concentration,  $\omega_s$  is the fall velocity of the suspended sediments,  $C^*$  is the depth-averaged suspended load concentration at equilibrium conditions, and  $C$  is the depth-averaged suspended load concentration.

The fall velocity of the suspended sediments for sand particles is computed using Van Rijn (1984b) recommendations. For particles smaller than about 0.1 mm,  $\omega_s$  is given by

$$\omega_s = \frac{(s - 1)gD_{50}^2}{18\nu}, \quad (2.17)$$

for suspended sand particles in the range 0.1 to 1 mm, the fall velocity is:

$$\omega_s = 10 \frac{\nu}{D_{50}} \left\{ \left( 1 + \frac{0.01(s - 1)gD_{50}^3}{\nu^2} \right)^{0.5} - 1 \right\}, \quad (2.18)$$

and for particles larger than 1 mm, the following equation is used:

$$\omega_s = 1.1[(s - 1)gD_{50}]^{0.5}. \quad (2.19)$$

The depth-averaged suspended load concentration at equilibrium conditions,  $C^*$ , reads (Van Rijn 1984b):

$$C^* = \frac{1}{\alpha} 0.005 \frac{T^{1.5}}{D^{*0.3}}, \quad (2.20)$$

where  $T$  is the transport stage parameter given by:

$$T = \frac{(U^*)^2 - (U_{crit}^*)^2}{(U_{crit}^*)^2}, \quad (2.21)$$

in which  $U_{crit}^*$  is the critical bed-shear velocity, that according to Shields (1936) reads:

$$U_{crit}^* = \sqrt{\frac{\tau_{crit}^*}{\rho}}, \quad (2.22)$$

and bed-shear velocity,  $U^*$ , reads (Van Rijn 1984b):

$$U^* = \frac{\sqrt{g}}{C'} \bar{U}, \quad (2.23)$$

in which  $C' = 18 \log(12R_b/3D_{90})$  is the Chézy-coefficient related to grains,  $R_b$  is the hydraulic radius related to the bed according to Vanoni-Brooks (1957), and  $\bar{U}$  is the mean flow velocity.

The system of Partial Differential Equations are solved using a first-order finite volume scheme based on the Monotonic Upwind Scheme for Conservation Laws (Van Leer 1979).

### 2.2.1.3. Description of model configuration data: topography, hydrodynamic parameters, boundary conditions

The Ebro River is strongly regulated with dams. The Mequinenza-Ribarroja-Flix reservoir system retains a large part of the sediment flow in the Ebro River (Fig. 2.20). Then, the domain of the numerical simulations to model the sediment transport to the Delta site should include the reservoir system. The modelling objectives are: (1) to study the alternatives to restore, at least in part, the sediment flow, (2) to estimate the quantity of sediments that can be mobilized, (3) to determine how long the sediments would take to reach the Delta site, and (4) to know how the sediment would be delivered to the Delta system.



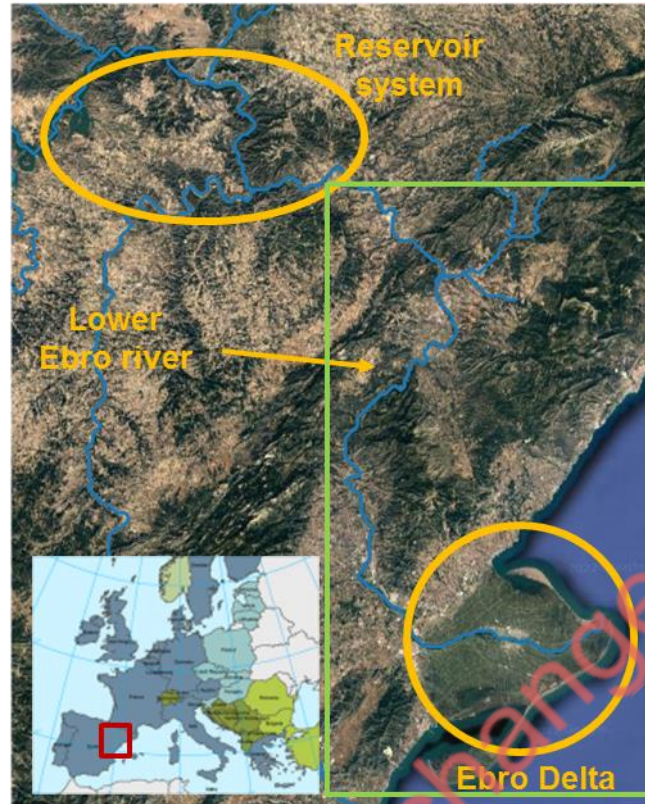
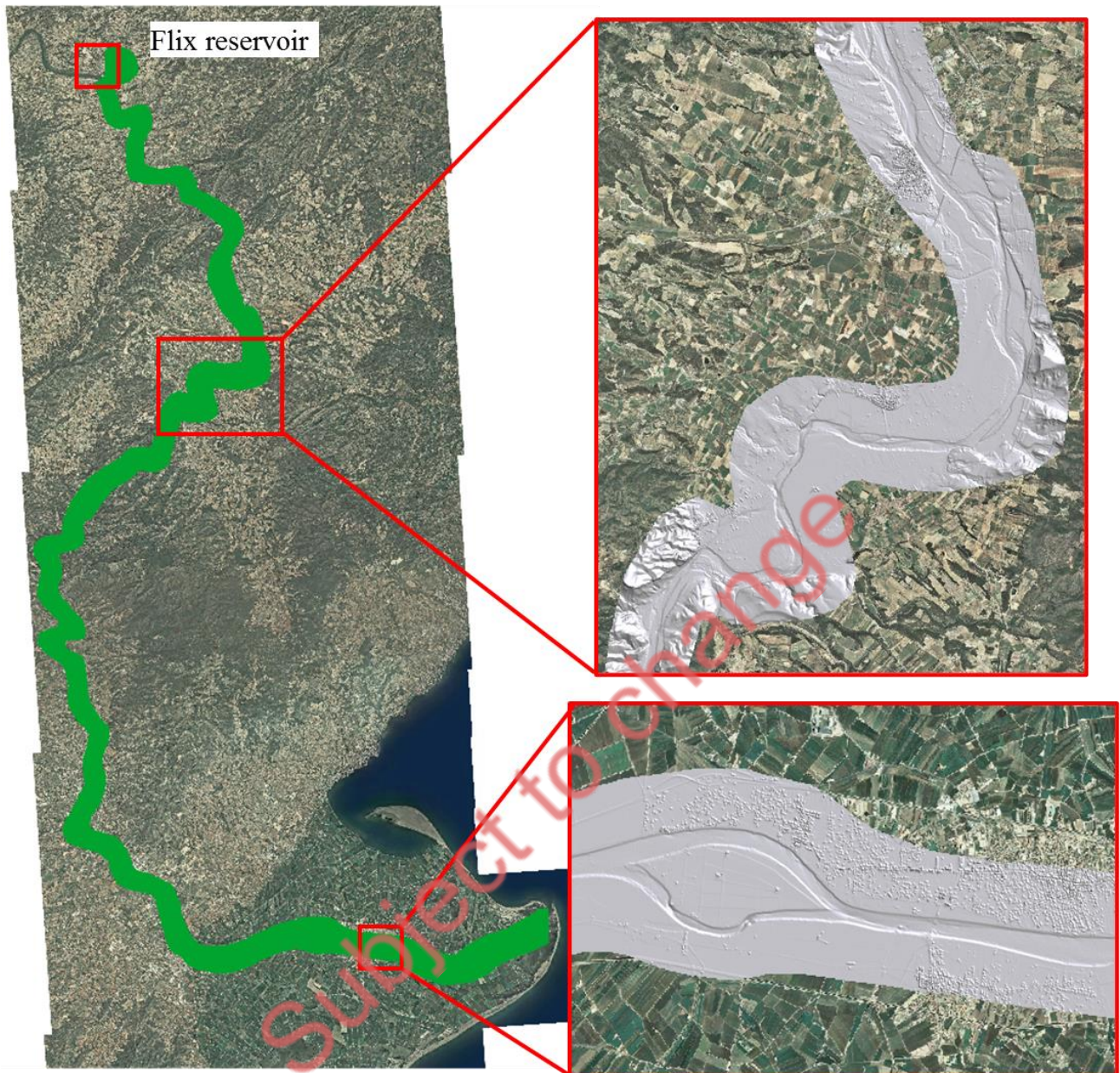


Figure 2.20. Ebro Delta pilot site

The topography of the simulated stretch is depicted in Fig. 2.20. We simulate the fluid flow and sediment transport from the Flix reservoir, located in Tarragona at 41.1 meters above sea level, up to the Delta site, located in the river mouth at 0 meters above mean sea level. The Flix dam is the last barrage on the Ebro River and is located about 100 km from the river mouth.

In our previous study, we performed the numerical simulations using a Digital Terrain Model (DTM) with a 1 m resolution of the Ebro basin provided by the Spanish National System for Flood Risk Mapping. However, this DTM do not map the bed river, instead, the free-water surface is mapped. In the new set of numerical simulations of this workpackage, the “Centro de Estudios y Experimentación de Obras Públicas” (CEDEX) provided us with a high-resolution Digital Terrain Model (DTM) with a 0.5 m resolution of the Ebro basin that included the bed river. Using this DTM, we created a Triangulated Irregular Network (TIN) model of the river with 0.1-meter tolerance, maximum side of 2000 meters, and minimum side of 12 m. Lastly, we import the TIN model in Iber. The left-hand picture in Fig. 2.21 depicts the TIN model of the Ebro topography in Iber in blue, and on the right-hand side, we include two snapshots of the topography. The model includes about 100 km of the Ebro River topography and it is composed of approximately 4,923,448 triangles.



*Figure 2.21. Domain of the numerical simulations in the Ebro Delta pilot site*

We compare both DTM in Fig. 2.22, i.e., (a) the 1-m resolution DTM provided by the Spanish National System for Flood Risk Mapping, denoted as “Old bathymetry” in the snapshots, and (b) the 0.5-m resolution DTM provided by CEDEX, denoted as “New bathymetry” in the snapshots. The snapshots in Fig.2.22 depicts three cross-sections of the river provided by both DTMs. The new DTM provided by CEDEX includes the bed river, as the southern cross section clearly shows.

The hydrodynamics boundary conditions of our numerical model are: (1) imposed flow rate in Flix in subcritical regime, and (2) outlet boundary condition in critical regime imposed on the sea.

We generated an unstructured mesh composed of about 4,923,448 triangles; each triangle of the TIN model is one finite volume in the numerical model, i.e. the TIN model is coincident with the computational mesh. As a result, the picture on the right-hand picture in Figure 2 is also the computational mesh.



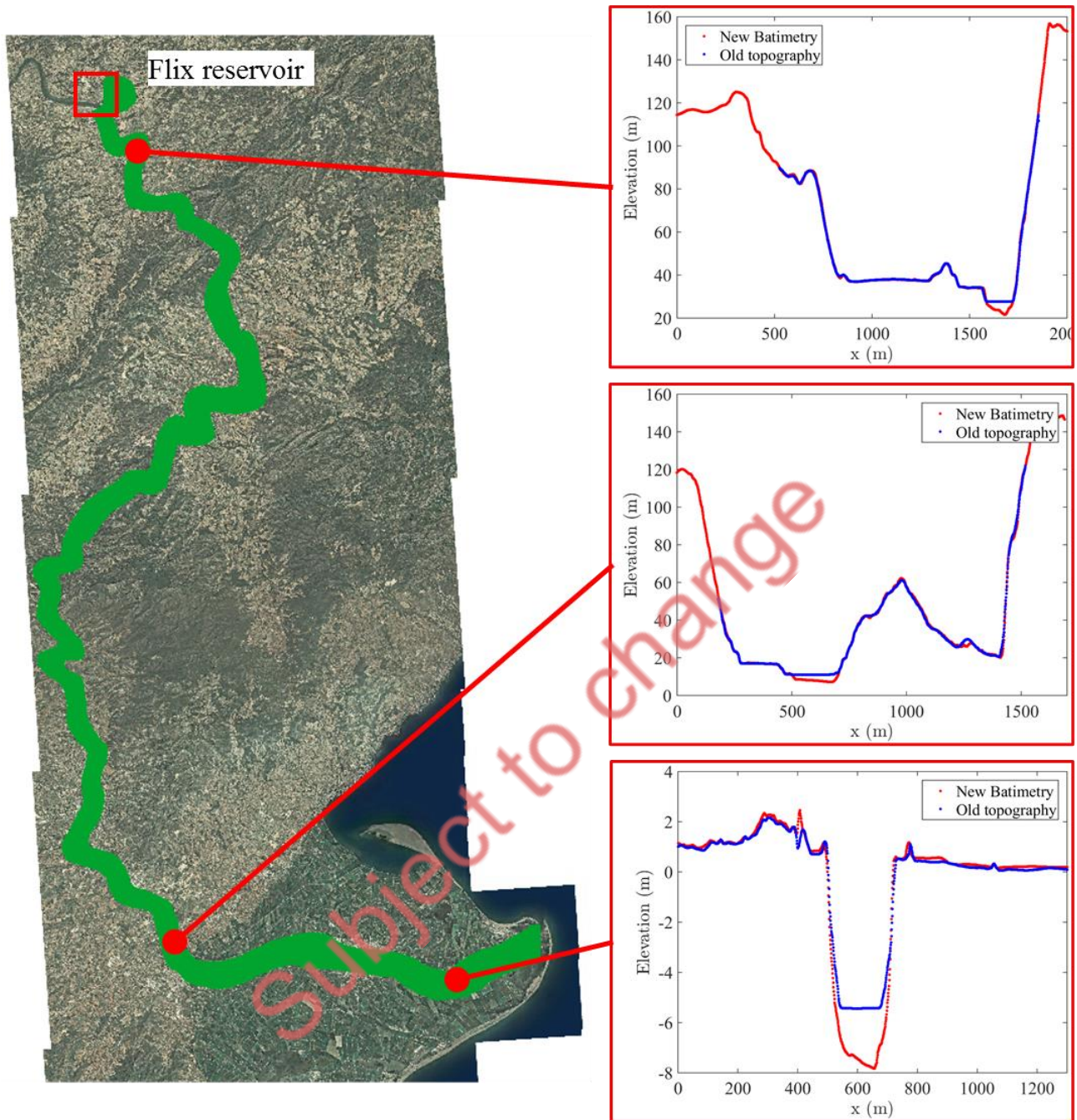


Figure 2.22. Cross sections of the Ebro river

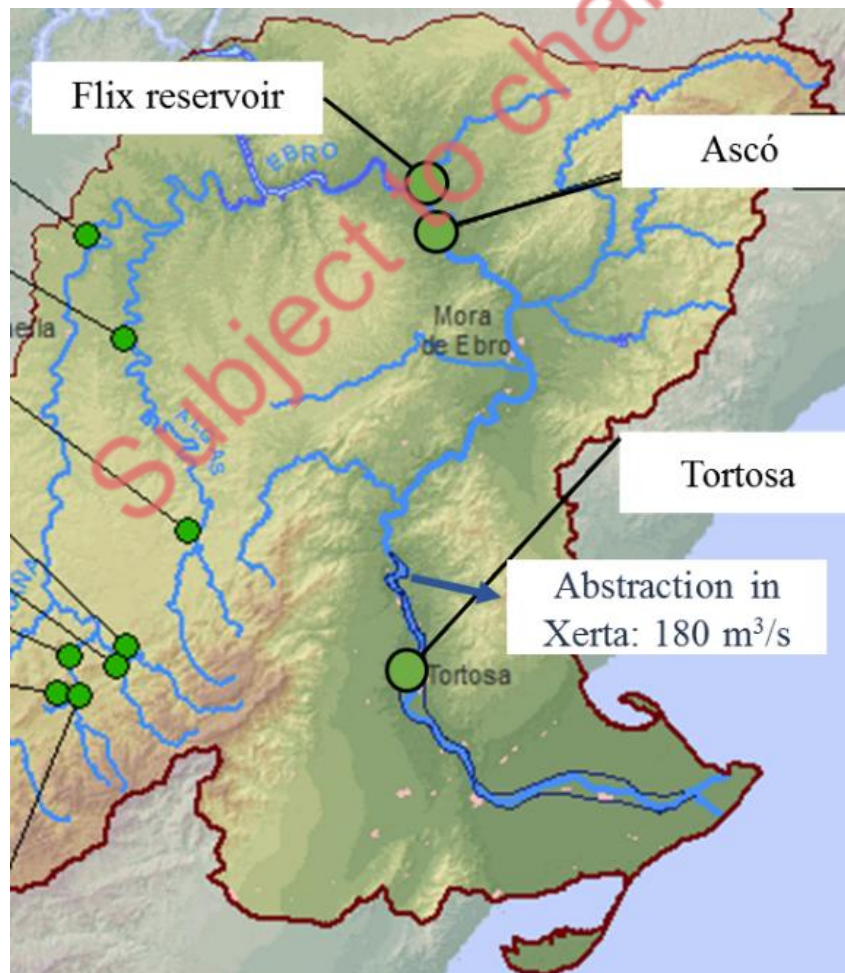
The hydrodynamics boundary conditions of our numerical model are: (1) imposed flow rate in Flix in subcritical regime, and (2) outlet boundary condition in critical regime imposed on the sea.

### 2.2.2 Hydrodynamic calibration of the model with controlled flood observations

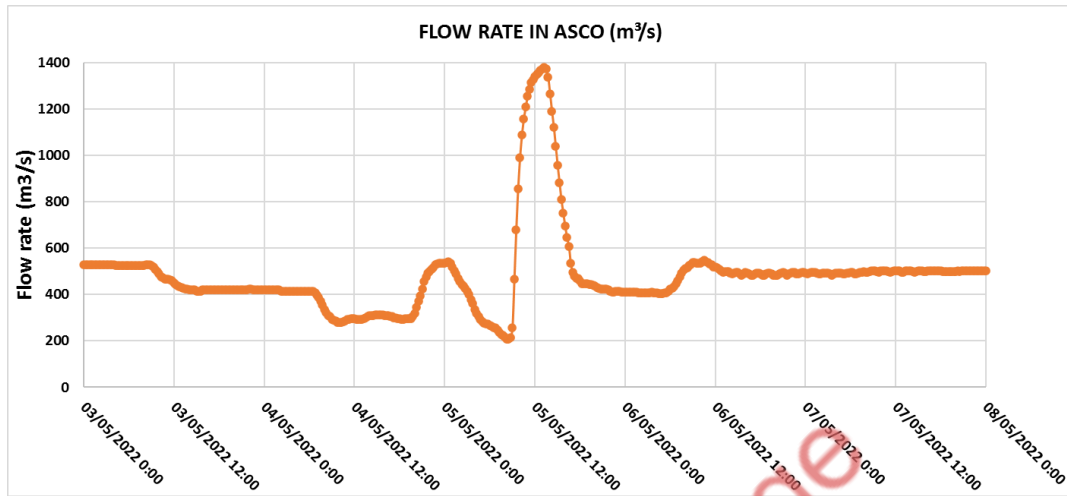
We calibrate the roughness of the model, given by Manning's coefficient, with the observed flood event on May 5th, 2022. This event also allows us to test the performance of the hydrodynamic module. The Ebro Automatic Hydrological Information System (SAIH) provides us with 30-minute flow rate observations at two points of the river: Asco and Tortosa -see Fig. 2.23 (a). Moreover, during the flood event, 205 m<sup>3</sup>/s were abstracted from the river in Xerta through an irrigation channel. The observed flow rate in Ascó gauge station is plotted in Fig. 2.23 (b) and Tortosa in Fig. 2.23 (c).

The boundary conditions of our numerical model are: (1) imposed flow rate in Ascó in subcritical regime given by the observed data plotted in Fig.2.23 (b), and (2) outlet boundary condition in critical regime imposed on the sea. Afterward, we run a set of numerical simulations with several values of Manning's coefficient. The best agreement between the simulated and the observed flow rate in Tortosa are got with Manning's coefficient equal to 0.03. The results are depicted in Fig. 2.24. Our model can capture the flood-wave propagation along the river in terms of time and flood peak downstream of the inlet. We also include a contour plot of the water depth at 5:30 p.m. on 5 May 2022 in Fig. 2.25.

(a)



(a)



(b)

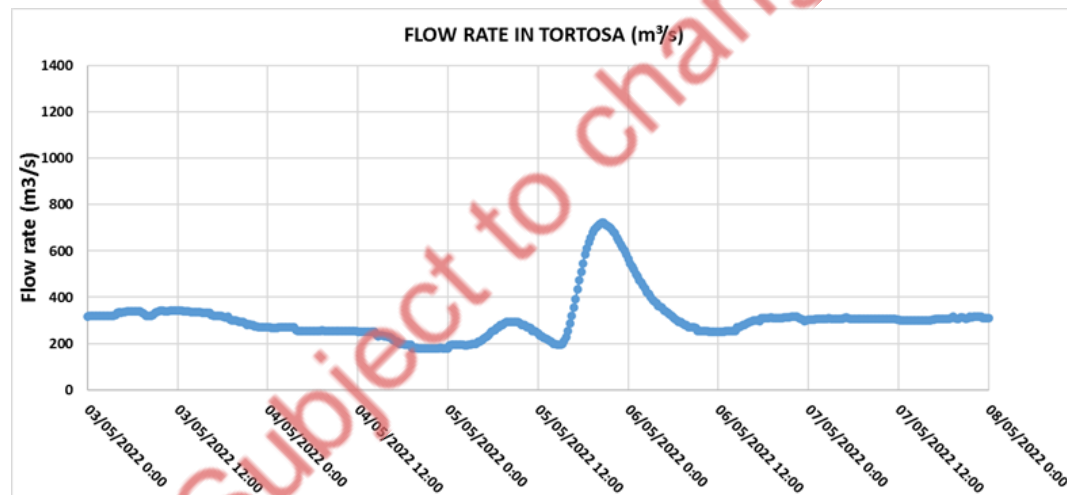


Figure 2.23. Ascó and Tortosa flow-rate gauge stations. (a) Location of Ascó and Tortosa flow-rate gauge stations. (b) Observed flow rate in Ascó flow-rate gauge station. (c) Observed flow rate in Tortosa flow-rate gauge station



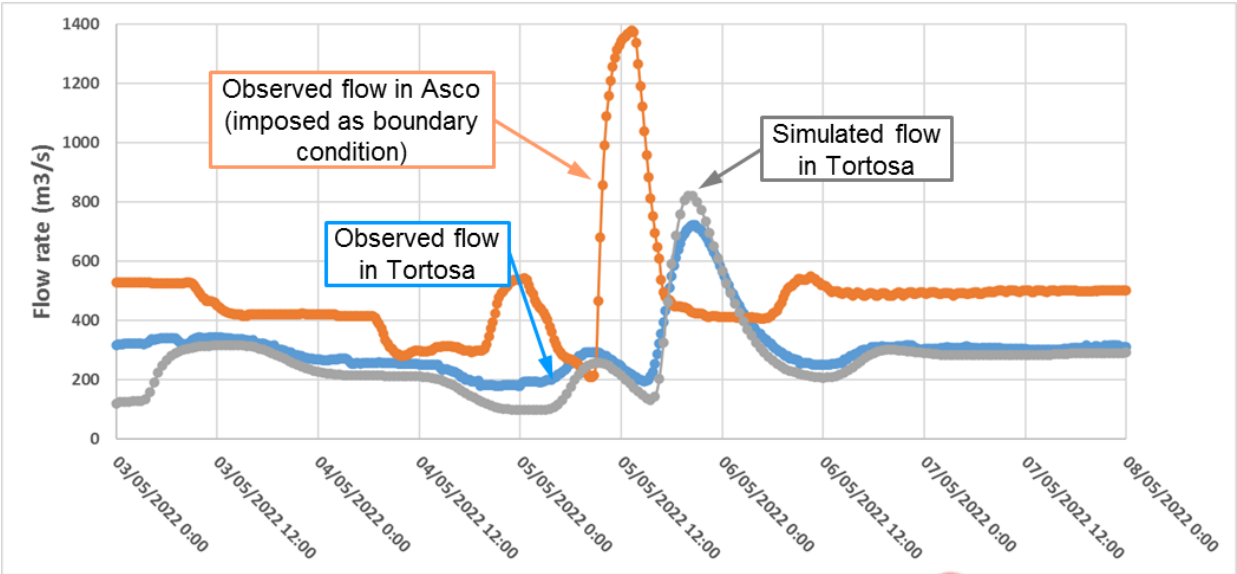


Figure 2.24. Observed and simulated flow rate in Tortosa.

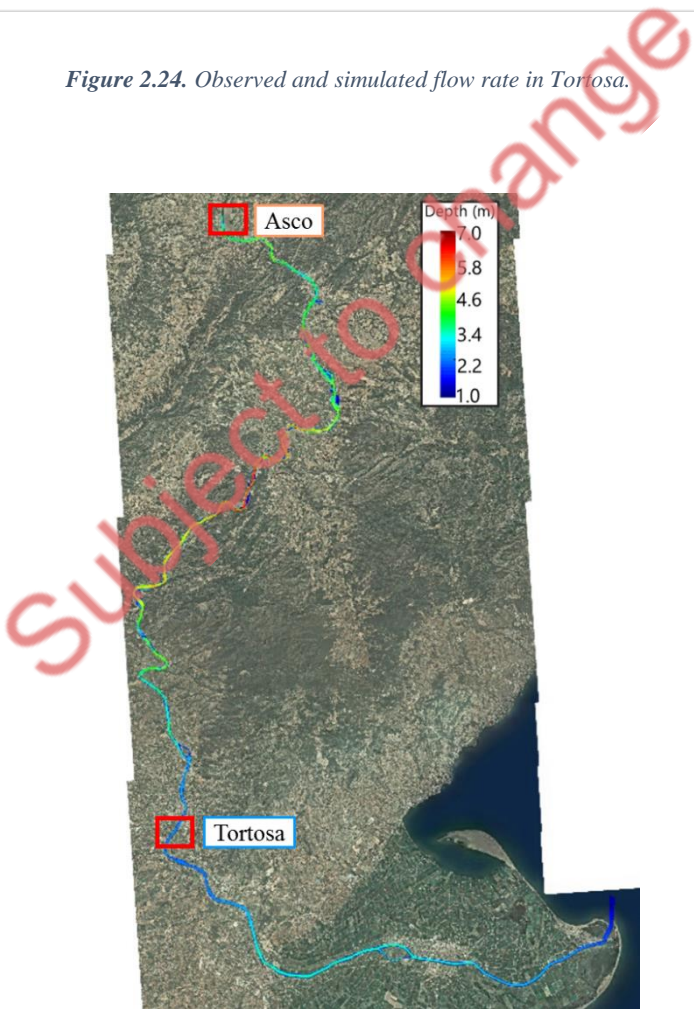


Figure 2.25. Water depth at 5:30 p.m. on 5 May 2022

## 2.2.3 Parameterization of hydro-morpho-eco interactions to simulate ESS

### 2.2.3.1. Approach to the characterization of sediment transport (based on historical observations)

Ibañez et al. (1996) studied the changes in the hydrological and sediment transport produced by large dams on the lower Ebro River and its estuary. They provided estimates of annual suspended sediment transport for several mean flows in Ebro River. Data were got from Gorria's experiments (Gorria, 1877), and they are listed in Table 2.2. Two flow regimes were adopted, i.e., the mean water flow, with high frequency over the hydrological year, and the annual flood regime, with low frequency over the hydrological year.

*Table 2.2. Annual suspended sediment transport from Gorria's data (Gorria, 1877) and Ibañez et al. (1996)*

Flow regime	Mean flow (m <sup>3</sup> /s)	Frequency (days/year)	Concentration of suspended sediment (g/l)
Mean water	710	256	0.9
Annual flood	1764	11	7.2

The values listed in Table 2.2 imply a total annual volume of 17.38 km<sup>3</sup>/yr and a sediment transport of 26.2 Mton/yr. We will assess the performance of our model by simulating both flow regimes, and evaluate whether our code can reproduce data from Table 2.2. In the following section, we include the parameters of our sediment transport model, we include several contour plots of the concentration of suspended sediments at several time steps, and we analyze the performance of our model.

### 2.2.3.2. Numerical analysis of sediment transport

We run two numerical simulations for the two flow regimes included in Table 2.2. We simulate river-flow hydrodynamics, as well as suspended sediment transport for both flow regimes. The hydraulic boundary conditions of our numerical model are: (1) imposed constant flow rate at the outlet of Flix reservoir in subcritical regime given by data in Table 2.2, (2) outlet boundary condition in critical regime imposed on the sea. Moreover, water at the inlet has a suspended sediment concentration given by data listed in Table 2.2. Our numerical simulations are aimed at analyzing whether Ebro River can transport those sediment concentrations up to the Ebro Delta or not.

We do not know the size of the suspended particles, characterized in the model with the median diameter, D50. We estimate the parameter D50 with a calibration process for the two flow and concentration values listed in Table 2.2, i.e., we run a set of simulations varying the value of D50 and we take as the value for D50 the maximum diameter that does not produce sedimentation in the river and the concentration in the whole river is the value reported in Table 2.2 for the two flow rates. We adopt the following features for the sediments: relative density is 2.65, friction angle is 30 degrees, suspended sediment dispersion is 0.001 m<sup>2</sup>/s, and the Schmidt number is 1.1. The best performance is obtained for a D50-value equal to 0.0005 mm, clay.

We include two contour plots of the suspended sedimentation concentration for two D50-values: 0.005 mm –silt–, and 0.0005 mm –clay– in Figure 7 after 1,5 days. These results are some simulations run during the calibration process. The flow is 710 m<sup>3</sup>/s in both cases.

We plot the suspended sediment concentration for the two types of sediments, silt, and clay, in Figure 7 after 1,5 days. The flow cannot transport such a big sediment as the silt, and consequently grains sediment during the transport process and the concentration decreases up to about 0.5 g/l in the delta, as depicted in Fig.

2.26(a). However, the flow can transport the clay with the given concentration, 0.9 g/l, up to the delta without sedimentation, as shown in Fig. 2.26(b).

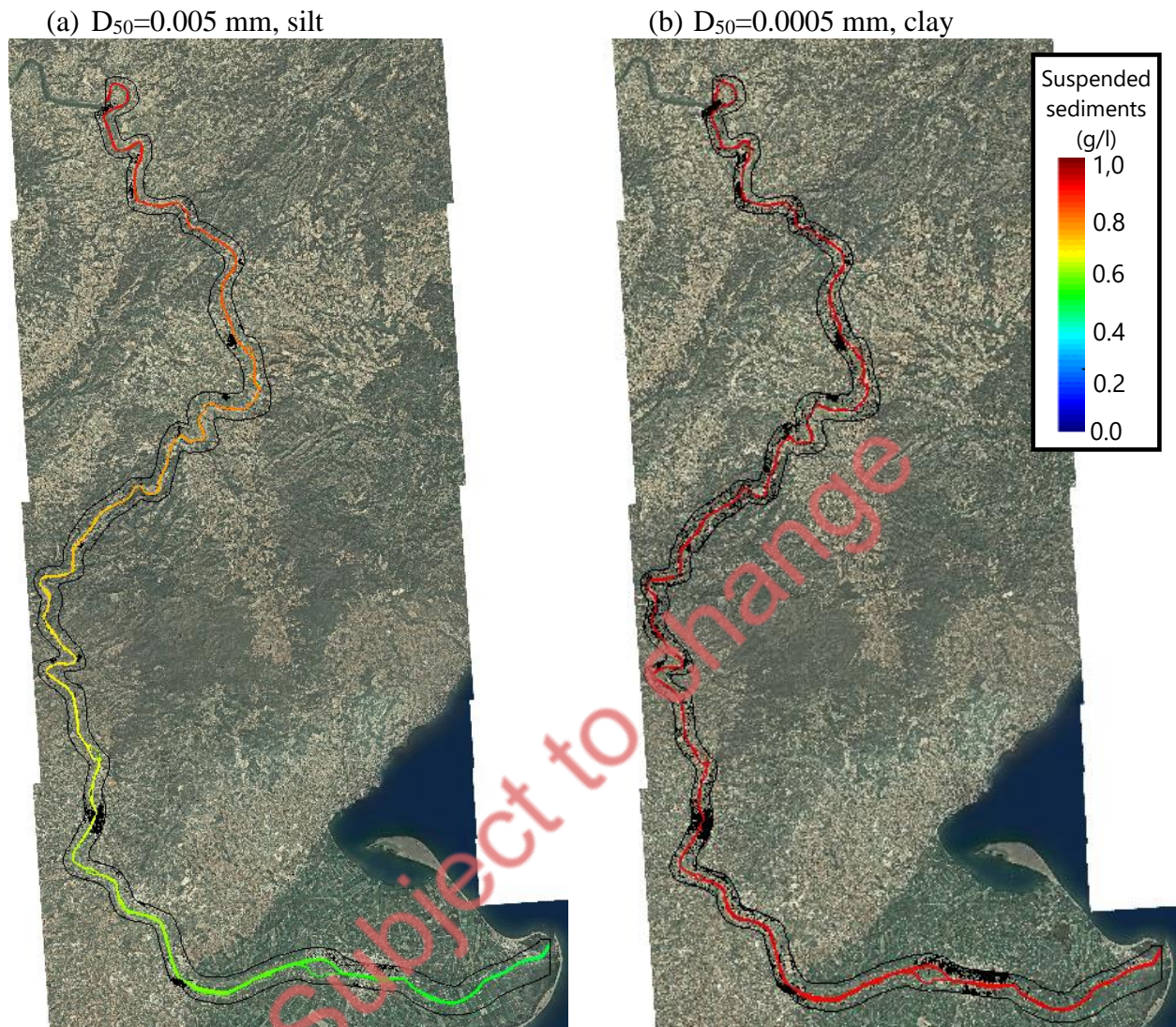


**Figure 2.26.** Suspended sediment concentration for the mean water regime given in Table 2.2 after 1,5 days. Flow water is  $710 \text{ m}^3/\text{s}$  and the sediment concentration at the inlet is  $0.9 \text{ g/l}$ . In the contour plot (a) we plot the sediment concentration for the simulation with a median diameter of the sediment equal to  $0.005 \text{ mm}$ , whereas in the contour plot (a) the median diameter of the sediments is  $0.0005 \text{ mm}$ , ten times smaller.

We plot the erosion computed for the simulation with the silt and the clay in Fig. 2.27. Negative values of the erosion mean sedimentation of the grains. The erosion in the simulation with silt is depicted in Fig. 2.27(a), and since the concentration of the sediments decreases as the water flows through the river, the sedimentation increases. The thickness of such sedimentation after 1,5 days of flow is about  $2 \text{ mm}$  in the inlet and decreases downstream. Nevertheless, the simulation in the clay shows no erosion, as shown in Figure 2.27(b), i.e., the flow can transport the clay but not the silt.



$D_{50}=0.005$  mm, silt



$D_{50}=0.0005$  mm, clay

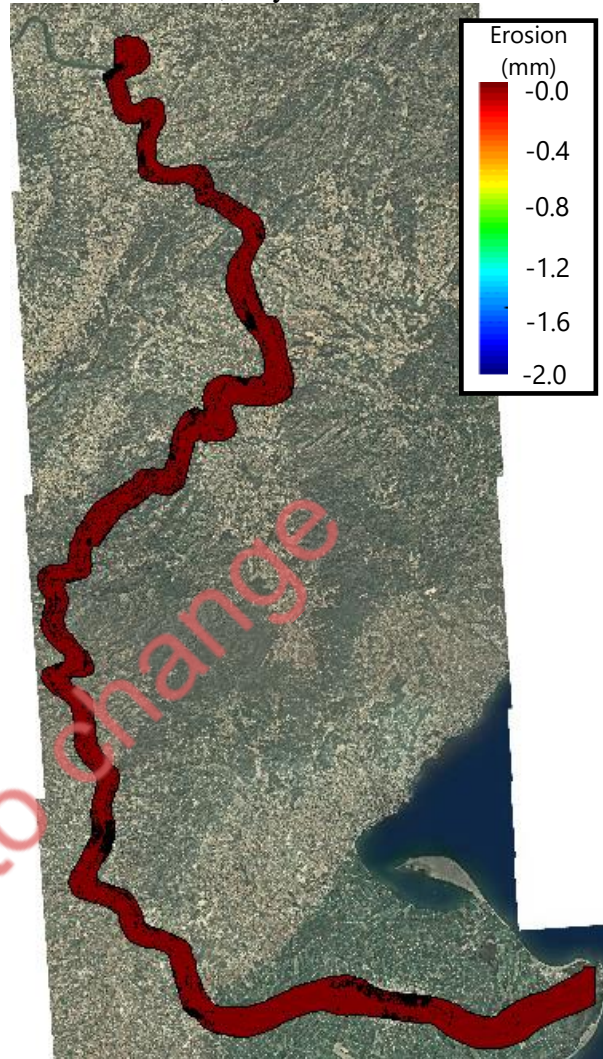


**Figure 2.27.** Erosion for the mean water regime given in Table 2.2 after 1,5 days. Flow water is  $710 \text{ m}^3/\text{s}$  and the sediment concentration at the inlet is  $0.9 \text{ g/l}$ . In the contour plot (a) we plot the erosion for the simulation with a median diameter of the sediment equals to  $0.005 \text{ mm}$ , whereas in the contour plot (b) the median diameter of the sediments is  $0.0005 \text{ mm}$ , ten times smaller. Negative values of erosion mean deposition of sediments.

In the following paragraphs, we show some results of the sediment transport simulations for the mean water flow regime. Initially, the water depth in the river is zero, i.e., the river is dry, and we introduce water through the inlet at the outlet of Flix reservoir. The flow at the inlet is  $710 \text{ m}^3/\text{s}$  and the concentration of sediments is  $0.9 \text{ g/l}$ . The flow propagates through the river and lastly, the steady-state regime is reached. Fig. 2.28 depicts the suspended sediment concentration at three-time steps. After 3 hours –Fig. 2.28(a)– the flow went down 11 km and reached Ascó town. The concentration of suspended sediments is  $0.9 \text{ g/l}$  along the whole stretch of Ebro River.

After 12 hours, flow is closed to Xerta –Fig.2.28(b)–, and the concentration of suspended sediments is  $0.9 \text{ g/l}$  along the whole stretch too. The sediment deposition at this time step is zero (not shown), which means the flow can transport the given sediment concentration along the river.



The steady-state regime is shown in Fig. 2.28(c). The concentration of suspended sediments is 0.9 g/l too, and the sediment deposition is zero. The flow can transport that sediment concentration from Flix reservoir to the Delta without deposition.

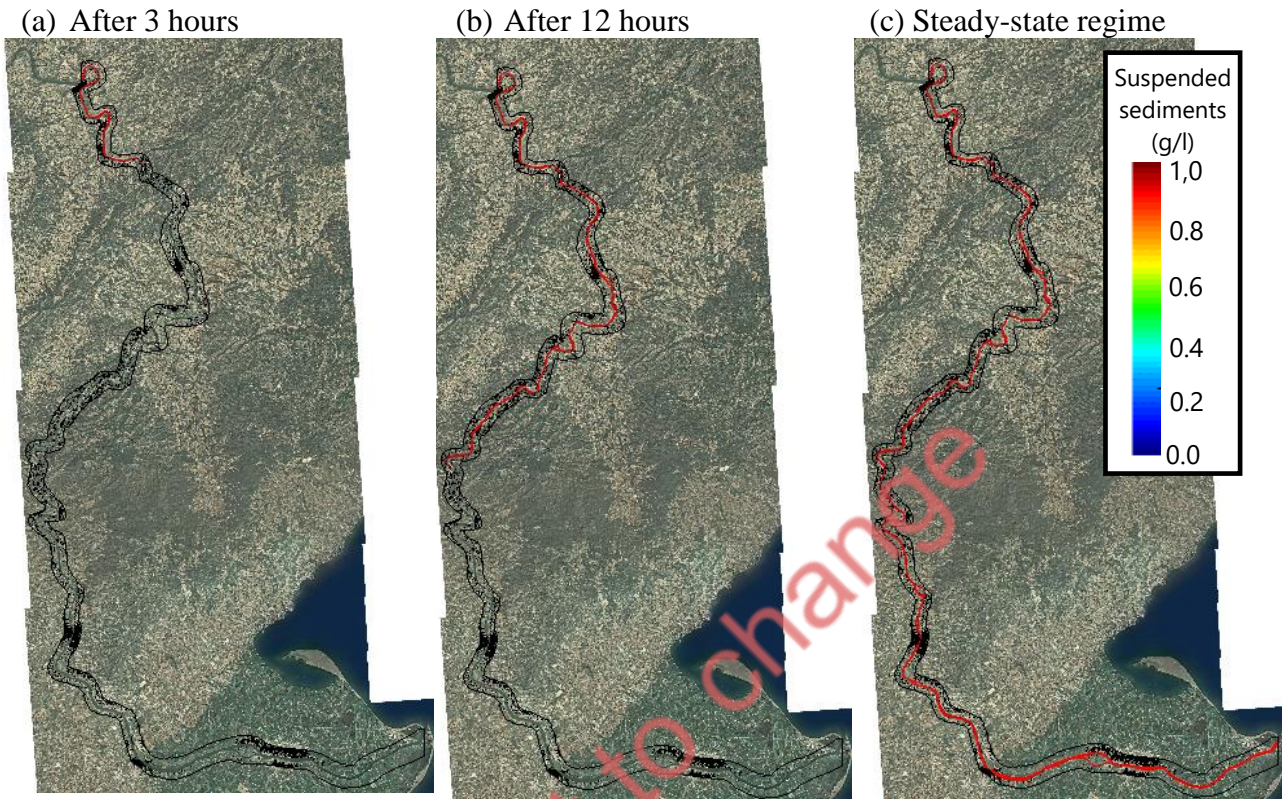


**Figure 2.28.** Suspended sediment concentration for the mean water regime given in Table 2.2. Flow water is 710 m<sup>3</sup>/s and suspended sediment concentration at the inlet is 0.9 g/l. We depict the contour plots of the concentration of suspended sediment after 3 hours in (a), after 12 hours in (b), and under the steady-state regime in (c).

We also show some results of the sediment transport simulation for the annual flood (Table 2.1). As in the previous case, initially, the water depth in the river is zero, and we introduce water through the inlet at the outlet of Flix reservoir. In this case, the flow at the inlet is 1760 m<sup>3</sup>/s and the concentration of sediments is 7.2 g/l. The flow propagates through the river and after several time-steps, the stationary state is reached. Fig. 2.29 depicts the suspended sediment concentration at three time-steps. After 3 hours (Fig. 29(a)) the flow went down further than during the mean flow regime. The concentration of suspended sediments is 7.2 g/l along the whole stretch of Ebro River, and the deposition is zero (not shown).

After 12 hours, flow is closed to Tortosa in this case (Fig. 2.29(b)), and the concentration of suspended sediments is 7.2 g/l along the whole stretch too. Lastly, Fig. 2.29(c) depicts the steady-state regime. The concentration of suspended sediments is 7.2 g/l too, and sediments do not deposit along the river. The river can transport this sediment concentration to the Delta during the annual flood.



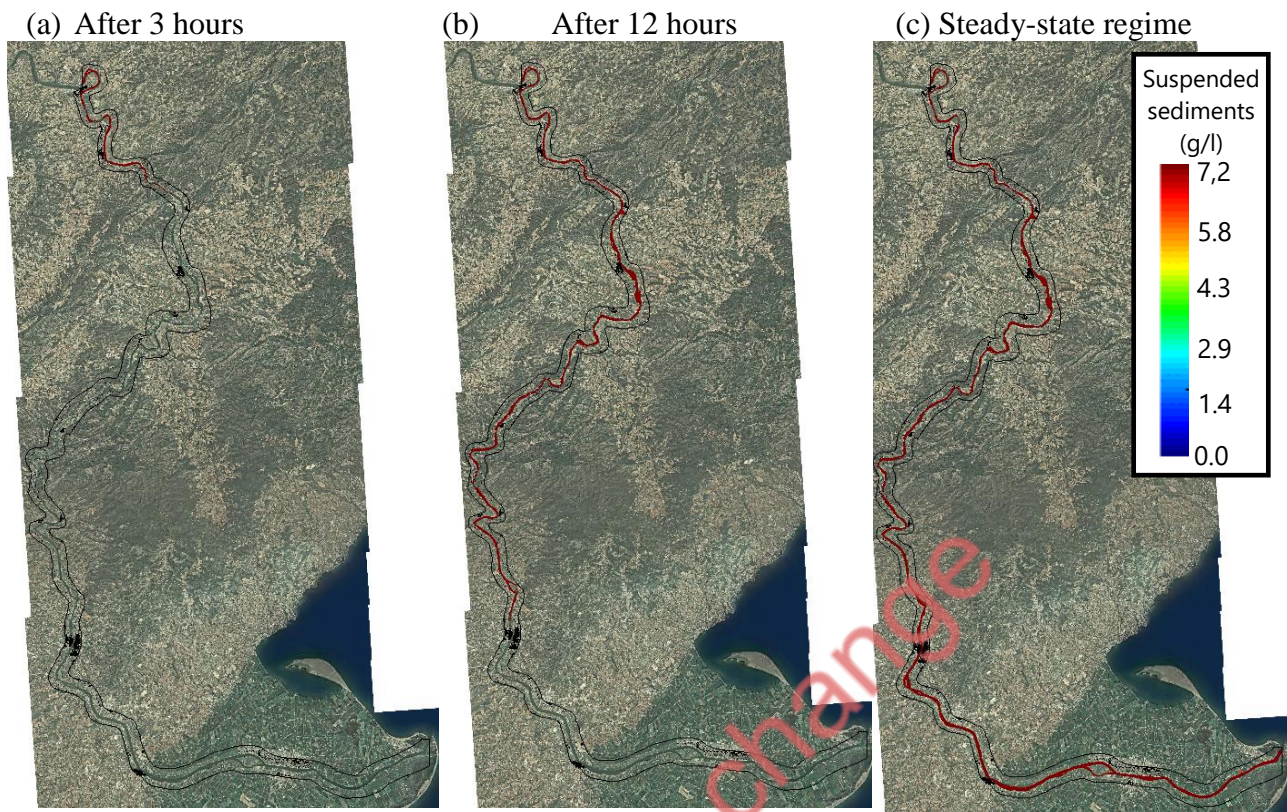


**Figure 2.29.** Suspended sediment concentration for the mean water regime given in Table I. Flow water is  $1764 \text{ m}^3/\text{s}$  and suspended sediment concentration at the inlet is  $7.2 \text{ g/l}$ . We depict the contour plots of the concentration of suspended sediment after 3 hours in Figure (2), after 12 hours in (b), and under the steady-state regime in (c).

#### 2.2.3.3. Sediment transport of clay of other flow rates

We assess the capacity of the flow to transport suspended sediments for other flow rates different from the values provided by Gorria (1877) and Ibañez et al. (1996). In the previous section, we estimated the features of the sediments for the concentration and flow rates observed by Gorria (1877). The features of the sediment are: the median diameter of the grains,  $D_{50}$ , is  $0.005 \text{ mm}$ , the relative density is  $2.65$ , the friction angle is  $30$  degrees, the suspended sediment dispersion is  $0.001 \text{ m}^2/\text{s}$ , and the Schmidt number is  $1.1$ .

We estimate the concentration of the sediments that Ebro river can transport to the delta for other flow rates without sedimentation. We include the results in Fig. 2.30 where a log-linear trend line is fitted to the data. We recall that concentration values for  $710$  and  $1764 \text{ m}^3/\text{s}$  flow rates are given values by Gorria (1877) and Ibañez et al. (1996).

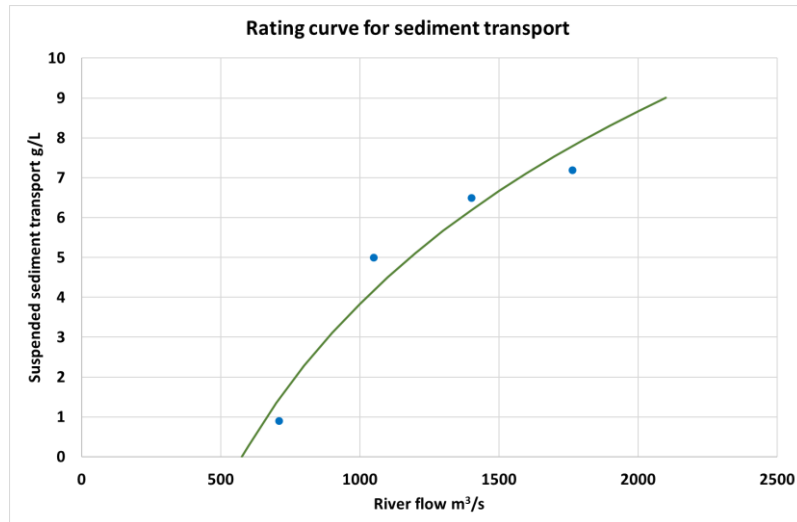


Figure 2.30. Suspended sediment concentration for several flow rates.

## 2.2.4 Assessment of current, potential and future sediment transport

In this section we evaluate current and potential sediment transport in the lower Ebro River to identify risks and assess the potential effects of mitigation actions.

### 2.2.4.1. Current sediment transport

We performed a simple analysis of current sediment transport using data available at the Ebro River streamflow and water quality measurement stations. The only continuous data available for suspended sediments is turbidity, which is measured regularly at the Ascó and Tortosa stations. Unfortunately, the availability of turbidity data is very low. The series have numerous gaps, and the years without failure are exceptional. The Ascó station has registered data since 1996, but Tortosa began measuring in 2011. Therefore, the periods of overlap of the flow and turbidity data are intermittent and do not allow continuous analysis. The available data were analyzed globally, regardless of the date to which they correspond. Fig. 2.31 presents the relationships between flow (in m<sup>3</sup>/s) and turbidity (in NTU units) in the two stations analyzed. The graphs on the left present the relationships in natural values and those on the right on the logarithmic scale. A linear fit was added in both cases. There is a certain tendency to increase turbidity when the flow rate is increased, but there is a great dispersion in the data and the trends are not clear. The R<sup>2</sup> coefficients of the correlations are very low, indicating that a linear relationship between the NTU and Q variables cannot be established for the current range of sediment transport. The station where the relationship is most clearly appreciated is that of Tortosa on a logarithmic scale, although the law between variables is not linear, but seems to correspond to a logistic function. The Ascó station shows a similar trend, although greater data availability produces a much larger dispersion. These results contrast with those published by Batalla and Vericat (2011), who obtained a clear linear relationship for the data taken in Mora de Ebro.

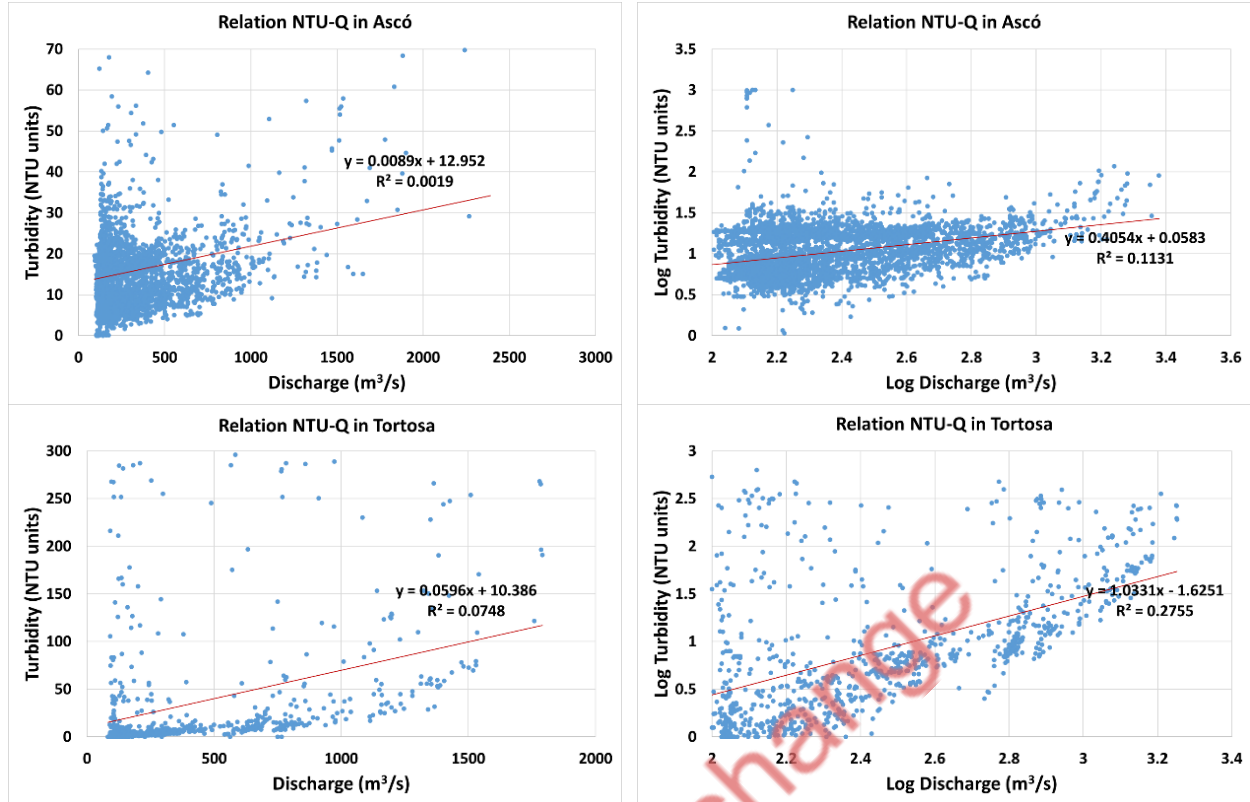
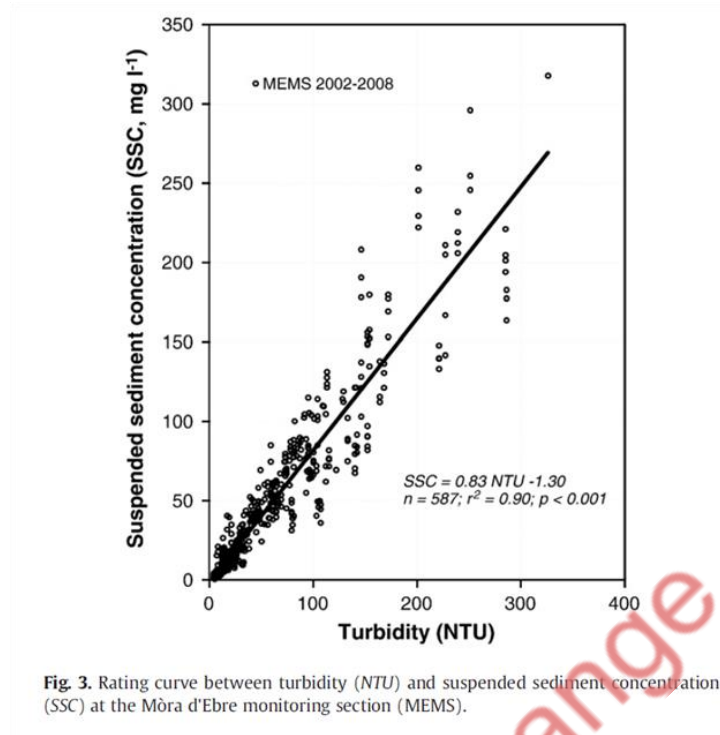


Figure 2.31. Relation between turbidity and discharge in two measuring stations in the Lower Ebro River. Left: Natural values. Right: logarithmic values

A rough estimate of current sediment transport can be made from the flow and turbidity data. The relationship between turbidity and suspended sediment concentration was taken from (Tena et al., 2011), who obtained an excellent correlation for the data they collected in Mora de Ebro (Fig. 2.32), with an  $R^2$  value of 0.90. Although this empirical relationship may be station specific due to the local characteristics of suspended particles, it can be used to obtain a rough estimate of sediment flow values from available measurements. The equation used is as follows:

$$SSC = 0,83NTU - 1,3 \quad (2.24)$$

Where SSC is the suspended load concentration in mg/L and NTU are the turbidity units. From the concentration and the average daily flow at the corresponding station, the daily sediment load was estimated for the days when both data were available. The resulting mean values are presented in Table 2.3. The results obtained are highly uncertain. The mean flow can be used as an indicator of the representativeness of the analyzed sample by comparing the mean flow for days with both the data available and the average flow in the stations for the period analyzed. The error in Ascó is less than 10% and that in Tortosa exceeds 30%. The values obtained are extremely low compared to the average sediment flow under natural conditions estimated by Gorria. These values are of the same order of magnitude as the results presented by other researchers, who obtained somewhat lower loads downstream of the Mequinenza and Ribarroja reservoirs (for example, 0.055 Mt/year in Ascó).



*Figure 2.32. Figure 3 from Tena et al., 2011 where they show the relationship between turbidity and suspended sediment concentration*

*Table 2.3. Estimated average values of sediment transport from the flow and turbidity data in the stations of Ascó and Tortosa*

Location	Mean flow 1997-2015 (m <sup>3</sup> /s)	Days with data	Mean flow for days with data (m <sup>3</sup> /s)	Turbidity NTU	Concentration (mg/L)	Sediment transport (Mton/yr)
Ascó	320.2.6	3923	291.6	15.5	11.6	0.120
Tortosa	284.9	981	372.1	32.6	25.9	0.500

#### 2.2.4.2. Potential sediment transport

The low transport rate observed is due to the lack of availability of sediments. In this section, we estimate the potential sediment transport that would be available if the reservoirs can be bypassed. The estimate is based on flow data and on the sediment transport rating curve derived from numerical simulations. Flow data under actual conditions is obtained from the Tortosa gauging station. Data are available from 1913, but there are several small gaps and a larger one from 1936 to 1951. The period when data are continuously available spans from the hydrological year 1953-34 to 2019-20. Potential sediment transport was estimated for that period by applying the sediment transport rating curve to daily flows measured in the Tortosa station. The average potential sediment transport is 24.36 Mton/yr, much larger than the observed sediment flow.

Flow data under natural conditions are obtained from the results of the SIMPA model, Spanish acronym for Integrated System for Precipitation-Runoff Modelling. SIMPA is a conceptual distributed hydrological model that simulates the average monthly flows in the natural regime at any point of the hydrographic network of Spain. The available simulated period is between the hydrological year 1940-41 and the year 2019-20. We obtained the monthly time series of the flow corresponding to the entire Ebro basin. Naturalized flows are only available at the monthly time scale, but observed flows are available at daily time scale. To compare



potential sediment transport under natural and altered conditions, average monthly flows must be used. An error will be introduced in the results because the sediment transport rating curve is nonlinear. To estimate the order of magnitude of the error, we compared the annual sediment transport rates computed at the daily and the monthly scales in the Tortosa gauging station. The results are presented in Fig. 2.33, which shows the comparison of the time sequence of both series and the scatter plot of the values, together with a linear fit. The difference does not appear to be very large. The slope of the linear fit is 1.22 and the coefficient of determination is 0.98. Therefore, it is acceptable to work at the monthly time scale, but sediment transport rates obtained at the monthly scale should be increased by 20% to account for the averaging.

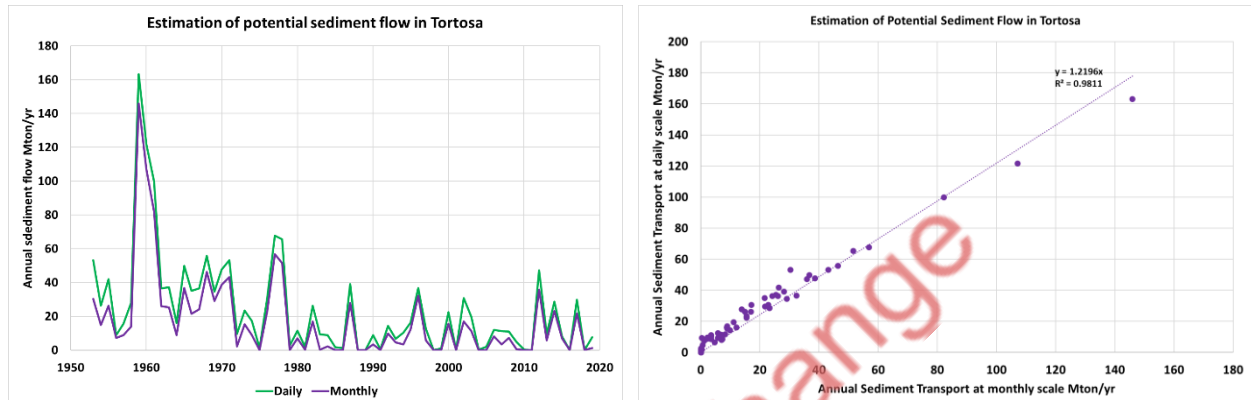


Figure 2.33. Comparison of the estimation of potential sediment transport in Tortosa at the daily and monthly scales. Left: annual flow. Right: sediment transport

Fig. 2.34 shows the time series of annual flows and potential sediment transport in the Lower Ebro River under natural and altered conditions. Natural flows were taken from the SIMPA model and altered flows from the Tortosa streamflow gauge. The values begin to diverge in the 1960s decade, when reservoir constructions in the Ebro basin allowed the development of irrigation and the corresponding water extraction. Although some irrigation is still being developed in the basin, the large irrigation districts were finished in the 1980s. The average flow measured in Tortosa in the last 40 years with data is 9.09 km<sup>3</sup>/yr, while the estimate under natural conditions from the SIMPA model is 15.13 km<sup>3</sup>/yr. The difference, 6.04 km<sup>3</sup>/yr, can be mainly attributed to irrigation abstractions. The Ebro River Basin Management Plan for the cycle 2021-2027 considers 924,400 ha of irrigated land with an annual demand of 8.141 km<sup>3</sup>/yr. The difference between natural and measured flow would correspond to a net loss of water to evapotranspiration of 75% of the bulk abstraction, which is a reasonable figure.

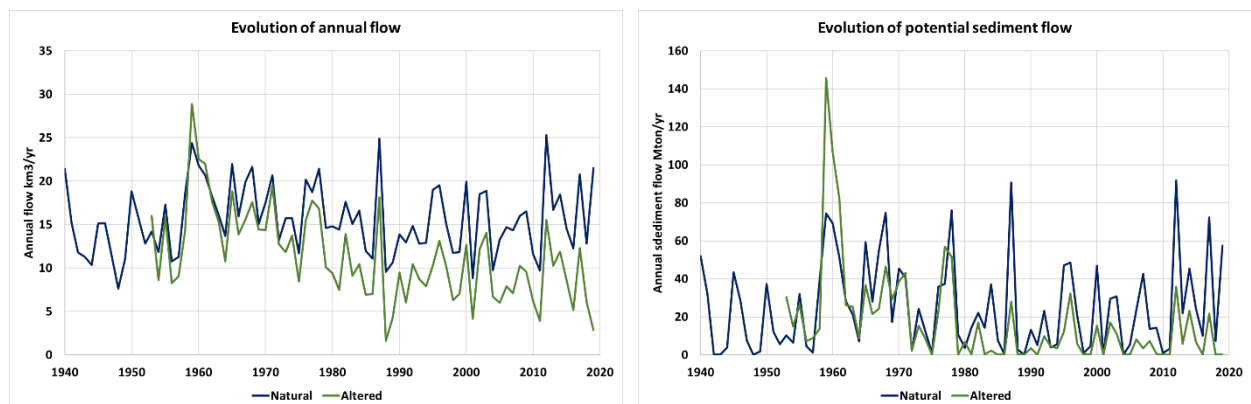


Figure 2.34. Evolution of annual flow and potential sediment transport in the Lower Ebro River under natural and altered conditions. Left: annual flow. Right: sediment transport

The impact of water abstractions on potential sediment transport is much greater than that of annual flow. Potential sediment transport was estimated by applying the sediment transport rating curve to monthly flows. The average value in the last 40 years is 22.39 Mton/yr under natural conditions and 6.93 Mton/yr under actual altered conditions, a 70% reduction versus 42% for annual flow. The rating curve shows that sediment transport requires a minimum flow of approximately 575 m<sup>3</sup>/s. This threshold was exceeded in 146 months in the last 40 years under natural conditions (30% of the time) and only 59 months under altered conditions (12% of the time). Fig. 2.35 shows the relation between annual flow and potential sediment transport in the Lower Ebro River under natural and altered conditions. Although both relationships were obtained from the same rating curve on the monthly scale, the representation on the annual scale shows slightly larger sediment transport under altered conditions for the same annual flow, particularly for low annual flow values.

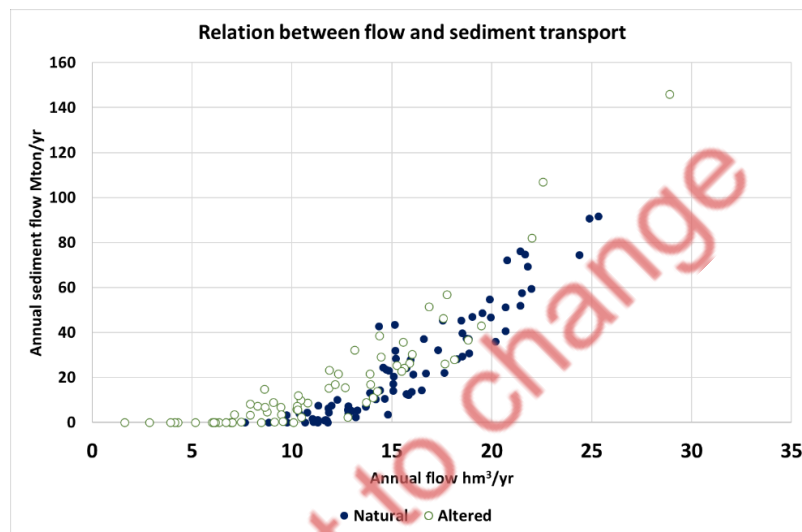


Figure 2.35. Relation between annual flow and potential sediment transport in the Lower Ebro River under natural and altered conditions

Fig. 2.36 presents the monthly average values of flow and potential sediment transport under natural and altered conditions. The figure shows that, in addition to water abstractions, flow regulation is also relevant to determine the potential transport of sediments under altered conditions. The seasonality of flows shows that most water abstractions occur during the spring, summer, and autumn months, leaving the average winter flows almost unchanged. However, altered winter flows are concentrated in wet years, when reservoirs release excess water. This leads to an increase in potential sediment transport in altered conditions during the winter months, which can be used to effectively manage the sediment bypasses in the reservoirs.

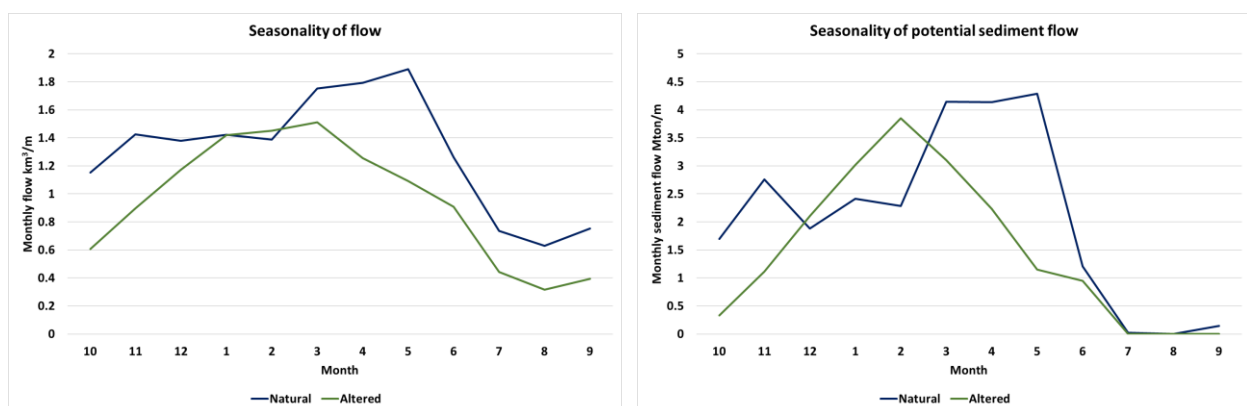


Figure 2.36. Mean seasonality of flow and potential sediment transport in the Lower Ebro River under natural and altered conditions. Left: annual flow. Right: sediment transport

In conclusion, the potential for sediment transport is significantly reduced under current conditions of water management in the Ebro River basin, but there is still capacity to transport almost 7 Mton/yr, which is a figure much larger than current observed sediment transport and exceeds what can be realistically expected to be bypassed from the reservoirs. However, it should be noted that in 14 of the 40 years analyzed there would be no sediment transport because discharges measured in Tortosa do not reach the transport activation threshold.

### 2.2.4.3. Potential sediment transport under different climate projections

In this section we obtain estimates of potential sediment transport for future scenarios using climate projections. The scenarios considered were taken from IPCC AR6. We selected the SSP1-2.6, SSP3-7.0 and SSP5-8.5 scenarios. The required data was obtained from the ISIMIP repository. The ISIMIP (Inter-Sectoral Impact Model Intercomparison Project) initiative is a collaborative research effort that aims to assess the impacts of climate change on various sectors of society and the environment.

#### Climate projections

The hydrological regime of the Ebro basin was taken from the results of global hydrological models H08 and CWatM, available in the ISIMIP repository. Two sets of climate scenarios were used: historical scenarios, for past times and future scenarios, for future times. Selected historical scenarios from ISIMIP are of two types: obsclim and historical. The denomination obsclim corresponds to impact models forced with observed climate in the actual time sequence. They are based on reanalysis data. This option was selected to validate the runoff obtained with the two global climate models against the results of the SIMPA model in the historical period. The denomination historical corresponds to impact models forced with results from climate models. This option was selected as a control reference to estimate changes of potential sediment transport in the future. Future scenarios correspond to the three emission scenarios of AR6 selected: SSP1-2.6, SSP3-7.0 and SSP5-8.5. In these options, climate models were forced with the emission patterns expected in each emission scenario. The simulations for future time periods start in 2015 and end in 2100. The hydrological models were forced with climate drivers in the corresponding scenarios. There are two types of climate drivers: based on observations and based on climate models. The climate driver based on observations is gswp3 and is used in the obsclim scenario. The climate drivers based on models are gfdl-esm4, mri-esm2, ipsl-cm6a-1r, mpi-esm1-2hr and ukesm1-0-11. They are used in the historical and future scenarios.

#### Validation against SIMPA data

The comparison of the time sequence of annual flows and potential sediment transport in the Ebro River produced by the SIMPA model and the two ISIMIP hydrologic models is shown in Fig. 2.37. Potential sediment transport was estimated from monthly average flows using the rating curve derived from numerical simulations. Both ISIMIP models show a good agreement with SIMPA in the overlapping period 1940-2019 for annual flows. The agreement of the CWatM model appears to be better. However, the comparison for potential sediment transport shows that both ISIMIP models produce much higher sediment transport than SIMPA model. The time sequence of potential sediment transport is very similar for the two ISIMIP hydrologic models.

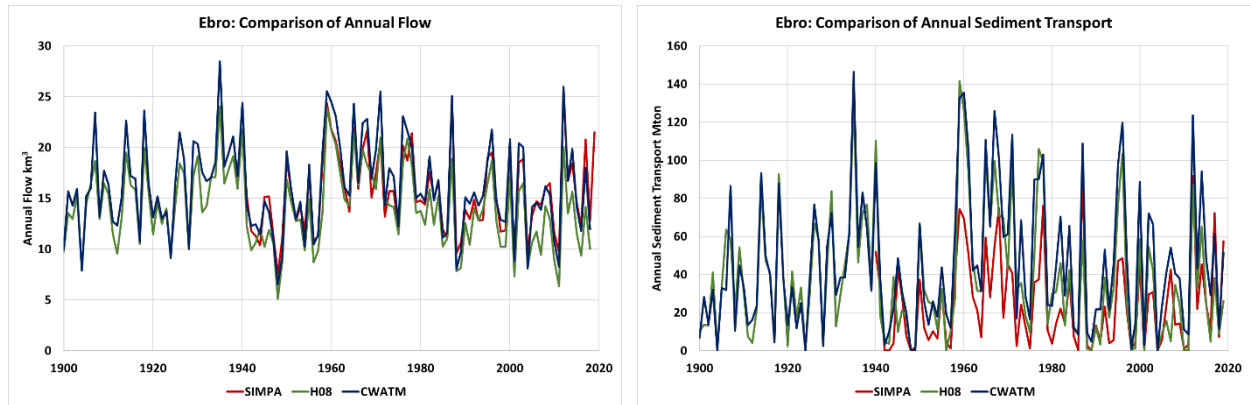


Figure 2.37. Comparison of the time sequence of annual flows and potential sediment transport in the Ebro River produced by SIMPA model and ISIMIP global hydrologic models. Left: Annual flows. Right: Potential sediment transport

Fig. 2.38 shows the scatter plot of annual flows in the Ebro River. The plot on the left shows the comparison between H08 model and SIMPA model and the plot on the right shows the comparison between CWatM model and SIMPA model. For the H08 model, the slope of the linear regression fit is 0.89, suggesting underestimation of annual flow values for the H08 model compared to the SIMPA model. The coefficient of determination is very high, 0.986. For the CWatM model, the results are much better. The slope of the linear regression fit is 1.04, suggesting only a small bias. The coefficient of determination is excellent, 0.994.

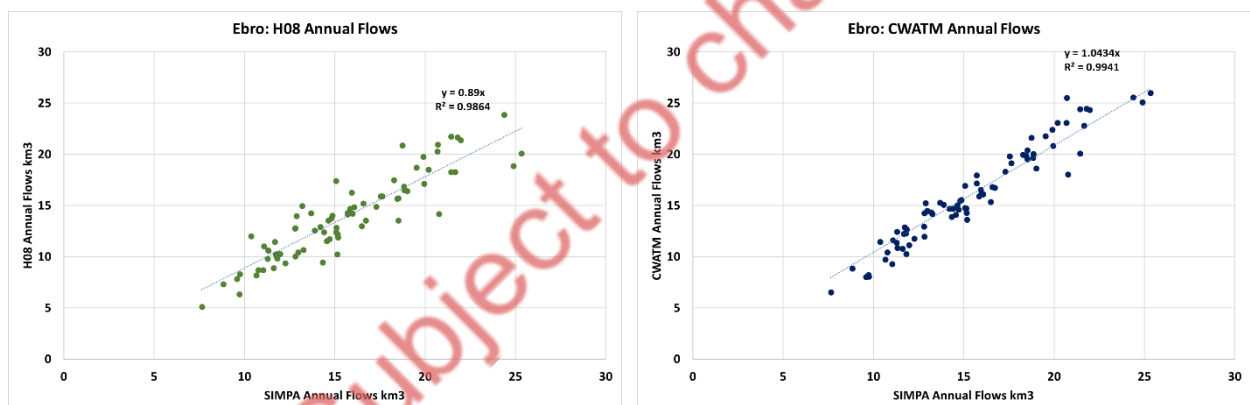


Figure 2.38. Comparison of annual flows in the Ebro River produced by ISIMIP global hydrologic models and SIMPA model. Left: H08 model. Right: CWatM model

Fig. 2.39 shows the scatter plot of potential sediment transport in the Ebro River. The plot on the left shows the comparison between H08 model and SIMPA model and the plot on the right shows the comparison between CWatM model and SIMPA model. The scatter is much larger than in the case of annual flows. For the H08 model, the slope of the linear regression fit is 1.32, suggesting a significant overestimation of annual flow values for the H08 model compared to the SIMPA model. The coefficient of determination is low, 0.802. For the CWatM model, the overestimation is even larger. The slope of the linear regression fit is 1.70. The coefficient of determination is better than in the case of the H08 model, 0.907. These results are surprising, because the agreement for annual flows is very good, especially for the CWatM model, and potential sediment transport is derived from annual flows using the same rating curve for all models.

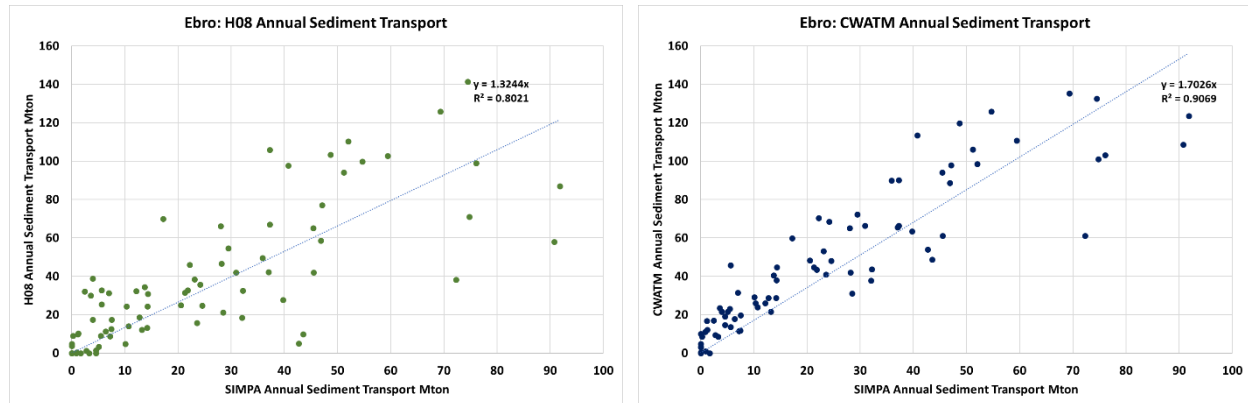


Figure 2.39. Comparison of potential sediment transport in the Ebro River produced by ISIMIP global hydrologic models and SIMPA model. Left: H08 model. Right: CWatM model

The causes for the disagreement in potential sediment transport can be identified by analyzing the seasonality, which is shown in Fig. 2.40. The plot on the left shows the monthly flow averages for the overlapping period and the plot on the right shows the monthly averages of potential sediment transport. The comparison of the distribution of monthly flows shows that ISIMIP models tend to overestimate flow in autumn and winter months and to underestimate flow in spring and summer months. The disagreement is probably due to a failure to properly capture the snow accumulation in winter and the snowmelt processes that produce the high flows of the Ebro River in spring. The overestimation of the winter flows is amplified by the nonlinearity of the sediment transport process and leads to a large overestimation of sediment transport.

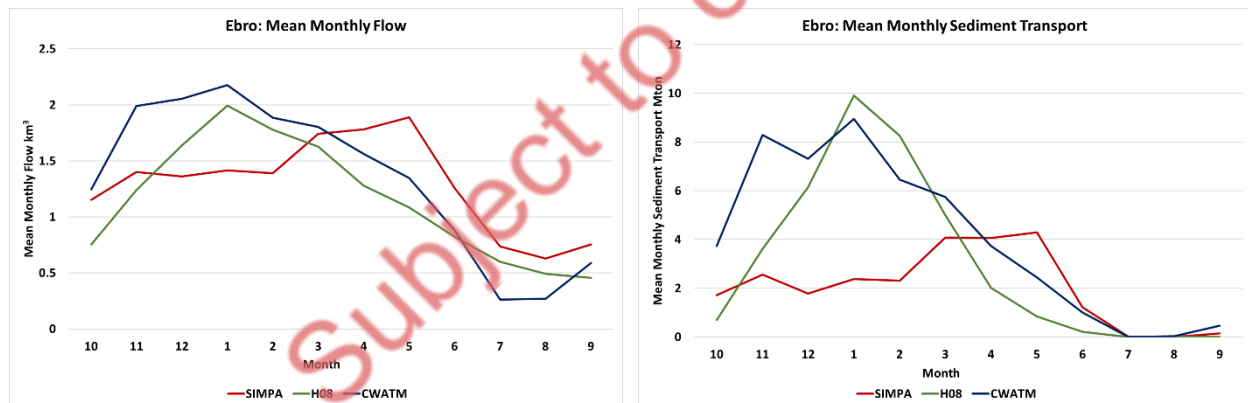


Figure 2.40. Comparison of seasonality of flows and potential sediment transport in the Ebro River produced by ISIMIP global hydrologic models and SIMPA model. Left: Seasonality of flows. Right: Seasonality of potential sediment transport.

The large disagreement between sediment transport estimated by the SIMPA model and by ISIMIP models suggest that a bias correction is required. The values of monthly flows of ISIMIP were corrected for monthly bias. The results of the effect of bias correction on potential sediment transport are shown in Fig. 2.41. The scatter is still significantly larger than that of annual flows. For the H08 model, the slope of the linear regression fit is 0.89 and the coefficient of determination is 0.850. For the CWatM model, the slope of the linear regression fit is 1.28 and the coefficient of determination is 0.881. These results improve the agreement for potential sediment transport between SIMPA model and ISIMIP models.

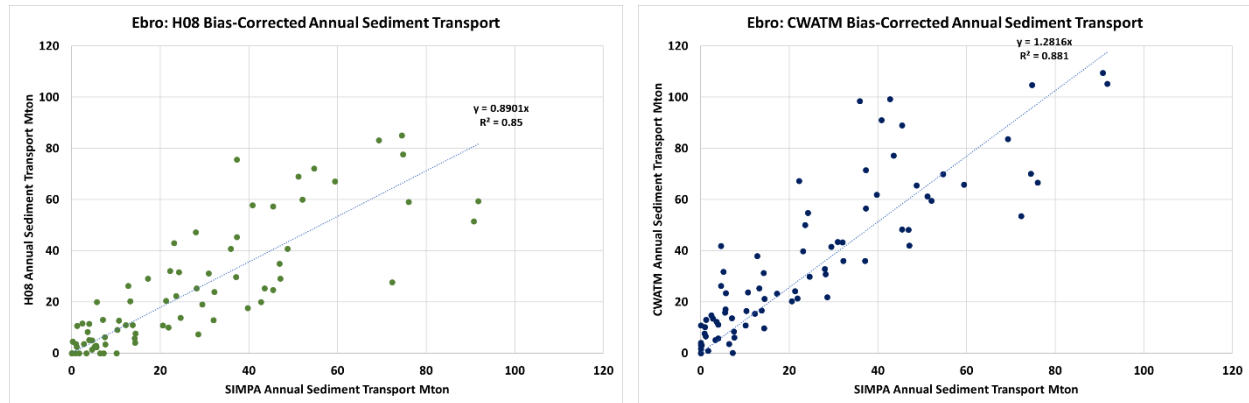


Figure 2.41. Comparison of bias-corrected potential sediment transport in the Ebro River produced by ISIMIP global hydrologic models and SIMPA model. Left: H08 model. Right: CWatM model

### Results of annual flows under climate projections

The results produced by SIMPA model and ISIMIP hydrologic models for mean annual flow in all scenarios analyzed are presented in Table 2.4. The values correspond to averages taken over 40-year periods. The time period for SIMPA and the obsclim scenario spans from 1979-80 to 2018-19. The time series of the historical scenario only cover up to year 2014, so the time period selected for this scenario is 1974-75 to 2013-2014. Two time periods were selected for the climate projections: 2020-21 to 2059-60 and 2060-61 to 2099-2100. The table presents the values of mean annual flow obtained for the SIMPA, the two ISIMIP models, and the average of the two ISIMIP models, in all scenarios considered. It also presents the average values obtained with all climate drivers in each scenario.

The results show a significant difference between the mean annual flow estimated with the two global hydrologic models. For the obsclim scenario, H08 provides a mean annual flow for the Ebro River of 12.63 km<sup>3</sup>/yr, while the estimate of CWatM is 15.17 km<sup>3</sup>/yr. The estimate of the SIMPA model, 14.97 km<sup>3</sup>/yr, is almost coincident with that of the CWatM model. The values for the average over the five climate drivers of the historical scenario are 13.49 km<sup>3</sup>/yr for the H08 model and 15.62 km<sup>3</sup>/yr for the CWatM model. The corresponding values of the obsclim scenario for the historical period, 1974-75 to 2013-2014, are 13.19 km<sup>3</sup>/yr for the H08 model and 15.63 km<sup>3</sup>/yr for the CWatM model, which means that there is an excellent agreement between the obsclim and the average of the results obtained with the five climate drivers used in the historical scenario.

The projections for future scenarios show some sensitivity to the climate drivers used, but they provide a consistent picture of the expected evolution of mean annual flow in the Ebro basin. Mean annual flow is expected to decrease in the Ebro basin for most scenarios. Only the mri-esm2 climate driver produced an increase in mean annual flow in some scenarios.



Table 2.4. Mean annual flow obtained in the simulations of the scenarios for the Ebro basin, in km<sup>3</sup>/yr

Scenario	obsclim 80-19	obsclim 75-14	historical 75-14	ssp126 20-59	ssp370 20-59	ssp585 20-59	ssp126 60-99	ssp370 60-99	ssp585 60-99
<b>SIMPA</b>	<b>14.97</b>	<b>15.19</b>							
h08_gswp3	12.63	13.19							
h08_gfdl			13.45	12.12	10.61	11.64	12.20	10.22	9.14
h08_mri			13.40	12.37	11.33	12.97	13.62	11.45	9.94
h08_ipsl			13.61	10.91	10.42	9.83	10.57	8.10	7.27
h08_mpi			13.03	10.95	10.33	10.61	11.39	8.80	8.55
h08_ukesm1			13.98	11.63	9.63	9.24	10.62	7.64	7.97
<b>mean h08</b>	<b>12.63</b>	<b>13.19</b>	<b>13.49</b>	<b>11.59</b>	<b>10.46</b>	<b>10.86</b>	<b>11.68</b>	<b>9.24</b>	<b>8.57</b>
cwatm_gswp3	15.17	15.63							
cwatm_gfdl			15.84	15.31	13.66	14.98	15.46	13.88	12.66
cwatm_mri			15.59	15.81	15.28	16.90	16.78	15.81	14.03
cwatm_ipsl			15.84	13.95	13.98	12.81	13.84	11.82	10.60
cwatm_mpi			15.44	14.02	12.90	13.71	14.49	11.73	11.87
cwatm_ukesm1			15.40	14.92	13.82	12.13	14.30	11.89	11.38
<b>mean cwatm</b>	<b>15.17</b>	<b>15.63</b>	<b>15.62</b>	<b>14.80</b>	<b>13.93</b>	<b>14.11</b>	<b>14.98</b>	<b>13.03</b>	<b>12.11</b>
gswp3	13.90	14.41							
gfdl			14.64	13.72	12.13	13.31	13.83	12.05	10.90
mri			14.49	14.09	13.31	14.93	15.20	13.63	11.98
ipsl			14.72	12.43	12.20	11.32	12.21	9.96	8.94
mpi			14.24	12.49	11.62	12.16	12.94	10.27	10.21
ukesm1			14.69	13.28	11.72	10.69	12.46	9.77	9.67
<b>mean</b>	<b>13.90</b>	<b>14.41</b>	<b>14.56</b>	<b>13.20</b>	<b>12.20</b>	<b>12.48</b>	<b>13.33</b>	<b>11.13</b>	<b>10.34</b>

The average values of projected mean annual flow obtained with the two hydrologic models for the five climate drivers in each scenario are shown in Fig. 2.42. To facilitate comparison, the figure shows the actual flow values obtained in the simulations and the bias-corrected values of mean annual flow. Both hydrologic models provide a similar picture of annual flow projection, but with different intensity. The SSP12.6 shows the least reduction of mean annual flow. The SSP37.0 predicts the largest reduction for the first time window 2020-2059, reaching -10% for the CWatM model and exceeding -20% for the H08 model. For the second time window, the largest reduction is predicted by the scenario SSP58.5: more than -20% for the CWatM model and more than -35% for the H08 model.

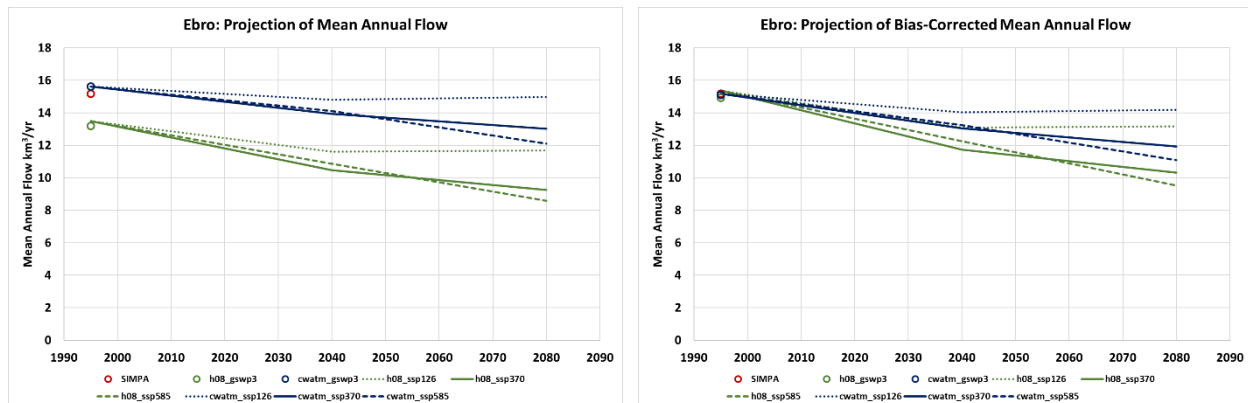


Figure 2.42. Projection of mean annual flow in the Ebro River under ISIMIP climate scenarios. Left: Actual value of mean annual. Right: Bias-corrected mean annual flow

### Results of potential sediment transport under climate projections

The time series produced by SIMPA model and ISIMIP hydrologic models in all scenarios analyzed were processed using the sediment transport rating curve to obtain projections of potential sediment transport in natural conditions. The analysis was performed on the bias-corrected series. The results are presented in Table 4. The values correspond to the same periods shown in Table 2.4. Table 2.5 presents the values of mean annual potential sediment transport obtained for the SIMPA, the two ISIMIP models, and the average of the two ISIMIP models, in all scenarios considered. It also presents the average values obtained with all climate drivers in each scenario.

*Table 2.5. Mean potential sediment transport obtained in the simulations of the scenarios for the Ebro basin, in Mton/yr*

Scenario	obsclim 80-19	obsclim 75-14	historical 75-14	ssp126 20-59	ssp370 20-59	ssp585 20-59	ssp126 60-99	ssp370 60-99	ssp585 60-99
<b>SIMPA</b>	<b>22.68</b>	<b>21.60</b>							
<b>h08_gswp3</b>	15.61	19.06							
<b>h08_gfdl</b>			20.50	14.34	10.81	11.84	13.82	7.37	5.63
<b>h08_mri</b>			23.33	19.20	10.32	25.54	25.13	19.36	9.85
<b>h08_ipsl</b>			23.92	12.46	11.34	7.50	14.98	8.32	3.81
<b>h08_mpi</b>			21.54	14.04	10.40	11.17	15.23	6.29	7.16
<b>h08_ukesm1</b>			26.93	15.81	6.78	7.02	11.55	5.54	7.36
<b>mean h08</b>	<b>15.61</b>	<b>19.06</b>	<b>23.24</b>	<b>15.17</b>	<b>9.93</b>	<b>12.61</b>	<b>16.14</b>	<b>9.38</b>	<b>6.76</b>
<b>cwatm_gswp3</b>	31.01	34.48							
<b>cwatm_gfdl</b>			36.95	33.65	26.38	30.74	35.93	26.43	23.38
<b>cwatm_mri</b>			39.95	44.13	35.42	50.28	43.20	43.91	33.19
<b>cwatm_ipsl</b>			36.95	32.29	33.27	21.72	37.62	26.76	18.49
<b>cwatm_mpi</b>			40.00	33.88	23.82	26.86	34.13	19.21	21.15
<b>cwatm_ukesm1</b>			36.72	38.12	27.42	20.78	35.66	25.46	22.54
<b>mean cwatm</b>	<b>31.01</b>	<b>34.48</b>	<b>38.11</b>	<b>36.41</b>	<b>29.26</b>	<b>30.08</b>	<b>37.31</b>	<b>28.35</b>	<b>23.75</b>
<b>gswp3</b>	23.31	26.77							
<b>gfdl</b>			28.73	23.99	18.60	21.29	24.87	16.90	14.51
<b>mri</b>			31.64	31.66	22.87	37.91	34.16	31.63	21.52
<b>ipsl</b>			30.44	22.38	22.30	14.61	26.30	17.54	11.15
<b>mpi</b>			30.77	23.96	17.11	19.01	24.68	12.75	14.15
<b>ukesm1</b>			31.83	26.96	17.10	13.90	23.60	15.50	14.95
<b>mean</b>	<b>23.31</b>	<b>26.77</b>	<b>30.68</b>	<b>25.79</b>	<b>19.60</b>	<b>21.35</b>	<b>26.72</b>	<b>18.86</b>	<b>15.26</b>

The results show a significant difference between the mean potential sediment transport estimated with the SIMPA model and those estimated with the two global hydrologic models, despite the bias correction. For the obsclim scenario, the estimate of the SIMPA model is 22.68 Mton/yr. H08 provides a mean sediment transport for the Ebro River of 15.61 Mton/yr (31% less than SIMPA), while the estimate of CWatM is 31.01 Mton/yr (36% more than SIMPA). These estimations are, therefore, highly uncertain. The values for the average over the five climate drivers of the historical scenario are 23.24 Mton/yr for the H08 model and 38.11 Mton/yr for the CWatM model. The corresponding values of the obsclim scenario for the historical period, 1974-75 to 2013-2014, are 19.06 Mton/yr for the H08 model and 34.48 Mton/yr for the CWatM model. The projections for future scenarios show more variability than in the case of annual flows. The potential for sediment transport under natural conditions is expected to decrease dramatically in some scenarios. The average values of projected mean potential sediment transport obtained with the two hydrologic models for the five climate drivers in each scenario are shown in Fig. 2.43. Despite the difference

in absolute values, the two ISIMIP hydrologic models provide a similar picture of the expected evolution of potential sediment transport, intensifying the effects observed in annual flow. The SSP12.6 shows the least reduction of potential sediment transport. The SSP37.0 predicts the largest reduction for the first time window 2020-2059, reaching -23% for the CWatM model and exceeding -55% for the H08 model. For the second time window, the largest reduction is predicted by the scenario SSP58.5: more than -70% for the CWatM model and more than -35% for the H08 model.

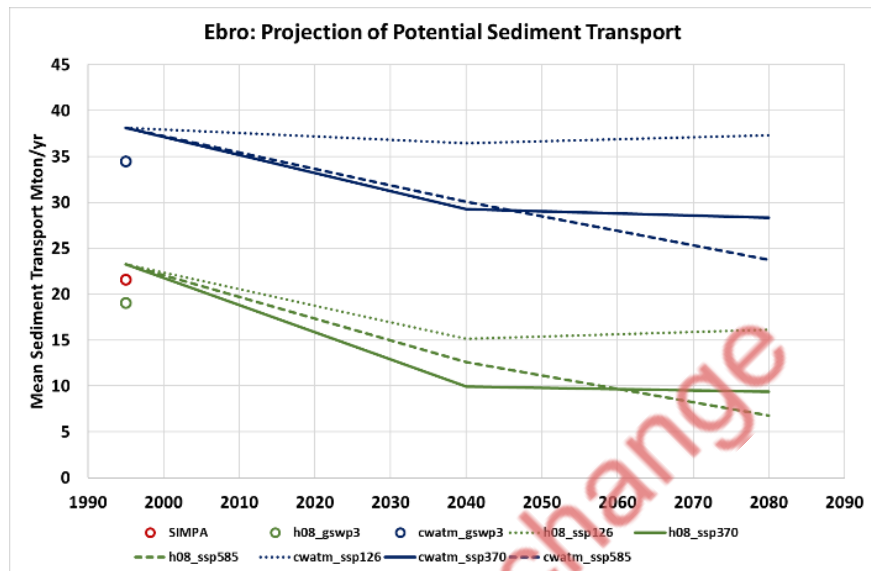


Figure 2.43. Projection of mean potential sediment transport in the Ebro River under ISIMIP climate scenarios

## 2.2.5 Conclusions

The projected reductions in mean annual flow will dramatically reduce the sediment transport capacity of the Ebro River under natural conditions, due to the nonlinearity of the sediment transport rating curve. The results of the analysis are summarized in Fig. 2.44, which shows the projected changes of mean annual flow and potential sediment transport in the Ebro River for the two hydrologic models of ISIMIP. Although the H08 and CWatM models produce different absolute figures, the relative projected evolution is very similar in both models. In the most likely scenario, SSP37.0, the expected reduction in the first time period, 2020-2059, ranges between 10% and 22% for mean annual flow and between 23% and 57% for sediment transport.

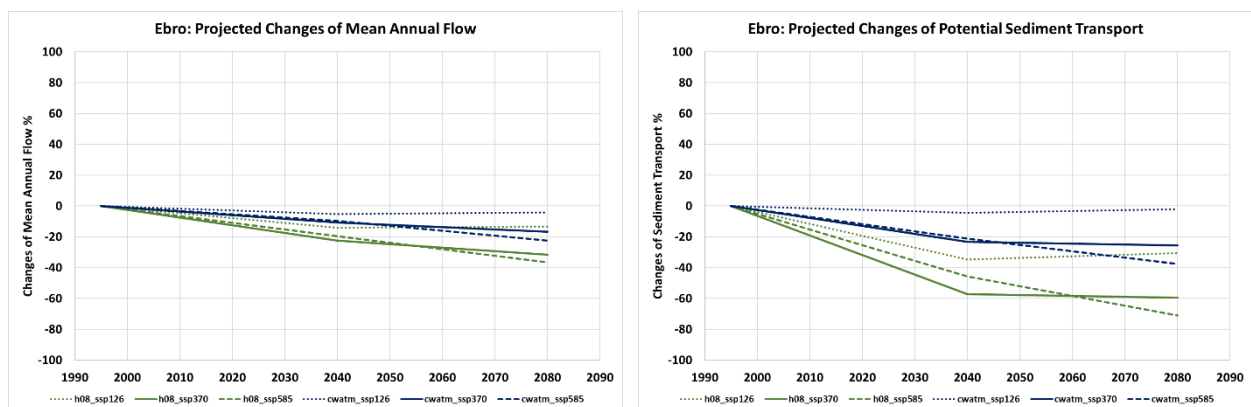


Figure 2.44. Projected changes of mean annual flow and potential sediment transport in the Ebro River under ISIMIP climate scenarios. Left: Changes of mean annual. Right: Changes of potential sediment transport

The impact of such reductions on the potential sediment transport capacity of the Ebro River under altered conditions will depend on how the Ebro River is managed in the future. Under the current management strategy, roughly 6 km<sup>3</sup>/yr are abstracted from the 15 km<sup>3</sup>/yr of natural flow, leaving 9 km<sup>3</sup>/yr in Tortosa. This reduces the potential sediment transport capacity from 22 Mton/yr under natural conditions to 7 Mton/yr, but this figure is still enough to convey the sediment required by the Delta. The projected reductions suggest a future mean annual flow between 12 km<sup>3</sup>/yr and 13.5 km<sup>3</sup>/yr. The potential sediment transport capacity for the natural regime is expected to be reduced to between 10 Mton/yr and 17 Mton/yr. If the potential sediment transport under altered conditions was similarly reduced, it would fall to a range between 3.5 km<sup>3</sup>/yr and 5 km<sup>3</sup>/yr and some carrying capacity would still remain in the river. However, if current abstractions of 6 km<sup>3</sup>/yr were maintained in the future, available flow would be reduced to 6 km<sup>3</sup>/yr to 7.5 km<sup>3</sup>/yr, which represent a larger reduction than that of natural flow. Therefore, it is very likely that the potential for sediment transport under altered conditions will be reduced more than that under natural conditions.

Subject to change

### 3 Multi-risk projections and climate warnings with ESS in Wadden Sea Pilot (DEL, HZG, FSK).

The Wadden Sea, located in the south-eastern part of the North Sea, is facing increasing risks of flooding and coastal erosion from extreme storms, which are becoming more frequent and intense in the context of global climate change. These risks pose a significant threat to the region's coastal communities and ecosystems, and we are committed to finding solutions to mitigate them.

A unique challenge in the Wadden Sea, a UNESCO World Heritage Site, is that the implementation of conventional hard and grey engineering solutions such as dams and breakwaters are less attractive. This reflects the need to preserve the ecological integrity and aesthetic values of the Wadden Sea, and underlines the delicate balance between conservation and the need for adaptive strategies. Therefore, the need for innovative, nature-based solutions has received more attention in recent years.

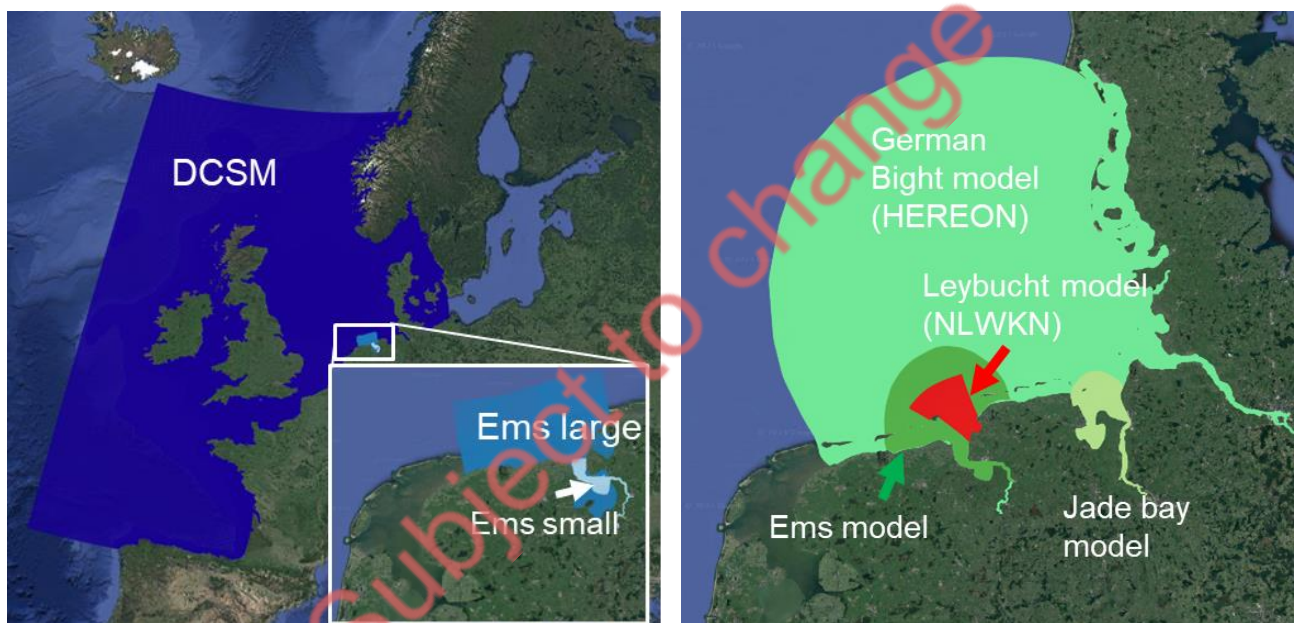


Figure 3.1. (a) Model domains Deltares

(b) Model domains Hereon and NLWKN

Seagrass restoration as a coastal protection measure could provide ecosystem buffers and has been shown to be effective in attenuating wave energy, reducing near-shore currents and stabilising the seabed. Recent studies have shown a positive trend in the natural recovery of seagrass meadows in the Wadden Sea area over the last two decades (Dolch, et al., 2017). Therefore, in the Wadden Sea case, we perform what-if scenarios on the size, location and layout of seagrass meadows to investigate the effectiveness of seagrass planting as a nature-based approach to mitigate coastal erosion caused by storm events.

#### 3.1 Multi-risk projections for ESS of NBS in the Wadden Sea

Within Rest-Coast project the pilot case partners of the Wadden Sea are concerned with the assessment of different Nature Based Solutions (NBS) that could provide an enhanced functioning of the following ecosystem services (ESS):

- Flood risk reduction
- Erosion risk reduction

- Carbon storage
- Water quality improvement
- food provisioning

For the present deliverable report D.2.2, risk reduction in relation to flooding and erosion is the focus of the work developed.

Using their respective modelling frameworks developed within Rest-Coast, the partners of Hereon, NLWKN and Deltares address respectively:

- the restoration of seagrass areas;
- the development of saltmarshes;
- and effective sediment management strategies;

as NBS with respect to potential improvements for different aspects of the ESS at concern.

As part of the risk projections strategy the evaluated measures for NBS are explored for different environmental and climatic conditions, involving the present day conditions as baseline for the ESS including an analysis on the seasonal variability; a focused analysis on extreme storm events of different severity, since storms are a major contributor to coastal erosion and flooding; and lastly different climate projections towards the end of the century that involve significantly elevated sea levels thus affecting coastal dynamics that might be steered differently by the applied NBS.

### 3.1.1 Criteria to assess risk reduction

For the five essential ESS provided by the NBS a set of key indicators was identified to evaluate the ESS performance based on the parameters that are provided by the partners modeling suits (described in 3.3) and are presented in Table 3.1.

*Table 3.1. Key metrics of risk reduction analyses for different scenarios*

ESS	Model parameter	Indicator system specific
Reduction coastal erosion	Erosion volumes	Annual mean erosion volume for a user-defined area
	Shoreline (where applicable as saltmarsh edge) retreat Vegetation/biotope cover on foreshore	Mean, min and max annual shoreline change for a user-defined area Area (in m2) per EUNIS ecotope in a user-defined area at the end of a time horizon
Reduction flood risk	Water levels during extreme/storm conditions Waves during extreme/storm conditions	Max, mean, 95 quantile during storm Max, mean 95 quantile during storm
Water purification	Mineral suspended solids Basic water quality parameters (T, O2, pH, salinity)	Annual mean and max per user-defined area (not in this deliverable)



Carbon sequestration	C-sequestration based on biotope (salt marsh, grassland, etc.) C-sequestration based on deposition volume	kg per year per user-defined area (not in this deliverable)
Food provisioning	Food production based on biotope	kg per year per user-defined area (not in this deliverable)

These metrics -as far as applicable for the respective case- are utilized to assess the multi risk factor related ESS efficiency within the environmental condition and climatic projections that are layout within the following.

For the pilot case the risks (3.2) and reduction are explored based on system specific key indicator metrics (Table 3.1) derived from the model parameters for investigated ESS.

### 3.1.2 Baseline risk reduction under present day conditions and seasonal variability

The evaluation of the risk reduction potential of the applied Nature Based Solutions is conducted under present day conditions. To assess the vegetation ESS, the year 2017 was chosen as the reference year to establish the baseline of expected merit from the restoration scenarios. Due to significant intra-annual variability in the study area, simulations and analysis are conducted separately for the summer and winter seasons.

The study compares seagrass during the summer and winter seasons using data from the 2017 simulation to examine seasonal differences. To represent seasonal variability in computationally heavy morphological simulations with Delft3D, which evaluate the impact of salt marsh development on erosion, the Hereon SCHISM simulations were extended to a two-year period. The simulations were then subjected to harmonic analysis to derive the seasonal variation of tidal constituents, which are implicitly modulated by meteorological variability. Based on the analysis data, we conducted time-compressed (scaling) simulations using SCHISM and Delft3D to perform coherent hydro and morphodynamic runs. We contrasted the summer and winter periods to obtain an indication of the range within one year.

### 3.1.3 Risk reduction under extreme weather conditions

The second part of the baseline analysis takes an event-based approach. Simulations were conducted for realistic historic storm events, rather than using a synthetic event construction. This approach allows for a coherent forcing across the multi-parameter hydrodynamic and meteorological forcing.

The first storm event analysed is Herwart, which is an example of a severe storm surge that occurred on 29 October 2017. Peak velocities of 120 to 140 km/h were recorded along the North Sea coast. This resulted in the highest water level in the North Frisian Wadden Sea, specifically on the west coast of Büsum, where it reached 2.06 m above mean high water. In Bremerhaven, on the coast of Lower Saxony, the water level reached its highest point at 2.60 m above mean high water. In Hamburg St.-Pauli, the water level rose to 3.34 m above mean sea level on the morning of 2017 (Pegelonline, BSH).

On December 5 and 6, 2013, the storm 'Xaver' caused peak gusts of 150 to 160 km/h (BSH) on the German North Sea coasts and in Denmark, classifying as a hurricane. The long persistence of north-westerly winds of

force 9 - 10 Bft over the German Bight allowed a series of three consecutive storm surges to build up, one of which reached the 'very severe storm surge' category (Sturmflut 2013\_bm1101 (bsh.de)). The water level in Hamburg St. Pauli reached a peak of 3.98 m above the mean high tide or 6.09 m above sea level, similar to the storm surge in February 1962.

These events can be classified with return periods of 2 years (Herwart) and 125 years (Xaver), respectively, when considering the combined variation of tidal anomaly and wave height (see also 3.2.2.1).

### 3.1.4 Risk reduction projection for end of the century future climate conditions under the RCP 8.5 scenario

Future risk projections are undertaken under the RCP8.5 scenario, which assumes a continuing growth of greenhouse gas emissions towards the end of the 21st century.

The probability of this emission trajectory has been doubted (Hausfather and Peters, 2020), yet it retains scientific value due to its high signal-to-noise ratio and is employed here to delineate the emerging signals of climate change. Policy-wise it represents the upper limit worst case scenario. Globally, the scenario indicates a rise in mean sea level by nearly 40 cm, with higher values regionally, such is the case in our study area. Within this scenario sea level can increase by up to 1m.

To cover the spread within this scenario, in the RCP 8.5 ensemble simulations, out of the climate forcing scenarios, the 5th, 50th and 95th percentiles ensemble members are chosen to derive the downscaled forcing, for our regional models.

To cover the spread within this scenario, in the RCP 8.5 ensemble simulations, out of the climate forcing scenarios, the 5th, 50th and 95th percentiles ensemble members are chosen to derive the downscaled forcing, for our regional models.

*Table 3.2. RCP scenarios considered by the partners*

Time	Scenario	Seagrass (Hereon)	Sediment strategies (Deltares)
2020	RCP 8.5 50%		+ 0.07 m (Garner et al., 2021)
2030	RCP 8.5 50%		+ 0.12 m (Garner et al., 2021)
2050	RCP 8.5 50%		+ 0.26 m (Garner et al., 2021)
2100	RCP 8.5 50%	+ 0.8 m in 2090 (Palmer et al., 2020)	+ 0.78 m (Garner et al., 2021)

## 3.2 Modeling framework

### 3.2.1 Modeling impact of seagrass as Nature-based solution (Hereon)

#### 3.2.1.1 Modeling workflow

Numerical simulations of seagrass recovery scenarios in the Wadden Sea are conducted with the semi-implicit cross-scale hydroscience integrated system model (SCHISM, Zhang et al. 2016) and run in coupled mode with the 3rd-generation wave model WWMIII (Roland et al. 2012) in a configuration for the German Bight to evaluate the potential impact on hydrodynamics.

The designated setup comprises 476,000 nodes and 932,000 triangular and quadrangular elements. The horizontal resolution varies, reaching a maximum of 1.5 km at the open boundary and decreasing to a minimum of 50 m in the estuaries. The vertical aspect is represented using 21 terrain-following sigma coordinates. Specifically, within the East Frisian Wadden Sea, the resolution spans between 100 and 300 m.

Model initialization and ocean boundary forcing are derived from the CMEMS AMM15/IBI (<http://marine.copernicus.eu/>) operational product as hourly time series for temperature, salinity, sea surface elevation, and 3D velocities. Atmospheric forcing is from the German Weather Service (DWD) (Kaspar et al. 2022), and spectral wave forcing from a Wave Watch 3 configuration of the North Atlantic.

To assess the impact of seagrass on morphodynamics north of the Norderney coast, we used the process-based morphodynamic model XBeach (Roelvink et al., 2009), which was regionally nested (one-way) to the SCHISM setup (see Fig. 3.2). The model domain extends 4.5 km along the shore and 14 km across the shore, with a horizontal spatial resolution of  $10 \times 10$  m. Hourly resolved sea surface elevations and variance density spectra from the SCHISM-WWM coupled model are used to force the model. The SCHISM-WWM coupled model is applied along the open boundaries of the XBeach domain (Chen et al. 2024).

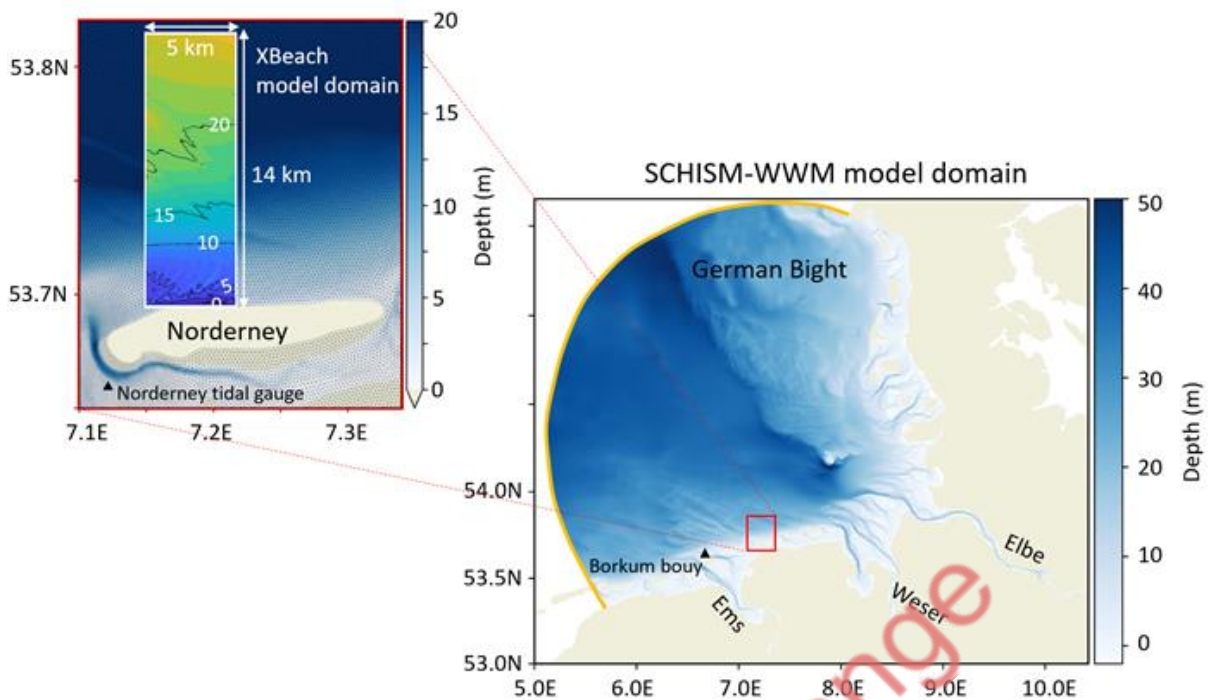


**Figure 3.2.** Domain and bathymetry of the SCHISM-WWM model (right) and the magnified box shows the study site, Norderney (left, red box). The white box indicates the domain and bathymetry of the XBeach model. The open boundary of the SCHISM-WWM model is illustrated with an orange curve

### 3.2.1.2 Modeling workflow for climate projections

For future climate scenarios, the boundary forcing is derived from downscaled regionalized projections of mean sea level (MSL) and coupled Remo climate scenario simulation output (Pein et al., 2023). The dynamical drivers in our study of future climate scenarios are global mean sea level change and coupled ocean-atmosphere variability. Global mean sea level rise is caused by thermosteric expansion, melting of polar ice caps and glaciers, and gravitational responses induced by the ice masses becoming liquid (Church et al., 2013; Gollidge, 2020). Regional exacerbation or mitigation of global MSL rise may be caused by vertical land movements such as postglacial isostatic rebound. Probabilistic estimates under the RCP8.5 scenario from the UKCP18 project are used for the prescription of MSL rise (Palmer et al., 2018; 2020).

The regionalised simulations of the Max-Planck-Institute Earth System Model Low Resolution (MPI-ESM-LR) ensemble runs under the RCP8.5 scenario were used to sample the coupled ocean-atmosphere dynamics. The downscaling of the global climate ensemble was performed by a regionally coupled climate system model with a nominal resolution of 5 km in the SNS (MPIOM-REMO, see Mayer et al., 2022; Mikolajewicz et al., 2005; Mathis et al., 2020; Lang and Mikolajewicz, 2020). The REMO atmospheric module has a resolution of approximately 7 km. In addition to atmospheric variables, this model predicts daily surface runoff, which serves as river input. The ensemble simulation dataset represents changes in ocean density and currents, as well as meteorological conditions, including atmospheric water transport, due to enhanced radiative forcing under climate change. The ensemble was created by initiating the global model from various historical states of the years 1950-1959 from three previous simulations using the same model system (Mathis and Mikolajewicz, 2020). The 6-hourly outputs of the global simulations were used as a forcing for the MPIOM-REMO regional climate modelling framework, which in turn provided the boundary forcing for the SCHISM simulations analyzed in this study. These ensemble simulations allow for the exploration of the internal variability of the climate system by varying the initial states across the 30 ensemble members. However, they do not account for MSL rise. Therefore, it is added here, along with the forcing data, using the probabilistic estimates (Palmer et al., 2018; 2020).



For the focus of this study on scenario spread, it is important to note that the spread of MSL is influenced by the variability of the global climate system, while ensemble spread is due to internal variability resulting from local synergies and feedbacks between geometry, density distribution, wind, and tidal forcing.

The performance of the model was assessed by comparing the simulations with different tide gauge stations in the German Bight for the period September and October. The overall correlation between the model and observations is between 0.95 and 0.99%, with a root mean square error mostly between 0.2 and 0.3m. The relative standard deviation is around 0.9. In general, the model reproduces the tidal amplitudes and timing accurately. Storm surge peaks during Herwart are correctly timed, but slightly underestimated in the EFWS (about 20-30 cm).

At Cuxhaven, the highest tide station in the German Bight, the peak of about 3.6 m on the south coast was underestimated by about 20%. The model predicted a peak of about 2.9 m. This underestimation was attributed to insufficient energy in the wind forcing, resulting in an underestimation of the wind-driven rise of the south coast water level (EFWS) in the hydrodynamic model.

Validation of the significant wave height at the Fino3 (FN3) and Westerland (WES) buoys, focusing on the week before and during the Herwart storm, shows that the model significant wave height is in good agreement with observations in terms of timing and general trends for HS. However, there is a tendency to underestimate the maximum significant wave height prior to the 29 October storm event at station Fino3. The measured (simulated) maximum significant wave heights during Herwart are about 6.9 (6.2) m at Fino3 and about 5.2 (4.8) m at Westerland. The correlation between model and observations is about 0.959 at FN3 and 0.963 at WES. The mean squared error is 0.322 m and 0.252 m respectively. The bias at these stations is about 0.115 and -0.06 m, respectively.

Subject to change

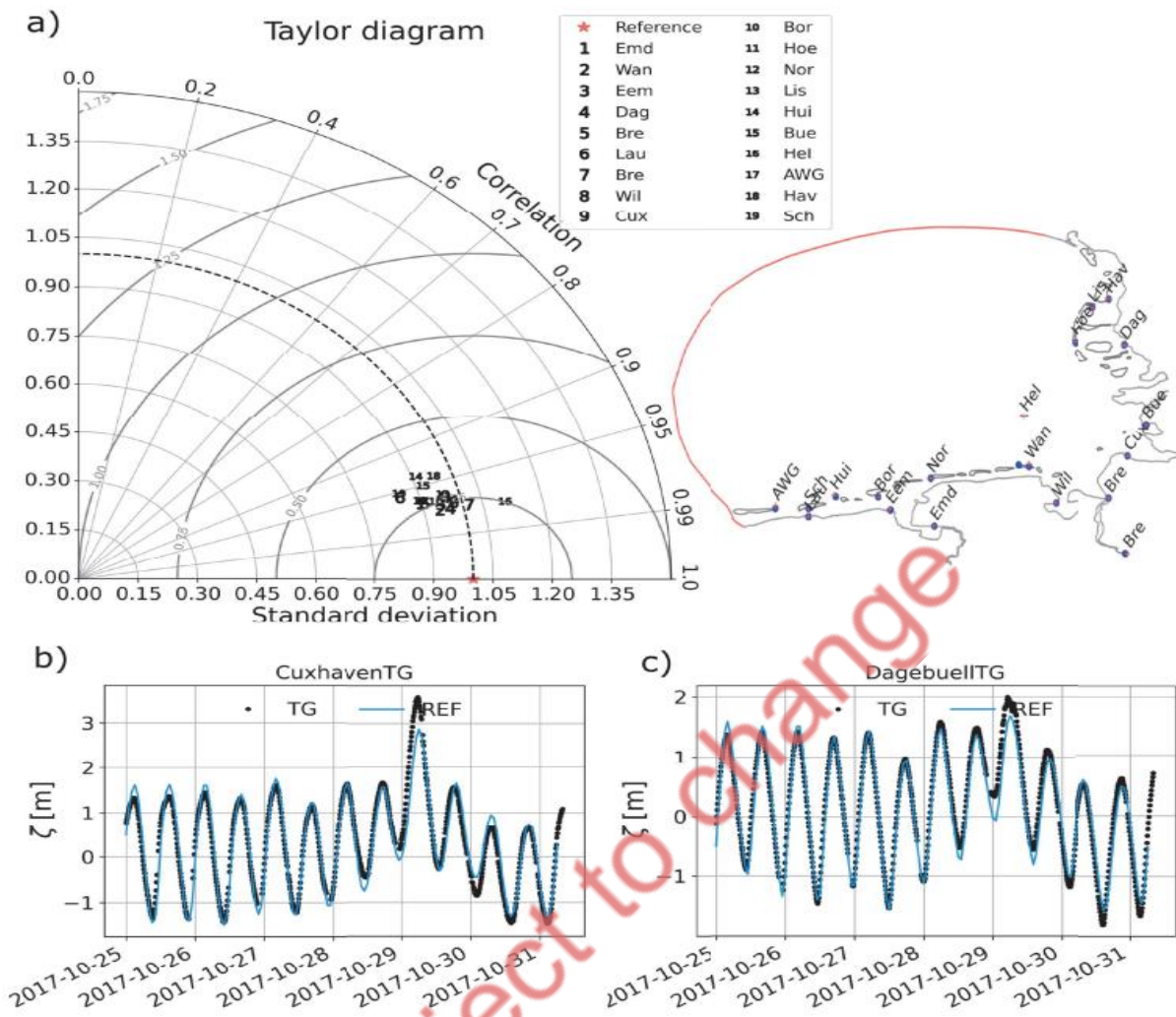


Figure 3.3. Validation of sea surface height against tide gauge stations within the German Bight in a Taylor diagram (a) for the period September-October 2017 and as time series comparison for the stations Cuxhaven (b) and Dagebuel (c). The location of the tide gauge stations is indicated by the map in a)

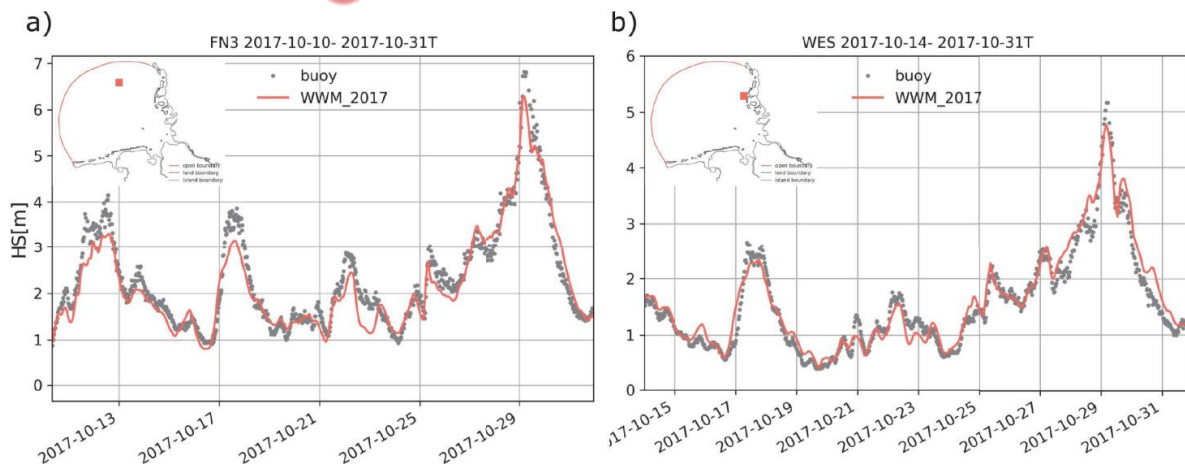


Figure 3.4. Validation of significant wave height against wave buoys Fino 3 (FN3, a) and Westerland (WES, b). The buoy location is indicated by the red square of the map in the upper left corner

### 3.2.1.3 Design of what-if scenarios for seagrass configurations

Both SCHISM and Xbeach account for the first order impact of vegetation on hydro and wave dynamics, in which seagrass is represented as rigid cylinders (e.g. Zhang et al. 2020). The dampening by seagrass is accounted for as additional drag term in the momentum equation:

$$\frac{Du}{dt} = f - g\nabla\eta + m_z - \alpha|u|uL(x, y, z) \quad (3.1)$$

f encompasses the numerically explicitly treated terms

$$f = f(v, -u) - \frac{g}{\rho_0} \int_z^\eta \nabla \rho d\zeta - \frac{\nabla p_A}{\rho_0} + F_m + R \quad (3.2)$$

The seagrass drag term alpha

$$\alpha(x, y) = D_v N_v C_{Dv} / 2 \quad (3.3)$$

parameterizes the vegetation density-related frictional scaling as the product of the individual's stem diameter ( $D_v$ ), the vegetation density ( $N_v$ , given as number of stems per  $m^2$ ), and  $C_{Dv}$ , the bulk form drag coefficient, typically ranging between values of 0 and 3 (Nepf and Vivoni 2000; Tanino and Nepf 2008) and, in our case, chosen as 1. In the 3D configuration of SCHISM, also the vegetation term is regulated active in the vegetated part of the water via L

$$L(x, y, z) = \begin{cases} \mathcal{H}(z_v - z), 3D \\ 1, 2D \end{cases} \quad (3.4)$$

$$\mathcal{H}(x) = \begin{cases} 1, x \geq 0 \\ 0, x < 0 \end{cases}$$

with H being the Heaviside step function and  $z_v$  the z-coordinate of the canopy height. The turbulence induced by vegetation is represented in the model as an additional source for turbulent kinetic energy. Further the wave damping is taking into account a sink term in the wave action equation of the wave model:

$$\frac{DN}{Dt} = S_{total} = S_{in} + S_{nl4} + S_{ds} + S_{nl3} + S_{br} + S_{bf} + S_{d,veg} \quad (3.5)$$

with the source function  $S_{tot}$  including the wind energy input,  $S_{in}$ , the nonlinear interactions in deep water ( $S_{nl4}$ ) and shallow, water ( $S_{nl3}$ ), and the energy dissipation in deep and shallow water due to white capping ( $S_{ds}$ ) and wave breaking ( $S_{br}$ ). Furthermore, it encompasses the dissipation due to bottom friction ( $S_{bf}$ ) and vegetation ( $S_{d,veg}$ ).

The model systems, which were developed as coupled model chains within Rest-Coast are used to explore the impact of restoration scenarios in different experiments (Fig. 3.6 Flowchart).

The experiments using SCHISM were constructed as academic 'what-if scenarios' evaluating the hypothetical dampening effect of seagrass at different extents and in different regions of the Wadden Sea. The scenarios explore the uppermost ceiling of seagrass expansion, as well as the distinguished effect of having seagrass in

highly energetic zones where it would interact with stronger currents and wave energy, and analogously the effect of seagrass recovery taking place in the low energetic zone (Jacob et al. 2023, Figure 6, table 4).

For those experiments the vegetation drag  $\alpha$  was configured, setting the plant geometry/property-related drag coefficient  $CD_v=1$ , the individual's stem diameter  $D_v$ , is generalized to  $D_v = 1.99\text{mm}$  for *Z. marina* dominated regions,  $D_v = 0.8\text{mm}$  for *Z. noltei* dominated regions, and in places of mixed occurrences (i.e., the majority of E1 and all areas in E3-E5) was set to the average value. The canopy height  $H_z$ , which influences the part of the water column that is influenced by seagrass interaction, was set to  $-H_z = 19\text{cm}$  for *Z. marina* dominated regions,  $-H_z = 9.8\text{cm}$  for *Z. noltei* dominated regions, – and in places of mixed occurrences (i.e., the majority of E1 and all areas in E3-E5) of both species  $H_z = 14.4\text{ cm}$  was set to the average value. Finally,  $N_v$  represents the areal coverage given as the number of shoots (cylinders) per  $\text{m}^2$ , which was derived for E1 from the areal coverage estimates according to Table 3.3.

*Table 3.3. Interval of seagrass areal coverage in data, and corresponding shoot density ( $N_v$ ) provided to the model*

Areal coverage (%)	Shoots ( $1/\text{m}^2$ )
5-19.9	450
20-39.9	1130
40-59.9	1530
60-79.9	3540
80-100	7360

*Table 3.4. Different Scenarios*

Experiment	Name	Seagrass cover
E1	Ref	Present-day (data) coverage
E2	Blank	No Seagrass (control)
E3	Vegmax	Entire WS between -1 and 4m
E4	VegLE	Shallowest 10% of Vegmax
E5	VegHE	Deepest 10% of Vegmax

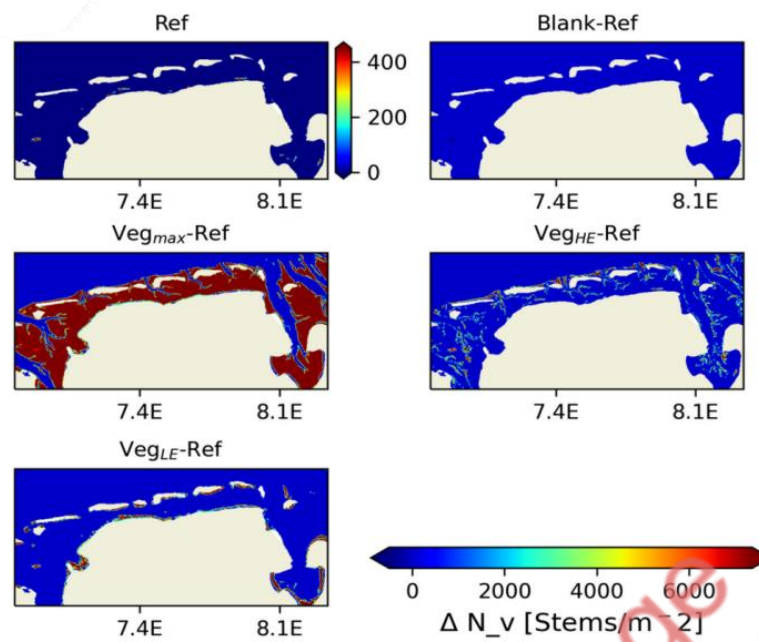


**Figure 3.5.** Seagrass coverage and shoot density in the different seagrass scenarios within the German Bight setup the EFWS: on left: shoot density in reference run (corresponding to the sparse seagrass coverage derived from observations), followed by differences of E2-E5 (Table 4) minus reference run

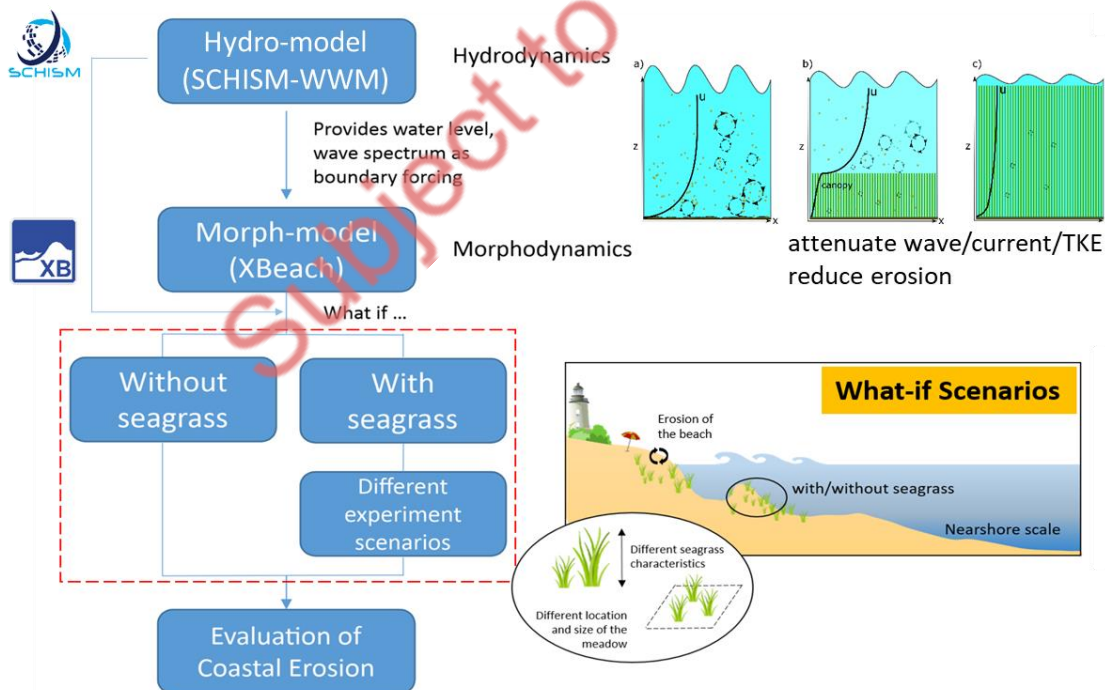


**Figure 3.6.** Flowchart showing the process applied when evaluating the impact seagrass has on coastal erosion

Moreover, the numerical experiments are conducted systematically in order to identify the effectiveness of various seagrass planting techniques in reducing coastal erosion and increasing coastal resilience to storm events. As illustrated in Fig. 3.7, the depth start planting seagrass  $h_s$  and the range in depth  $h_r$  control the location and size of the seagrass meadow. Area of all experiments are normalized with respect to the



experiment that  $h_s$ - $h_r$  combination reaches the largest seagrass meadow, which is assigned to 1. The normalized area  $A$  for all experiments with different combinations of  $h_s$  and  $h_r$  in the prototype XBeach modeling domain are plotted in Fig. 3.8(a). Fig. 3.8(b) and (c) show two examples of seagrass layouts for different combination of  $h_s$  and  $h_r$ . In general, a wider range of depths requires a larger area of seagrass. However, since the slope of the shoreface varies in the alongshore direction, the area and distribution of seagrass change when the plantings start at different depths and have different sizes. The height of the seagrass and density of seagrass stem per square are determined by  $a_h$  and  $b_v$ . Varying the two parameters as well as  $h_s$  and  $h_r$  describe different characteristics of the seagrass meadow and seagrass at different phase of lifetime. Details of all experiments are listed in Table 3.1.

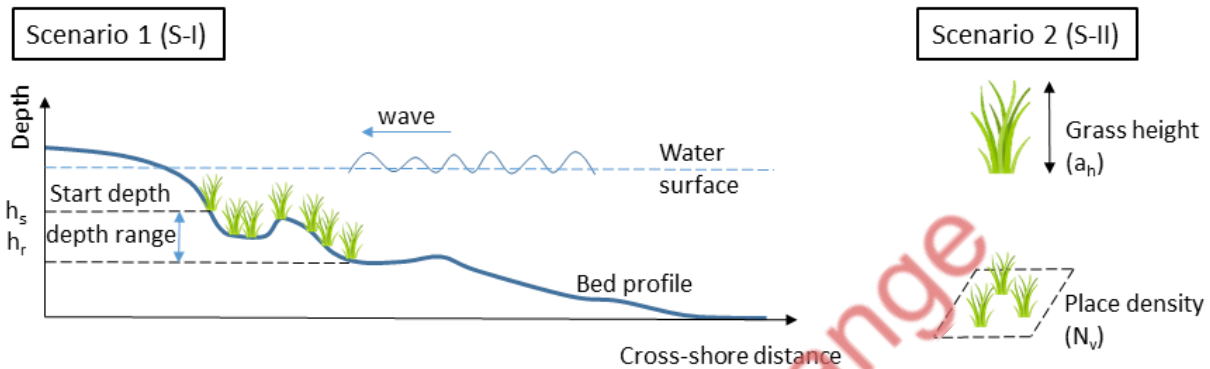


**Figure 3.7.** Experimental design of the scenario for different combinations of initial planting depth  $h_s$  and planting range  $h_r$ . The design scenario for the different characteristics of the seagrasses namely the seagrass height  $a_h$  and density  $N_v$  are also shown

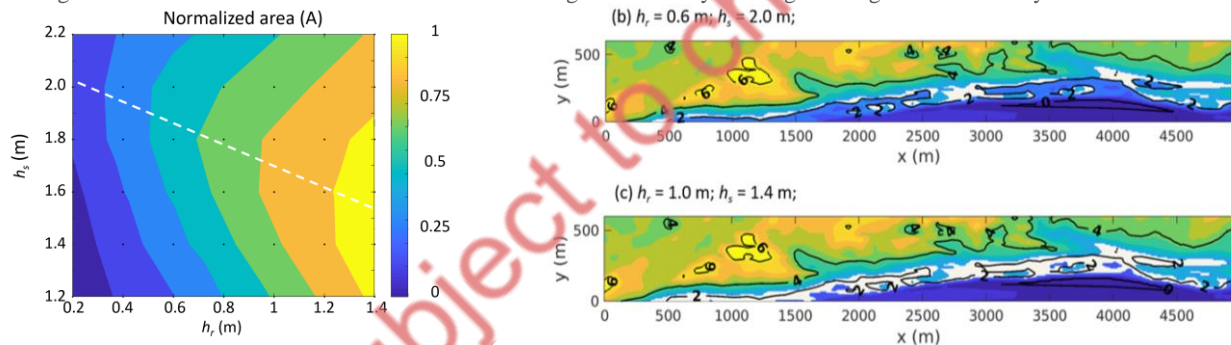


**Figure 3.8.** (a) Seagrass meadow in normalized area  $A$  for experiments as a function of  $h_r$  and  $h_s$ . The black dots indicate experiments with different  $h_r$  and  $h_s$  combinations. The seagrass area reaches an extreme when the combination of the two parameters intersects the white dashed line; (b) and (c) are two examples of seagrass layouts (white blank zones) for different ' $h_s$ ' and ' $h_r$ ' combinations. The  $x$  and  $y$  are along-shore and across-shore directions and the contour values indicate the water depth

**Table 3.1.** Overview of all what-if model simulations

What-if	Run	Abbr.	No.Exp.	Description
no seagrass	Reference scenario	Ref.	1	----
with seagrass	Default scenario	Default	4	Seagrass characteristics: $a_h=50$ cm; $b_v=1$ cm; $N_v=1000/m^2$ ; Rectangular seagrass meadow places at different across-shore locations from the coast;

with seagrass	Scenario I	S-I	42	Seagrass characteristics are the same as Default runs, but with the meadow size and location depends on hr and hs.
with seagrass	Scenario II	S-IIa	33	bv=1 cm; Nv=1000/m <sup>2</sup> , but ah= varies from 0 to 50 cm; Three hr-hs combinations are selected such that meadow size and location represents different typical meadow distributions; determined after S-I.
		S-IIb	30	as S-IIa, but for Nv varies from 0 to 1000;

### 3.2.2 Potential application of salt marsh as a Nature-Based-Solution (NBS) for coastal protection (NLWKN)

The main objective is to investigate the potential use of salt marsh as a nature-based-solution (NBS) for coastal protection. The present work focused on the evaluation of hydrodynamics, sediment transport and bed evolution during extreme events. The contribution of NBS to these processes was analyzed by comparing the hydromorpho results without NBS (WT - NBS) and with NBS (NBS) applications.

#### 3.2.2.1 Scenarios

Occurrence of three events was selected for the analysis representing two scenarios, Base-case (1) and extreme events (2). The base-case extends from 26-Jul-2017 23:00 to 31-Jul-2017 13:00 covering a 110 h of summer period, in which the occurrence of wave heights represents fair weather conditions (e.g., maximum Hs at 20 m depth < 2 m). The first extreme event (Xaver) occurred in December 2013 (max. Hs ~ 7.5 m at 20 m depth), while the second (Herwart) was in October 2017 (max. Hs ~ 6.0 m at 20 m depth). Storm periods of each event were selected following the statistical approach of Dissanayake et al. (2019). They combined the variation of tidal anomaly (TA=total water level-astronomical tide) and wave height (Hs) and classified that TA+Hs > 3.4 m as a storm event in the study area. Accordingly, Xaver occurred from 04-December-2013 16:30 to 09-December-2013 09:00, which covers a 112.5 h period (Figure 3a). Herwart spanned from 28-October-2017 09:00 to 30-October-2017 08:00 for a period of 47 h (Fig. 3.9b).

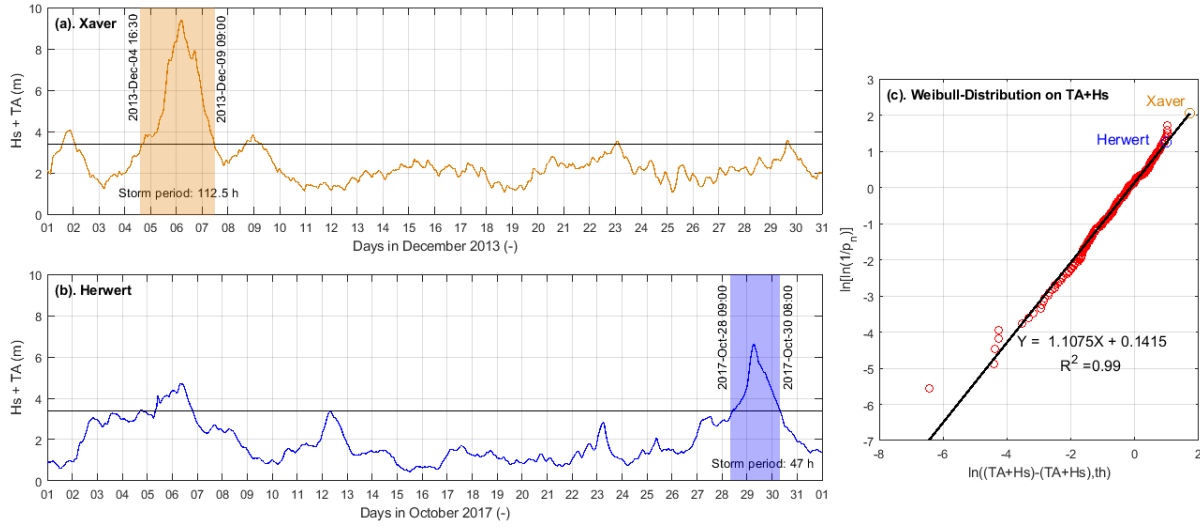


**Figure 3.9.** Variation of wave height (Hs) and tidal anomaly (TA) with the selected extreme events, *Xaver* in December 2013 (a) and *Herwart* in October 2017 (b). Colour-window indicates the identified storm period following the storm classification of Dissanayake et al. (2019) (black-line). Severity of storm events is shown with the agreement of Hs+TA with the theoretical extreme value distribution: Weibull (c)

Severity of each storm event was analyzed by comparing the sample data with an extreme value distribution, Weibull (Fig. 3.9c and Eq. 3.6: Probability density function) (Coles, 2009). The comparison indicates a good agreement between the sample data and the theoretical distribution ( $R^2=0.99$ ). Accordingly, *Xaver* is a very extreme event (return period 125 years) than *Herwart* (2 years).

$$f(x; \lambda_0, k) = \left\{ \frac{k}{\lambda_0} \left( \frac{x}{\lambda_0} \right)^{k-1} e^{-\left( \frac{x}{\lambda_0} \right)^k}, x \geq 0 \quad 0, x < 0 \right. \quad (3.6)$$

where,  $x = Hs+TA$  (m);  $k$ , shape parameter (-);  $\lambda_0$ , scale parameter (-)

Using the aforementioned two scenarios, 6 simulations were carried out applying WT-NBS (3) and NBS (3) (Table 3.6). Each model was forced with tide, wave and wind and simulated with the modelling tool Delft3D (Lesser et al., 2004) to investigate hydrodynamics, sediment transport and morphological changes, and to analyze the effect of NBS.

**Table 3.2.** Model simulations with Tide+Wave+Wind and morphology for the selected two extreme events, *Xaver* and *Herwart*. Derived return levels of the events by comparing Hs+TA with the extreme value distribution Weibull

Scenario	Without NBS (WT-NBS)	With NBS (NBS)	Return period comparing Hs+TA with the Weibull-distribution (years)
Base-Case	Fair-weather	Fair-weather	-
Extreme events	Xaver	Xaver	125
	Herwart	Herwart	2

### 3.2.2.2 Grid and bathymetry

Our study area is Ley Bay, which is located at the landward end of the tidal basin between Borkum and Juist barrier islands, and spans an area of about 5 km x 5 km. A high resolution grid (OEMS: Figure 3b) and bathymetry (Figure 3c) were developed within the present project to investigate the potential effect of NBS on hydrodynamics and morphological evolution. The OEMS domain consists of parts from both North Sea and Wadden Sea to provide a good interaction between North Sea and Wadden Sea processes, and covers an area of about 920 km<sup>2</sup>. The highest resolution in the Ley Bay is 30 m x 80 m, which is sufficient to represent the existing channel and shoal pattern (Fig. 3.10c) and to optimize the computational cost. The bathymetry was developed using the LiDAR data, which was measured in 2015 by the field measurement department of NLWKN.

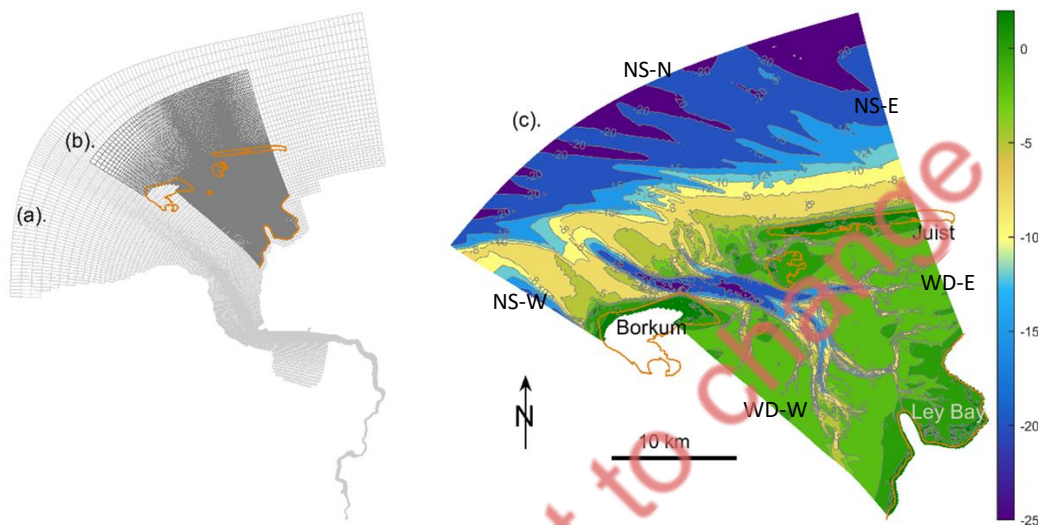


**Figure 3.10.** EMS-grid (a), OEMS-grid (b) and OEMS-bathymetry (c). For clarity, only every other grid is shown. The orange-line indicates the land boundary, and the investigation area is Ley Bay. Color bar indicates water depths with respect to MSL. There are 5 open boundaries: 2 at Wadden Sea, East (WD-E) and West (WD-W), and 3 at North Sea, East (NS-E), North (NS-N) and West (NS-W)

### 3.2.2.3 Bed sediment composition

In any sediment transport and morphological simulation, it is of utmost importance to implement the bed sediment composition as accurately as possible. Therefore, we used spatial varying 6 sediment fractions based on the NLWKN measured data covering littoral and eulittoral areas (e.g., grab sampling, sediment cores) (Mascioli et al., 2021). These data represent the bed sediment composition in 2015 (Figure 3.1). For the modeling purpose, they were implemented in two layers, in which the top layer has a maximum thickness of 1 m and the second layer represents the rest of the sediment thickness down to the Holocene layer. Initially, a quasi-equilibrium sediment distribution of each fraction was established by simulating the model for the sediment distribution without bed level change (Dissanayake and Wurpts, 2013). These sediment maps were then used as the initial bed sediment composition of the model to simulate the scenarios.



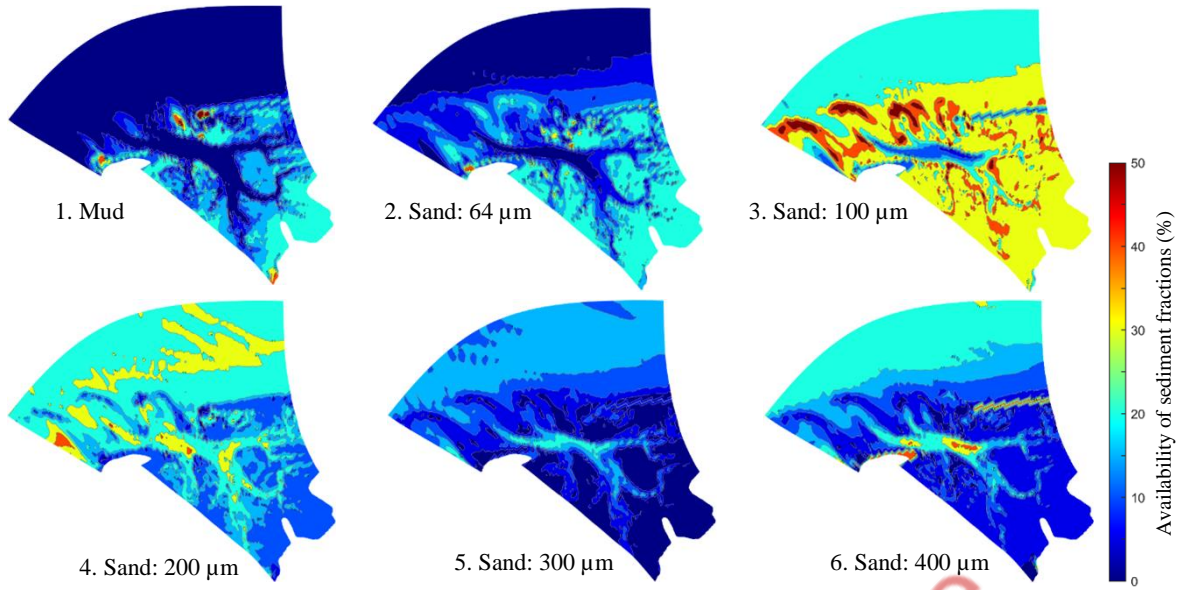


**Figure 3.1.** Bed sediment composition of the OEMS-domain. Color indicates the spatial availability of the adopted sediment fraction at the top layer: Mud (1), Sand 64  $\mu\text{m}$  (2), Sand 100  $\mu\text{m}$  (3), Sand 200  $\mu\text{m}$  (4), Sand 300  $\mu\text{m}$  (5) and Sand 400  $\mu\text{m}$  (6)

### 3.2.2.4 Implementation of Salt Marsh

Salt marshes are vegetated coastal wetlands that are flooded and drained as a result of fluctuations of sea level. In tidal systems, salt marshes are populated at the upper part of intertidal zone: sea-land interface. The entire salt marsh area of Wadden Sea accounts for about 400 km<sup>2</sup> (3%) (Esselink et al., 2017), while it is about 12 km<sup>2</sup> (38%) in Ley Bay.

In this study, the models were simulated in the 2DH-mode (depth-averaged). Therefore, the presence of Salt marsh was implemented using a Trachytopes approach (Delft3D, 2023), which has been developed following Baptist (2005), to estimate the vegetation exerted drag force to flow considering submerged and non-submerged plants. According to these formulations, the presence of vegetation leads to higher bed roughness and thus higher bed shear resulting in higher sediment transport, which is unrealistic, because the presence of vegetation tends to decrease sediment transport. Therefore, he has further introduced a reduction factor  $f$  considering the overall bed roughness: background roughness (i.e., situation without salt marsh) + roughness generated due to salt marsh, flow resistance (Chap. 4 in Baptist, 2005).

However, in Delft3D, this issue is resolved by adding an additional term in the momentum equation:  $-\frac{\lambda}{2}u^2$  ( $\lambda$ , flow resistance due to vegetation and  $u$ : velocity) (Delft3D, 2023). Therefore, the two roughness components are separately computed in the area of the salt marsh: background roughness ( $C_b$  in Eq. 3.7 for the case of submerged vegetation:  $h > h_v$ ) and salt marsh roughness (second term in right-hand of Eq. 3.7). The first is used to estimate bed shear stress, which determines the sediment mobility, while the second is used to estimate the vegetation exerted drag force on flow.

$$C = C_b + \frac{\sqrt{g}}{\kappa} \ln\left(\frac{h}{h_v}\right) \sqrt{1 + \frac{C_D n h_v C_b^2}{2g}} \quad (3.7)$$

$$\lambda = C_D n \frac{h_v C_b^2}{h C^2} \quad (3.8)$$

where,  $C$ , net bed roughness ( $m^{1/2}/s$ );  $\kappa$  is Von Kármán constant (-);  $n = mD$ , Vegetation density (m);  $h$ , water depth (m);  $g$ , gravitational acceleration ( $m^2/s$ )

At the transition region  $h=h_v$ , the second term of Eq. 3.7 goes to zero. For the non-submerged  $h < h_v$ , the flow resistance and bed roughness are explicitly separated.

$$C = C_b \quad (3.9)$$

$$\lambda = C_D n \quad (3.10)$$

Few parameters need to be provided into the model to set up the salt marsh configuration: number of cross sections stems/branches per  $m^2$  (m), diameter of branches/stems (D), plant height ( $h_v$ ), drag coefficient (CD) and background roughness ( $C_b$ ). Multiple bifurcations can be applied to implement a more realistic plant structure considering different depth layers, whereas only in the 3D applications. According to our study area (Fig. 3.12), these values were applied as 100 (m), 0.008 m (D), 0.5 m ( $h_v$ ), 1.65 (CD) and 45  $m^{1/2}/s$  ( $C_b$ ). The salt marsh area (green-polygon in Fig. 3.12c) is located above the high-water line ( $\sim 1.5$  m + MSL) along the land boundary. Therefore, it can be expected that this area is hardly submerged during fair weather conditions.

It should be noted that the present configuration of salt marsh does not allow vertical variation of plants and the adjustment of plants based on flow velocity (i.e., 2DH approach). Furthermore, in a long-term morphological simulation, the growth of the plant configuration needs to be updated off-the-shelf. These demand improvements of the salt marsh implementation in the model, which would be undertaken in the cause of the project upon the time allowance.

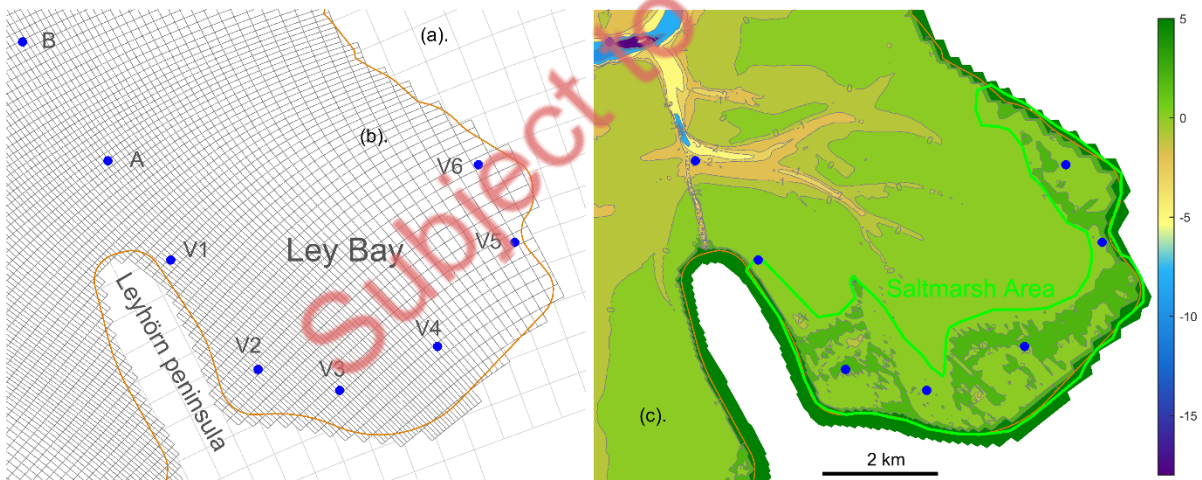


**Figure 3.2.** EMS-grid (a), Grid in the Ley Bay area from the OEMS-grid (b) (for clarity every other grid is shown) and bathymetry in the Ley Bay area (c). Salt marsh coverage is indicated with the green-polygon. Analysis points A (Depth: -1.4 m), B (-8.4 m) (see Figure 13), and V1 (1.3 m), V2 (2.0 m), V3 (1.9 m), V4 (1.0 m), V5 (1.9 m) and V6 (2.0 m). Color bar indicates water depths with respect to MSL

### 3.2.2.5 Model boundary forcing

The OEMS model was simulated by force with tide, wave and wind. Both tide and wave were developed for the OEMS by coupling with the EMS model (Fig. 3.12a). The OEMS model has 5 open boundaries: 3 at the North Sea side (i.e., NS\_E, NS\_N and NS\_W) and 2 at the Wadden Sea side (i.e., WD\_E and WD\_W) (Fig. 3.12c). All 4 lateral boundaries were implemented as velocities, while the north boundary (NS\_N) is water level. Water level and current boundaries were set up based on the predicted values of the EMS model. For

waves, both models were simulated simultaneously applying the offshore wave boundary for the EMS model. Based on a sensitivity analysis, the optimal wave prediction around the Ley Bay area was found, when the EMS model is forced with spatiotemporal wind fields (DWD, 2023) and the OEMS is forced with uniform wind measured at the station of Norderney: the next island to the east of Juist (DWD, 2023). For the storm events, Xaver and Herwart, the boundary forcing for the EMS model was obtained from a North Sea model of HEREON SCHISM (Section 3.2.1.1).

### 3.2.2.6 Calibration and validation

The model calibration was carried out for the period of October 2015 applying different bed roughness schemes (Table 3.3). The accuracy of the model predicted water levels was compared with the measured data at the station A (Fig. 3.12a). In general, it is found that there is no significant variation among the different schemes ( $R^2$  in Fig. 3.13a). However, the most optimal prediction resulted with M2-roughness-scheme, in which the bed roughness is similar to an existing Ley Bay model (Dissanayake and Wurpts, 2013). Note that this existing model restricts to the Wadden Sea area only, and does not cover North Sea, and thus the new model setup (2.1) was required and developed for the present project. The validity of the M2 roughness was then investigated simulating two independent periods: November 2015 (Fig. 3.13b) and December 2015 (Fig. 3.13c). Statistical comparison indicates a reasonable agreement between measured and predicted water levels ( $R^2 = 0.95$  and  $rmse = 0.22$  m).

Performance of the wave propagation in the Ley Bay area was analyzed using different bed frictions, breaker parameters and wind fields for the wave model. The optimal wave prediction at B (Fig. 3.12a) is shown in Fig. 3.13d applying a bed friction of 0.07, a breaker parameter of 0.73 and uniform wind fields from the station Norderney (DWD, 2023). Generally, there is a reasonable agreement of wave heights between the measurements and the model prediction ( $R^2 = 0.82$  and  $rmse = 0.05$  m). The observed variations are expected mainly due to the applied wind fields (i.e., spatial constant), in which they are not able to capture local scale small variations.

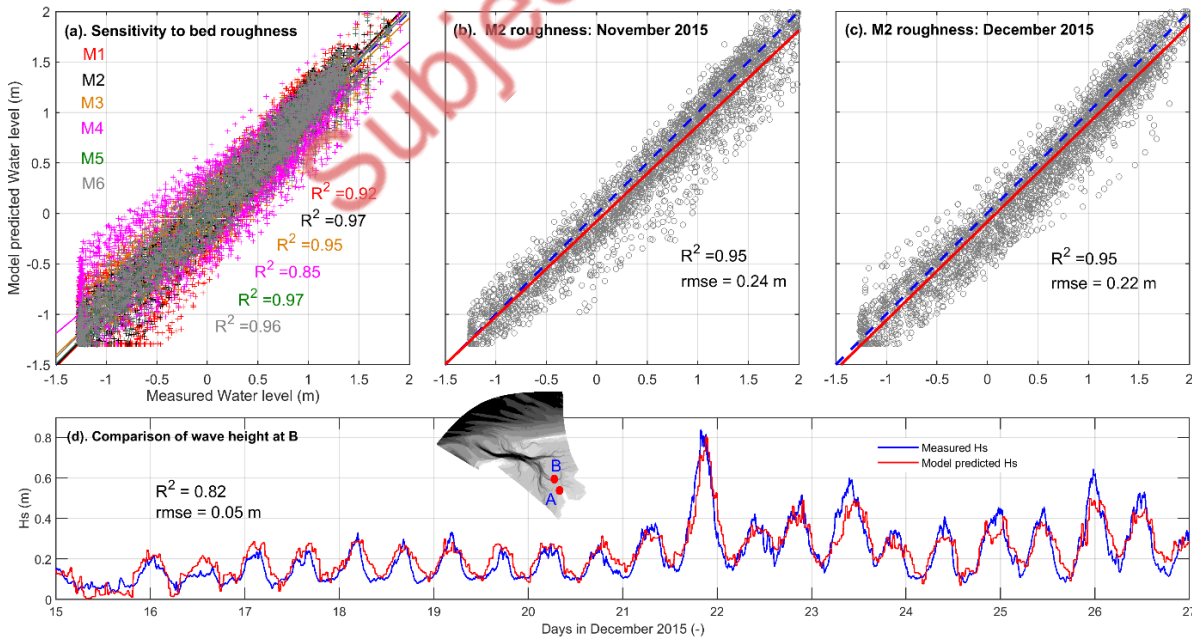


**Figure 3.3.** Calibration and validation of water level prediction at A (see on the OEMS-bathymetry: insert view). Comparison of predicted water levels for October 2015 with different bed roughness schemes (see Table 2) (a), validation using the optimum roughness (M2) for two independent periods; November 2015 (b) and December 2015 (c). Dash-line indicates the perfect agreement,

while solid-line shows the agreement between measured and predicted water levels. Comparison of wave height prediction at B (d). For clarity, only the final result is shown through different wind fields and roughness values in the wave model were investigated

Selected bed roughness schemes for the model calibration are summarized in Table 3.3.

**Table 3.3.** Sensitivity simulations applying different bed roughness schemes to calibrate the OEMS model.  $z_0$  is bed roughness length, where  $z_0 = k_s/30$ ,  $k_s$ : Nikuradse roughness length

Model	Description of bed roughness scheme
M1	White-Colbrook from the EMS model (Oberrecht, 2020): spatial varying $z_0$
M2	Different Mannings as in the existing Ley Bay model (Dissanayake and Wurpts, 2013): depth-class specific values
M3	Chèzy = 50 m <sup>1/2</sup> /s: spatial constant
M4	Chèzy = 40 m <sup>1/2</sup> /s: spatial constant
M5	Chèzy = 60 m <sup>1/2</sup> /s: spatial constant
M6	Different $z_0$ in White-Colbrook: open coast $z_0=0.0002$ , tidal basin $z_0 = 0.006$ (WMO, 2008)

### 3.2.3 Role of morphological feedbacks on the effectiveness of Nature-based solutions (Deltares)

#### 3.2.3.1 Model premise

The Ems Estuary is a strongly engineered system, of which the high turbidity leads to large maintenance dredging volumes and negatively influences primary production (van Maren et al., 2015). One of the drivers for high turbidity values is the loss of natural sediment sinks (van Maren et al., 2016). Reclamation of the various natural tidal inlets and salt marshes along the Wadden Sea Coast has resulted in a loss of environments for natural sedimentation. As a consequence, the Ems-Dollard estuary experiences gradually increasing suspended sediment concentrations. This has motivated the development of measures to (1) promote settling of sediment (through constructions or vegetation; reducing local hydrodynamic energy), and (2) extract sediments (either through dredging and landward transport, or by inundating land). Both are expected to reduce the turbidity in the Ems Estuary. Settling of sediment may also have additional benefits, such as wave dissipation and trapping of carbon.

Predicting the effect of nature-based solutions in the Ems estuary on reducing flooding, reducing turbidity, and promoting carbon storage therefore revolves around the prediction of sediment dynamics on short timescales and on long timescales. On short timescales the trapping effects of vegetation and/or interventions are relevant, requiring modeling of waves and currents. Long-term modeling requires coastal adaptation to Sea Level Rise (SLR) under the influence of both waves and currents. Most previous studies investigating the adaption of tidal basins to SLR were limited to tidal forcing only (i.e. Elmilady et al., 2020). Ignoring waves has two clear benefits: it saves computational time (which is important for long-term simulations) and it simplifies numerical modeling because introducing waves requires parameterisations for development of strength of the intertidal flats (using consolidation models as in Winterwerp et al., 2018 or inundation frequency as Nguyen et al., 2022). These flats typically develop during tide-dominated conditions when fine, easily erodible particles are transported landward. After deposition these sediment beds develop



strength through consolidation, which prevents excessive erosion during periods of higher wave conditions (Colosimo et al., 2023).

The prediction of morphological change in the Ems estuary is crucial for understanding how ecosystems evolve in the estuary. The presence of ecosystems may be estimated from physical boundaries (inundation frequency, salinity, hydrodynamic energy, and substrate) and shown in ecotope maps (Baptist et al., 2019). While such ecotope maps exist for the Wadden Sea in its current state, there is limited knowledge on how ecotopes will evolve over time (especially in relation to Sea Level Rise), and even less so if NBS considered in the Ems Estuary can significantly contribute to preserving or effectively restoring such ecosystems.

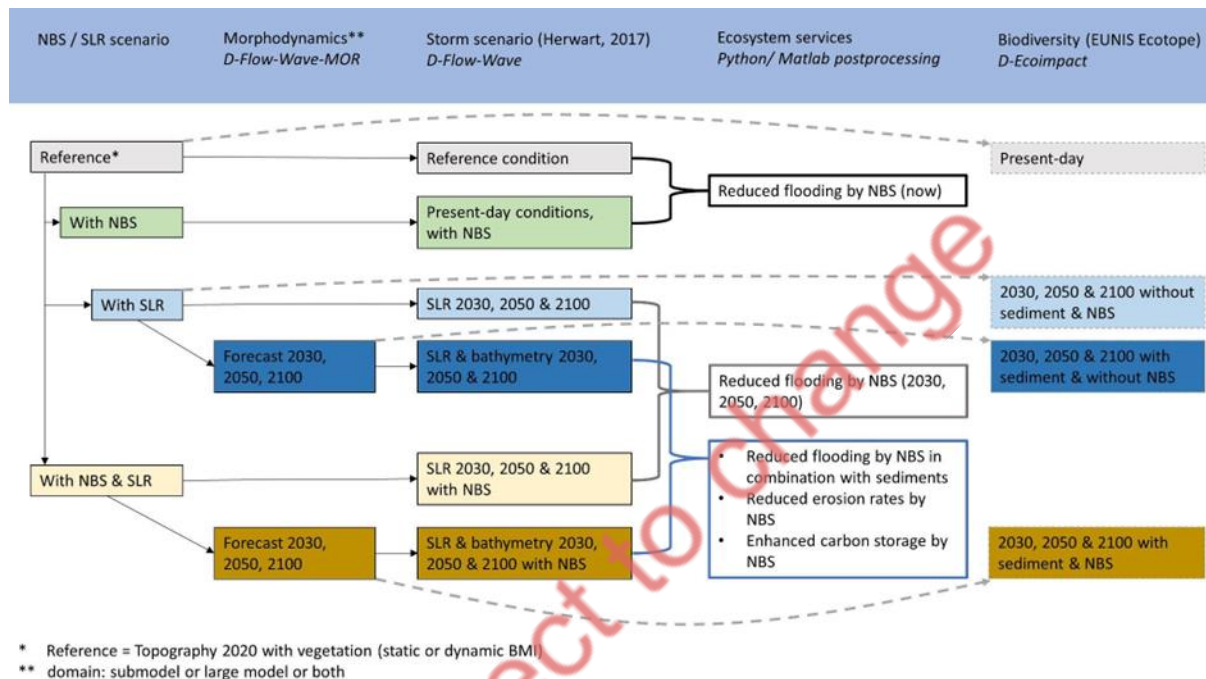


Figure 3.4. Flowchart of model scenarios

We develop a model framework (Figure 3.4) in which we compute the impact of various nature-based solutions on four ecosystem services (reduced flooding, reduced erosion, and increased food provisioning and carbon storage) through quantification of ecotopes. We develop a morphodynamic model accounting for sediment accretion with SLR under the influence of tides, waves, vegetation and nature-based solutions. This model will predict bed levels in the year 2030, 2050, and 2100. These morphodynamic simulations are post-processed 1) into ecotopes and scored on ecosystem services provided. Additionally, the predicted bed levels are used as input for models in which storm scenarios are evaluated for different SLR and nature-based solutions. The reduction in flood risk is herein defined as a reduction in wave height per dike segment.

### 3.2.3.2 Model set-up

#### Grid and bathymetry

The morphodynamic model consists of two models, a larger model covering the Wadden Sea and part of the North Sea as in Schrijvershof (2023) (

A) and a smaller model nested within it covering the Ems-Dollard (

B). The purpose of the large model is to characterize the alongshore sediment fluxes and to provide boundary conditions for the smaller model domain. The smaller domain is computationally more efficient allowing predictions up to the year 2100. The bathymetry used is a composite of vaklodingen (a dataset of bathymetries of the Dutch coast) by the Dutch authority Rijkswaterstaat between the years 2017 and 2020, with preference given to the latest dataset during compositing. Offshore bathymetry in the North Sea was obtained from EMODnet while bed levels of the Ems River are derived from the Digitales Geländemodell (DGM).

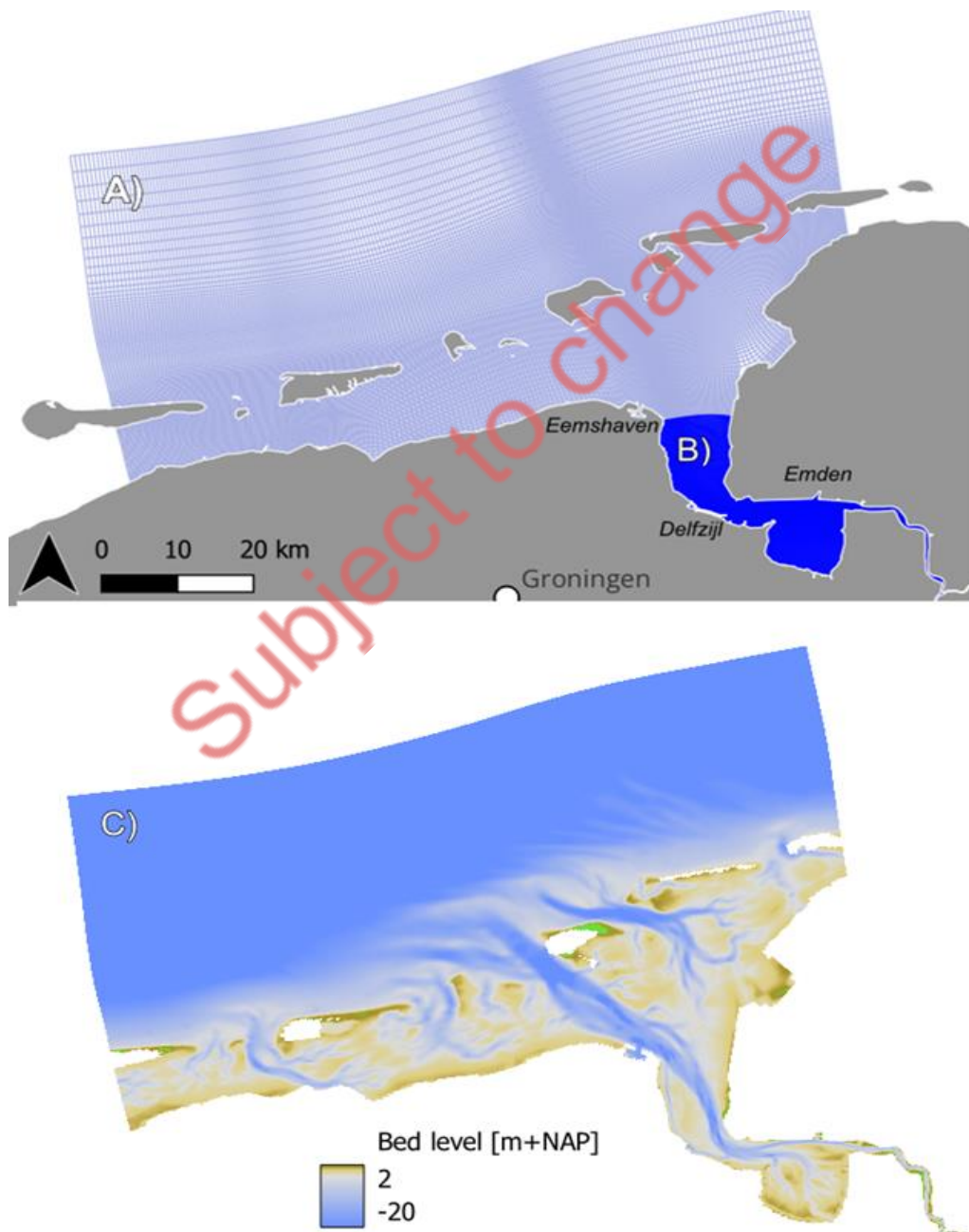


**Figure 3.5** A) the outer modelling domain covering the Ems Estuary and Wadden Sea, B) the inner modeling domain covering the Ems-Dollart. C) the bathymetry composited from vaklodgingen by Rijkswaterstaat (2017-2020), DGM (2015) for the Ems river, and EMODnet bathymetry for offshore bathymetry ([http://data.europa.eu/88u/dataset/EMODnet\\_bathymetry](http://data.europa.eu/88u/dataset/EMODnet_bathymetry) )

## Hydrodynamic forcing

Hydrodynamic boundaries (waterlevels and velocities) at the North Sea are obtained from the Dutch Continental Shelf model (Zijl, Groenenboom, Laan & Zijlker, 2022) and reduced into a cyclic synthetic spring-neap tide (Schrijvershof, 2023). In this approach, the harmonic components of the tide are reduced into signals that repeat every spring-neap cycle. The approach ensures a tidal boundary forcing that is appropriate for morphodynamic up-scaling, while conserving the amplitude and phase variance in the original signal. With reduced inter-annual variability in the forcing, the morphodynamics are accelerated by a factor 24, such that each hour in the simulation effectively equates to one day of morphodynamic development. The applied river discharge is taken from the winter of 2018-2019 (time period of the EDOM campaign) and repeated for subsequent years.

Meteorological forcings are obtained from the HIRLAM Weather model (<https://registry.opendata.aws/hirlam>). Waves at the offshore boundaries are based on observed wave heights, periods, and directions near the island of Schiermonikoog (<https://rijkswaterstaatdata.nl/waterdata/> ). The wave time-series are implemented directly in the storm scenarios. The long-term morphological simulations require a reduced forcing. The Method by Scheel (2017) is applied to derive 12 representative wave and meteo classes from the 30 years of wave data (Figure 3.6). The wave-meteo classes are ordered in a random sequence to synchronize the wave forcing with the consecutive repetitive tidal spring-neap cycles (Figure 3.7).

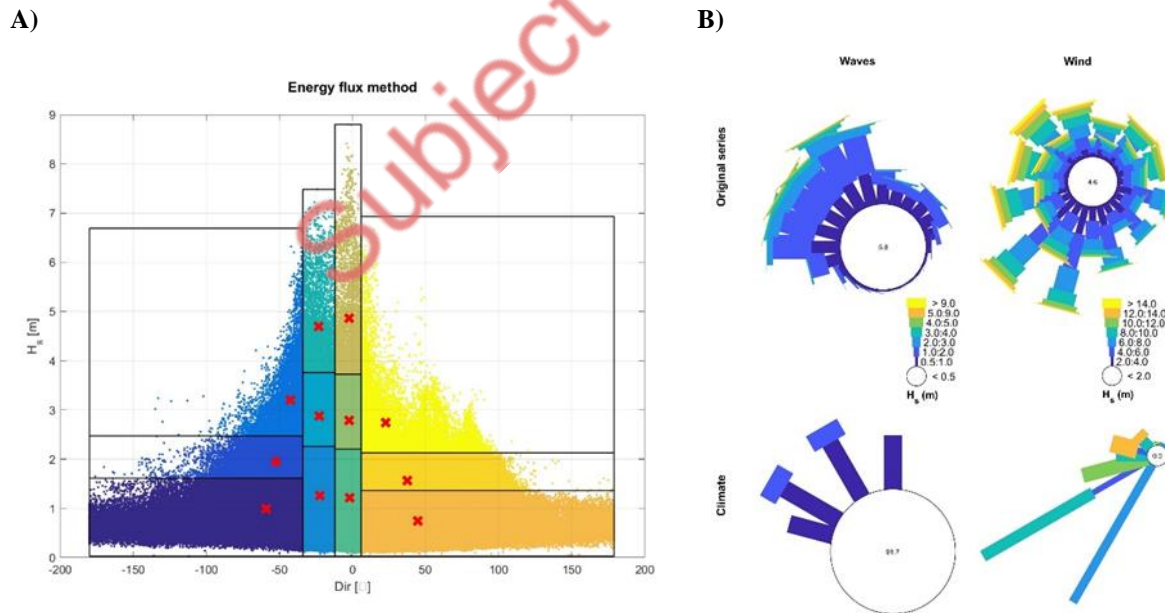


**Figure 3.6.** Reduction of the wave- and wind climate into representative 12 representative classes. A) wave climate (significant wave height  $H_s$  versus mean direction) classes represented against data points at Schiermonnikoog, B) Wind and wave rose from the station at Schiermonnikoog versus the schematized climate

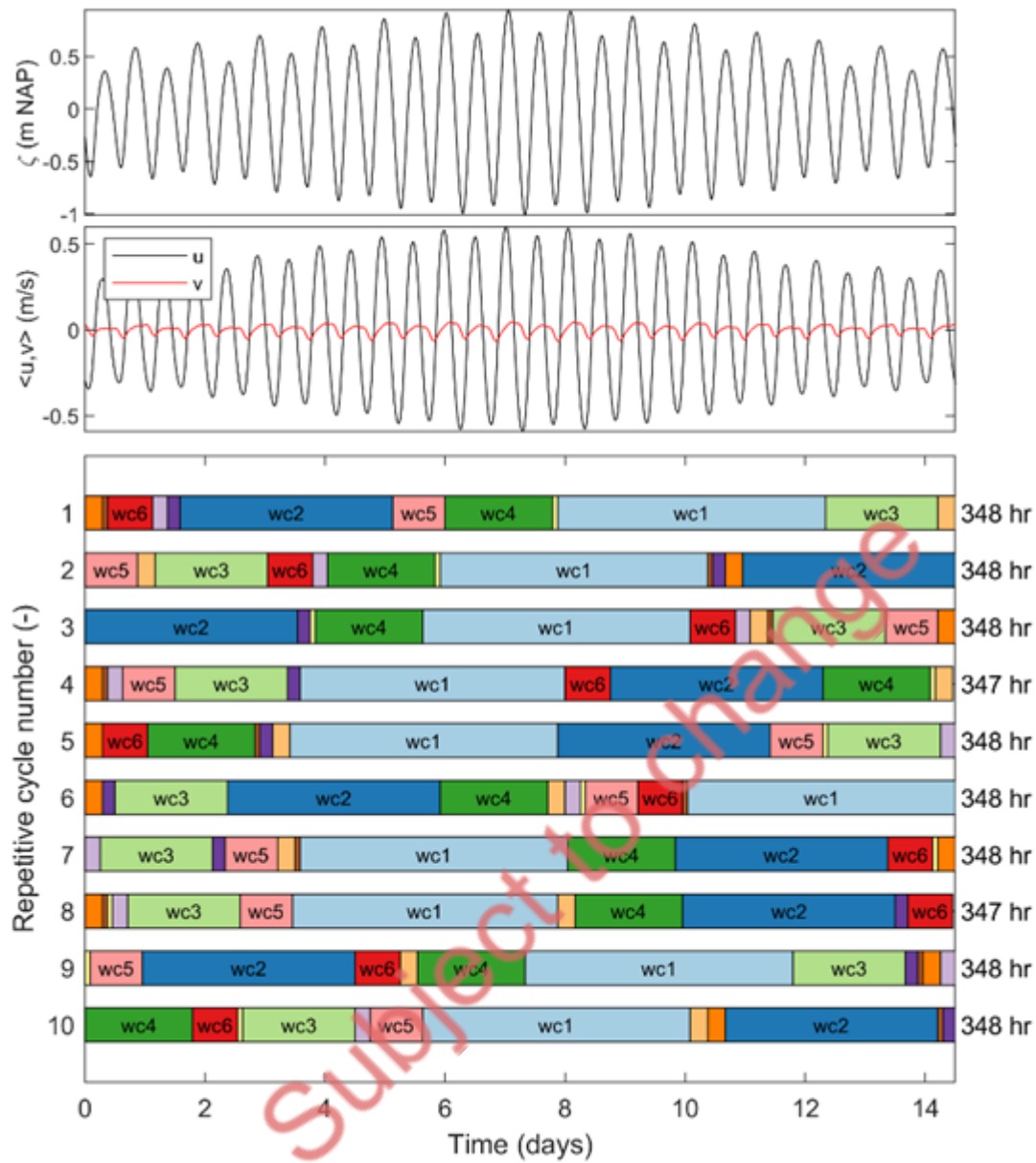


Figure 3.7. Example of a single synthetic representative spring-neap cycle for waterlevels (top), flow velocities in the  $u$  and  $v$  direction (middle), and sequencing of the wave and meteo climate conditions



### 3.2.3.3 Model calibration and validation

#### Tidal propagation

Tidal asymmetry driven sediment transport is the main import mechanism for sediment into the Dollard. The model by Schrijvershof (2023) was further calibrated to improve and validate tidal propagation in the Ems estuary. A varying manning roughness ranging from 0.019 s m<sup>-1/3</sup> in the Wadden sea, to 0.017 s m<sup>-1/3</sup> in the Dollard, and 0.015 s m<sup>-1/3</sup> decreasing to 0.010 s m<sup>-1/3</sup> in the Ems was found to best reproduce the tidal signal in the overall modelling domain (Figure 3.8) and the tidal water level fluctuations and velocity patterns in the Emden Fahrwasser in particular (Figure 3.9).

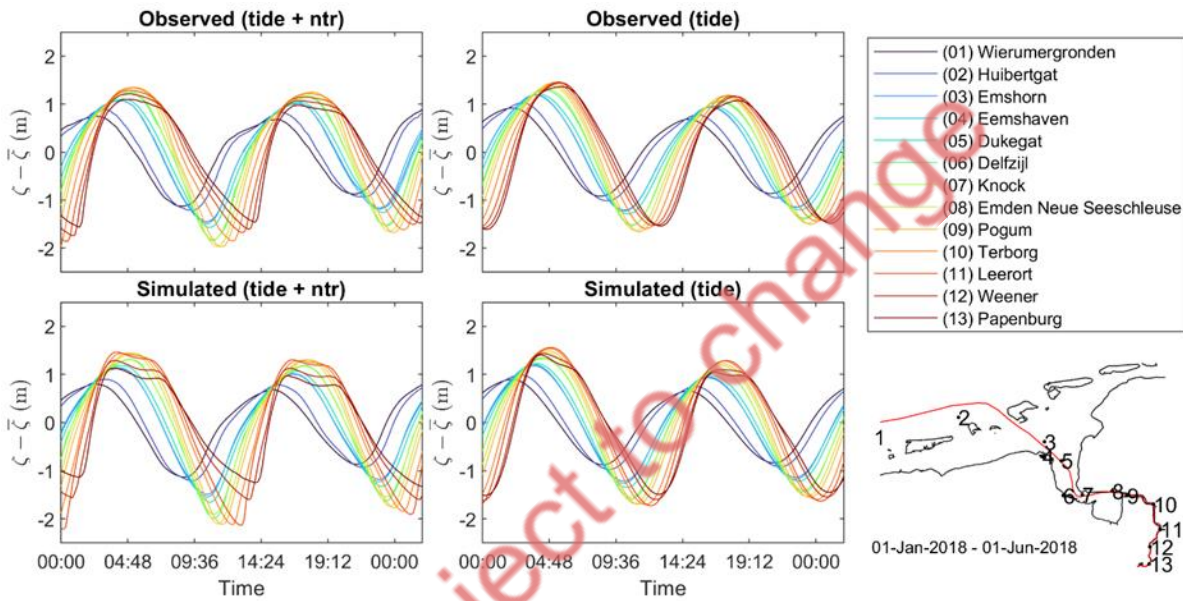


Figure 3.8. Tidal curves of observations (top) and the roughness-calibrated model

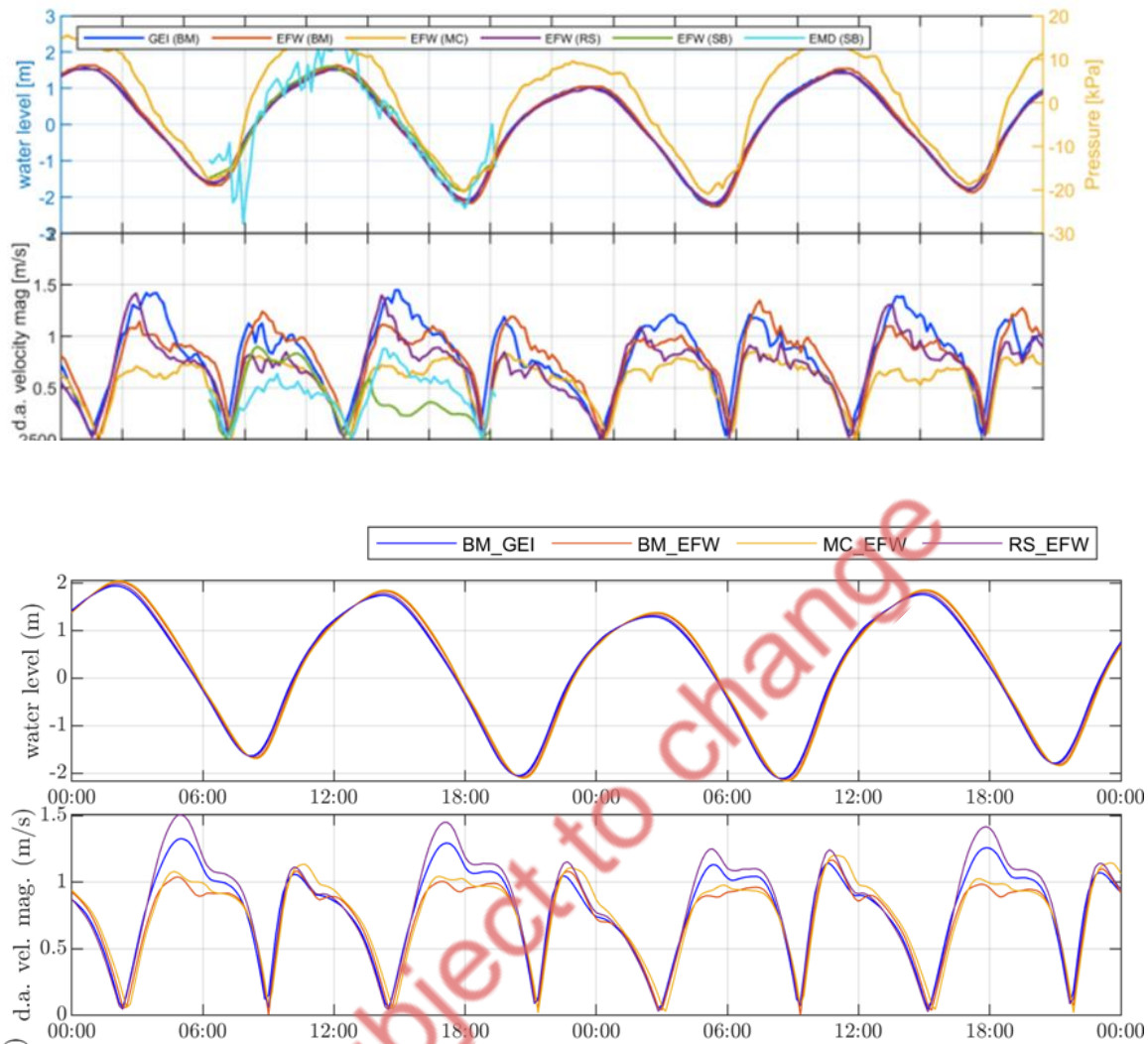


Figure 3.9. Water levels and depth averaged velocities observed (top two panels) and simulated (bottom two panels) in the Emden Fahrwasser in the winter of 2018-2019 during the EDOM campaign

## Wave propagation

The wave model was calibrated by forcing the model with wave information from the three observation stations Borkum, Schiermonnikoog Noord, and F3 platform (see section 3.2.3.2). Based on a comparison of wave simulation results using these three boundary forcings and in-situ wave observations at various stations in the Ems estuary mouth, Schiermonnikoog Noord produced the best fit for simulating wave heights within the estuary (Table 3.4).

Storms Xavier (December 2013) and Herwart (October 2018) are used as scenarios for evaluating flood risk reduction in the Wadden Sea pilot. These specific storms were validated using the boundary conditions derived at Schiermonnikoog Noord. In Figure 3.12 the observed and modelled waves are plotted for station Randzelgat Noord at seaward end of the estuary and station oude Westereems zuid as the most landward station available. The model can reasonably reproduce the wave heights during the storm events but does suffer in predicting the duration of the high waves during the event, possibly due to the lower time resolution (1 hour) for updating waves in the hydrodynamic simulation.

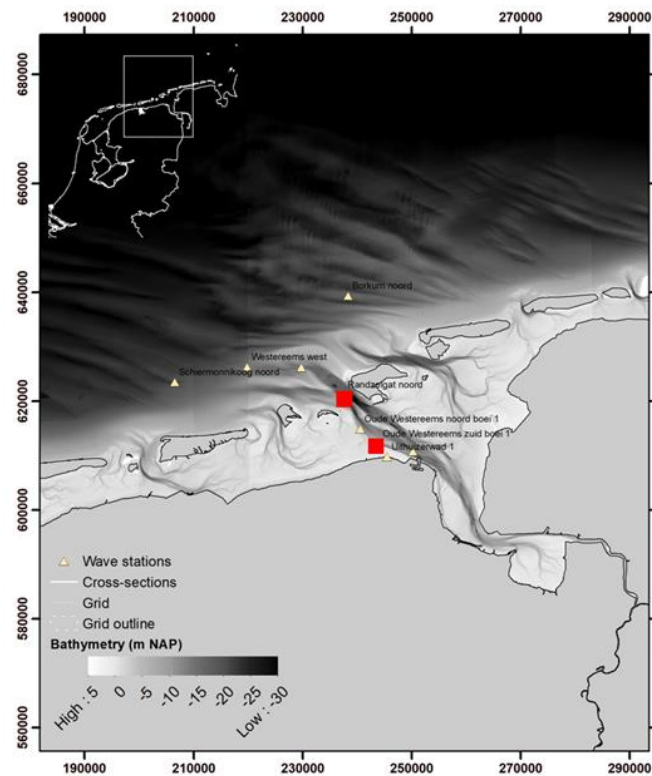


Table 3.4 Error statistics for one-year from Schiermonnikoog BC

Wave parameter	Statistic	
Hm0	Bias (m)	0.02
	RMSE (m)	0.23
Tm02	Bias (s)	-0.72
	RMSE (s)	1.08
Th0	Bias (°)	5.17
	RMSE (°)	42.28

Figure 3.10. Locations of wave stations. The red squares represent the stations Randzelgat noord (top) and Oude Westereems zuid boei 1 in Figure 3.11 and Figure 3.12

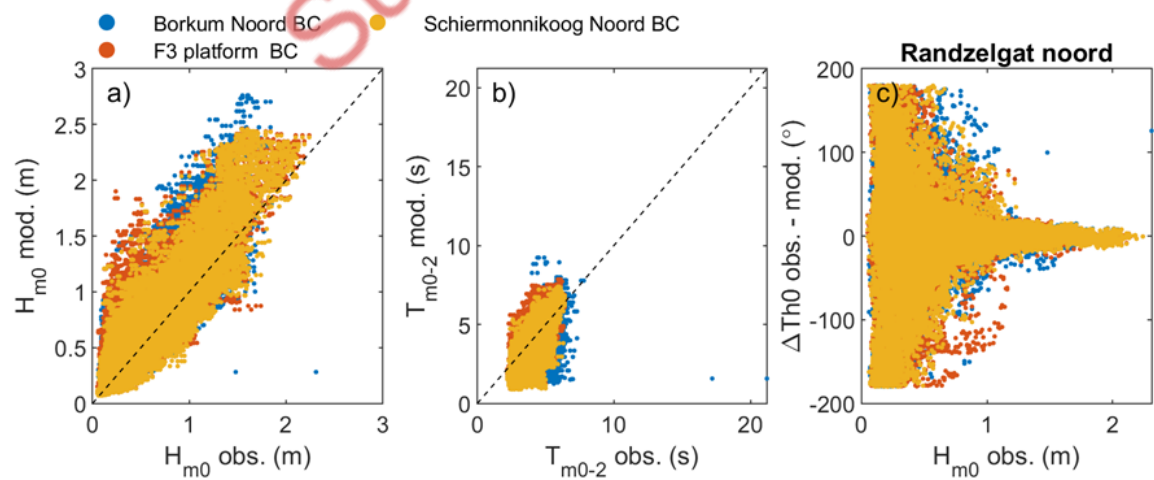
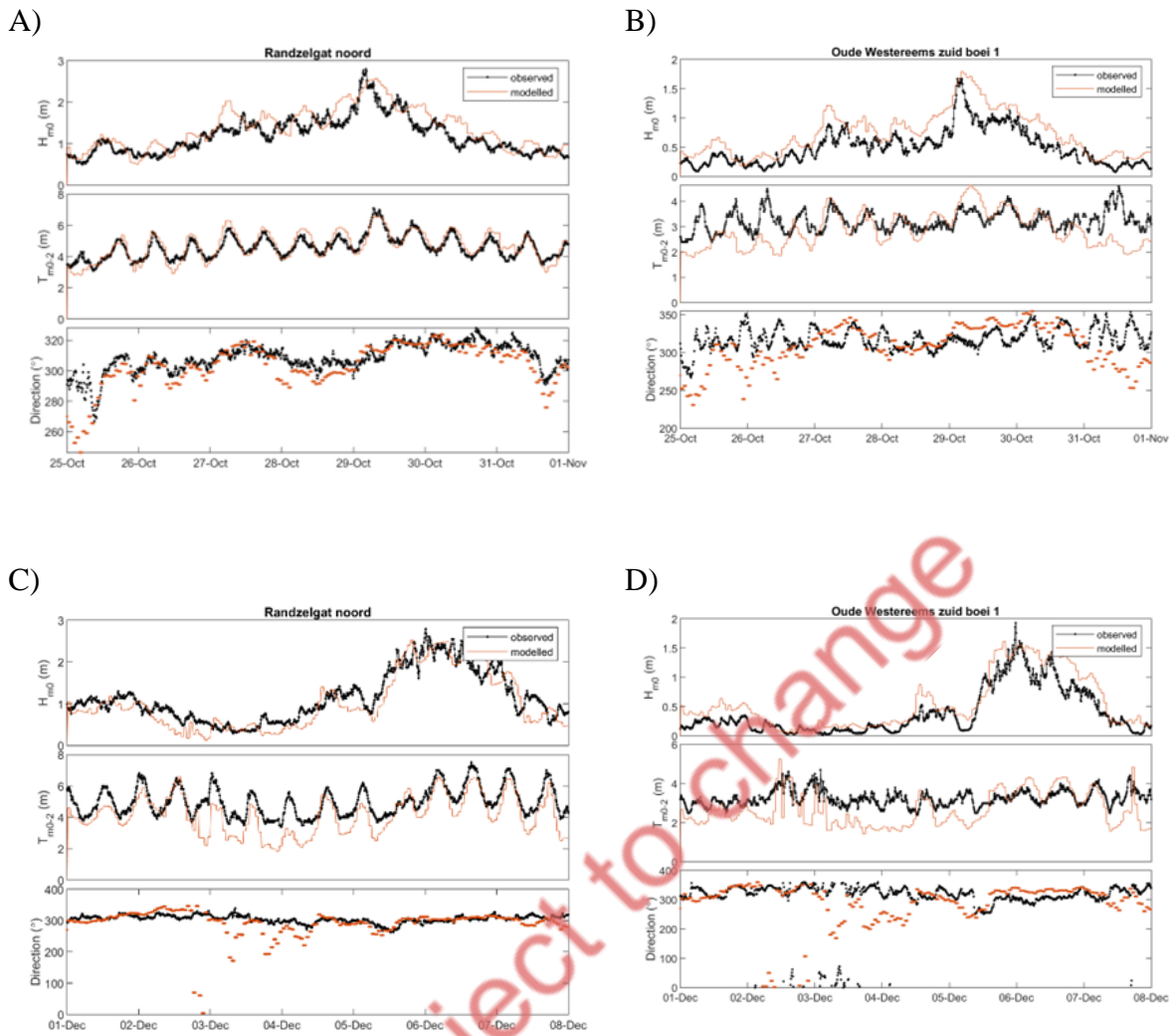


Figure 3.11. Scatter plot of wave heights at wave stations using wave boundaries calibrated on Borkum Noord (blue), Schiermonnikoog Noord (yellow), and F3 platform (orange)



**Figure 3.12.** Comparison of modelled and observed wave heights during storm Herwart (2018), panels A and B, and Xaver (2013), panels C and D

## Morphodynamics

The model is calibrated by comparing sedimentation and erosion patterns that develop within one year of hydrodynamic simulation (=24 years of morphological change) and the mud fraction in the top layer. While initial results look promising, further validation of sedimentation rates and comparison with known sediment sinks (e.g. by comparing dredging volumes) is required.

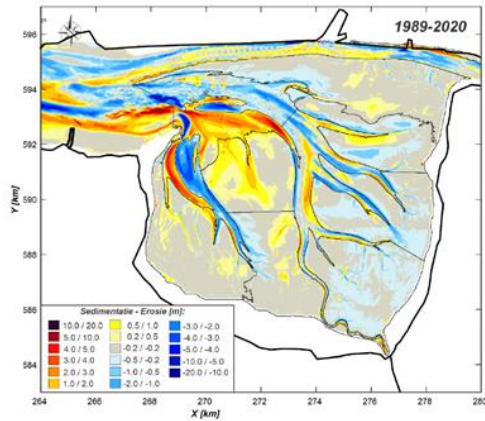


**Figure 3.13.** Observed sedimentation- erosion patterns in the Dollard (Elias, 2021)

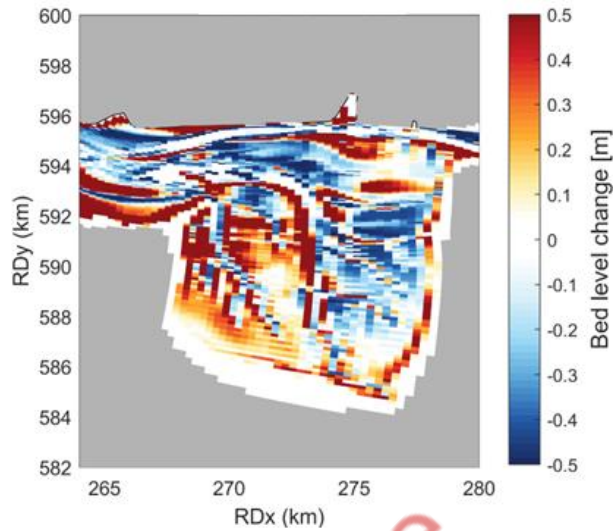


**Figure 3.14.** Modelled sedimentation and erosion patterns after 24 years of morphological simulation initializing the model with a thin (15 cm) initial layer of mud

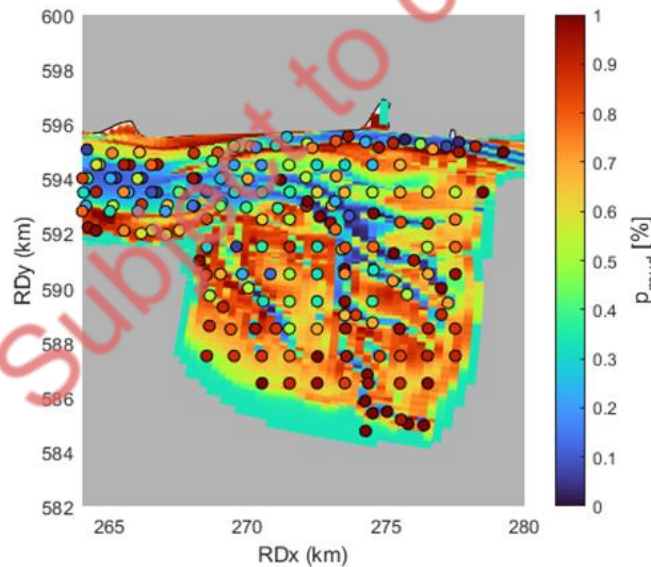


**Figure 3.15.** Modeled mud fraction in the top soil after initial calibration compared to the sediment atlas of the Wadden Sea as dots [https://svn.oss.deltares.nl/repos/openearthrawdata/trunk/rijkswaterstaat/sedimentatlas\\_waddenzee/](https://svn.oss.deltares.nl/repos/openearthrawdata/trunk/rijkswaterstaat/sedimentatlas_waddenzee/)

### 3.2.3.4 Ecotope quantification

#### Conversion of model results into ecotopes and ESS

The main goal of the morphological model is to quantify the effect of nature-based solutions on ecosystem services. Some of these ecosystem services are quantified with the change in ecotopes over time, both due to sea-level rise and in response to measures implemented in the area. The conversion of modelling output



into ecotopes is based on the ZES.1 classes for classifying ecotopes (Bouma, 2005). In cooperation with task 4.1 of REST-COAST these classes are adapted into EUNIS ecotopes based on the Delft3D-FM model output (Table 3.5,

Table 3.6).

**Table 3.5.** Adapted ecotope class boundaries from the ZES.1 system into variables for classification in EUNIS using Delft3D-FM output. Abbreviations in table: MLWS = Mean Low Water Spring, MHWN= Mean High Water Neap, = silt fraction, = average bed shear stress, TMAP coastal vegetation S.X = coastal vegetation classes, see Bouma (2005)

Variables	Classes	Class boundaries	Adapted for Delft3d-FM output and EUNIS classification	Code
		ZES.1		
Mean salinity	Fresh	yearly mean < 0.5 ppt	yearly mean < 0.5 ppt	0
	Brackish	0.5 ppt ≤ yearly mean < 18 ppt	0.5 ppt ≤ yearly mean < 18 ppt	1
	Marine	yearly mean ≥ 18 ppt	yearly mean ≥ 18 ppt	2
Salinity variability	Stable	st. dev./mean ≤ 0.25	st. dev./mean ≤ 0.25	0
	Variable	st. dev./mean > 0.25	st. dev./mean > 0.25	1
Substratum	Sediment	soft sediment	Determined in post-processing	0
	Hard	dikes, dams, quays, etc.		1
Littoral zone	Deep sublittoral (Circalittoral zone)	depth < -5 m MLWS	depth < -5 m MLWS	0
	Shallow sublittoral (Infralittoral zone)	-5 m MLWS ≤ depth < 4% mean exp.	-5 m MLWS ≤ depth < 4% mean exp.	1
	Low littoral	4% ≤ mean exposure < 25%	4% ≤ mean exposure < 25%	2

## D2.2 Good practice criteria Multi-variable risk projections

	Middle littoral	$25\% \leq \text{mean exposure} < 40\%$	$25\% \leq \text{mean exposure} < 40\%$	3
	High littoral	$40\% \leq \text{mean exposure} < 85\%$	$40\% \leq \text{mean exposure} < 85\%$	4
	Supralittoral	$\text{mean exposure} \geq 85\%$	$\text{mean exposure} \geq 85\%$	5
Hydrodynamics	Low dynamic	max. current velocity < 0.8 m/s	max. current velocity < 0.8 m/s	0
	High dynamic	max. current velocity $\geq 0.8$ m/s	max. current velocity $\geq 0.8$ m/s	1
Sediment	Silt	Silt content $\geq 25\%$		1
	Fine sand	$D_{50} < 250 \mu\text{m}$	and	2
	Coarse sand	$250 \mu\text{m} < D_{50} < 2000 \mu\text{m}$	and	3
Salt marsh	No vegetation	TMAP coastal vegetation S.0	Depth > MHWN	0
	Potential pioneer zone	TMAP coastal vegetation S.1	Depth < MHWN; inundation frequency > 300 times $\text{yr}^{-1}$	1
	Low marsh	salt TMAP coastal vegetation S.2	$300 \text{ times } \text{yr}^{-1} \leq \text{inundation frequency} < 150 \text{ yr}^{-1*}$	2
	upper-mid marsh	TMAP coastal vegetation S.5	$150 \text{ times } \text{yr}^{-1} \leq \text{inundation frequency} < 50 \text{ yr}^{-1*}$	3
	High marsh	salt TMAP coastal vegetation S.3	$50 \text{ times } \text{yr}^{-1} \leq \text{inundation frequency} < 5 \text{ yr}^{-1}$	4

*Table 3.6. Conversion of class boundary codes into EUNIS ecotopes*

Litoral zone code	Sediment code	Salinity code	Salt marsh code	EUNIS2019C	EUNIS2019D
-------------------	---------------	---------------	-----------------	------------	------------

## D2.2 Good practice criteria Multi-variable risk projections

0				MC521	Faunal communities of Atlantic circalittoral sand
1		2		MB523	Faunal communities of full salinity Atlantic infralittoral sand
1		1 or 0		MB524	Faunal communities on variable salinity Atlantic infralittoral sand
2, 3, 4 or 5	0 or 2			MA52	Atlantic littoral sand
2, 3, 4 or 5	1	2		MA621	Faunal communities of full salinity Atlantic littoral mud
2, 3, 4 or 5	1	1 or 0		MA622	Faunal communities of variable salinity Atlantic littoral mud
2, 3, 4 or 5	3	2		MA321	Faunal communities on full salinity Atlantic littoral coarse sediment
2, 3, 4 or 5	3	1 or 0		MA322	Faunal communities on variable salinity Atlantic littoral coarse sediment
2, 3	1, 2		1	MA225	Atlantic pioneer saltmarshes
3, 4	1, 2		2	MA224	Atlantic mid-low saltmarshes
4, 5	1, 2		3	MA223	Atlantic upper-mid saltmarshes and saline and brackish reed, rush and sedge beds
6	1, 2		4	MA222	Atlantic upper saltmarshes

The distribution of ecotopes is calculated for each modelled sea-level rise scenario and implementation of an NBS measure. The ecotopes are derived from the bed level and bed composition at the specified morphological year and a hydrodynamic simulation of two spring-neap cycles to derive the classes as expressed in Table 3.5 using the software D-EcoImpact (<https://github.com/Deltares/D-EcoImpact>). From

the ecotope map, the location of salt-marsh is determined. Two storm events (Herwart from 2018 and Xaver from 2013) are simulated to test how the new distribution of (salt marsh) ecotopes affects the distribution of wave heights on coastal defenses in the estuary.

The effect of salt marsh ecotopes on wave dampening is implemented in the DWaves module in Delft3D-FM through the formula of Suzuki et al. (2019). In it, vegetation properties such as plant height, stem density, and stem diameter are used to calculate an additional energy loss term for waves in vegetated areas. Vegetation parameters for each marsh ecotope are based on a representative plant species with parameters from Vuik (2017) as measured at the end of the growing season when storms are most likely to occur. The vegetation parameters used are presented in Table 3.7.

*Table 3.7 Vegetation parameters used per ecotope*

EUNIS Code	Representative species	Vegetation height (cm)	Stem diameter (mm)	Stem density (n. of stems /m2)
MA225	Spartina anglica	47	3.3	232
MA224	Suaeda maritima	57	2.7	274
MA223 & MA222	Elymus athericus & repens	50	1.3	405

### Validation of ecotope classification

The map produced from the Delft3D-FM model for the year 2020 (Fig. 3.19) was compared with the most recent EUNIS ecotope map of the Wadden Sea produced by Martin Baptist in WP4.1 of RESTCOAST (Fig. 3.18). This map was in turn based on an earlier study by Baptist (2019).

The Delft3D-FM model is able to reproduce the current extent of ecotopes remarkably well despite a relatively coarse resolution (about 100 m) and only depth-averaged velocities. Crucially, the salt marsh, the main ecosystem of interest for its flood risk, is well represented. As expected, there is a perfect correspondence between the location of circalittoral and infralittoral zones since no morphological changes have been simulated yet. Nevertheless, the inundation frequency and exposure boundaries (Table 3.5) are well captured in the modeling.

There are also key differences between the two maps. The most notable is that ecotopes MA525 (bivalve-dominated littoral muddy sand) and MA523 (barren or amphipod-dominated littoral mobile sand) are not

classified from the model. With only one sand fraction in the model available for transport, inherent uncertainties in the mud content of the sandy soil, and no further information aside from the boundaries in Table 3.11 to estimate the presence of bivalves or amphipods, it was considered classification beyond littoral sand (MA52) and saline / brackish littoral mud (MA621, MA622) would not be sufficiently reliable. This is seen in Figure 3. where littoral mud and littoral sand replace MA525 from Figure 3.16. The mobile sand (MA523) is replaced by coarse sediment (MA321) because it was assumed no fine sand could accumulate in areas with high bottom stresses. It should be considered to replace MA321 with MA523 in the future as the considered ecotope boundary of bed shear stress does not distinguish areas of mobile (fine) sand and stable coarse sand taking into consideration that large areas of littoral coarse sediment are rare inside the Ems estuary (Figure 3.16). Finally, the 2D simulation of salinity means that the spread of fresh water across the Geisedam from the Ems into the Dollard is not well-represented. However, this discrepancy is an acceptable trade-off to considerably speed up the model during morphological simulations.

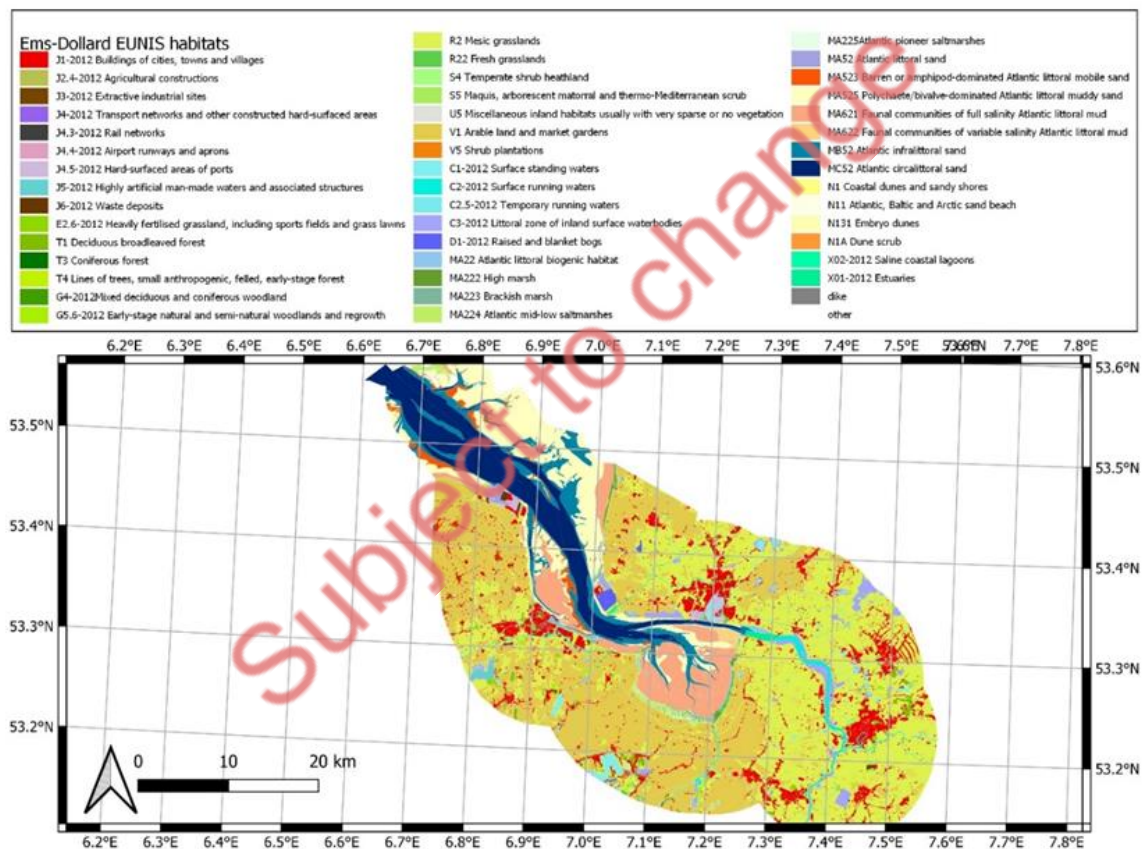


Figure 3.16. EUNIS map of the Ems estuary produced in WP4.1 of RESTCOAST, based on Baptist (2019)



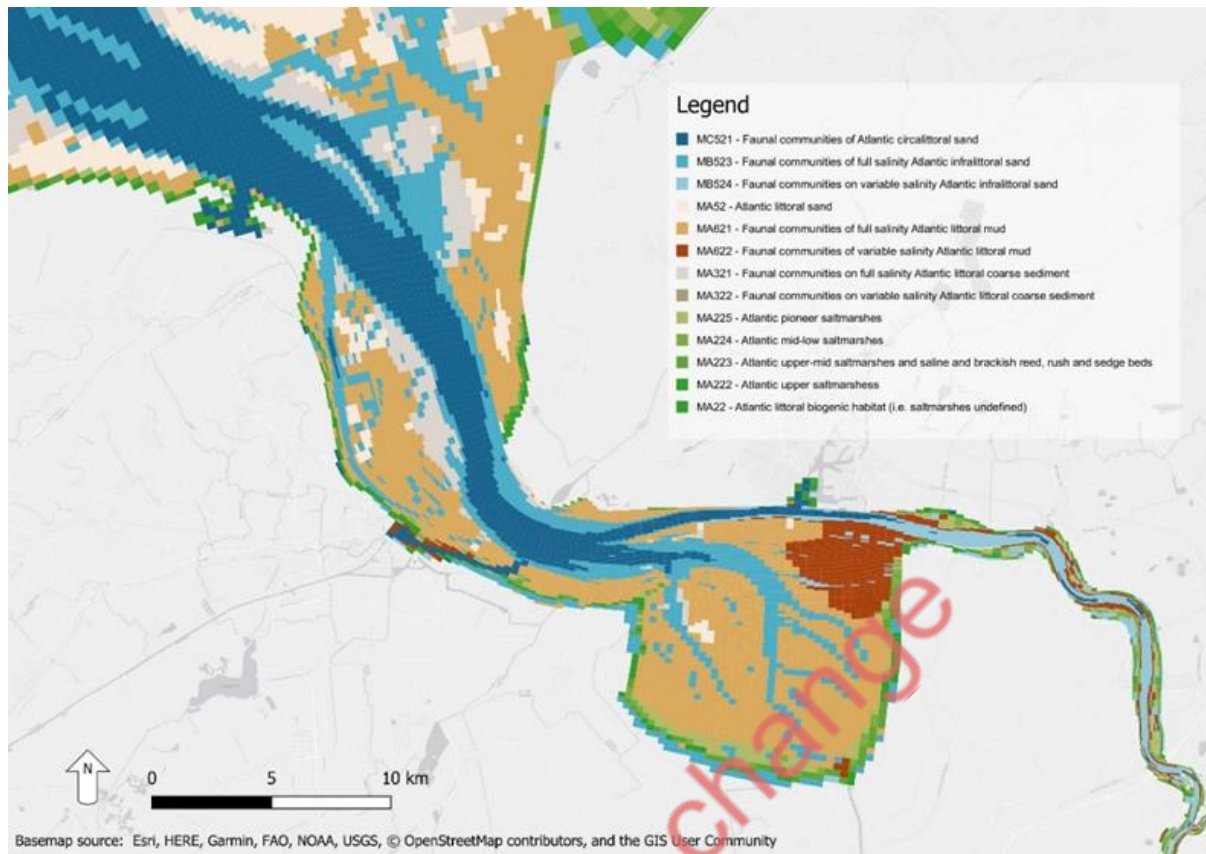


Figure 3.27. EUNIS map produced by output from the Ems-Dollard model

### 3.3 Efficiency of sea-grass in coastal protection (Hereon)

#### 3.3.1 Present day baseline

The study analysed the potential impact of seagrass on coastal hydrodynamics by running simulations of seagrass expansion scenarios for 2017 using the German Bight model. Monthly statistical analyses were performed, focusing on changes in the temporal mean and the 95th percentile for the month of October. These values indicate the hydrodynamic engineering capacities of seagrass on average and under extreme conditions.

##### 3.3.1.1 Water level

The impact of seagrass on sea surface height (SSH) is generally limited and varies only within a range of a few millimetres to centimetres under average conditions (Fig. 3.28). Seagrass tends to reduce the sea level where it is located, although this is not always the case, particularly in high-energy scenarios (VegHE) where seagrass occurs at the side of channels and there is no uniform response.

When seagrass expands in large amounts (Vegmax), it can reduce the average sea level within the meadow, but increase it in the adjacent unvegetated area. Seagrass can significantly reduce the sea level height at the 95th percentile, up to more than 15 cm or 10-15% for the maximum seagrass coverage scenario. In scenarios where seagrass expands in approximately 10% of the areas (E4:VegL E, E5:VegH E), the reductions are mostly

a few centimeters. For scenario E3, sea level is reduced in both the Wadden Sea and adjacent regions, not just in terms of quantiles.

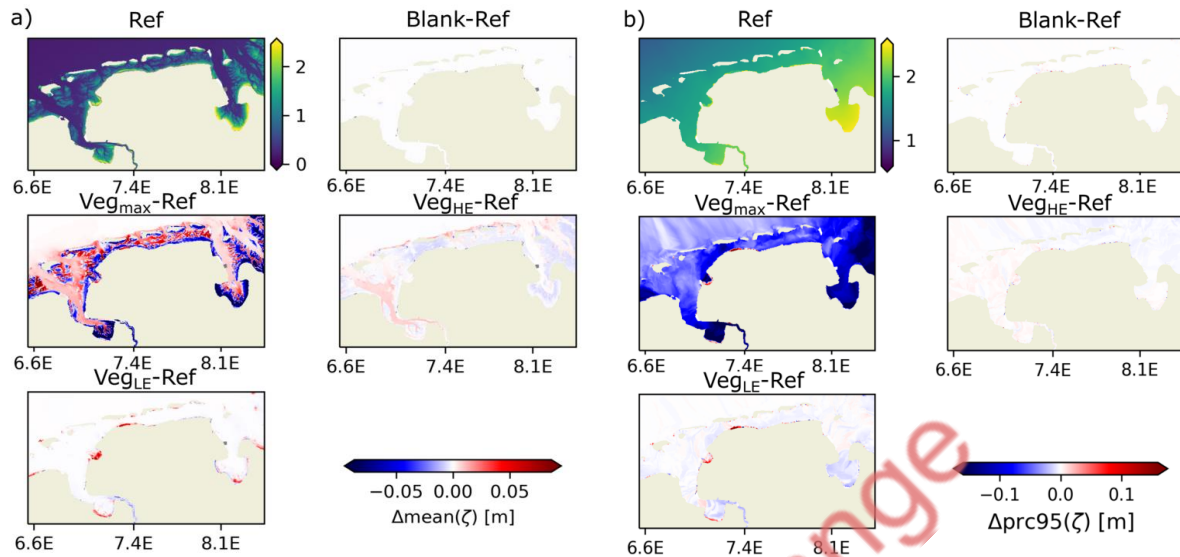


**Figure 3.17.** Comparison of temporally averaged (a) and 95% quantile (b) of sea surface height in EFWS, showing from left to right values for reference and difference of scenarios (E2–E5) minus reference

The results demonstrate that seagrass has a negligible impact on sea level until it appears in very large quantities, then it has a mild reduction tendency for sea level extremes.

### 3.3.1.2 Current Velocities

Seagrass has a significant impact on current velocity. Within seagrass meadows, current velocity can decrease by more than 10-30 cm/s, with the most significant reduction occurring in the depth interval of -1 to 1m, compared to areas without seagrass. This reduction represents a relative decrease of over 50% to nearly 80% concerning the monthly mean.

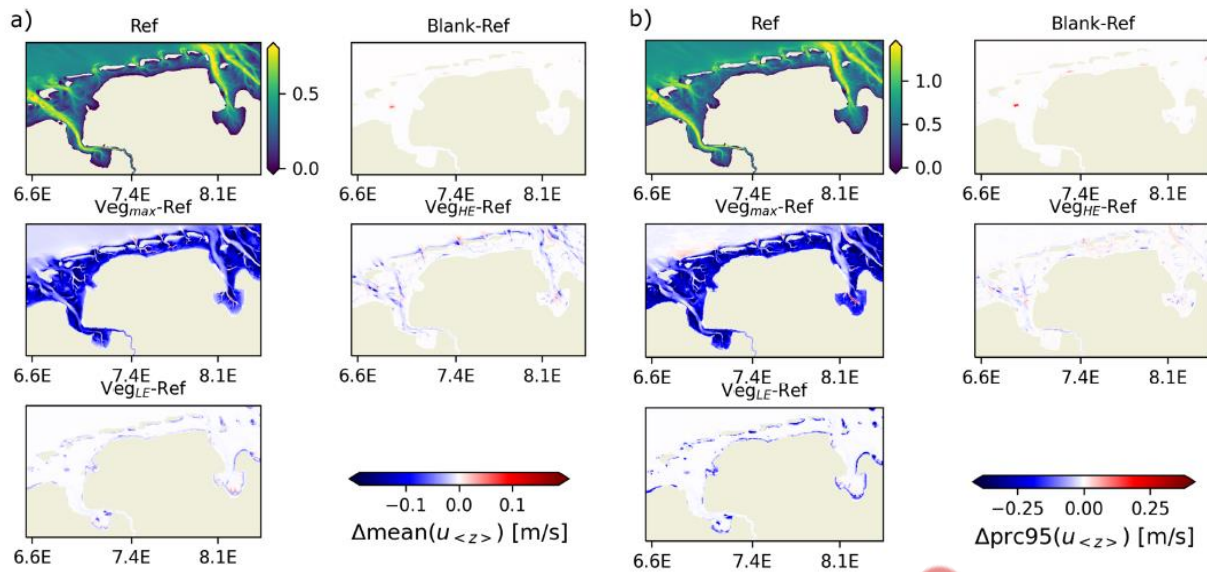


**Figure 3.18.** Comparison of temporally averaged (a) and 95% quantile (b) of depth-averaged velocity in EFWS, showing from left to right values for reference and difference of scenarios (E2–E5) minus reference

The reduction in current velocity is widespread, but it is partially offset by increased velocities in seagrass-free tidal channels. This localized increase in velocity is most prominent in the Vegmax scenario and, to a lesser extent, in the VegHE scenario where seagrass borders the channels. Examples of such channels include those near Langeoog and Spiekeroog, as well as Jade in the EFWS. In the VegLE scenario, there are localized tendencies of minor increases in velocity beyond coastal seagrass meadows where current velocity is attenuated. Extreme values exhibit a qualitatively similar reduction at slightly higher magnitudes (up to 25 cm/s), representing similar relative changes compared to the changes in monthly mean velocity magnitude (> 20% and approaching more than 80% for the shallowest zones).

### 3.3.1.3 Wave Heights

Wave heights near barrier islands typically range from 1 to 1.5 meters on average, with the 95th percentile reaching 1.5 to 2 meters. As the waves enter the back barrier Wadden Sea, their heights decrease due to the shallow bathymetry, dropping below 0.5 meters. The presence of seagrass (Blank-Ref) further reduces wave heights by a few centimeters on average and over 40 cm locally. Seagrass expansion scenarios indicate that there will be additional reductions in shallow areas and an average reduction of 40 cm, with a reduction of 60 cm for the 95th percentile in deeper areas. Seagrass generally reduces wave heights by over 20% in deeper regions and over 50% in areas shallower than 1 meter. In the shallowest vegetated regions, waves are almost completely attenuated.

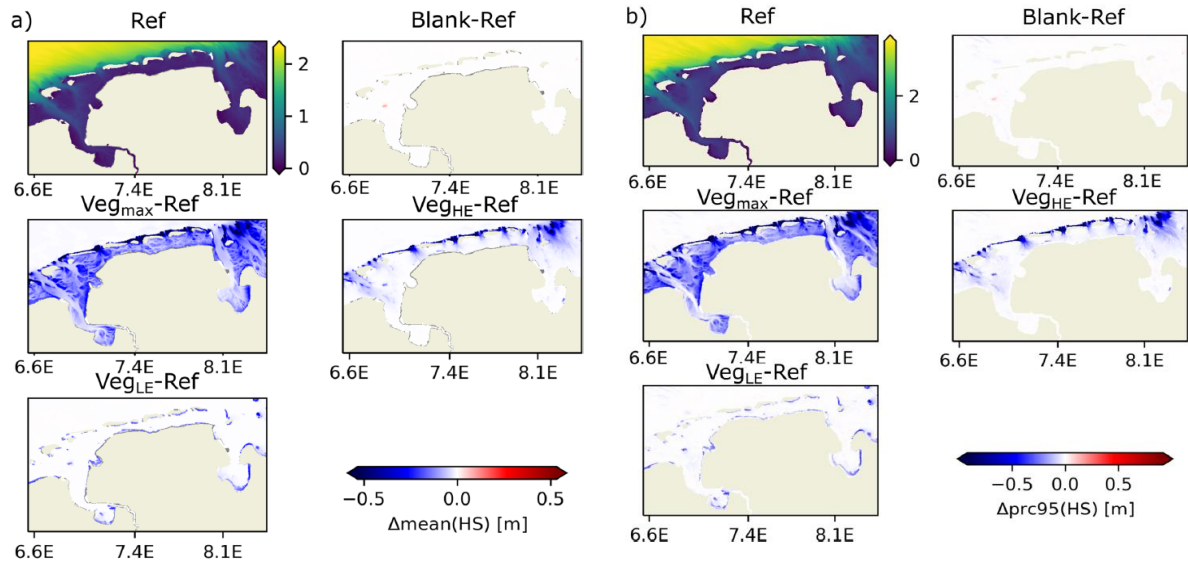


**Figure 3.19.** Comparison of temporally averaged (a) and 95% quantile (b) of significant wave height in EFWS, showing from left to right values for reference and difference of scenarios (E2–E5) minus reference

#### 3.3.1.4 Bed shear stress and sediments

In the Wadden Sea areas, a decrease in bottom stress leads to reduced sediment mobilization. This results in local reductions of over 30% in bottom concentrations compared to the Ref scenario.

During strong current conditions, sediment mobilization, represented by the 95th quantiles, decreases by over half a gram per liter. Minor increases in areas neighboring recovery zones are associated with slight boosts in current velocity and bottom stress. In the shallow intertidal zone below 0m, the sediment concentration is almost zero, demonstrating significant reductions.

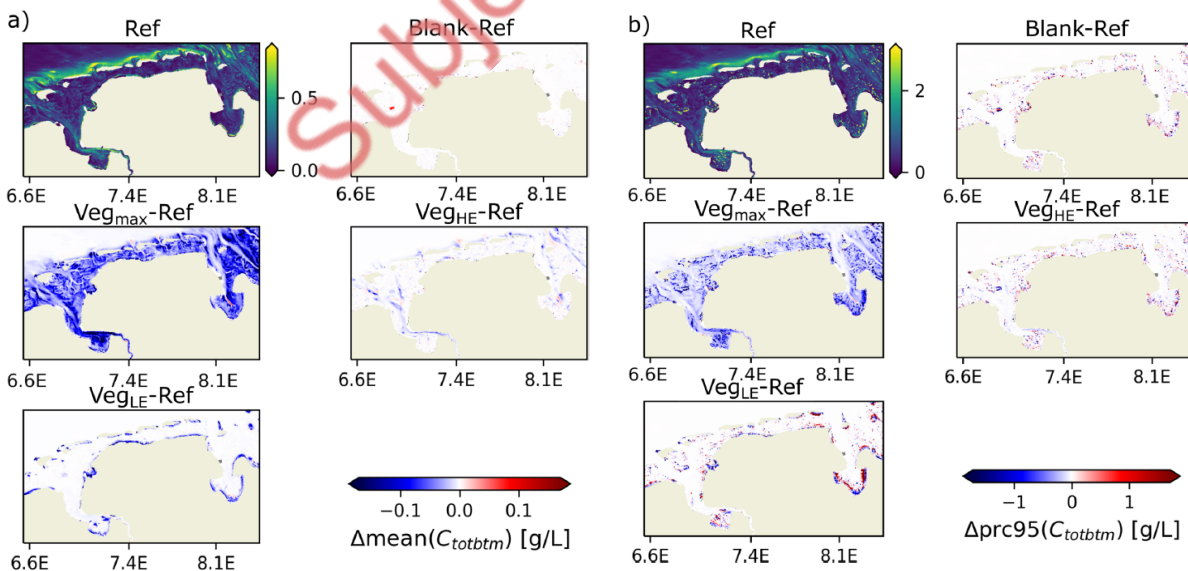


**Figure 3.20.** Comparison of temporally averaged (a) and 95% quantile (b) of total SPM concentration near bottom in EFWS, showing from left to right values for reference and difference of scenarios (E2–E5) minus reference

The monthly analysis compared different scenarios with and without seagrass, demonstrating a strong dissipative effect of seagrass on a local scale. An increased seagrass extent and patch densities resulted in decreased currents and waves, leading to a reduction in bottom stress and significantly lower sediment concentrations. This indicates lower rates of resuspension and the potential to reduce coastal erosion.

As seagrass impacts on sea level are minor, their contribution to flood protection is mostly indirect. Seagrass can reduce erosion and promote sedimentary conditions, potentially supporting the vertical height growth of the Wadden Sea to maintain bathymetric control under increased sea level in the future. This provides a long-term contribution of seagrass to coastal protection.

### 3.3.2 Seasonal variability

The analysis expands to compare the reduction potential of the maximum area seagrass scenario, Veg\_max, to gain insight into the intra-annual variability of the beneficiary effects of seagrass for coastal protection. The current seagrass configuration in the model framework is time-invariant. Attenuation capabilities for different seasons were explored by contrasting the 95th quantiles of various variables from the summer and winter months of the present-day reference simulation for the year 2017.

Although maximum sea levels in winter appeared higher, the number of strong wind events was insufficient to significantly raise the 95th percentile, leaving both summer and winter periods relatively unchanged. The statistics for wave quantiles showed slightly higher waves in the back barrier of the Wadden Sea. On average, the quantiles for velocities and bottom stress remained similar, but in winter, they tended to increase in the tidal flat area and decrease in the channels.

As shown in Fig. 3.32, the reduction capabilities at the scale of multi-monthly quantiles do not change significantly for most variables (see the strong agreement of figures in the first and second columns). Due to higher waves, the absolute reduction in HS is enhanced in winter and appears almost uniform. The velocity quantile reduction in the flat areas increases by roughly 10% in winter, with a difference in the seagrass-induced reductions of about 2-5 cm/s. Analogously, stress reductions at the bottom are enhanced in tidal flat areas, with a minor opposing trend for the channels that are free of vegetation. The greater erosive potential during the winter months is sufficiently buffered by the seagrass, leading to additional reductions of bottom layer quantiles approaching 0.25 g/l. Overall, seagrass remains an effective buffer against meteorological conditions corresponding to the winter season.



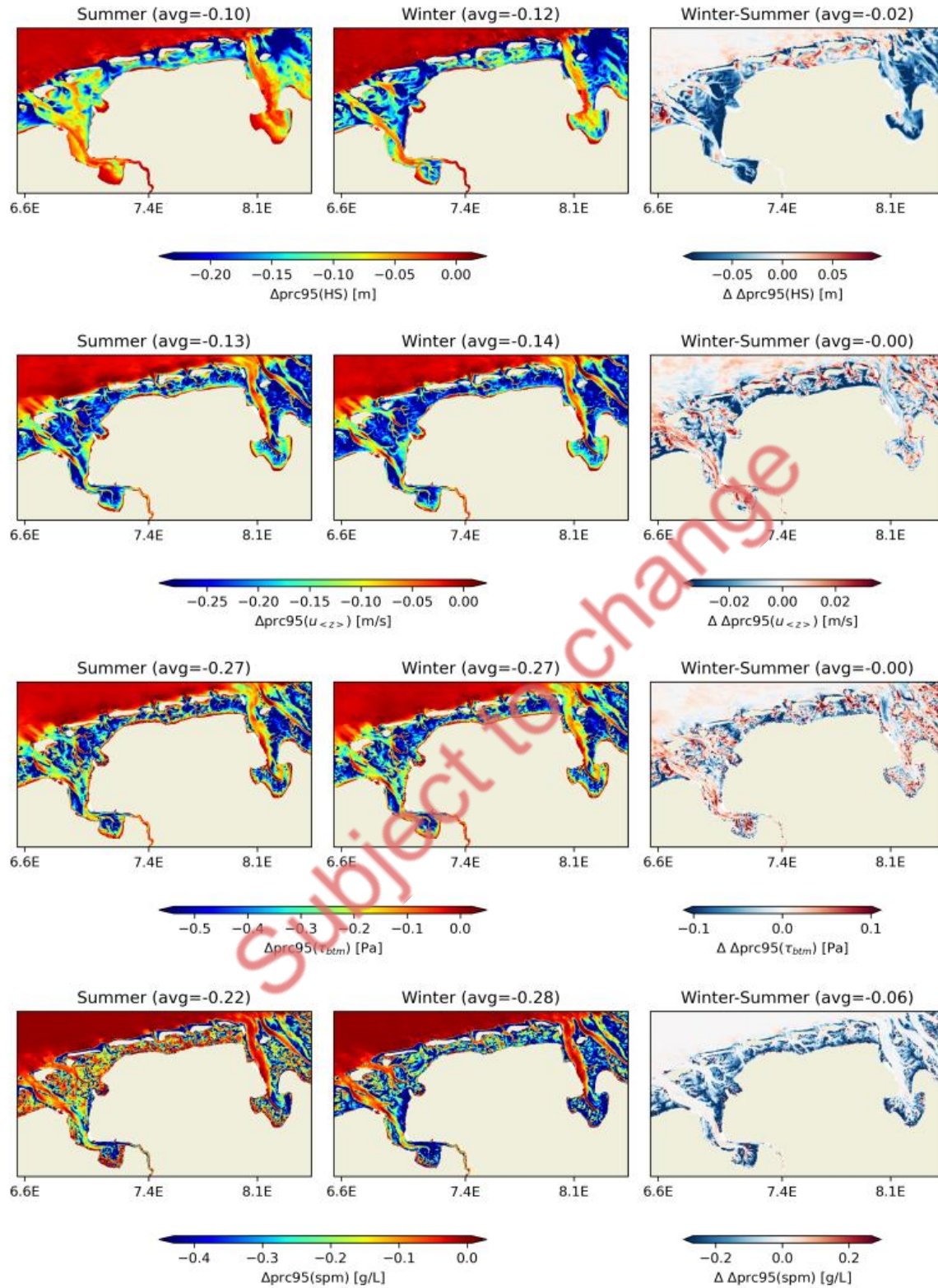


**Figure 3.21.** Reductions in 95<sup>th</sup> seasonal percentiles in Veg\_max scenario with respect to Veg\_CNTRL scenario during summer (first column) and winter season (second column, difference in third column). From top to bottom this is with respect to the variables significant Wave Heights, depth averaged velocity, bottom stress, and bottom layer total suspended sediment concentration. Number in the respective title denotes the spatial average for the depicted domain

### 3.3.3 Extreme events with different return periods

#### 3.3.3.1 Reduction of kinematics during extreme events

Under storm conditions, wave and current attenuation appeared slightly increased compared to that under calm weather conditions. However, this attenuation was reduced in relative terms. To compare the effectiveness of attenuation during severe and calm weather, we compared two tidal cycles (from October 28th until October 30th) during the storm event to the tidal cycles 10 days prior to the storm (October 18th–October 20th) using the previous statistical measures (mean and 95th percentile). Overall, the hydrodynamic values increased during the storm, causing a corresponding increase in the attenuation due to the seagrass. The reductions compared to the realistic scenario with sparse seagrass (Ref) remained relatively similar for significant wave height, bottom stress, TKE, and SPM concentrations. For the variables referenced at the bottom, reductions of over 90% are found in areas shallower than 2m, and decreases of over 10% occur within areas up to 4m depth for the Veg\_max scenario.

To investigate how the reduction potential of seagrass changes depending on the magnitudes reached during the extreme event, the impact on kinematics is compared for the Herwart and Xaver events for different variables based on the maximum levels reached during the respective storms.

##### 3.3.3.1.1 Water level

Within the EFWS study area, peak sea levels during Xaver exceed those during Herwart by more than 1m, as shown in Fig. 3.33. The highest sea levels occur in the eastern part of the study area and increase with the tidal range along the coast. Seagrass has a minimal effect on reducing peak sea levels, with a maximum reduction of about 10 cm, which is equivalent to 3 to 4% during Herwart. During Xaver, the sea level reduction for Xaver is similarly low, even 2 to 3 cm lower, resulting in a relative sea level reduction of 1% or less. In some parts of the supra littoral area, seagrass even increases the maximum observed sea levels.

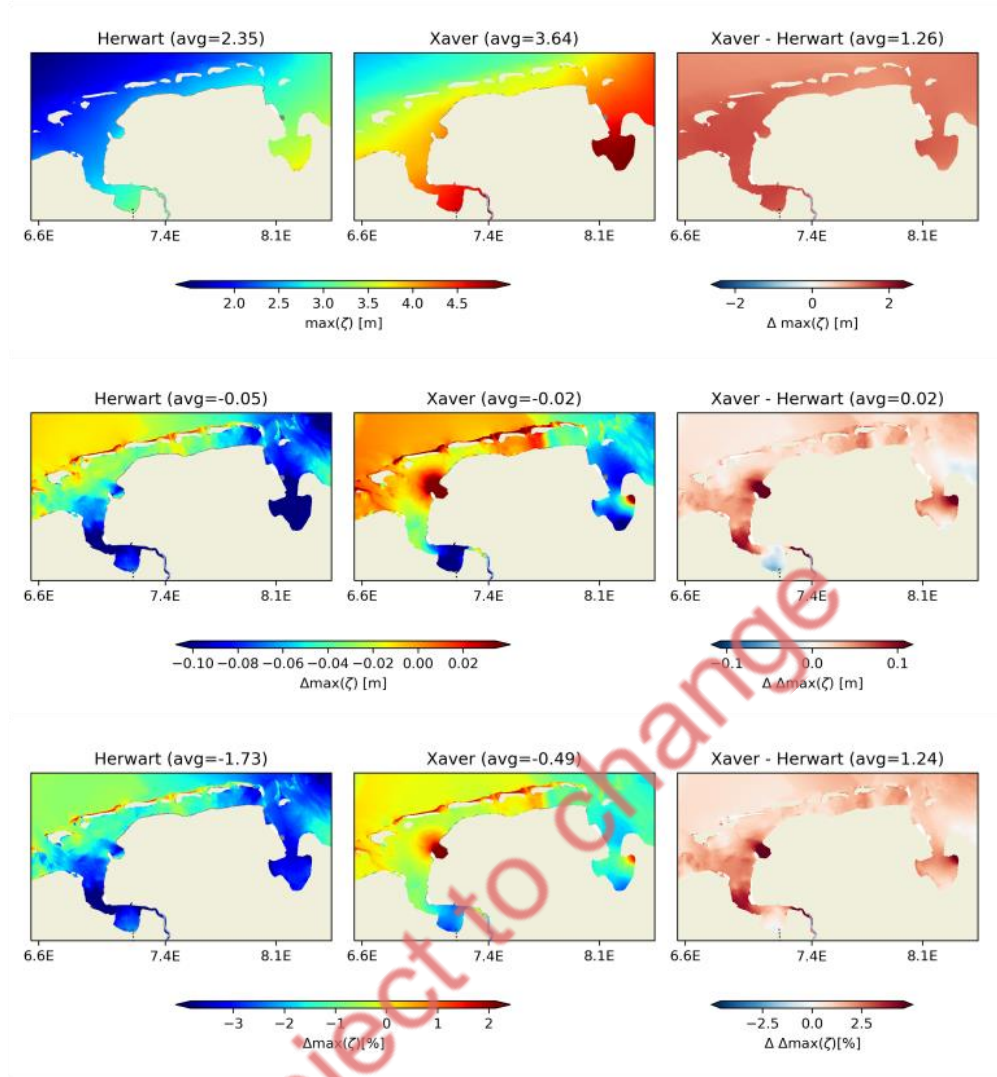


**Figure 3.22.** Maxima in Sea Surface Height and their reduction due to seagrass (Veg\_max scenario): Top row shows peak values during Herwart and Xaver and the differences. The middle row depicts the respective difference for the maximum coverage seagrass scenario - the no seagrass scenario, and the difference in differences (positive values in the 3rd column denote a weaker reduction during Xaver). The bottom row is analogous to the middle row comparing reductions relative to the absolute values without seagrass instead. Number in the respective title denotes the spatial average for the depicted domain

### 3.3.3.1.2 Wave Heights

During Xaver, simulated maximum significant wave heights are approximately 1 metre higher directly in front of the Barrier islands (see Fig. 3.34). Beyond the Barrier Islands, waves are significantly reduced due to breaking on the shallow bathymetry, but still remain at slightly higher levels during Xaver. The shallow Wadden Sea bathymetry efficiently breaks and dampens the waves. The wave trains passing by the barrier islands via the tidal channels are reduced by around 0.2 to 0.4 metres in the tidal flat area. During Xaver, peak waves in the back barrier Wadden Sea were slightly dampened by 5 to 10 cm, except for the sea ward channels of Ems and Jade Bay, where Xaver resulted in lower maximum wave heights. The overall peak wave height reduction reached about 20-40 percent among the tidal flats and between 0 and 10% within the channels. While wave damping tends to increase with larger waves during severe storms, it causes a similar reduction across the tidal flats, with a tendency to be lower by around 5%.

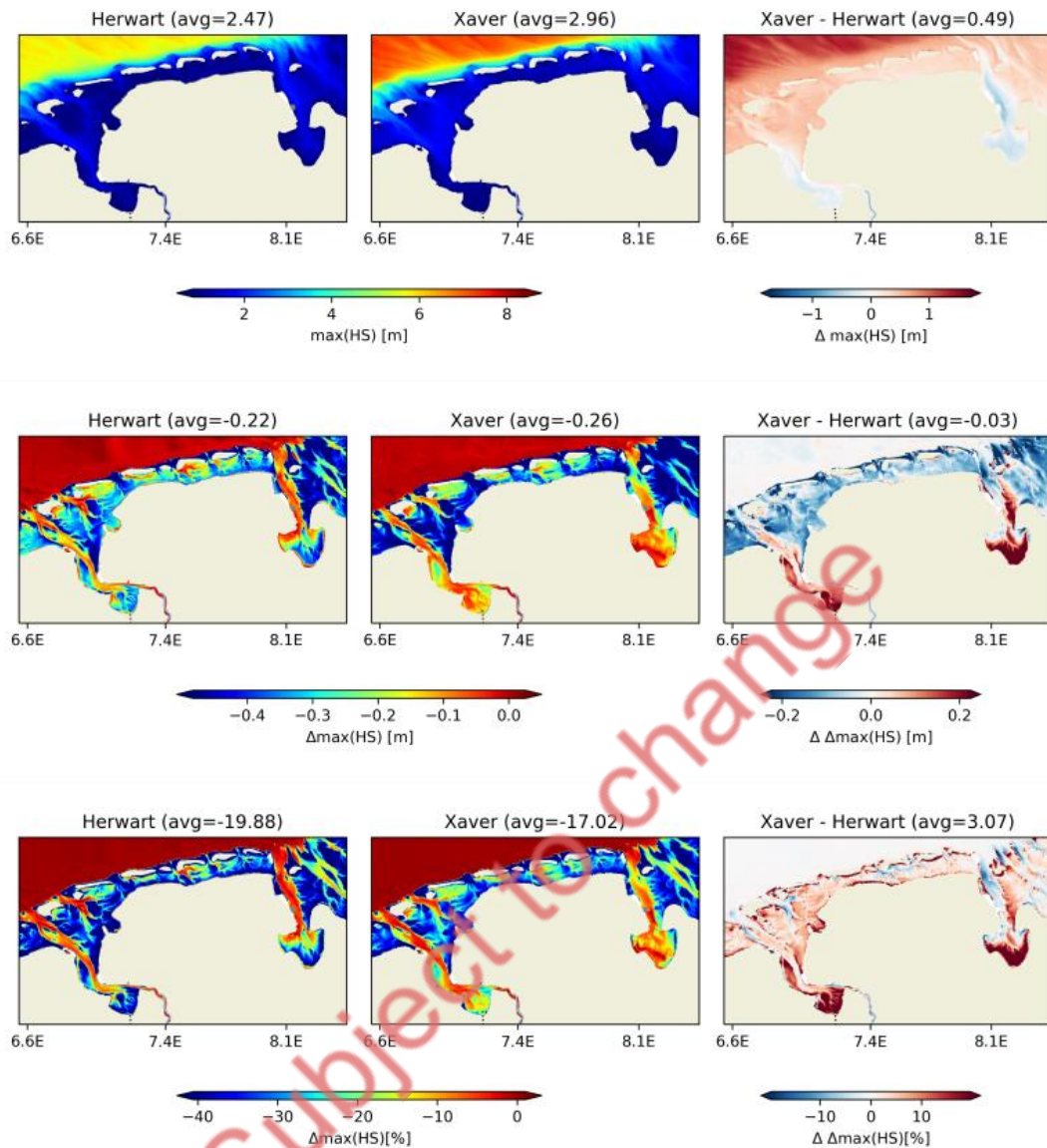


**Figure 3.23.** Maxima in Significant Wave Height and its reduction due to seagrass (Veg\_max scenario): Top row shows peak values during Herwart and Xaver and the differences. The middle row depicts the respective difference for the maximum coverage seagrass scenario - the no seagrass scenario, and the difference in differences (positive values in the 3rd column denote a weaker reduction during Xaver). The bottom row is analogous to the middle row comparing reductions relative to the absolute values without seagrass instead. Number in the respective title denotes the spatial average for the depicted domain

### 3.3.3.1.3 Current Velocities

Vertically averaged velocities reach up to 1 m/s in the narrow tidal channels during Herwart and below 0.6 in the shallow Wadden Sea. The largest values are found in Jade Channel, reaching up to 1.5 m/s (see Fig. 3.34). During Xaver, peak velocities are approximately 0.5 m/s higher in front of the islands and within the tidal basin centers. They are also increased in the tidal flat area due to higher water levels and reduced friction damping. The average depth velocities during Xaver were reduced compared to Herwart. This reduction is due to the effective dampening of seagrass in the vegetated layer above the ground, which is approximately 20 cm. Although the reduction during Xaver is higher in this layer, the much larger sea level setup results in a higher water column in the Wadden Sea. As a result, the upper layers of the water column are less affected by the bottom frictional damping.



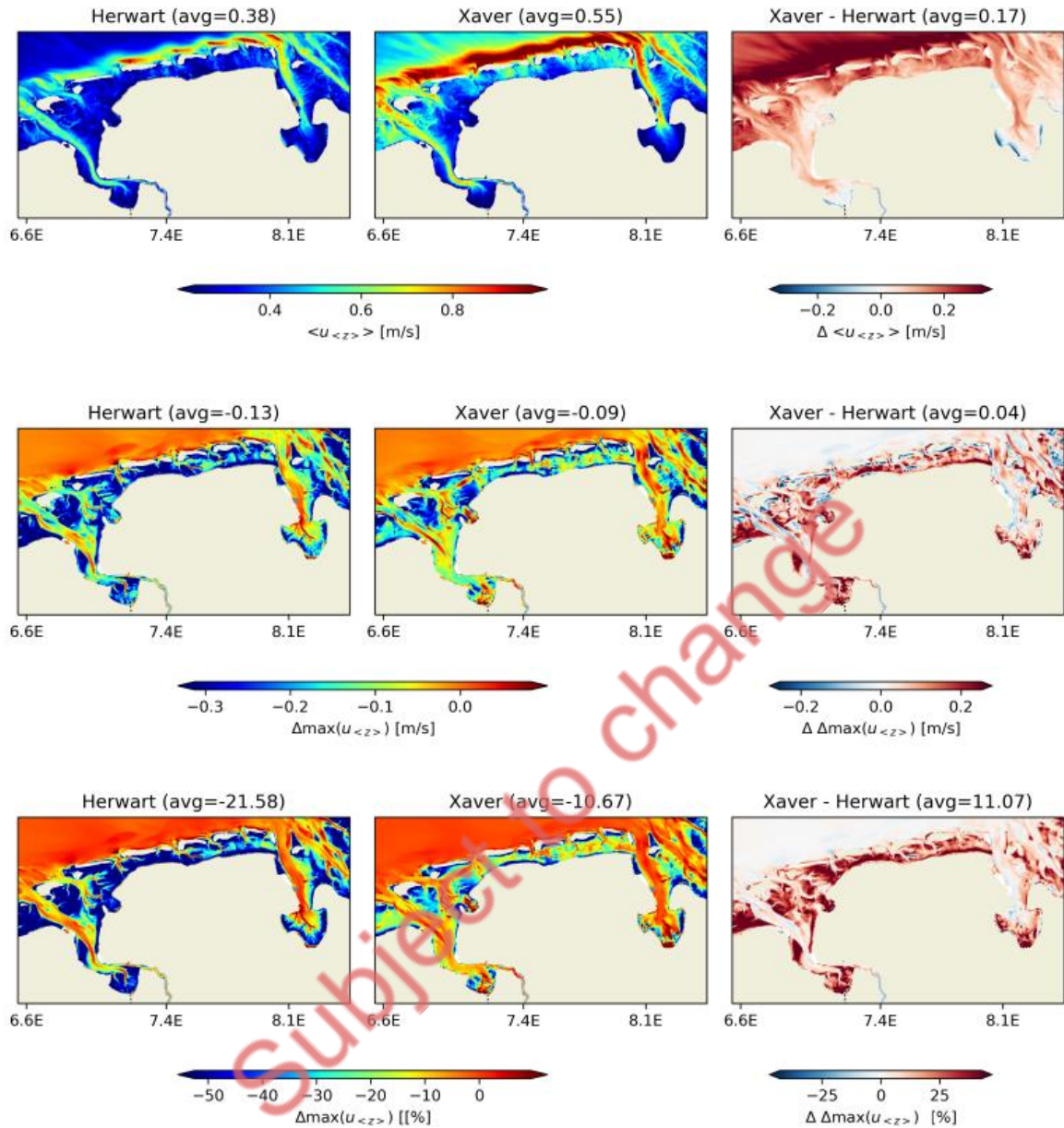


**Figure 3.245.** Maxima in depth averaged velocity and its reduction due to seagrass (Veg\_max scenario): Top row shows peak values during Herwart and Xaver and the differences. The middle row depicts the respective difference for the maximum coverage seagrass scenario - the no seagrass scenario, and the difference in differences (positive values in the 3rd column denote a weaker reduction during Xaver). The bottom row is analogous to the middle row comparing reductions relative to the absolute values without seagrass instead. Number in the respective title denotes the spatial average for the depicted domain

#### 3.3.3.1.4 Bed shear stress and sediments

The increase in velocities among secondary channels and tidal flat areas caused bottom stress maxima during Xaver to exceed those during Herwart by a few centipascal (refer to Fig. 3.36). In the majority of regions where bottom stress during Xaver significantly exceeds bottom stress during Herwart, the reduction in bottom stress during Xaver is predominantly more pronounced in absolute values compared to Herwart. However, the relative reductions do not scale proportionally with the increase in absolute value. As a result,



the relative reduction in the tidal flat areas is less and closer to 30-40%, as opposed to more than 50% across the tidal flat regions surrounding the channels.

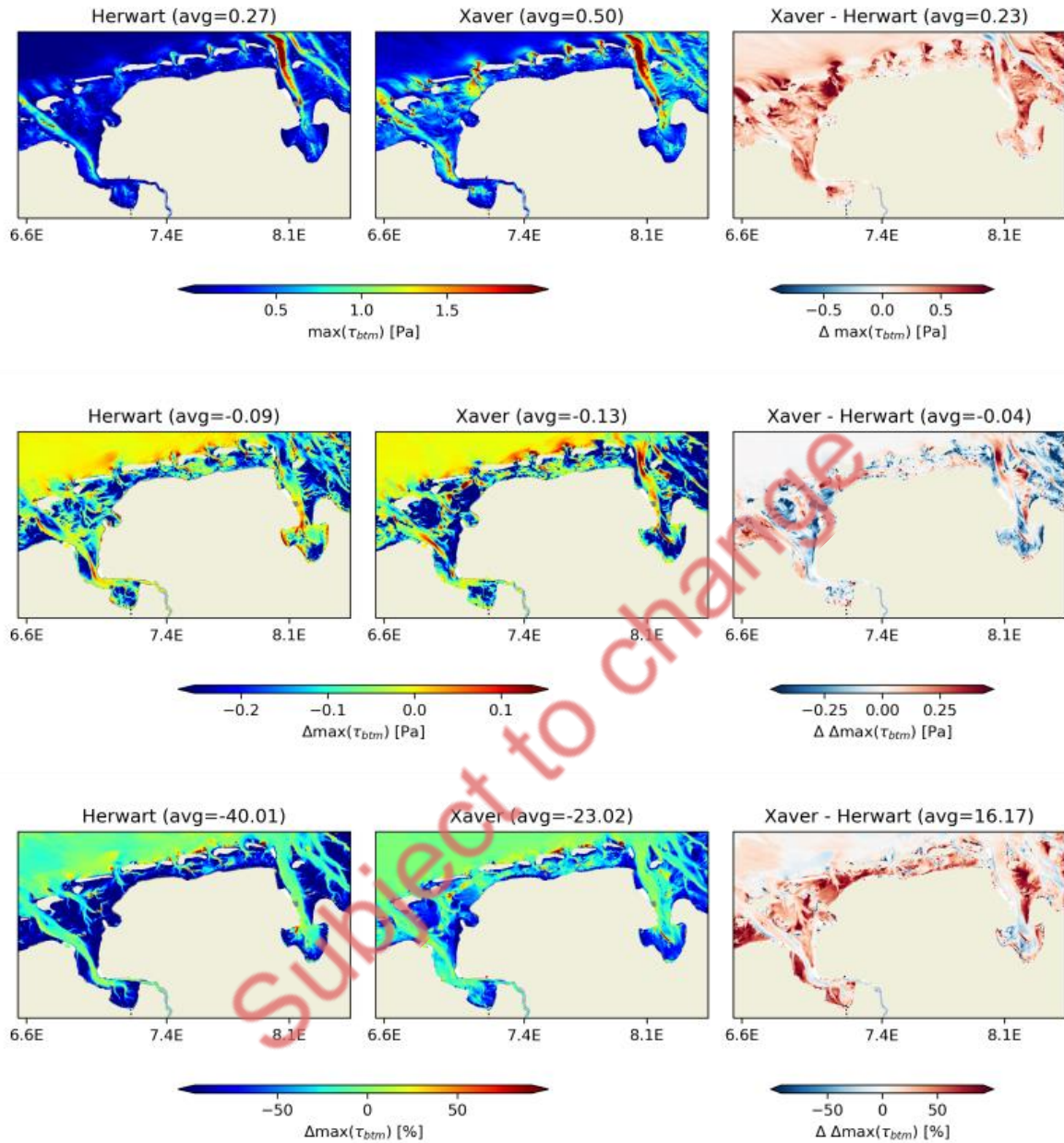


**Figure 3.256.** Maxima in Bottom Stress and its reduction due to seagrass (Veg\_max scenario): Top row shows peak values during Herwart and Xaver and the differences. The middle row depicts the respective difference for the maximum coverage seagrass scenario - the no seagrass scenario, and the difference in differences (positive values in the 3rd column denote a weaker reduction during Xaver). The bottom row is analogous to the middle row comparing reductions relative to the absolute values without seagrass instead. Number in the respective title denotes the spatial average for the depicted domain

The maximum concentration of bed layer sediment increased by 30% during Xaver over Herwart. The presence of seagrass resulted in a reduction of peak concentration, ranging from 0.2 to 0.4g near the channel edges and 0.6 to 0.8 on the tidal flats. This reduction was more than 80% during Herwart and between 60% and 80% during Xaver, compared to the tidal flats.

During heavier storms, there is a higher level of stress on the soil, resulting in increased sediment erosion from unprotected areas. Despite this, erosion reduction is still effective during stronger storms, although it appears to be 20% less effective.

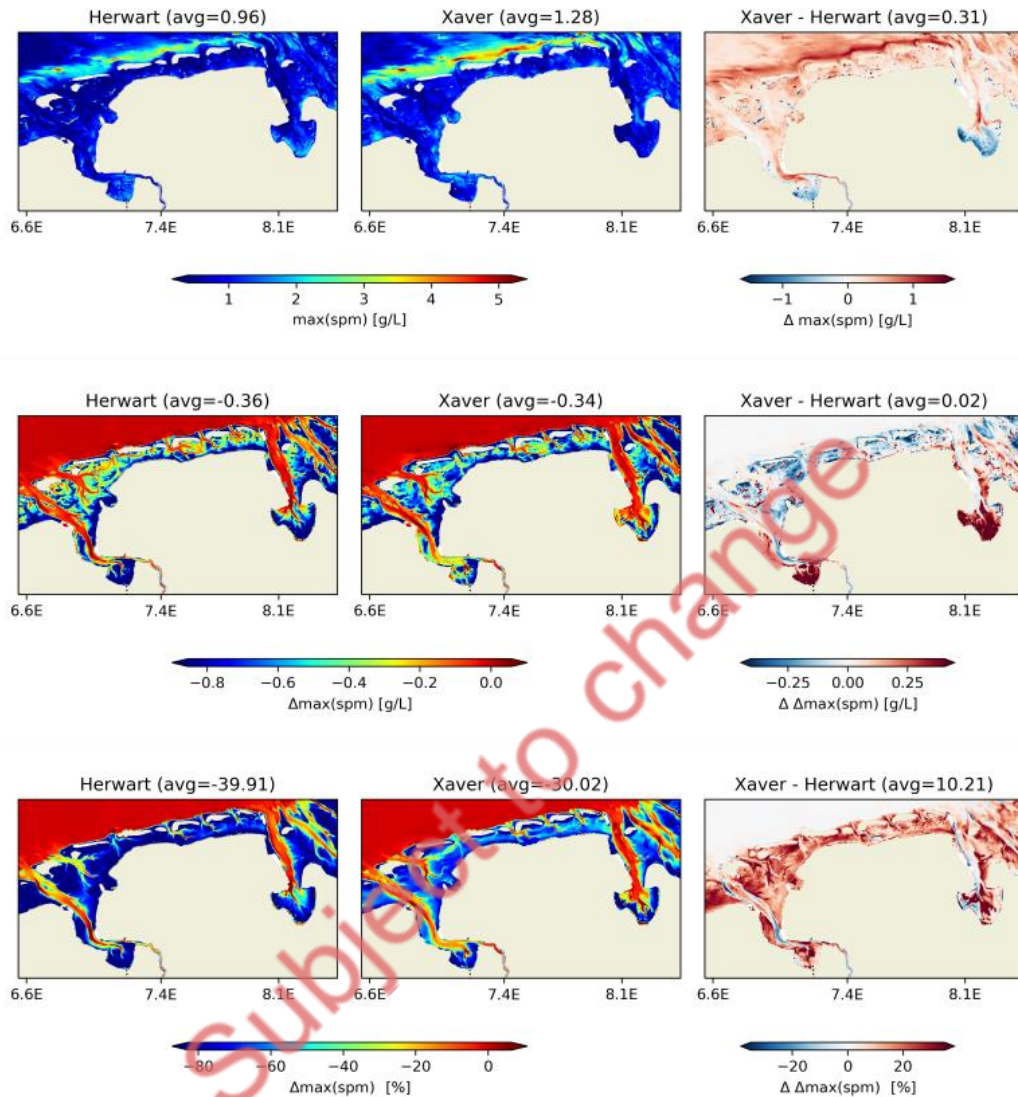


**Figure 3.267.** Maxima in Bottom layer total suspended matter concentration and its reduction due to seagrass (Veg\_max scenario): Top row shows peak values during Herwart and Xaver and the differences. The middle row depicts the respective difference for the maximum coverage seagrass scenario - the no seagrass scenario, and the difference in differences (positive values in the 3rd column denote a weaker reduction during Xaver). The bottom row is analogous to the middle row comparing reductions relative to the absolute values without seagrass instead. Number in the respective title denotes the spatial average for the depicted domain

Overall baseline values in hydrodynamics were significantly higher during Xaver compared to Herwart. Under these amplified circumstances, seagrass is suggested to maintain its attenuation capabilities. It tends to lead to an increased reduction in absolute terms. Therefore, it remains beneficial for coastal protection. However, it becomes less effective in relative terms as the attenuation capacities do not scale linearly with the magnitude of currents and waves.

### 3.3.3.2 Reduction of Erosion during extreme events

The reduction in sediment erosion was more sensitive to the increasing depth range of the seagrass plantings ( $h_r$ ) than to increasing the starting depth ( $h_s$ ). This is because a larger depth range implies a wider seagrass meadow in the cross-shore direction. However, the relationship between the reduction in erosion and seagrass location/size is not monotonic. A negative correlation was observed between the initial depth of the seagrass plantings and the decrease in seabed erosion as the depth range increased. When the depth was  $h_r = 1.4$  m, increasing  $h_s$  resulted in a smaller reduction in total erosion. This is because planting seagrass at a shallower depth covers more of the highly dynamic shore-breaking regions than planting it at the same depth range but starting at a deeper water depth. Fig. 3.38(a) shows the combinations of  $h_r$  and  $h_s$  when the reduced erosion reaches the extrema. Fig. 3.38(b) and 3.38(c) illustrate the patterns of erosion and deposition that correspond to two distinct situations of seagrass distribution. Specifically, Fig. 3.38(b) depicts a scenario where seagrass begins at a deeper depth but spans a narrow range (as shown in Fig. 3.8(b)).

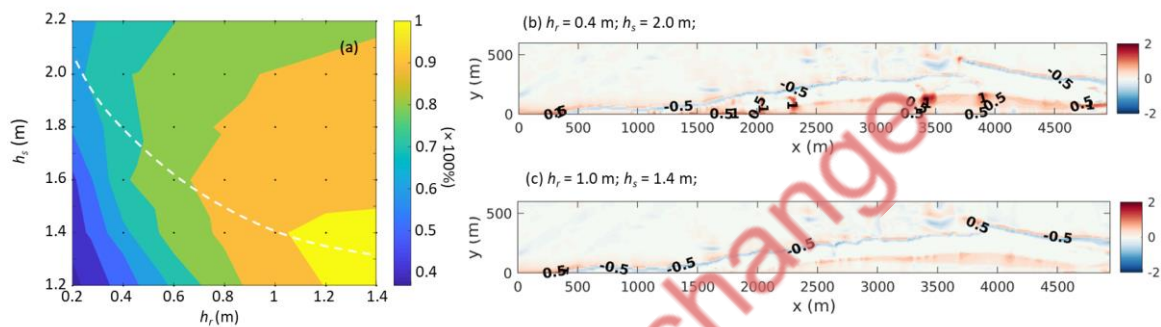


**Figure 3.38.** (a) The reduction of erosion with respect to the erosion from the default run ( $E$ ) for experiments as a function of  $h_r$  and  $h_s$ . The black dots indicate experiments with different  $h_r$  and  $h_s$  combinations. Panel (b) illustrates the erosion/deposition pattern for the ‘deep start-narrow range’ scenario (i.e.,  $h_r = 0.6$  m and  $h_s = 2.0$  m); (c) is the same as (b) but for the ‘shallow start-wide range’ ( $h_r = 1.0$  m and  $h_s = 1.4$  m). The dashed curve denotes the  $h_r$ - $h_s$  combination at which  $E$  reaches the extrema

The efficiency of erosion reduction,  $R$ , which measures the ratio between,  $E$ , a volume of erosion reduced relative to the non-seagrass situation (Table 3.1) and,  $A$ , the normalized seagrass area for various combinations of ‘ $h_s$ ’ and ‘ $h_r$ ’ is shown in Fig. 3.39. The maximum efficiency rate of  $R$  equal to 6.5 is obtained when  $h_r = 0.2$  m and  $h_s = 1.2$  m (bottom left of the figure). This combination reduces erosion by approximately 40% while utilizing only approximately 6% of the maximum seagrass area. Though increasing seagrass range (or planting in deeper water), seagrass meadows may cover less erosive high energy shallow areas and hence be less efficient. However, it is important to note that erosion reduction values that are too low should be avoided as they may potentially lead to intense regional erosion. The steepest increase in  $R$  occurs along the direction of the normal, as represented by the gray dashed line in Fig. 3.39. Along this line, the ‘optimal’ combination can be found at point ‘i’, intersecting with the white dotted curve line at  $h_r = 0.85$  m and  $h_s = 1.35$  m. The white dotted curve line denotes the ‘ $h_s$ - $h_r$ ’ combination at which  $E$  reaches the extrema. Thus, for this combination, the maximum  $E$  is approximately 0.9 and is furthest from the maximum seagrass area. At this point,  $R$  is approximately 2.

The gray line further crosses with the straight dotted line at ‘ii’ ( $h_r = 1.25$  m,  $h_s = 1.6$  m). At this point,  $R \approx 1$ . The straight dotted line indicates the combinations of ‘ $h_s$ ’ and ‘ $h_r$ ’ that maximize the seagrass area for a given ‘ $h_r$ ’. In practice, when considering a stronger storm, the maximum erosion reduction will be achieved by increasing seagrass meadow size. Thus, a larger depth range is needed for a given starting depth  $h_s$  to achieve similar storm buffering effectiveness. The two white lines in Fig. 3.39 will progressively approach each other. The most efficient seagrass allocation occurs when the area of the meadow is maximized. The optimal  $h_r$ - $h_s$  combination ‘i’ aligns with ‘ii’ (Fig. 3.39), implying the achievement of the potential maximum effective coastal erosion protection.

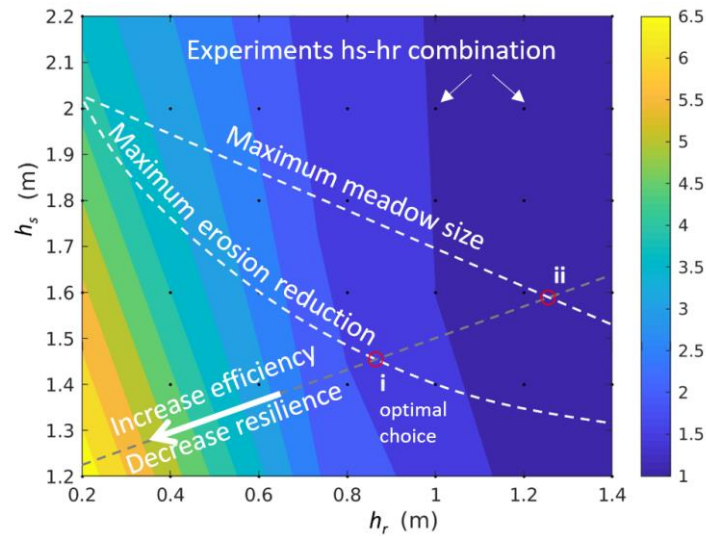


**Figure 3.279.** The ratio  $R$  between the relative erosion reduction  $E$  and the normalized seagrass area  $A$  for different combinations of  $h_r$  and  $h_s$ . The gray dashed line denotes the normal direction in which  $R$  decreases with increasing  $h_r$  and  $h_s$

### 3.3.4 Evaluating the benefit of sea-grass under end of the century climate conditions

After demonstrating the efficiency of seagrass under current conditions, it is important to consider to what extent the hydraulic engineering capabilities of seagrass will remain under future climate conditions. This is particularly relevant as sea levels are expected to rise significantly, and seagrass will occupy less space vertically in the water column.

To limit the computational costs of running the German Bight SCHISM configuration for multiple seagrass scenarios over several years, we had to restrict the number of simulations. Therefore, we focus solely on the RCP8.5 scenario ensemble mean realization of regionalized sea level rise and ocean-atmosphere variability for the year 2090, which was available to us. In relation to the seagrass scenarios, we compare the scenarios with no seagrass and maximum seagrass coverages (3.2.1.3) without altering the scenario configuration used under present day conditions.

As we are only simulating a one-time slice, it is important to maintain objectivity and avoid subjective evaluations. Therefore, we will use the bathymetry identical to present day conditions, as any future changes are highly speculative. However, given a sediment supply, an accumulation of sediment in the tidal flats would be expected.

The simulations based on the RCP 8.5 projection for the year 2090 were compared to the reference simulations for 2017. The maximum aerial coverage seagrass scenario (Vegmax) was contrasted with the no seagrass scenario (VegCntrl) in the SLR scenario. In the EFWS area, the average sea level is expected to rise by approximately 0.7m, which is about 0.9m higher than the 95th percentile and almost 1.8m higher than the annual maximum. As demonstrated by the present-day baseline analysis, seagrass has only a marginal impact on peak water levels. Therefore, this analysis focuses solely on the impact of seagrass on waves, currents, bottom stress, and sediment concentrations in bottom layers, which serve as erosion proxies.

#### 3.3.4.1 Wave Heights

Under the projected wind climate, the 95th quantiles in significant wave heights are reduced in the North Sea seaward of the Barrier islands. However, among the tidal flats in the back barrier Wadden Sea future scenario, the 95th percentiles



in HS appear increased, albeit only slightly by a few centimetres while being slightly decreased coastward in the embayments of Ems and Jade (see Fig. 3.40). On a large scale, the wave damping effect of seagrass remains similarly strong between the present and future sea level scenarios. Seagrass tends to dampen the 95th quantile HS by around 5-10 near the channels and between 20 and 50% among the flats. The increased future tidal flat wave heights are damped by the intertidal seagrass, leading to an increase in absolute attenuation of around 5 cm. In relative terms, the efficiency is almost the same, but there is a minor reduction of 5-10%.

In the coastal supra littoral, the efficiency is further reduced. However, these areas experience waves mostly during strong wind events, even at present-day sea level.

#### 3.3.4.2 Current Velocities

The 95th percentiles baseline level for depth averaged velocities is slightly increased by about up to 0.2 m/s in the future sea level rise scenarios (s. Fig. 3.40). The attenuation slightly enhances within the majority of the seagrass covered tidal flat areas, as the seagrass on average interacts with larger velocities there while SLR decreases the frictional damping. However the impact for damping on the channel velocities weakens. Overall the structure of velocity reductions do not change strongly, the velocity attenuation strengths for the tidal flat Wadden Sea is reduced by about 5-10%

Subject to change



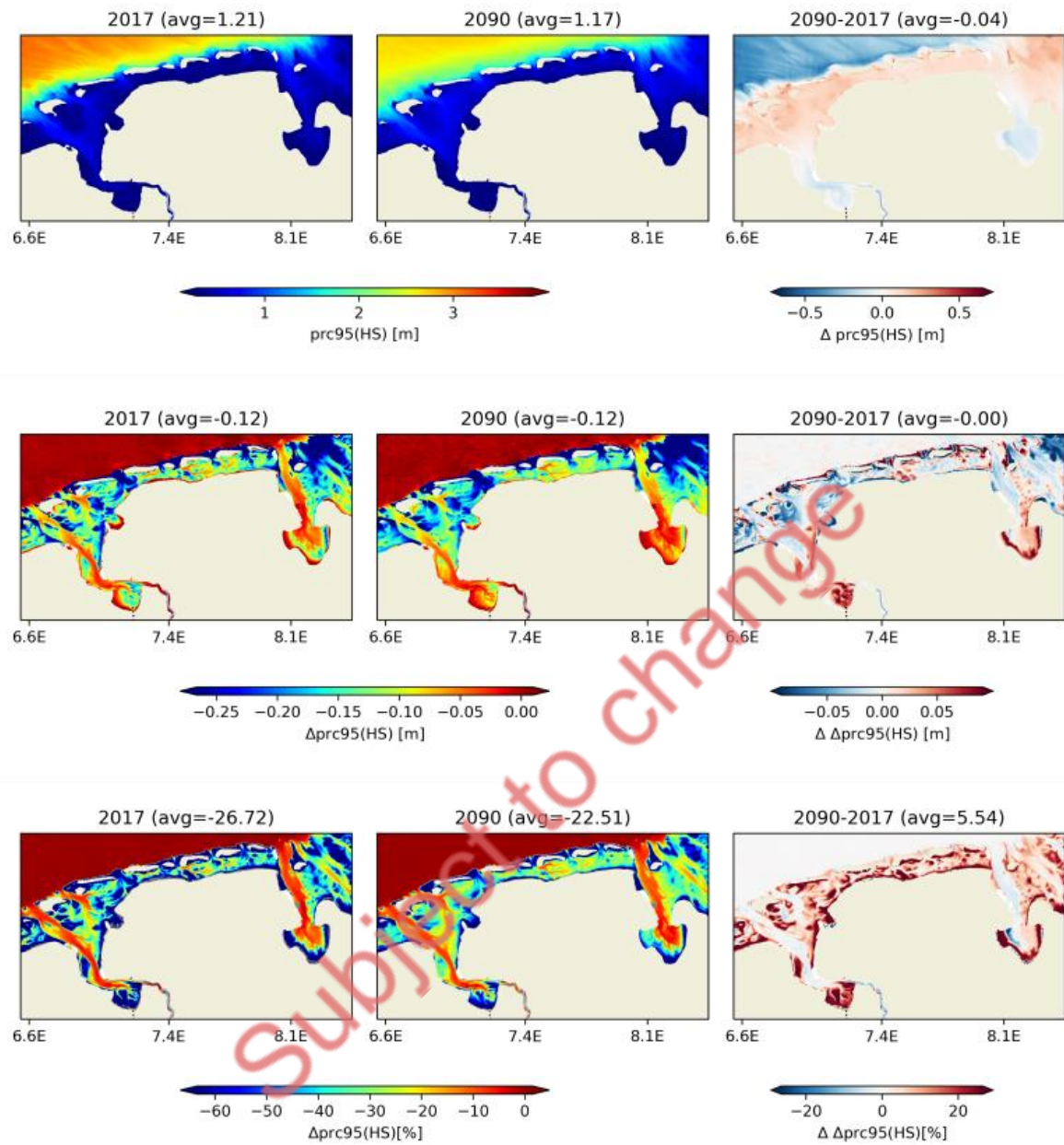


**Figure 3.40.** 95<sup>th</sup> Annual percentile in significant Wave Height (HS) and its reduction due to seagrass (Veg\_max scenario): Top row shows peak values in 2017 and 2090 and the differences. The middle row depicts the respective difference for the maximum coverage seagrass scenario - the no seagrass scenario, and the difference in differences (positive values in the 3rd column denote a weaker reduction in 2090). The bottom row is analogous to the middle row comparing reductions relative to the absolute values without seagrass instead. Number in the respective title denotes the spatial average for the depicted domain

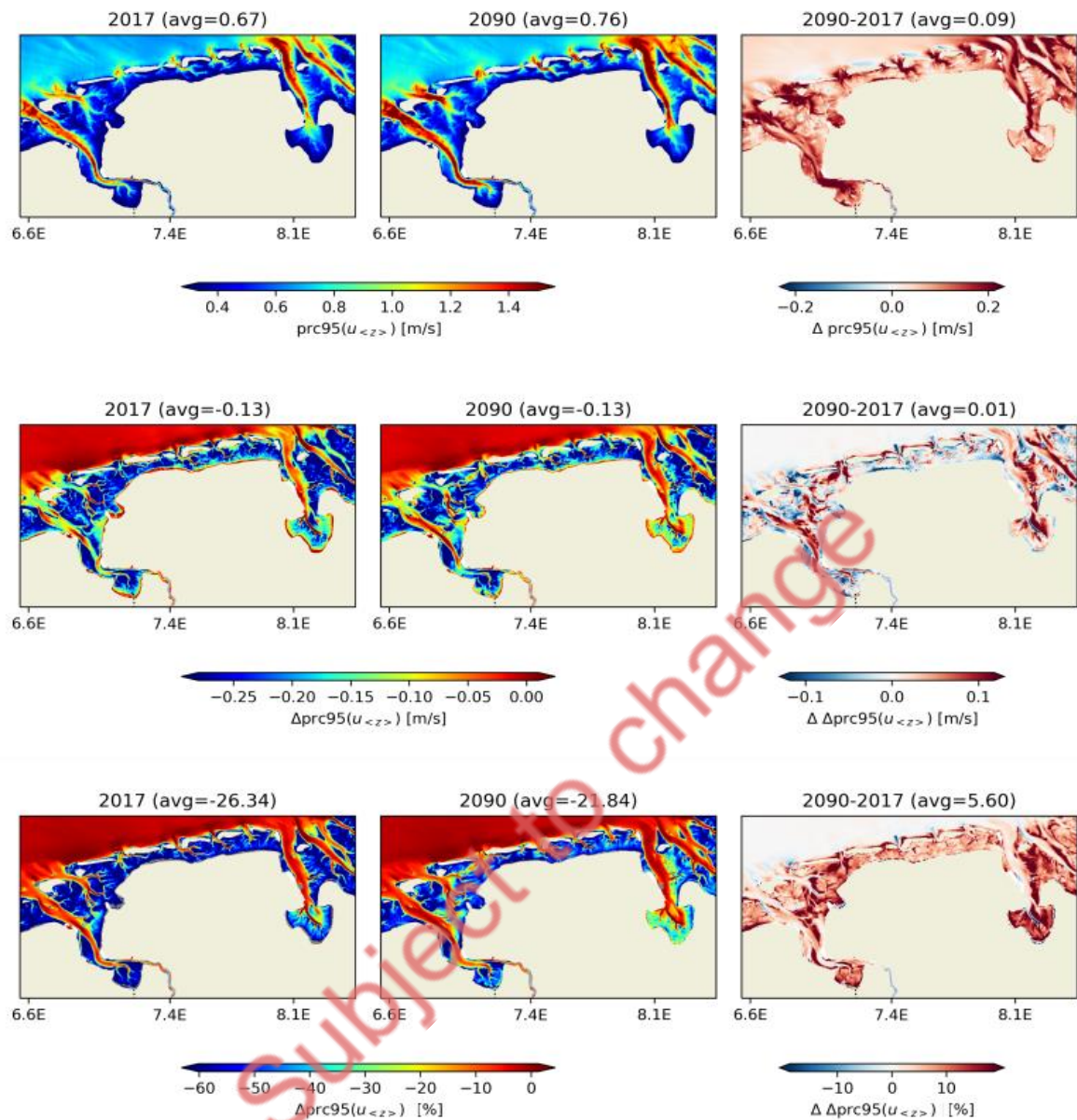


**Figure 3.41.** 95<sup>th</sup> Annual percentile in depth averaged velocity and its reduction due to seagrass (Veg\_max scenario): Top row shows peak values in 2017 and 2090 and the differences. The middle row depicts the respective difference for the maximum coverage seagrass scenario - the no seagrass scenario, and the difference in differences (positive values in the 3rd column denote a weaker reduction in 2090). The bottom row is analogous to the middle row comparing reductions relative to the absolute values without seagrass instead. Number in the respective title denotes the spatial average for the depicted domain

#### 3.3.4.3 Bed shear stress and sediments

With the SLR in 2090, there is an increase in the baseline of the bottom stress percentiles, which is more like a week in the shallow areas, but reaches 1 Pa within the tidal channels as a result of the increased flow velocities. Overall, eelgrass remains similarly effective in reducing stress in the covered zones, reducing bottom stress there by up to 0.5 Pa or more than 80% in relative terms. The effect is less pronounced in the transition zone from the seagrass-covered flats to the larger main channels (especially the Jade and Ems channels), where the reduction falls below 40%, i.e. 20% less than at present sea level.

In relative terms, this results in a similar localised reduction in erosion control efficiency as proxied by the 95th percentile total spm concentrations, while within the seagrass meadows the reduction efficiency remains almost the same, reducing sediment resuspension by 80% and more.

Subject to change

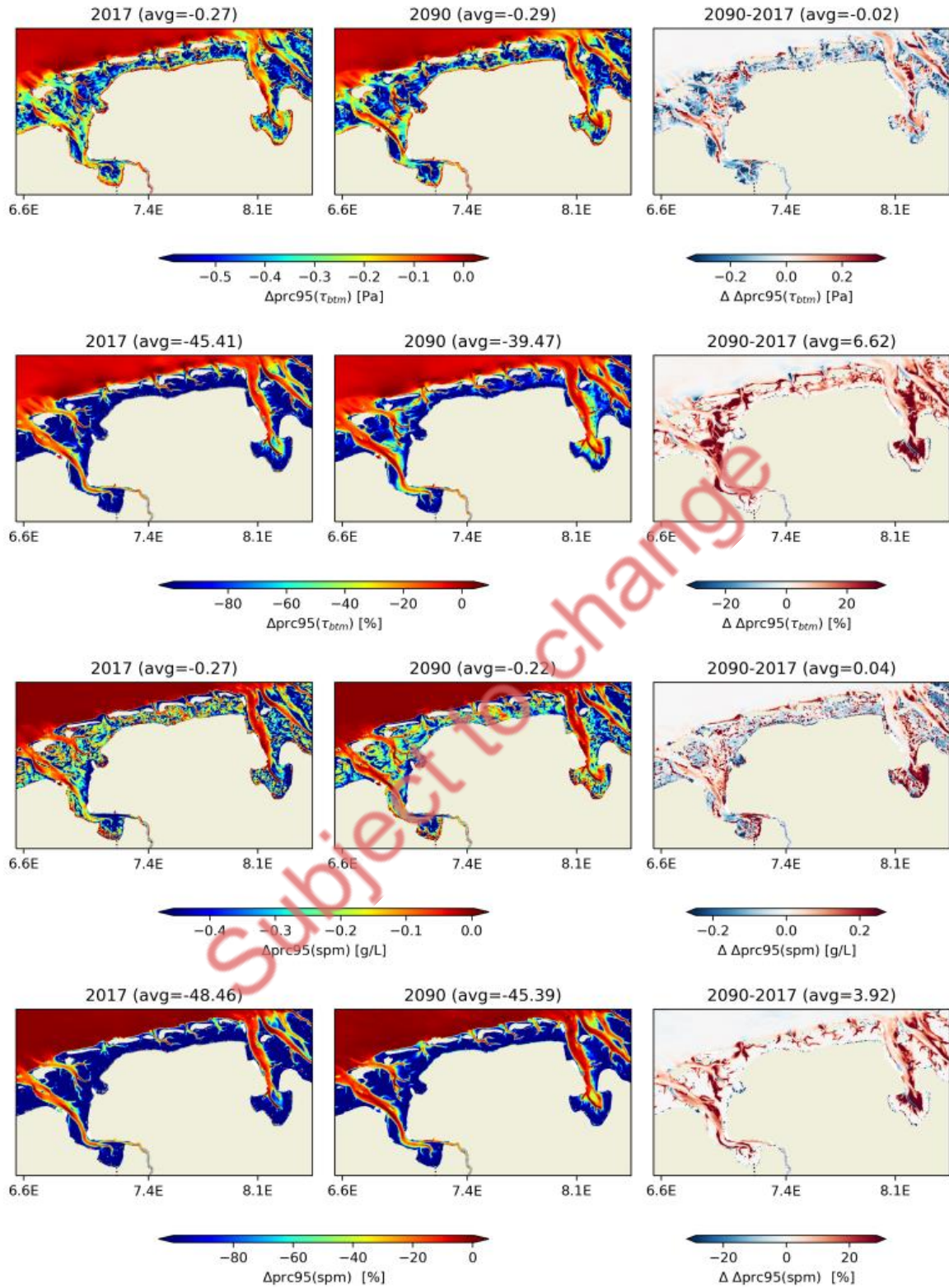


**Figure 3.42.** 95<sup>th</sup> Annual percentile in reduction due to seagrass for erosion proxy variables bottom stress and bottom layer sediment concentration. (Veg\_max scenario): Top row shows peak values in 2017 and 2090 and the differences. The middle row depicts the respective difference for the maximum coverage seagrass scenario - the no seagrass scenario, and the difference in differences (positive values in the 3rd column denote a weaker reduction in 2090). The bottom row is analogous to the middle row comparing reductions relative to the absolute values without seagrass instead. Number in the respective title denotes the spatial average for the depicted domain



Overall, the future projections show that for the same seagrass restoration scenarios, the overall efficiency of kinematic reduction is reduced and in particular the extended effect of how the flats affect the adjacent channels is reduced. Nevertheless, it remains an effective solution, especially in terms of reducing bottom stress and sediment mobilisation.

### 3.4 Effect of saltmarsh on hydrodynamics and morphology (NLWKN)

Effects of NBS on water level, wave height, velocity and bed shear stress were analyzed at the stations from V1 to V5 (Fig. 3.12). Spatial effects of NBS in the Ley Bay were then investigated with respect to bed shear stress, sediment transport and morphological changes during the three events.

#### 3.4.1 Water level

For clarity, water level comparison only for three stations V2, V4 and V5 is shown in Fig. 3.43. Additionally, the offshore water level variation (at 20 m depth of the boundary of EMS, see Figure 3a) of the respective event is added to the right y-axis (gray-line) for a better comparison with the local changes.

Three events indicate different trends of water level in the salt marsh area. During the fair weather condition, the maximum water level rise is lower than 1.5 m, while the salt marsh area is located at around the level of 1.5 m + MSL. Therefore, the salt marsh area remained dry during this period. In Xaver, the offshore maximum water level is about 2.7 m, which resulted in a similar water level rise at V4. Both V2 and V5 have low water levels than V4, but they are similar (maximum ~1.7 m). These indicate that the furthest location along Ley Bay experienced high water levels due to reflection of tidal wave from the surrounding dykes. NBS has delayed both rising and draining of water, and thus resulting low water levels before the storm peak and high water levels (red-line) after the storm peak than WT-NBS (blue-line). Herwart had lower water levels (max. 1.6 m) than Xaver. Therefore, all locations submerged only during the storm peak. However, such water level rise in NBS is completely damped at the stations in the middle of the salt marsh (e.g., V2, V4), and showed increase of water levels only at V5, which is located at the seaward edge of salt marsh. These results suggest that there is a considerable water level variation within the salt marsh area, and NBS delays rising and draining of water levels.



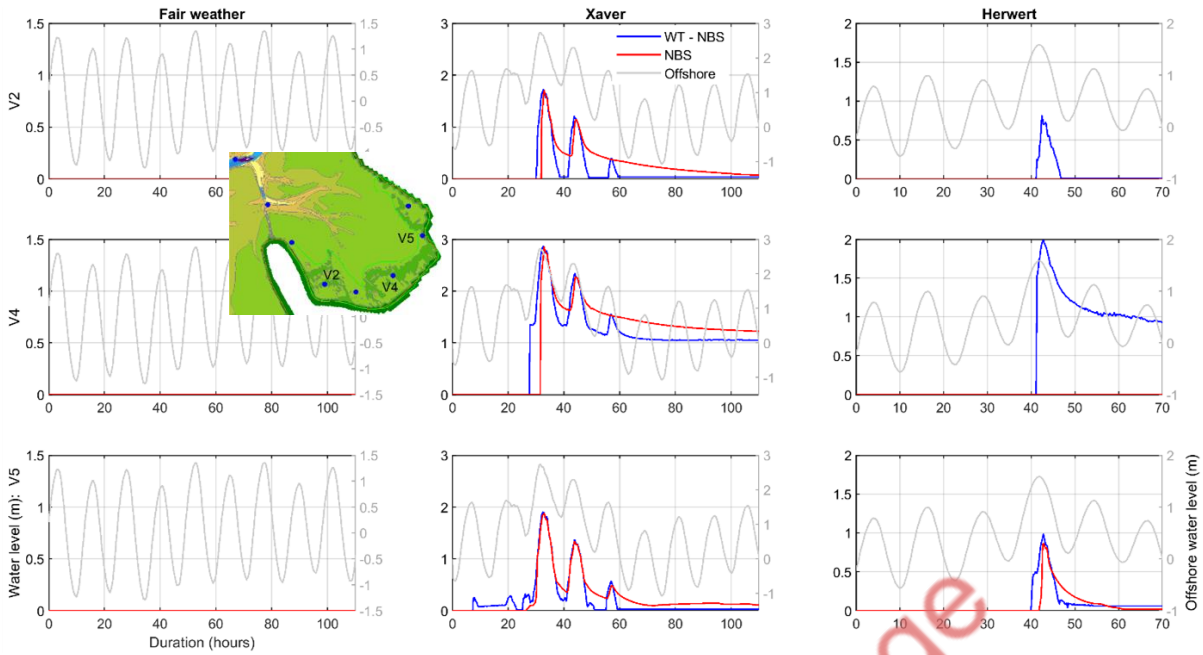


**Figure 3.43.** Comparison of water levels at the selected locations V2, V4 and V5 (see on Ley Bay bathymetry: insert view), without NBS (WT – NBS: blue-line) and with NBS (red-line) for fair weather, Xaver and Herwart events. Respective offshore water levels (20 m depth) are shown with the gray-line. For clarity, y-axes in a row of events have different scales

### 3.4.2 Bed shear stress

Spatial variability of the maximum bed shear stress at each grid-cell during the events was then analyzed for the two scenarios (Figure 34). In the fair weather, high bed shear stresses are generally found along the channels. During flood and ebb, the maximum velocities occur at mid-tide. Therefore, high bed shear is concentrated at channels, which are submerged at mid-tide. There is no difference between WT – NBS and NBS applications due to the occurrence of low water levels (see Fig. 3.43). High water levels in Xaver (maximum 2.7 m) together with high waves (0.7 m) in Ley Bay resulted in high bed shear stresses in the channels as well as at the shallow areas, particularly in the salt marsh area. In the NBS application, the bed shear stresses in the salt marsh area are significantly decreased. For example, the maximum value is about 0.1 N/m<sup>2</sup>, while it is over 1 N/m<sup>2</sup> in WT – NBS. Furthermore, it is shown a remarkable decrease at seaward side along the salt marsh edge. In Herwart, the bed shear stresses are lower than Xaver due to low water levels and wave heights. It should be noted that some locations along the channels experienced lower bed shear than even the fair weather condition. This could be due to the fact that the velocities in the flooding and ebbing processes within the channels are counteracted during this weak storm event. However, as in Xaver, a significant decrease of bed shear is found within the salt marsh area as well as along the edge. These results clearly indicate that NBS significantly decreases bed shear stresses not only within the salt marsh area but also at the seaward side close to the salt marsh edge, and that directly affects on the potential bed sediment transport.

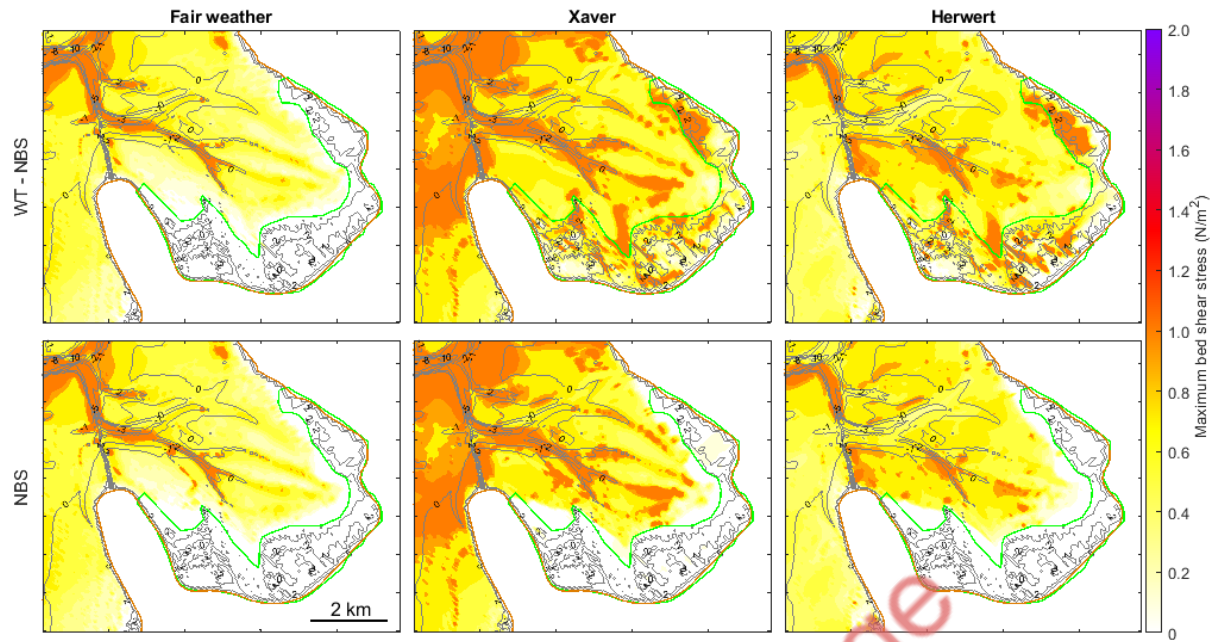


**Figure 3.44.** Comparison of the maximum bed shear stress (color-bar) in the Ley Bay area during fair weather, Xaver and Herwert events for the scenarios applying no salt marsh (WT-NBS) and with salt marsh (NBS). Salt marsh area is indicated by the green-polygon. Initial bed topography is shown by depth contours

### 3.4.3 Sediment transport and bed evolution

Similar to the maximum bed shear stress, sediment transport was estimated during the events for the two scenarios. Suspended and total sediment transports (both bed and suspended together) were separately analyzed in order to investigate the effect of NBS on each component separately.

In the fair weather condition, both suspended and total transports are generally strong in the channels, and they indicate a sediment transport pattern away from Ley Bay. In the salt marsh area, no sediment transport occurred due to low water levels (see Figure 33), and thus no difference is found between WT – NBS and NBS. Xaver resulted in the strongest transport within the entire area, in which the orientation of the total transport is still similar to that of the fair weather condition. In the NBS application, there is a considerable decrease of transport compared with that of WT – NBS. The transport within the salt marsh area in NBS is predominantly driven by the suspended transport (see Figure 35: no bed shear stress). Furthermore, it is shown that lower transport in Ley Bay compared with WT – NBS. This indicates a reduction of sediment contribution from the salt marsh area to Ley Bay in NBS. At the east part of the salt marsh area, NBS caused strong suspended transport, which can be occurred due to the flow diversion from the rest of salt marsh. The entire Ley Bay experienced a similar sediment transport pattern in Herwert albeit lower than Xaver. Particularly, there is very weak transport within the salt marsh area in NBS due to low water levels and wave heights. Therefore, NBS decreases sediment transport. However, suspended transport can be increased depending on the severity of a storm event.

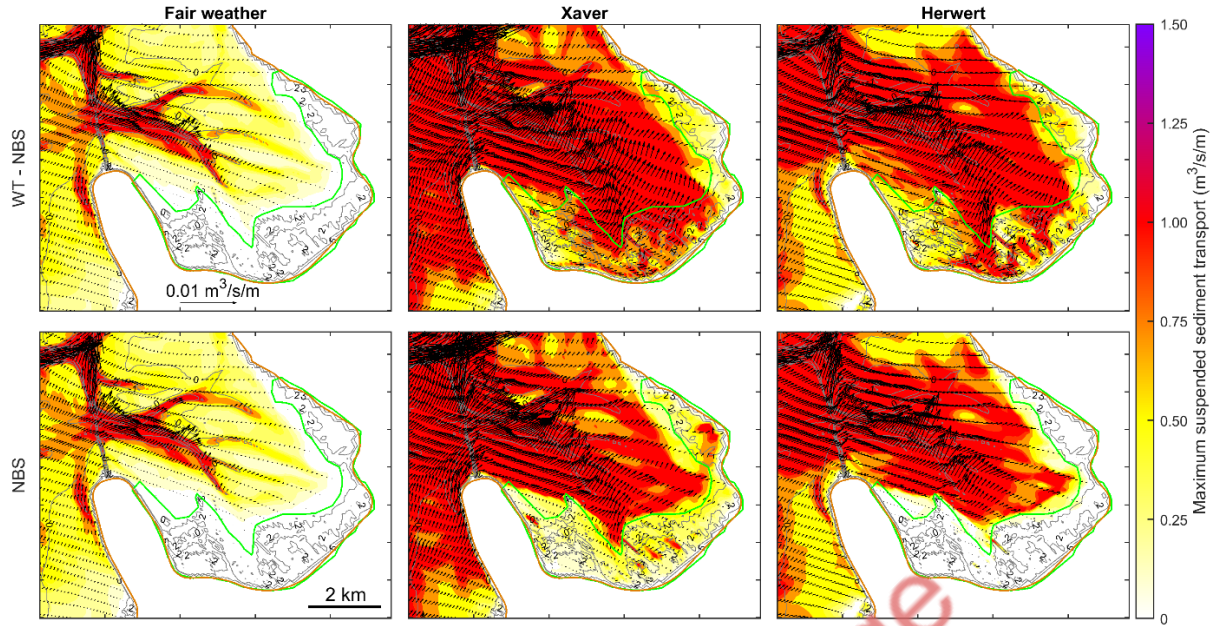


**Figure 3.45.** Comparison of the maximum suspended sediment transport (color-bar) and the maximum total transport (vectors: for clarity every 8<sup>th</sup> vector is shown) in the Ley Bay area during fair weather, Xaver and Herwart events for the scenarios applying no salt marsh (WT-NBS) and with salt marsh (NBS). Salt marsh area is indicated by the green-polygon. Initial bed topography is shown by depth contours

Bed evolution during the events was compared by analyzing erosion and sedimentation patterns for the two scenarios (Figure 36). In all cases, the maximum erosion and sedimentation occurred at channels, which vary between -0.2 m to 0.3 m. In fair weather, the bed evolution above MSL (0 m depth contour) is very small and the salt marsh area is not affected. The patterns indicate, there is no difference between WT – NBS and NBS. Xaver caused strong erosion at the channel banks and sedimentation in the channels. Furthermore, strong erosion and sedimentation occurred within the salt marsh area, which depend on the location, and they considerably decreased in NBS. In Herwart, similar patterns are found for erosion and sedimentation, whereas they are not prominent as in Xaver. Particularly, salt marsh area in NBS has experienced very weak bed evolution.

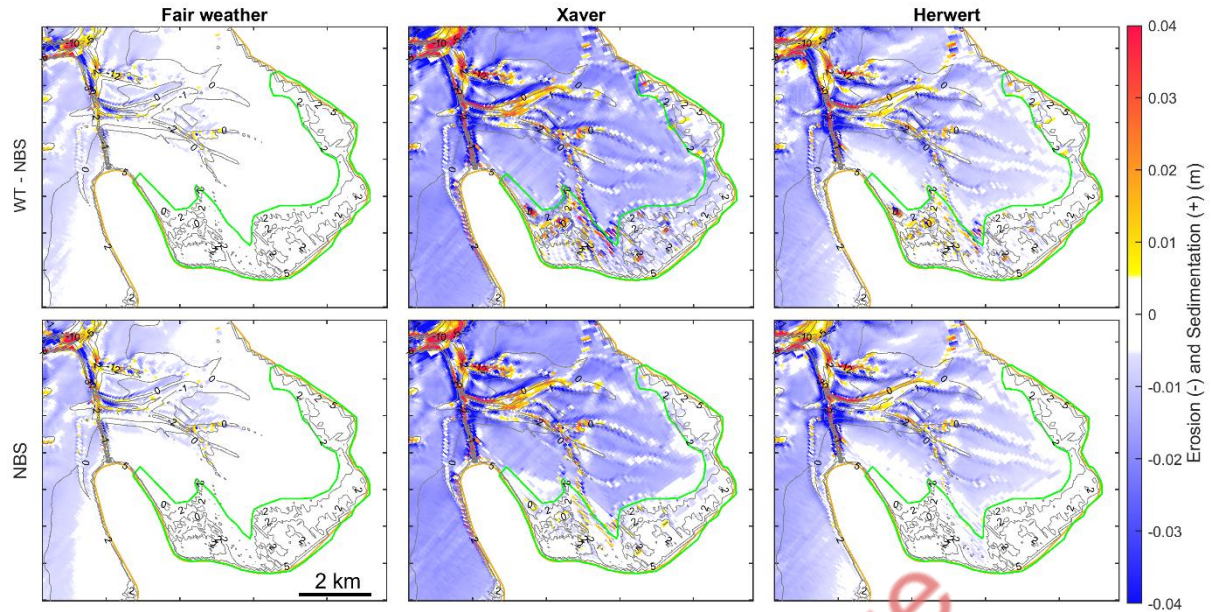


**Figure 3.286.** Comparison of the bed evolution pattern (color-bar) in the Ley Bay area during fair weather, Xaver and Herwert events for the scenarios applying no salt marsh (WT-NBS) and with salt marsh (NBS). Salt marsh area is indicated by the green-polygon. Initial bed topography is shown by depth contours

Volume of bed evolution within the salt marsh area was estimated for erosion and sedimentation during the events (Figure 37a). Positive values in relative reduction imply a higher volume change in WT – NBS than NBS, and the higher the value the lower the effect of NBS (Figure 34b). Negative values indicate a higher volume change in NBS than WT – NBS, and the lower the value the higher the effect of NBS. Zeros occur, when both are similar. As found earlier, the salt marsh area experienced no bed evolution in the fair weather condition irrespective to the NBS applications (a). In Xaver, maximum erosion ( $-75 \times 10^3 \text{ m}^3$ ) and sedimentation ( $15 \times 10^3 \text{ m}^3$ ) occurred. Both decreased more than 60% in NBS (b). Similar trend is found in Herwert. However, the sedimentation volume in NBS is very small ( $0.4 \times 10^3 \text{ m}^3$ ). Therefore, the relative reduction increased up to 96%. These indicate that strong erosion in the salt marsh area resulted in strong sedimentation and vice versa. Furthermore, the eroded sediments from the salt marsh area escape into Ley Bay rather sedimentation therein.



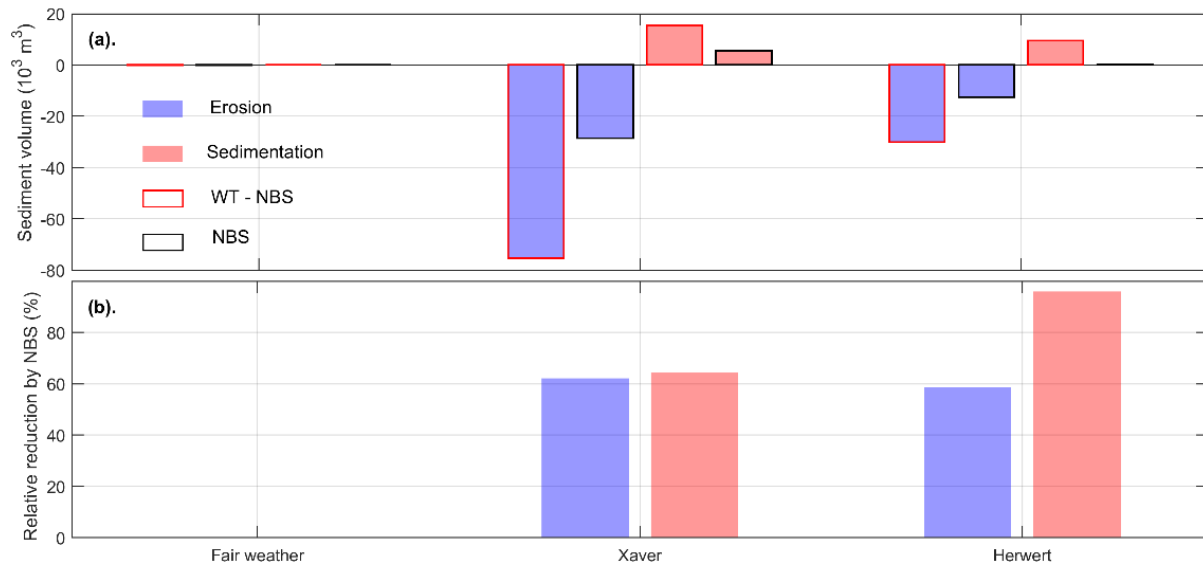


**Figure 3.297.** Erosion and sedimentation volumes within the salt marsh area without NBS (WT - NBS) and with NBS (NBS) applications (a) and the relative reduction of volume in erosion and sedimentation with respect to the WT - NBS application:  $\left(\frac{[WT - NBS] - [NBS]}{[WT - NBS]} \times 100\%\right)$  (b)

Sensitivity of the salt marsh configuration to the bed evolution was finally investigated applying different plant density, plant diameter and height (see section 3.2.2.1). The most extreme event Xaver was simulated with three different values for each parameter, and the relative reduction of volume with respect to WT-NBS was estimated and compared.

Both plant density (i.e., number of plants per square meter) and plant diameter indicate a relative reduction of volume about 60% in erosion and sedimentation though the value of each parameter is increased by a factor of 2 and 4 (Figure 38a and b). Therefore, these two parameters have less sensitivity to the bed evolution within the salt marsh area. The plant height shows increased effects of NBS as the value increases (Figure 38c). The erosion volume within the salt marsh area in NBS increases up to  $-16 \times 10^3 \text{ m}^3$ ,  $-28 \times 10^3 \text{ m}^3$  and  $-86 \times 10^3 \text{ m}^3$  while sedimentation decreases down to  $7.8 \times 10^3 \text{ m}^3$ ,  $5.5 \times 10^3 \text{ m}^3$  and  $2.3 \times 10^3 \text{ m}^3$  as the plant height increases from 0.25 m, 0.50 m to 1.00 m respectively. The erosion and sedimentation of WT - NBS are  $-75 \times 10^3 \text{ m}^3$  and  $15 \times 10^3 \text{ m}^3$ . Therefore, the relative reduction of volume decreases in erosion and increases in sedimentation. As found earlier, the sedimentation decreases though the erosion increases with increasing plant height, which indicates that the eroded sediment escaped from the salt marsh area. Accordingly, only plant height is sensitive to the bed evolution rather than plant density and diameter.



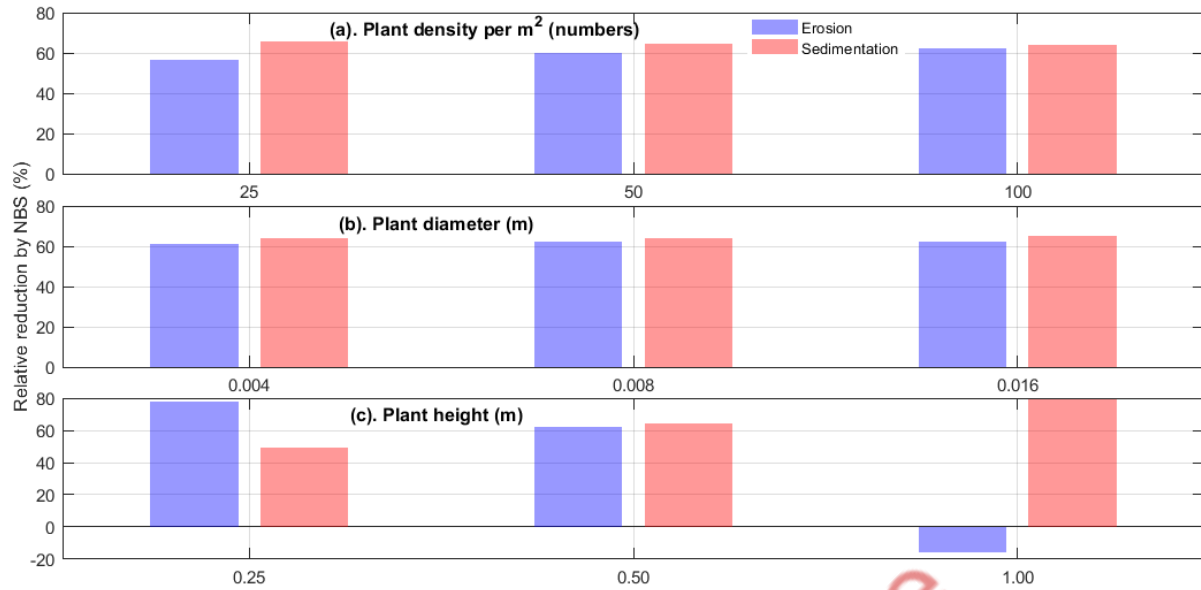


**Figure 3.308.** Relative reduction of volume change in erosion and sedimentation with respect to the WT - NBS application,  $(([WT - NBS] - [NBS]) / [WT - NBS] \times 100\%)$ , for different salt marsh configurations: Plant density per square-meter (a), Plant diameter (b) and Plant height (c)

### 3.4.4 Conclusions

#### 3.4.4.1 High resolution domain needs to investigate salt marsh effects

A high-resolution model setup was developed within this project to investigate the effects of salt marsh on hydrodynamics and bed evolution. Small channel and shoal patterns in Ley Bay can be accurately represented with a high-resolution model grid. However, applying very fine grids (e.g., 0 (10 m)) increases the number of grid cells over the OEMS area (920 km<sup>2</sup>) exploding the computational time. Therefore, we applied a maximum resolution of 30 m x 80 m as this model setup will be used for the long-term morphological simulations. In the initial phase, the sensitivity of the grid resolution was investigated by lowering and increasing the resolution by a factor of 2. This analysis revealed that the increased resolution can represent the channel and shoal configuration as similar as in the measured data. However, the present resolution is sufficient to represent the main channel and shoal structure without missing the main features.

The model domain has a direct connectivity between Wadden Sea and North Sea, in which offshore North Sea boundary is located at about 20 m depth. This facilitates to accurately represent the influence of nearshore processes into Wadden Sea. For example, it is very important to consider the contribution of sediments from the ebb-tidal delta and the adjacent coasts, while simulating extreme events (as in the present study) and long-term morphodynamics (e.g., sea level rise).

#### 3.4.4.2 Salt marsh has an unique vertical structure

The model was simulated in the 2DH mode, and thus the salt marsh configuration needs to be provided as averaged values over the water column: density, diameter and height. The drawbacks of this approach are twofold. First, it is required to estimate the roughness to the bed shear and the salt marsh induced flow resistance separately. Second, there is no change of the plant structure along the water column, and that is

a high schematisation of salt marsh in general, and Ley Bay in particular. Applying different vertical layers (i.e., full 3D model) allows providing vertical variation of the plants and the effect of vegetation on the 3D flow and turbulence (Houwing et al., 2000). However, such an approach demands high computational time, which could not be completed by the time of this report albeit under progress now. In the 2DH approach, the model bed had 6 spatial varying sediment fractions and the forcing from tide and wave together with wind. These however support the increase in the accuracy of the hydromorphodynamic processes in Ley Bay.

Sensitivity analysis of plant parameters indicated, both erosion and sedimentation considerably vary only with the plant height. Furthermore, it was found that erosion increases and sedimentation decreases as the plant height increases. Increasing the density by a factor of 2 and 4 caused decreasing erosion only by 8% and 11%, and increasing sedimentation only by 3% and 5% respectively. Similarly, increasing the plant diameter by a factor of 2 and 4 resulted in decreased erosion only by 2% and 3%, and decreased sedimentation by 0% and 2%. The vegetation – flow interaction approach after Baptist (2005) is well validated and implemented in the model. The tendencies observed here have to be further investigated though. This work is in progress at the time of this report. It is assumed that 3D model runs will further improve the sedimentation. Also, the consideration of the stabilization of the sediment bed by the plant roots could contribute here. This ongoing work will determine whether it is required to improve the model formulation to provide better interactions between plants and flow, and between plants and sediment movements.

#### 3.4.4.3 Selected NBS has a potential application for coastal protection

In this study, application of salt marsh was selected as NBS, and its effects for coastal protection were investigated during extreme events. Two extreme events, Xaver and Herwart, which have different severity levels (i.e., occurrence of TA+Hs has 125 and 2 years return levels respectively) were simulated. Therefore, it can be expected to have different effects with the application of NBS. Furthermore, the salt marsh area in Ley Bay is located above the High-Water line ( $\sim 1.5$  m + MSL), and thus it is hardly submerged during fair weather conditions.

Results indicated that NBS has significant impacts on hydrodynamics, sediment transport and morphological changes. Variation of water levels within the salt marsh area showed that NBS delayed rising and falling of water levels, and the latter is prominent. Therefore, it can be generally expected to have more sedimentation as there is more time for settling of sediments. However, this process depends on the storm severity as well as the locations within the salt marsh area. During the low severity event (Herwart), water levels were completely damped in the middle of the salt marsh area, whereas at the seaward edges, showed a similar rising and falling trend. Wave height, velocity and bed shear stress followed the similar trend for events of different severity and locations within the salt marsh. For example, at the seaward salt marsh edge, both mean velocity and mean bed shear stress during Xaver decreased by about 85% and 100% respectively. Sediment transport within the salt marsh area notably occurred only during the high severity event, and it was mainly dominated by the suspended-load transport. Furthermore, it was found that the sediment transport outside the salt marsh area decreases, particularly along the salt marsh edge. Bed evolution significantly decreased within the salt marsh area, resulting in low volume of sediments from erosion and sedimentation depending on the severity of a storm event. During both storm events, salt marsh area supplied sediment into Ley Bay causing erosion therein, which remarkably decreased in the application of NBS.

These preliminary results clearly indicate that the selected NBS, application of salt marsh, is a potential agent for coastal protection, which enables the resistance against the adverse impacts during storm events. A

previous project of NLWKN, A-KUEST (Niemeyer et al., 2014; Kaiser et al., 2010), revealed that increased sedimentation in the salt marsh areas of the Ems-Dollard estuary improves the adaptation to sea level rise. Furthermore, the higher salt marshes the lower the wave heights during storm surges resulting in the reduction of wave runup and overwash. Ongoing work further investigates this NBS to increase the credibility of the outcome using different modeling techniques (e.g., 2DH vs 3D, improving formulations for stabilization by plant roots) and future scenarios (e.g., sea level rise).

### 3.5 Role of morphological feedbacks on the effectiveness of Nature-based solutions (Deltares)

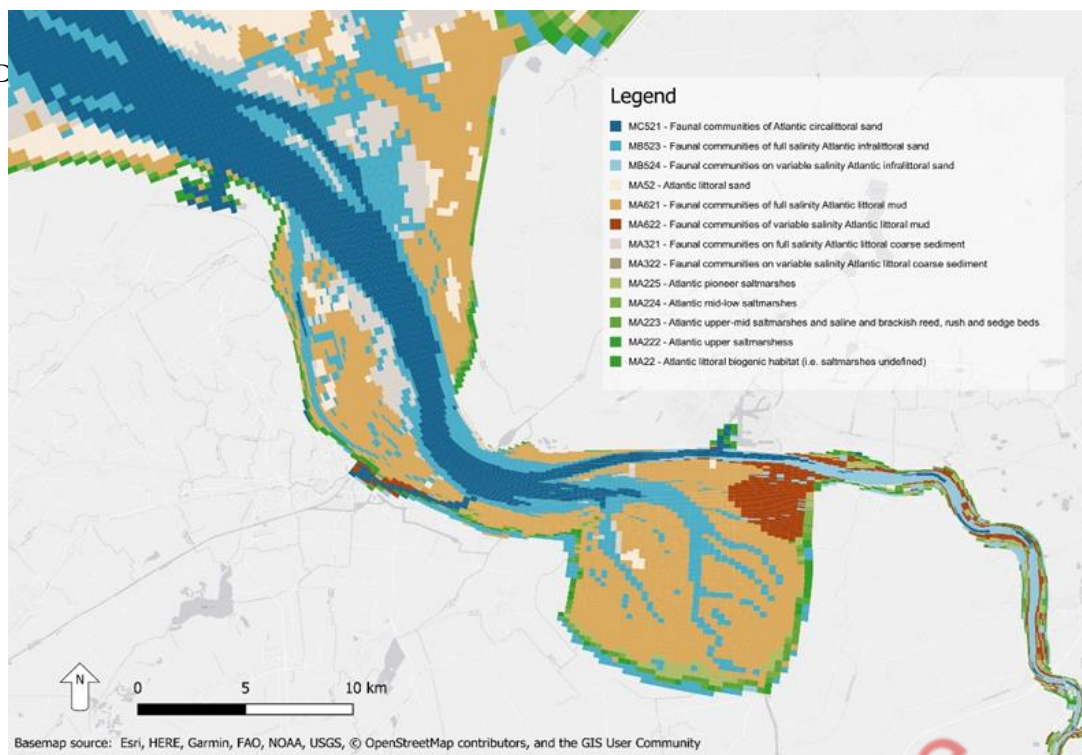
#### 3.5.1 Role of SLR on ecotopes and flood risk, without morphodynamic adaptation

##### 3.5.1.1 Ecotopes

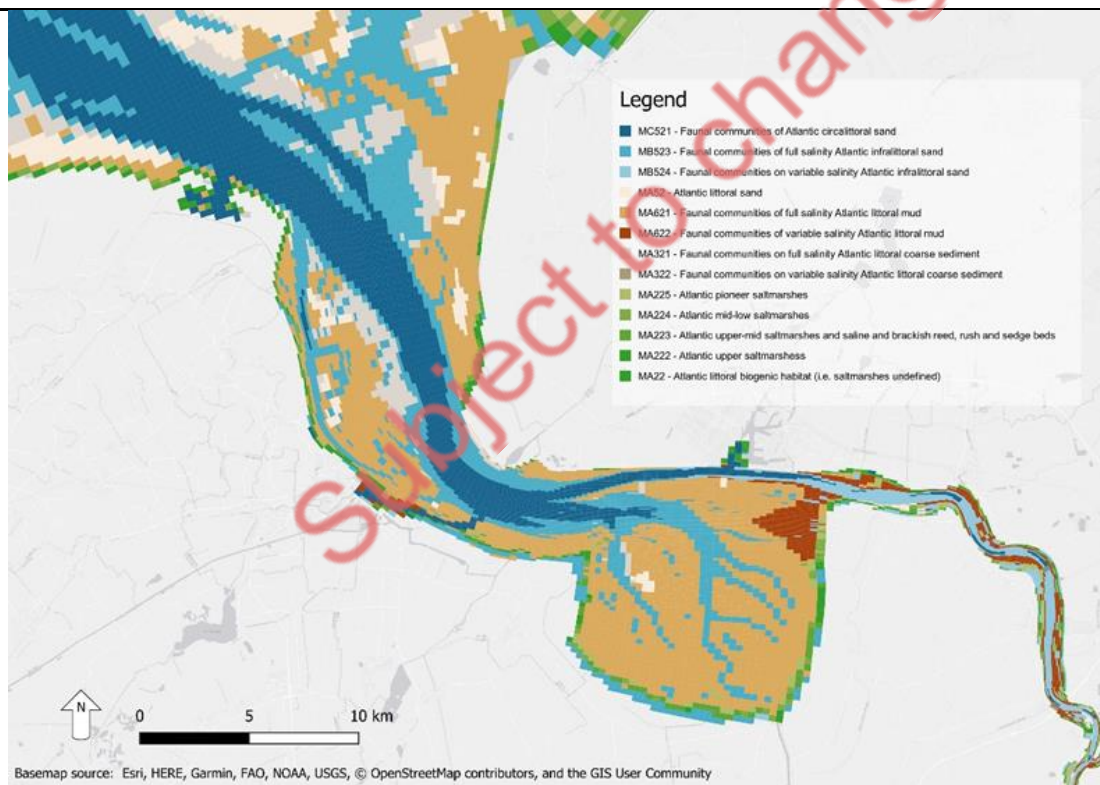
To establish a baseline for the delivery of ecosystem services provided, model simulations for the sea-level rise scenario ssp 585 (median) are simulated in the absence of morphodynamic adaptation. Below are the projected changes in ecotopes.

The most sensitive ecotope to the change in sea-level are the marshes. Already in 2030 there is clear loss of pioneering marsh visible. By 2100 no more marsh is present aside from areas that had been high marsh in 2020. However, it should be noted that around the edges of the model due to the model's resolution the elevation is influenced by the height of flood defences. Therefore, the perseverance of marsh around the model edged may no longer reflect an actual marsh being present.

Another change relevant for the ecotopes is an increasing salinity in the Dollard in response to sea-level rise. Even though this is less obvious from the ecotope classification where only the area classified as "brackish" around the Geisedam appears affected. Nevertheless, the shift in the 18 ppt salinity boundary reflects a general increase in salinity of the Dollard. Not unexpected but still notable is the increase in the infralittoral ecotopes at the expense of littoral sand and mud ecotopes by 2100.



**A) EUNIS map 2030**



**B) EUNIS map 2050**



### C) EUNIS map 2100

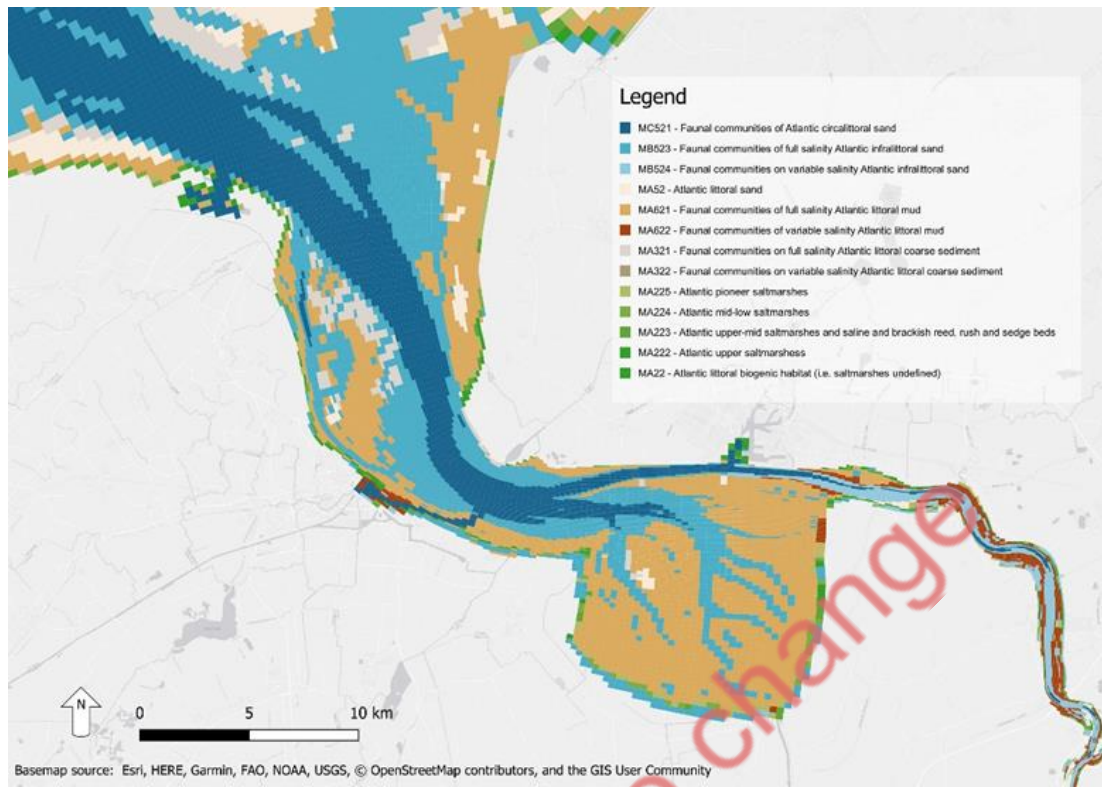


**Figure 3.49.** Projected change in EUNIS ecotopes in the Ems estuary in the absence of morphological change

#### 3.5.1.2 Flood risk

As a proxy for changing flood risk the change in maximum wave height relative to 2020 is plotted for storms Herwart (Fig. 3.49) and Xaver (Fig. 3.50) in the years 2030, 2050, and 2100. The main finding even in the absence of morphological feedbacks is that not all areas are equally affected by sea-level rise. In general, the southern areas of the estuary along the Dutch coast are more sensitive to climate change than the German side of the estuary. The main hotspots of increasing wave height are the stretch east of Delfzijl, and the flood defences along the southern stretch of marshes at the Dollard. Storm Xaver featured slightly higher waves and storm surge than storm Herwart. Sea-level rise and ecotope changes affect wave heights slightly less for storm Xaver compared to Herwart. This is most noticeable for the stretch along the Dollard marshes.

**A) Change in wave height during storm Herwart by 2030**



**B) Change in wave height during storm Herwart by 2050**



C) Change in wave height during storm Herwart by 2100



**Figure 3.50.** Changes in maximum wave height during storm Herwart compared to the same storm event simulated without sea-level rise and changes in ecotopes for the years A) 2030, B) 2050, and C) 2100 in climate scenario ssp 585. The color represents the change as % compared to 2020. The size of each dot represents the associated wave height

A) Change in wave height during storm Xaver by 2030



**B) Change in wave height during storm Xaver by 2050**



**C) Change in wave height during storm Xaver by 2100**



**Figure 3.51.31** Changes in maximum wave height during storm Xaver compared to the same storm event simulated without sea-level rise and changes in ecotopes for the years A) 2030, B) 2050, and C) 2100 in climate scenario ssp 585. The color represents the change as % compared to 2020. The size of each dot represents the associated wave height



### 3.5.2 Scenarios of measures

Several scenarios of measures are being developed to be simulated as part of D2.3, the portfolio of restoration measures. These include:

- Autonomous development / business as usual: no new measures are implemented.
- The plan VLOED: the creation of new intertidal wetland to facilitate sediment extraction.
- Sediment trapping: increase sedimentation in the Dollard with brushwood dams.
- Disposal of dredged material on Paap island: generating new habitat on Hond Paap by disposal of sand on the island

It is important to note that these measures are still being discussed with the stakeholders in RESTCOAST as part of the portfolio for restoration measures in D2.3. The final measures being simulated may therefore be different.

#### 3.5.2.1 Autonomous development

Autonomous development is a reference scenario. It is the expected change in the absence of any measures so the effect of measures can be assessed.

#### 3.5.2.2 Measure VLOED

The measure VLOED comprises three phases after which a total area of approximately 300 hectares will be converted into new tidal wetland. The idea behind the measure is that sediment will accumulate in the area from where it can be extracted for beneficial use in heightening agricultural land and improving flood defenses.

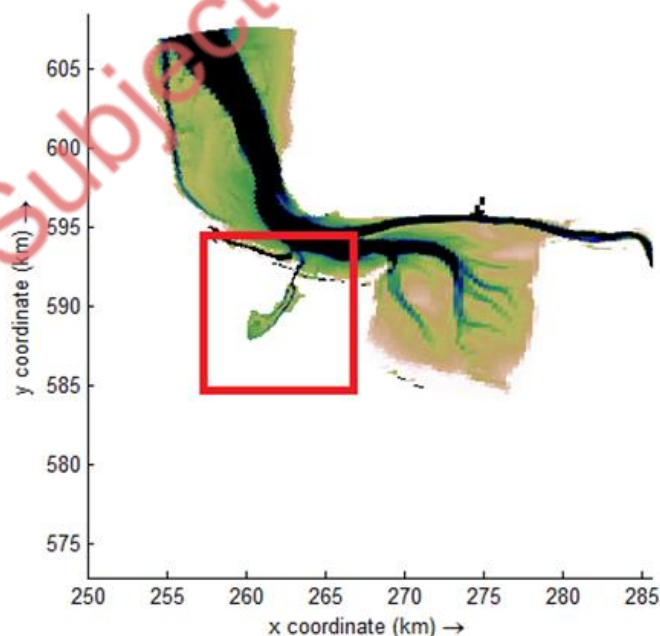


*Figure 3.52. Additional intertidal wetland created for sediment extraction in the measure VLOED*

## Sediment trapping

Brushwood dams have been used for centuries in the Ems estuary and beyond to reclaim land from the sea. This old technique could be used to help facilitate sedimentation again, but with the purpose of enhancing the resilience of wetlands against sea-level rise instead of land reclamation. This part of a pilot currently being considered (Fig. 3.53).

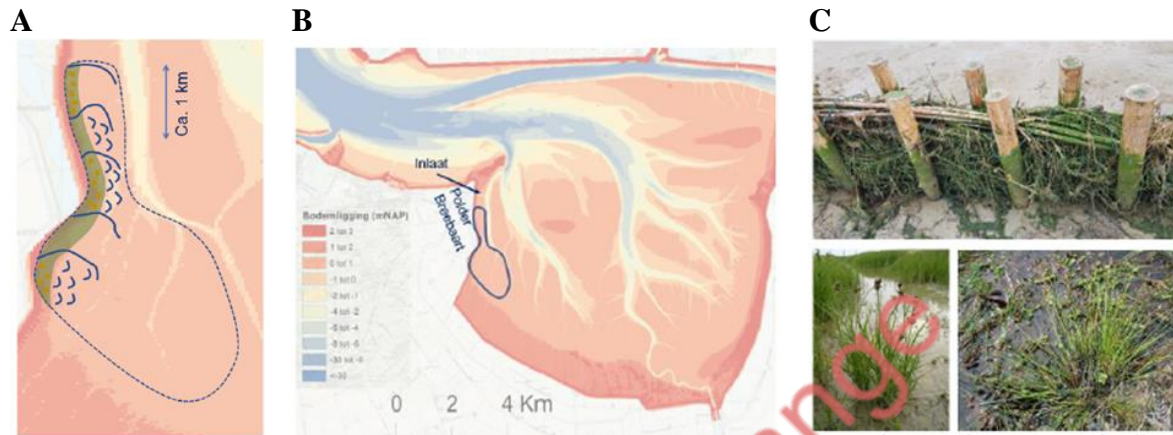


**Figure 3.53.** Pilot for sediment trapping on the intertidal flats as (source: Rijkswaterstaat)

### 3.5.2.3 Disposal of sand on Paap Island

This measure is being discussed with stakeholders. The idea would be to raise part of Hond Paap with dredged sand such that sea grass can remain present on the island. In turn the sea grass may provide ecosystem services in reducing flood risk and coastal erosion.

## 4 Multi-risk projections and climate warnings with ESS in Venice Lagoon Pilot (CMCC, COR)

### 4.1 Introduction

This Deliverable is oriented to the assessment of the role of restoration activity during future hydrodynamics and extreme wave condition at the Venice pilot. The simulations have been carried out using the models and the domain previously described in Deliverable 2.1. Considering that the topic of this study concerns the impact of the restoration activity, we presented the results on a reduced domain (hereafter called as pilot site). The REST-COAST pilot site is located in the central-southern lagoon and includes the restoration of 8 salt marshes (Fig. 4.1). To simplify the further discussion, we roughly ranked the salt marshes in northern (orange box in Fig. 4.1) and southern (blue box in Fig. 4.1). The restoration of these salt marshes follows two phases: i) the creation of a containment barrier (designed and adjusted to the features of the area restored – e.g., containment barrier with fascines, piles or mattresses), and ii) the refilling of the perimeter with dredged materials. These type of restoration activities are being executed as part of the Piano Morfologico, a lagoon wide plan executed by the Provveditorato Interregionale per le Opere Pubbliche per il Veneto, Trentino Alto Adige e Friuli Venezia Giulia (PROVV.) since 1992 to reverse the degradation of the lagoon morphology, and in addition to salt marsh restoration include actions such as the excavation of channels, the creation of tidal flats, re-naturalisation and seagrass transplantation (Tagliapietra et al., 2018).

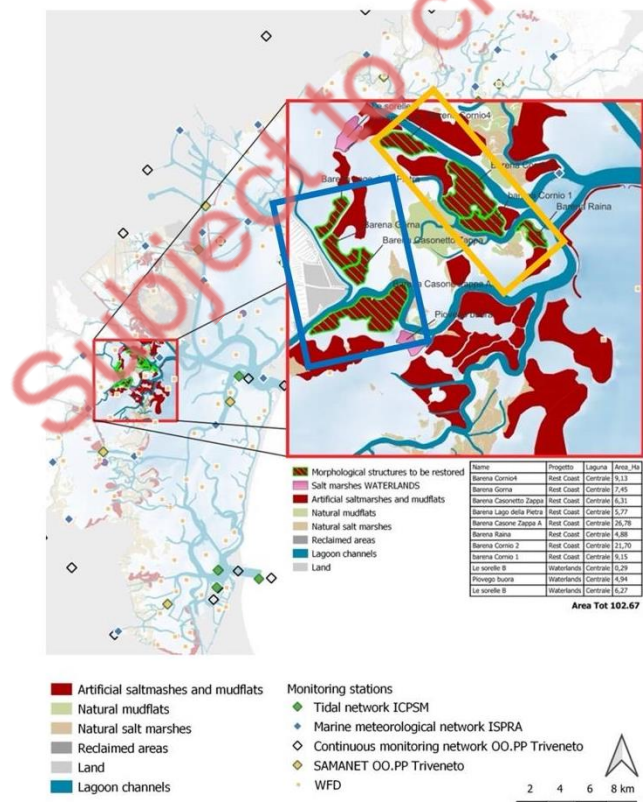


**Fig. 4.1** Location of the REST-COAST pilot site in the Venice Lagoon, highlighting the 8 salt marshes subjected to restoration in green. Blue box highlights the southern salt marshes, while orange box the northern salt marshes.

Climate change is one of the main drivers of extreme flooding in Venice and is projected to increase with rising sea levels in Venice expected by the end of the 21<sup>st</sup> century (Alberti et al., 2023). The Venice Lagoon, and the city of Venice, are affected by Acqua Alta. Three of the most devastating event occurred on 04/11/1966, 29/10/2018, and 12/11/2019, causing significant damage to the city (Faranda et al., 2023). In 2003 the construction of the MOSE (MODulo Sperimentale Elettromeccanico: Experimental Electromechanical Module) started, and responds to the objectives set by the Law of Venice 798/84 to protect the lagoon from high tides (<https://www.mosevenezia.eu/>). The structure consists of 79 elements of mobile barriers at the Lagoon inlets that are raised if tides are expected to surpass 1.10 m – and is functional up to 3 m (Janowski et al., 2020). Since its activation at the end of 2020, barriers' closures have an average closing time of  $\pm 4/5$  h and have been activated more than 50 times (Alberti et al., 2023).

## 4.2 Methodological approach

In this section the methodological approach is described, introducing the datasets, "what-if" scenarios, the scenario selection, and the numerical implementations, detailing not only their individual composition, but also how they are linked together. Additionally, the influences of the MOSE system are described as well as how this relates to this deliverable. Before going through each of the sections, we graphically summarized the workflow in the following diagram (Fig. 4.2). Starting from the Copernicus Climate Change Service (C3S) datasets we defined two groups of simulations, for waves and hydrodynamics respectively. We identified 8 "what-if" scenario for waves and 6 for hydrodynamics. Each scenario has been simulated by 4 different configurations: a reference with closed and open MOSE conditions, and the restoration intervention in closed and open MOSE conditions. We obtained 32 simulations for Significant wave height, 24 simulations for the sea level, and 24 for currents. At the end, the reference and the restoration intervention have been compared to assess the impact of the restoration intervention on the variable investigated.

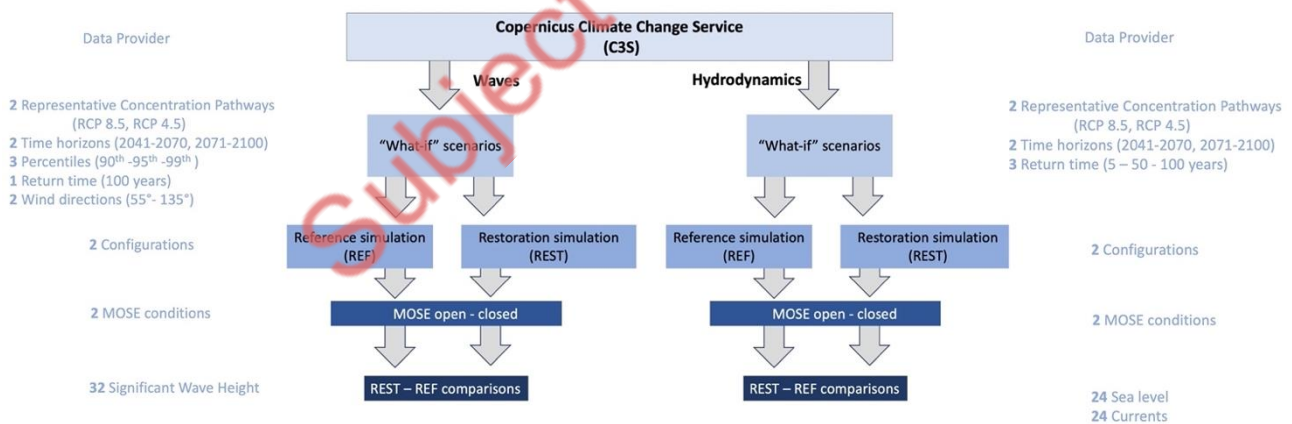


**Fig. 4.2** Schematic representation of the workflow adopted in this deliverable. The diagram summarizes all the simulations, variables, scenarios and configurations

### 4.2.1 "What-If" scenarios

Climate projections come with a range of uncertainties, stemming from various sources. Different emission scenarios lead to diverse climate outcomes, introducing uncertainty in predicting future climate conditions. Also, the future trajectory of greenhouse gas emissions depends on factors such as technological advancements, economic developments, and societal choices which are complicated to be predicted. In



addition to that, some natural processes, such as volcanic eruptions, solar variability, and internal climate oscillations, can influence short-term climate trends. Predicting the timing and magnitude of these events introduces uncertainties into long-term climate projections.

Climate models are complex representations of the Earth's climate system, but despite that, they have some simplifications or assumption which could introduce uncertainties in the solution. Some of the limitations are related to the model resolution, the representation of physical processes, and the inability to fully capture regional-scale variations. Understanding and quantifying these uncertainties are crucial but is out-of-the-scope of this task. To limit the uncertainty of our results, we did not provide numerical simulation for the future, but we provided a range of simulations forced by statistical descriptors of climate projections. This methodology is known as "what-if" scenarios. "What-if" scenarios are hypothetical situations or simulations that explore the potential consequences of certain changes or events in the oceanic system under specific environmental forcings. These scenarios are often used in climate projection studies to understand how various factors may influence the ocean environment. Some common "what-if" scenarios in oceanography include:

- Sea Level Rise Scenarios: Investigating the impact of different rates of sea level rise due to factors like melting ice caps and glaciers.
- Ocean Temperature Changes: Examining how alterations in global temperatures may affect ocean temperature profiles, leading to phenomena like ocean warming or cooling.
- Ocean Acidification Scenarios: Studying the potential consequences of increased carbon dioxide levels in the atmosphere on ocean pH levels and marine ecosystems.
- Changes in Ocean Circulation Patterns: Assessing the effects of alterations in ocean circulation patterns, such as shifts in major currents like the Gulf Stream.
- Extreme Events: Exploring the potential impact of increased frequency or intensity of extreme weather events, such as waves.

"What-if" scenarios are crucial in climate projection for several reasons:

- They help in the assessment of the risks associated with different climate change scenarios, allowing to identify potential vulnerabilities and impacts on both marine ecosystems and human activities.
- Scenario analysis assists policymakers in developing adaptive strategies and policies to mitigate or cope with the potential impacts of climate change on oceans.
- Understanding the consequences of different scenarios helps in sustainable resource management.
- Contribute to a better understanding of the complex interactions within the oceanic system, providing insights into the underlying mechanisms driving climate variability.

#### 4.2.2 Climate change scenarios selection and description

The Copernicus Climate Change service (C3S) is the provider of the forcing data used for setting up the different scenarios. Two datasets were taken into account:

- Water level change indicator: <https://cds.climate.copernicus.eu/cdsapp#!/dataset/sis-water-level-change-indicators?tab=overview>
- Ocean wave indicator: <https://cds.climate.copernicus.eu/cdsapp#!/dataset/sis-ocean-wave-indicators?tab=overview>

These datasets provide information along all the European seas. For the purpose of this study, data closest to the boundaries of our models were extracted and utilized to force the simulations. This deliverable mainly focused on currents and sea-level which has the main impact on the Venice Lagoon, but also significant wave height is included in the study. For hydrodynamics six future scenarios were simulated. The climate

simulations are based on Representative Concentration Pathways (RCPs), a set of four global carbon emissions pathways developed for climate modelling. Of the four RCPs, which radiative forcings span from 2.6 to 8.5 W/m<sup>2</sup>. The selection of the RCP is on related to what the authors of the C3S datasets consider most plausible. Following, their comment: “Due to the large climate variability in sea level, and the fact that extreme sea levels, takes multiple decades before the climate signal can be detected from the natural climate variability, we started our future climate simulations in 2040. At present global carbon emissions are tracking just above the RCP8.5 pathway. As such, regarding the mid-term future (2040-2070) we apply the RCP8.5 pathway. This is a high-emission scenario that assumes high population growth combined with relatively slow income growth with modest rates of technological change. However, countries across the world have committed to limit the global temperature change to 1.5 degree Celsius in the Paris Agreement. This requires very rigorous reductions in the global carbon emissions reductions. It is argued that RCP 2.6 is currently unfeasible, therefore, we apply the RCP 4.5 pathway to the long-term future (2070-2100). RCP4.5 is one of the more optimistic pathways that assumes human emissions of greenhouse gases will stabilize soon and then decline after a few decades”.

To model the distribution of the extreme values, we use the Gumbel distribution over the annual maxima values for each epoch. Each epoch/scenario consist of 29 years of data (2041-2070, 2071-2100), from which the annual maxima value for each station is computed. These 29 values are then fitted to the Gumbel distribution to derive the parameters defining the function, which can in theory be evaluated for any given return period. The starting value for low return periods will be strongly determined by the location's sea level rise and tidal range. While the Gumbel method is simple and widely used, the maximum return period for which the Gumbel function is evaluated here is 100 years. This is on the limits of the extrapolation capabilities of the method for a set of 30 years' sample values, as the uncertainty greatly increases for increasing return periods. Three return periods have been considered in this study, for taking into account common extreme events (5 years), rare extreme events (50 years) and very rare extreme events (100 years). The simulated scenarios for hydrodynamic conditions and related nomenclature are summarized in Table 4.1.

*Table 4.1. Hydrodynamic condition scenarios simulated in this work. Acronym, climate scenarios with related temporal scenario, event return time, and simulation parameters are provided.*

Experiment Name	Climate scenario	Temporal horizon	Return Time	Mean Sea Level [m]	Total water level [m]	Tidal Range [m]
H1	RCP 4.5	2071-2100	5 years	0.34	1.84	1.04
H2	RCP 4.5	2071-2100	50 years	0.34	2.26	1.04
H3	RCP 4.5	2071-2100	100 years	0.34	2.38	1.04
H4	RCP 8.5	2041-2070	5 years	0.25	1.62	1.03
H5	RCP 8.5	2041-2070	50 years	0.25	1.94	1.03
H6	RCP 8.5	2041-2070	100 years	0.25	2.02	1.03

Despite the main stressor for the Venice lagoon is related to circulation and sea level, we included in our set of numerical experiments a set of wave simulation. As already shown in Deliverable 2.1, due to the very shallow lagoon depth (> 1m on average) and the small fetch, wind-waves are not able to develop large height inside the lagoon. In addition, due to the sheltering, swell from the Adriatic Sea is not able to affect the lagoon. The simulation conditions have been defined by investigation of the climatic characteristic for the area, using CMS data for waves<sup>1</sup> and ECMWF-ERA5 (Hersbach et al., 2020) for wind. In Fig. 4.3 the 99<sup>th</sup> percentiles both for wind and waves is shown. The climate assessment distinguished two main conditions for the area:

<sup>1</sup> [https://data.marine.copernicus.eu/product/MEDSEA\\_MULTIYEAR\\_WAV\\_006\\_012/description](https://data.marine.copernicus.eu/product/MEDSEA_MULTIYEAR_WAV_006_012/description)

- The highest waves are SE oriented (while the prevalent waves are NE oriented).
- The highest winds are NE oriented.

These results indicated that the highest waves approaching the Venice lagoon are generated by the long fetch of the Adriatic Sea, but because of the sheltering, they are almost all dissipated at coast without affecting the lagoon. On the contrary, the highest waves inside the lagoon are generated under NE wind conditions, which is the strongest wind for the area. Thus, we included in our set of simulations both the conditions above mentioned.

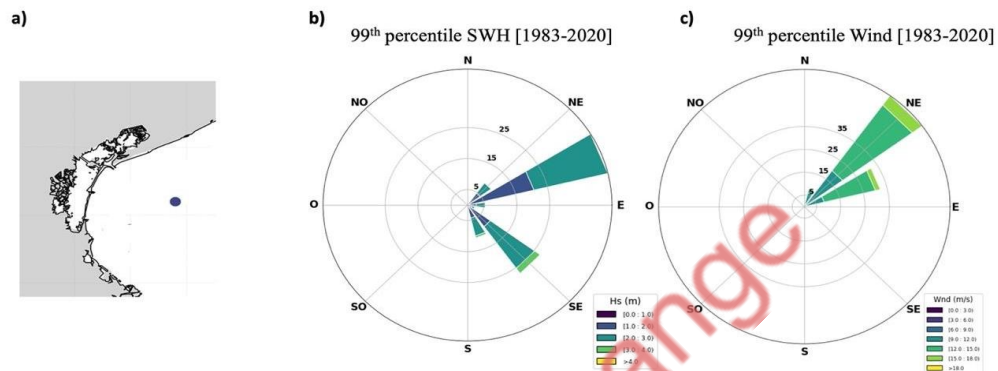


Fig. 4.3 Wave and wind climate for the Venice lagoon pilot. Sub-plot (a) shows the location for the climate analysis, (b) shows the 99th percentile of SWH, (c) shows the 99th percentile for wind.

A first assessment of the wave climate data projections (Fig. 4.4) indicated that significant wave height (hereafter SWH) for the Northern Adriatic Sea will show a slight negative trend ( $\sim -7\text{mm}/10\text{years}$  for the RCP 4.5 scenario). The negative trend is even lower for the RCP 8.5 scenario ( $4\text{mm}/10\text{years}$ ). Considering that both the scenarios showed almost the same future conditions we simulated the “what-if” scenarios under only one RCP scenario. To be conservative, we selected RCP 8.5 because showed the lowest negative trend. Unfortunately, the C3S dataset does not provide for waves the same statistics provided for hydrodynamics (return time 5, 50 and 100 years). The summary of the wave scenarios is provided in Table 4.2.

**Table 4.2.** Wave condition scenario simulated in this work. Acronym, climate scenarios with related temporal scenario, considered statistics and simulation parameters are provided

Experiment Name	Climate scenario	Temporal horizon	Statistics	Wind direction
W1a	RCP 8.5	2041-2100	90 <sup>th</sup> perc.	135°
W2a	RCP 8.5	2041-2100	95 <sup>th</sup> perc.	135°
W3a	RCP 8.5	2041-2100	99 <sup>th</sup> perc.	135°
W4a	RCP 8.5	2041-2100	100 years	135°
W1b	RCP 8.5	2041-2100	90 <sup>th</sup> perc.	55°
W2b	RCP 8.5	2041-2100	95 <sup>th</sup> perc.	55°
W3b	RCP 8.5	2041-2100	99 <sup>th</sup> perc.	55°
W4b	RCP 8.5	2041-2100	100 years	55°

#### 4.2.3 Numerical implementations

Every future scenario has been simulated with four different numerical configurations. The main configuration, which represents the benchmark for this study, is the ESS configuration (hereafter REF or reference configuration) we presented in the D2.1. The reference configuration set-up included both seagrass and salt marshes, which remained consistent across time evolution and scenarios. The second configuration (hereafter REST configuration) includes the future restoration activity planned in the Venice Lagoon and which will be carried out in the coming years, starting with the salt marsh restoration in the pilot site in 2023. This configuration is based on the Piano Morfologico<sup>2</sup>, focusing particularly on the restoration of morphological structures including the 8 salt marshes in the central-southern lagoon that are included in the REST-COAST project. The works are based on historical analyses of the morphological changes in the past century, on hydraulic optimisation studies and reuse the dredged sediments from the channel excavation (Tagliapietra et al., 2018). Fig. 4.5 shows the REF and REST configurations, with a magnification view at the pilot site to highlight the distinctions between the two configurations.

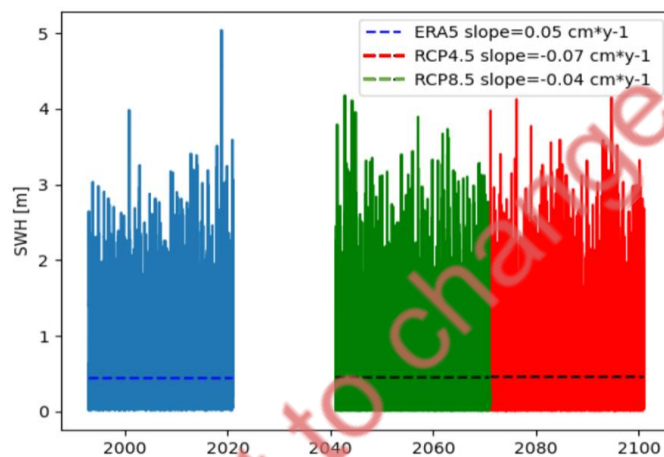


Fig. 4.4 Significant wave height and related trends for past (1990-2020), RCP8.5 (2041-2070) and RCP4.5 (2071-2100) scenarios

The REST implementation allowed to study the effect of the restoration intervention on circulation and waves. The last two configurations included the MOSE infrastructure in both REF and REST. A summary of the numerical set-ups and related acronyms is presented in Table 4.3. The motivation for employing four configurations was to juxtapose the outcomes of REF and REST experiments, involving the computation of result differences. This approach provided an indirect means to evaluate the influence of the restoration intervention on hydrodynamics and waves within the pilot area. Furthermore, we investigated whether the closure of MOSE could yield different impacts on the pilot area in the REF and REST configurations.

Table 4.3 Summary of the four configurations used in the numerical simulations, with experiment name and related description.

Configuration	MOSE	Short description
REF	open	Benchmark configuration for both hydrodynamics and waves. Seagrass and salt marshes are included in the simulation. Further details about the configuration are described in deliverable D2.1
REST	open	As REF configuration with exception of the inclusion of the restoration intervention.
REF_MOSE	closed	As REF configuration, in which we simulated the MOSE barriers closure

<sup>2</sup> <http://provveditoratovenezia.mit.gov.it/introduzione.html>

REST_MOSE	closed	As REST configuration, in which we simulated the MOSE barriers closure
-----------	--------	--

The last part of the study aims to understand if the effect of the restoration activity on hydrodynamics is affected by the MOSE barriers closure. For this reason, we compared the configurations REST and REF both with closed MOSE barriers. This would correspond with the current conditions, as the MOSE can be activated when a surge is predicted to be at least +110 cm. The comparison further of open/closed MOSE barriers, despite being an interesting topic, goes beyond the objective of this work, and will not be investigated in depth here. In Fig. 4.6 we presented a comparison between one example scenario (H3 in this case) with open (a) and closed (b) barriers, at lagoon scale, to provide an insight on the barriers effect on the sea level during an extreme storm surge.

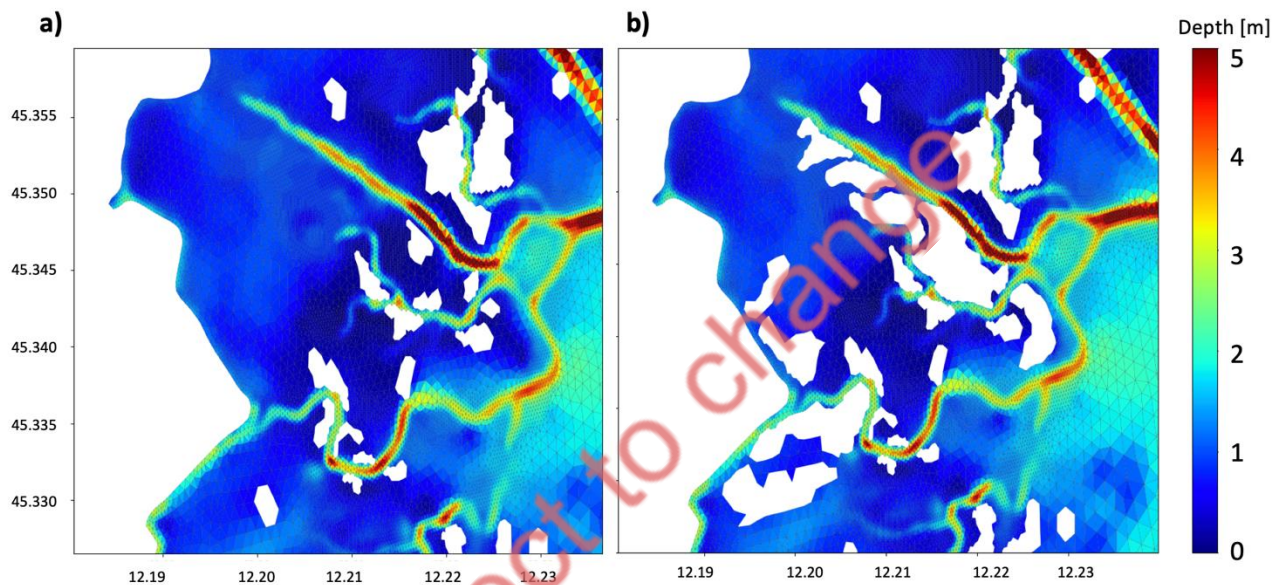


*Fig. 4.5 Magnification of the numerical grids and bathymetry on the pilot site. a) shows the REF configuration, b) shows the REST configuration*

## 4.3 Results

### 4.3.1 Circulation

The results of the investigation of the currents are summarized comparing the simulations in two different locations (Fig. 4.7 Location of the comparison between numerical configurations: the black dot indicates the pilot area, and the red dot shows the location of the Adriatic Sea.). The selection of the points aimed to have results from:

- the pilot area, which is the main topic of the project,
- the Adriatic Sea, as control of the forcing, and where the impact of the restoration should not be effective.



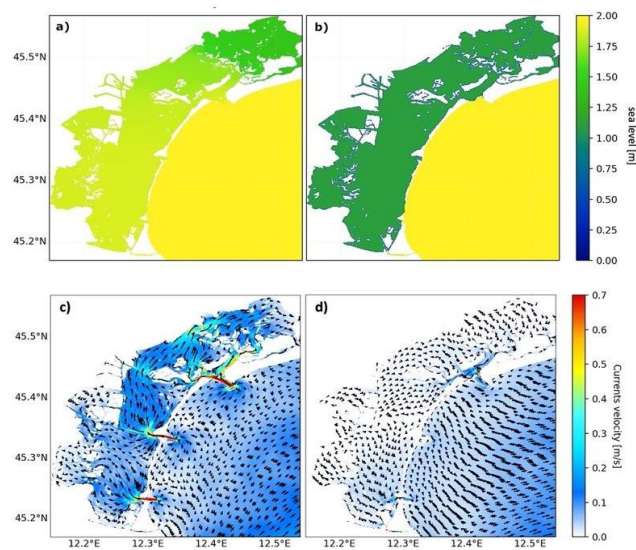
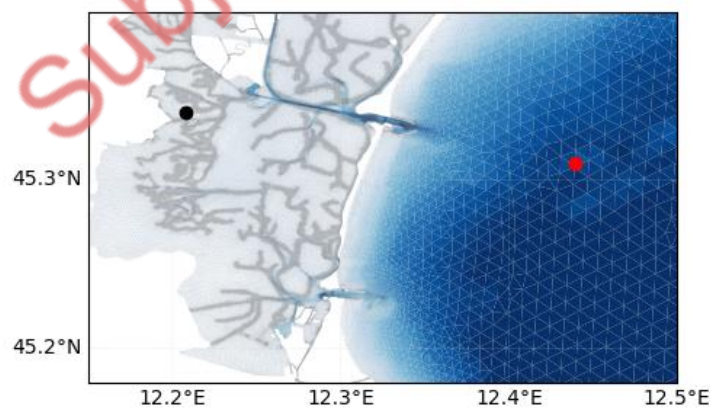


Fig. 4.6 Comparison of extreme sea level with open (a) and closed MOSE (b) and corresponding current (c,d)

In Fig. 4.8a, we show the sea level at the Northern Adriatic Sea for the six simulations, representing different storm surges approaching the Venice lagoon, while in Fig. 4.8c the water currents at the same location. These timeseries are from the REF simulation, which represent the benchmark for the study. Comparing the a-sub plot with the corresponding timeseries at pilot site (b), it is evident a time lag in the occurrence of the extreme events around 3-4 hours, and a reduction in sea level elevation of ~15cm maximum. However, the reduction in elevation at the pilot site compared with the Adriatic Sea is more evident for higher sea-levels (H1, H6). The evaluation of water currents at the two locations (c-d) reveal more differences, mainly related to the fact that the open sea has higher velocity during the ebb phase of the events, while the pilot area reveals the currents peak during the flooding.



Location	Longitude	Latitude
Adriatic Sea	12.43941	45.30998
Pilot area	12.20781	45.34029

Fig. 4.7 Location of the comparison between numerical configurations: the black dot indicates the pilot area, and the red dot shows the location of the Adriatic Sea.

The comparison of the results from the REST and REF configurations allowed to describe the effect of the restoration intervention. As expected, when the comparison is carried out at open sea, no difference is evident, thus we do not show the plot in this document. On the contrary, small difference, around  $\pm 4$  mm maximum, are shown by the sea level comparison (e), and currents mainly increased in the REST configuration (f), up to +3 cm/s. In detail, the differences in sea level is around  $\pm 1.8$  mm during the normal tidal cycle (before and after the extreme event occurs - up to hour 60 and after hour 84 in the timeseries), and here all the scenarios have almost the same difference between REST and REF configurations. After hour 60 the extreme event approaches to the lagoon and the difference REST-REF is sensitive to the magnitude of the event. Higher scenarios showed a higher increase of sea level (exceeding +4 mm in H3), but even a more rapid and intense decrease in water level: during the ebb phase H4 reaches  $\sim -3.5$  at hour 86, while H3 reaches  $\sim -3.5$  mm at hour 80 and  $\sim -5$  mm at hour 86.

The overall results showed how the restoration activity conducted at the pilot area has negligible significant effect on local sea level. The difference between the REST and REF configuration is of the order of few millimetres for all the simulated scenarios, and thus not appreciable in the timeseries. Despite that, we want to show this difference as map (Fig. 4.9) **Error! No se encuentra el origen de la referencia.** to better highlight that the restoration intervention, because of the presence of salt marshes which reduced the section for the water flow, has a lag time with respect to the upstream area. Consequently, this leads to a phase shift of the sea level oscillation and the intensification of currents between the restored salt marshes.

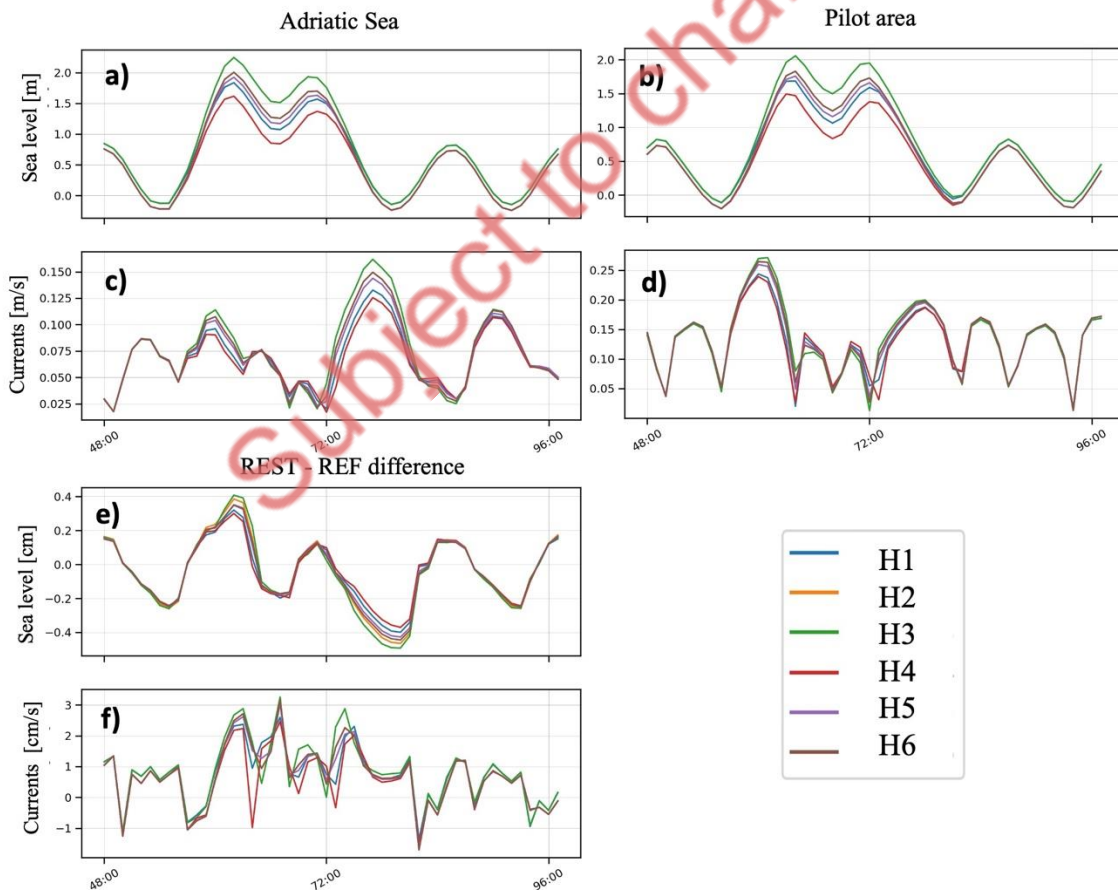


*Fig. 4.8 Timeseries of water level (a-b) and currents (c-d) at Adriatic Sea (a-c) and the pilot site (b-d) for the six scenarios. The difference between REST and REF configurations is shown in sub-plots (e) for sea level and (f) for currents.*

In Fig. 4.10 we show the map for the lowest (a) and the highest (b) currents difference between REST and REF configurations. In the figure we show only one of the simulations because all of those revealed very similar pattern and intensity. The lowest difference in currents occurs in the slack phase, and from the map we observed a general reduction of circulation around the restored salt marshes, around  $-3/-5 \text{ cm s}^{-1}$ . The highest difference is evident in the flooding phase, where some areas of reduced currents are evident about  $-5/-10 \text{ cm s}^{-1}$ , reaching the highest currents reduction downstream the easternmost restored salt marshes, around  $-30 \text{ cm s}^{-1}$ . On the contrary, all the funnelling made up by the intervention increased the water velocity along these new channels of around  $10/15 \text{ cm s}^{-1}$ , with exception of the northernmost restored salt marshes where the currents increase up to  $30 \text{ cm s}^{-1}$ .

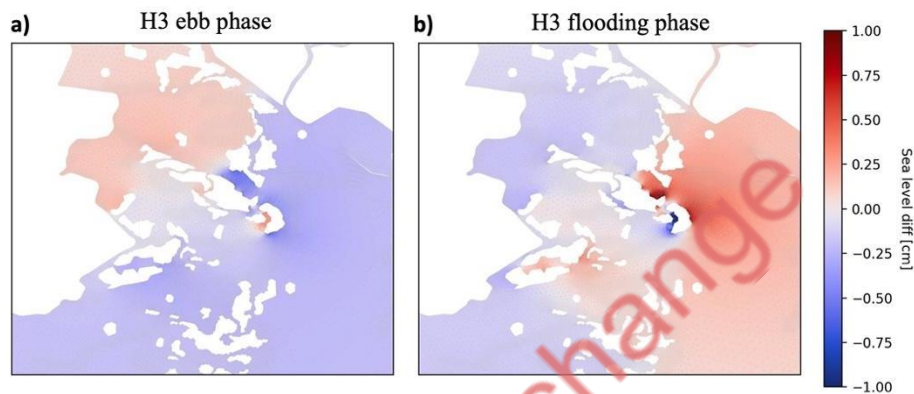


*Fig. 4.9 Sea level difference computed as REST - REF simulations for H3 during the ebb phase (a) and the flooding phase (b).*

Despite the primary focus of the study concerns the pilot site and the impact of the restoration activity, we recognize the broader importance of addressing the flooding risk for the entire Venice lagoon. To support this understanding, additional information about the land surface flooded during various storm surges for future scenarios in the entire lagoon is provided. For each of the six simulated scenarios, we calculated the maximum floodable area, which signifies the theoretical maximum surface that could be flooded during an event. We choose to reference this parameter with respect to the real simulated inundation for two reasons: i) the flooding is function of time. In our scenarios we set up the time of the extreme event growing phase to 6 hours, keeping the maximum value of the surge signal constant for 6 hours (with subsequent addition of the tidal component), and allowing for an 8-hour receding phase, and the receding phase of 8 hours. Naturally, the extreme events could have shorter surge peak and in-phase/ not in-phase tides-surge which significantly affects the flooded area; and ii) the flooding is function of land usage and coverage. These land characteristics are influenced by both human activities and natural processes (sometimes extreme conditions), making predictions challenging. The area potentially submerged by the most frequent extreme event we simulated for the time-period 2041-2070 ranges between 210 and 271  $\text{Km}^2$ , while for the time-period 2071-2100 the area is sensibly larger, ranging from 262 and 371  $\text{Km}^2$ . The maximum flooded area at lagoon scale, for every scenario, see Table 4.4.

*Table 4.4 Maximum floodable areas for the six hydrodynamic “what-if” scenarios. The investigation is performed for the entire lagoon area.*

Experiment Name	Maximum floodable area ( $\text{Km}^2$ )
H1	262
H2	365
H3	371
H4	210

H5	262
H6	271

4.3.2 Waves

Results from wave simulations (Fig. 11) indicated how the restoration intervention significantly increased the local dynamics at the pilot area. For both the simulated directions, S-E (subplots **a**, **c**) and N-E (subplots **b**, **d**), within the numerical experiments of the same group (Wa and Wb), the difference in SWH showed the same distribution pattern, but with different intensity. It is noteworthy that under lower wave conditions (W1 and W2), REF simulations generally resulted in higher waves compared to REST simulations, with exception of the area located within the southern and northern groups of restored salt marshes. However, as the wave height increased (in W3 and W4 scenarios), the positive difference between the two simulations diminished, and the negative one intensified. For this reason, we showed in Fig. 4.11 **¡Error! No se encuentra el origen de la referencia.**only the lowest (W1a and W1b) and the highest (W4a and W4b) conditions.

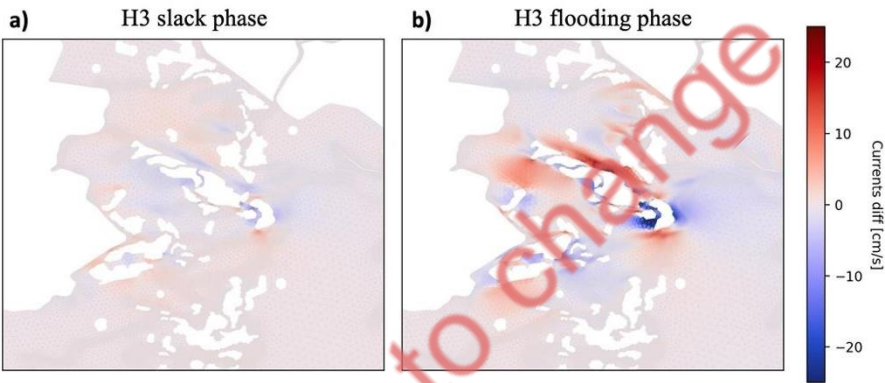


*Fig. 4.10 Currents difference for REST and REF configuration in the H3 simulation both on the slack phase (a) and the flooding phase (b).*

In detail, concerning the distribution patterns (Fig. 4.12**¡Error! No se encuentra el origen de la referencia.**) of the REST – REF difference we observed in Wa scenarios an increased SWH along the deep canals surrounding the salt marshes (~+40%), and in the northern part of the restored salt marshes (~+20%). On the contrary, it is highlighted a slight reduction (~-10%) of SWH in the area located between the two groups of restored salt marshes. As anticipated, the area of SWH reduction is more evident for higher wave scenarios (~-20%), while the northern part of the restored salt marshes revealed only ~+10% in the higher scenarios. In the Wb scenarios, the increase of SWH in REF simulations along the deep canals of the pilot area is still evident, but at a lower extent compared to Wa scenarios. In lower waves conditions the central area between northern and southern groups of restored salt marshes showed ~+15% of SWH in REF. On the contrary, when higher scenarios are considered, the difference reduced and becoming negative in some cases. In all the Wb scenarios, the southern group of restored salt marshes indicated a reduction of SWH (~ -10-20%). It is worth to notice that the magnitude of the SWH for REF configuration (Fig. 4.12) is very low in the area (~ <40 cm), and just on few canals traits SWH exceed 60 cm.



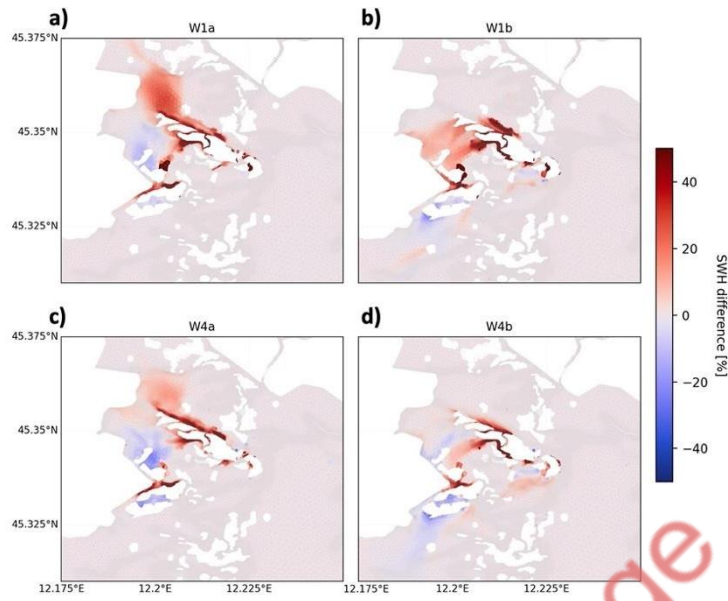


*Fig. 4.11 Significant wave height difference (expressed in percentage) computed as  $REST - REF$  configurations for the scenarios a) W1a, b) W1b, c) W4a and d) W4b.*

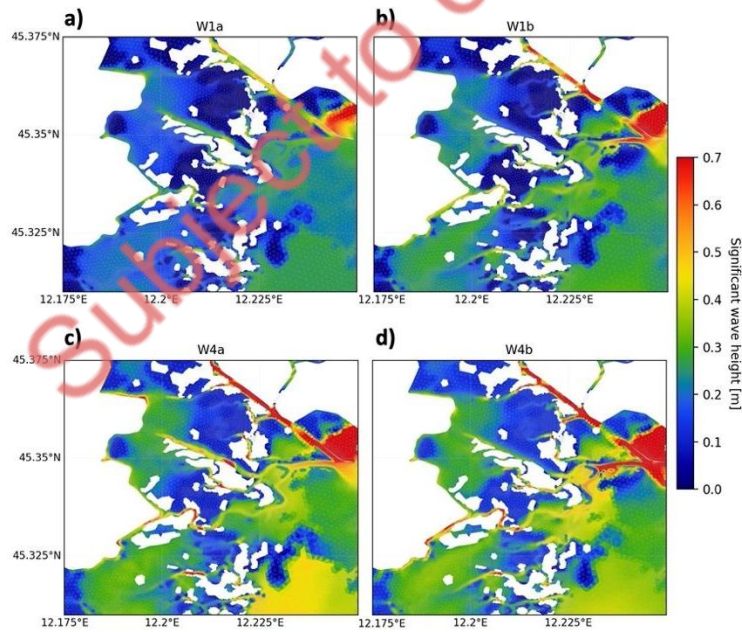


*Fig. 4.12 Significant wave height for the REF configuration and for the scenarios a) W1a, b) W1b, c) W4a, and d) W4b*



### 4.3.3 MOSE barriers closure

The closure of the barriers is endeavoured to limit the flooding of the low-lying lands around the lagoon, protecting the Venice city. The MOSE closure determines the sea level height inside the lagoon, which remains almost constant during the storms. The limitation of the water exchange between lagoon and North Adriatic Sea defines a net reduction of the lagoon circulation (Fig. 4.6*Error! No se encuentra el origen de la referencia.*d). Our results revealed that the presence of the restoration intervention has negligible effect on sea level when the barriers are closed, as shown in (Fig. 4.13).

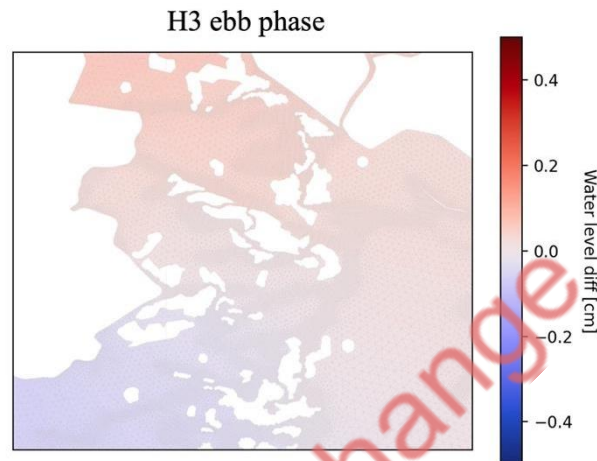


*Fig. 4.13 Water level difference between REST and REF configurations when MOSE barriers are closed.*

Concerning the investigation on the wave field, the difference between the REST and REF configuration with closed MOSE mirrors precisely the difference observed in Fig. 4.11, where the MOSE barriers were open. This parallel pattern arises due to the lagoon's confinement, preventing the influence of Adriatic Sea swell on the lagoon's wave dynamics. Consequently, the waves in the lagoon are predominantly driven by wind forces and locally developed. This study revealed that the largest REST- REF difference occurs on currents (Fig. 4.14*Error! No se encuentra el origen de la referencia.*), despite this is approximately one order of magnitude lower than the open MOSE condition. During slack phase (Fig. 4.14a), currents exhibits no differences around the southern group of salt marshes while in the northern group is highlighted a reduction of circulation around the westernmost part, and an increase along their northern side. During the flooding phase (Fig. 4.14b) there is a generalized increase of currents ( $\sim 1 \text{ cm s}^{-1}$ ) at the pilot site, with the exception of the area between the two southernmost salt marshes, where currents show a reduced intensity.

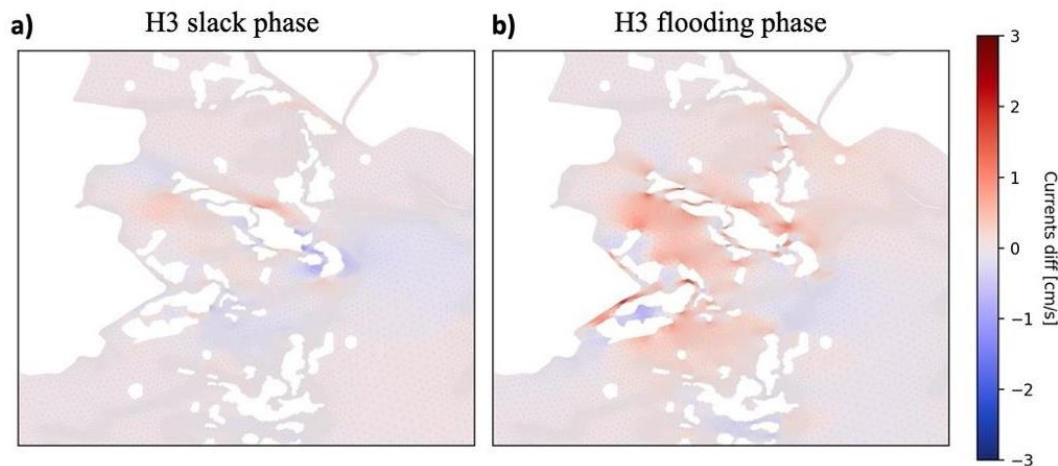


*Fig. 4.14 Currents difference for REST and REF configuration and closed MOSE barriers in the H3 simulation both on the slack phase (a) and the flooding phase (b).*

#### 4.4 Conclusions

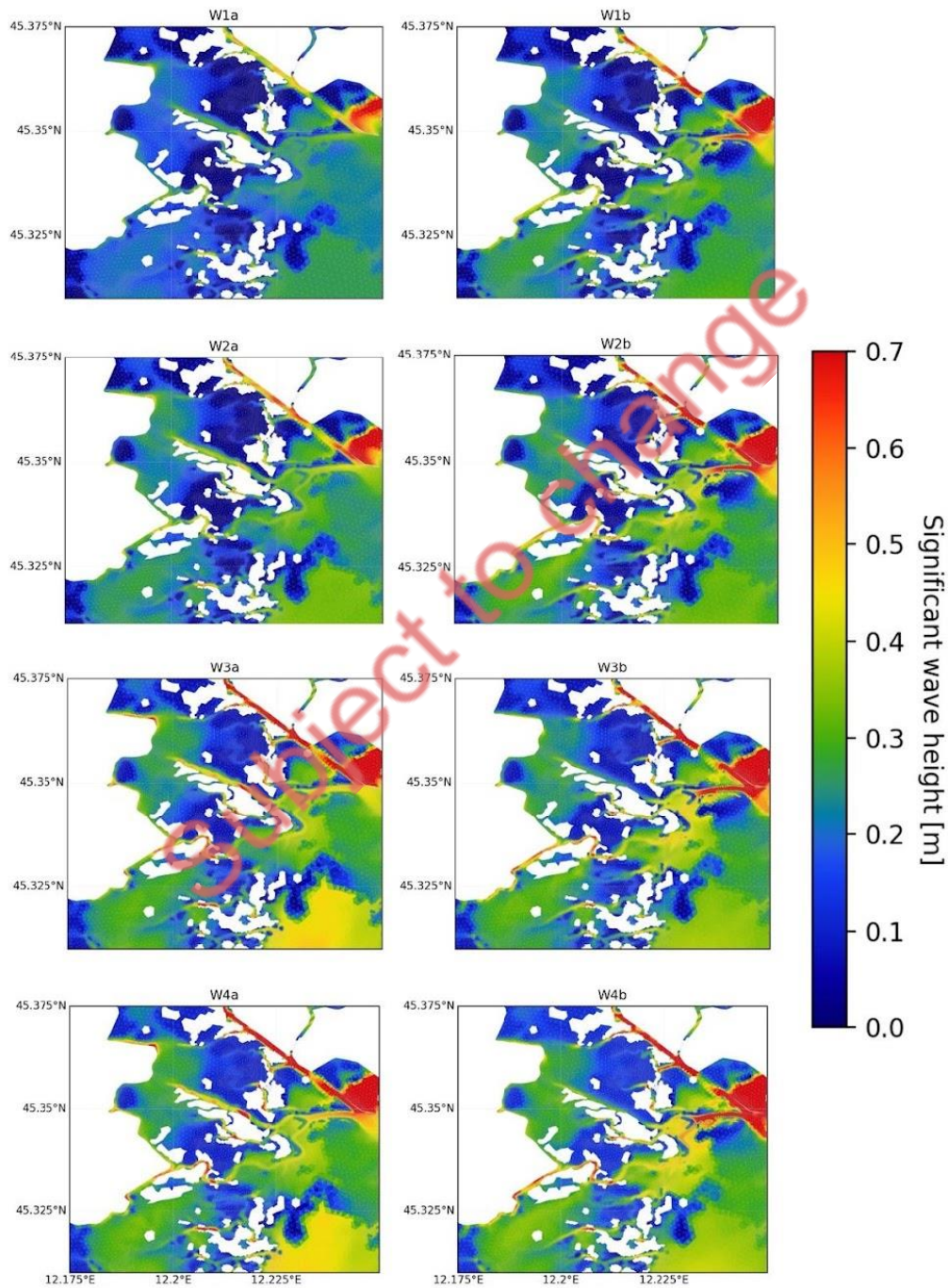
This study represents a comprehensive assessment of the effect of restoration intervention on both hydrodynamics and wave conditions, for various storm surges approaching the Venice pilot site during the 2041-2070 and 2071-2100 scenarios. Despite the primary focus of the study concerns the pilot site and the impact of the restoration activity, we recognize the broader importance of addressing the flooding risk for the entire Venice lagoon. The analysis of maximum floodable areas underscores the varying scenarios, with a range of approximately 60 Km<sup>2</sup> observed for the period 2041-2070 and an expanded area of about 110 Km<sup>2</sup> for the 2071-2100 scenarios. The restoration intervention manifests its influence on hydrodynamics through changes in currents, particularly during the flooding phase. Sea level experiences a slight adjustment, typically within the range of  $\pm 1$ cm, primarily attributed to the constrained water flow caused by the presence of salt marshes.

Concerning the wave climate, the investigation of the projections suggests minimal alterations in wave conditions towards the end of the century. When examining the inclusion of restoration intervention, higher waves are more effectively attenuated by the restoration intervention. The placement of salt marshes emerges as a critical factor, with those close to deeper channels inducing significant increases in significant wave height (SWH) and currents. Notably, the western part of the northern group of salt marshes and the area between the two southernmost salt marshes present the lowest currents in the REST configuration. In addition, the southern group is identified as affected by wave reduction.

When the MOSE barriers are closed the lagoon undergoes to a remarkable reduction in currents by one order of magnitude. However, during the MOSE closure, the restoration intervention induces a general low ( $\sim 1$  cm s<sup>-1</sup>) increase in currents at the pilot site, with a few small exceptions. This observation holds significance as it mitigates the anticipated reduction in currents induced by the barrier closure. The northern side of the northern salt marshes group stands out as the most exposed area, experiencing an increase in significant wave height and currents velocity, whether MOSE is open or closed. This underscores the importance of meticulous positioning of salt marshes during restoration activities, especially considering their proximity to deep canals or channels, as it could lead to a significant increase in SWH and currents. Such insights are pivotal in refining restoration strategies for the Venice lagoon, ensuring a balanced and effective approach to hydrodynamic management.

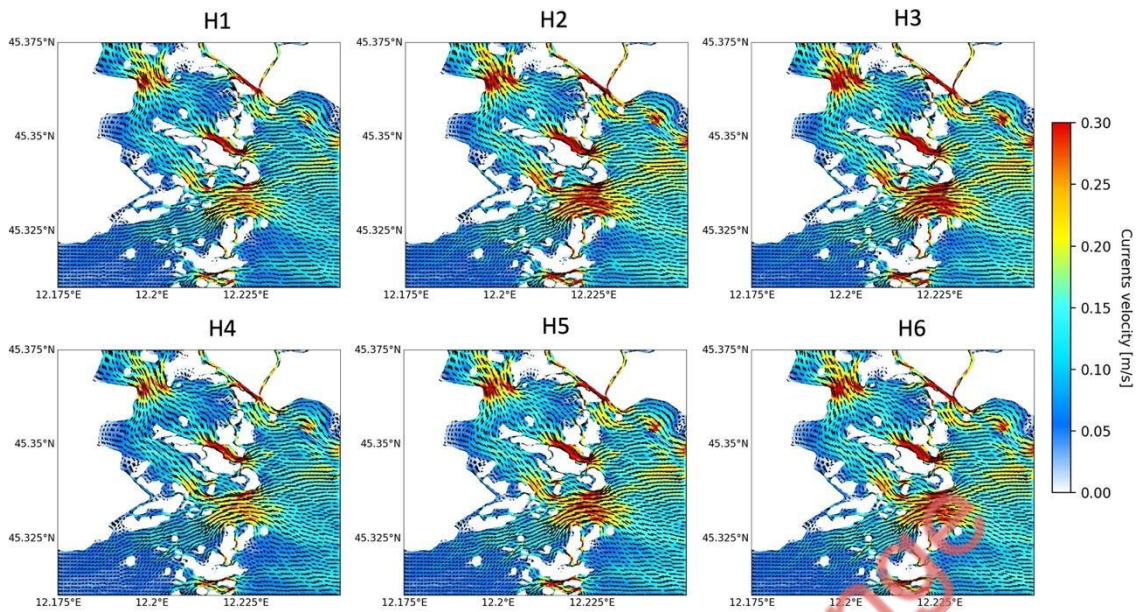
## 4.5 Annexes

In the appendix are attached plots showing significant wave height, water level and currents from various simulations conducted in this study. For both wave height and water level the plots illustrate the REST configuration at the peak of each event. Currents plots refer to a different time step, specifically when the currents reach their maximum intensity. Additionally, for currents, also the REF configuration is shown. Last annex shows the maximum flooded area for every scenario at lagoon scale.

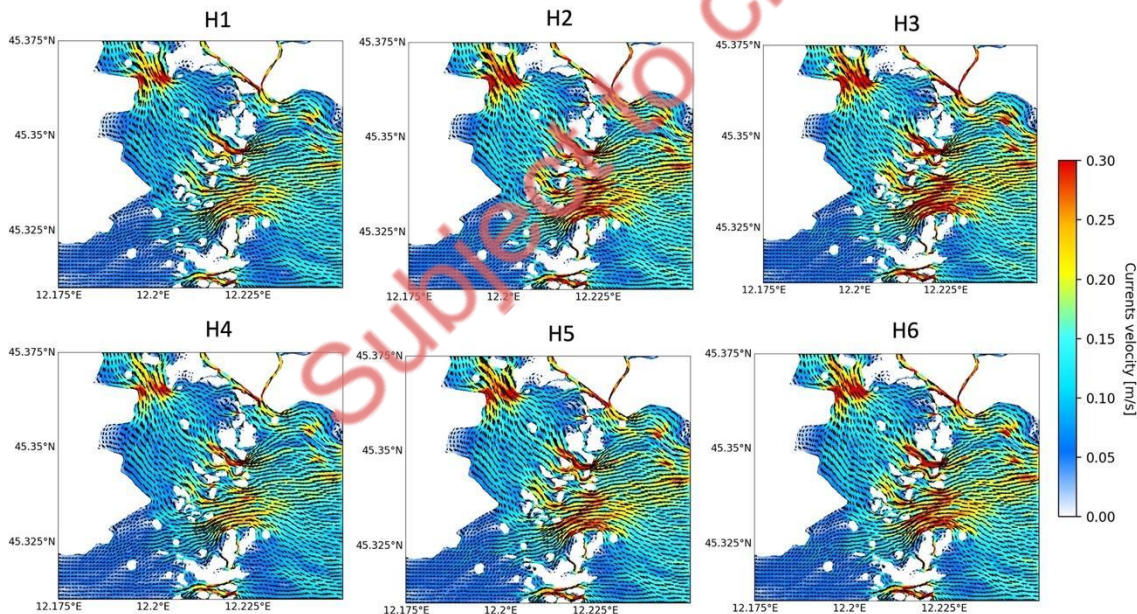


*Annex 1 What-if scenarios of significant wave height at the pilot site*



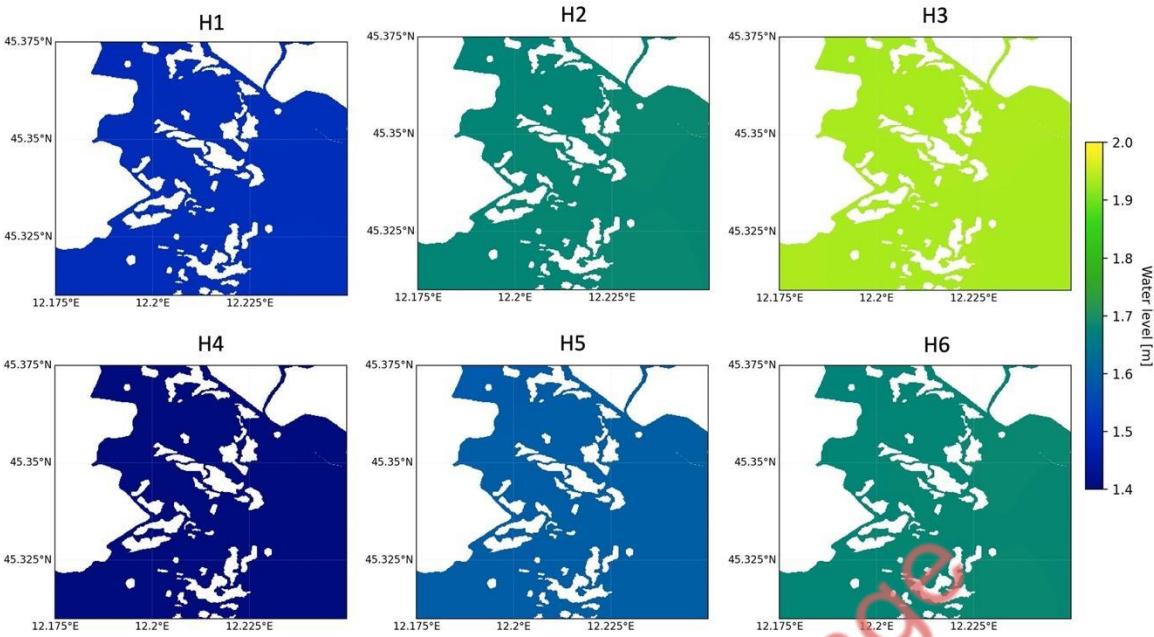


Annex 2 Currents for REST configuration

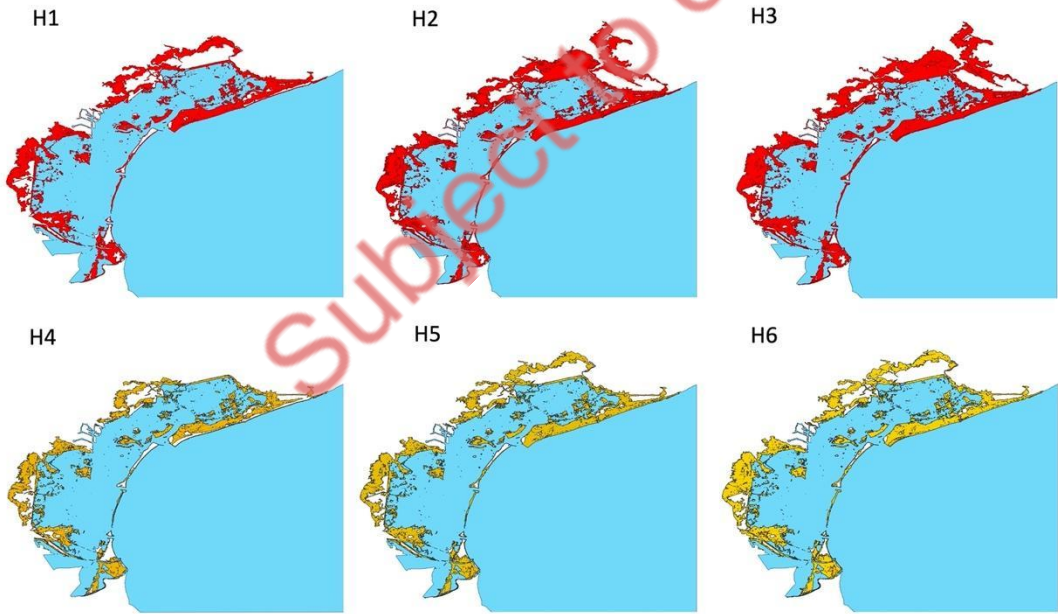


Annex 3 Currents for REF configuration





*Annex 4 Water level for REST configuration*



*Annex 5 Maximum flooded area at lagoon scale for every of the six scenarios*

## 5 Multi-risk projections and climate warnings with ESS in Arcachon Bay Pilot (EGIS, INR)

### 5.1 Introduction

#### 5.1.1 Context

In the Arcachon Bay, seagrass is experiencing a chronic decline observed since the beginning of the 21st century (Auby et al. 2011). Consequently, the research in WP2 focuses on examining the impact of seagrass restoration on sediment dynamics and subsequent changes in coastal morphology through numerical modeling. This investigation aims to evaluate the potential reduction in coastal erosion risk and the corresponding socioeconomic benefits, such as decreased dredging requirements and improved navigability for fishing and tourism activities.

#### 5.1.2 Objectives

To assess the risk reduction linked to various seagrass restoration approaches (to be executed in Task 2.3), the effects of seagrass on bio-physical and socio-economic factors in the Arcachon Bay are initially analyzed for the present baseline scenario and across different climatic projections (Task 2.2). Specifically, this study endeavors to characterize the socio-economic consequences related to enduring morphological shifts under diverse climatic circumstances, achieved through a combined eco-morphodynamic modeling methodology.

#### 5.1.3 Methodology

Initially, a comprehensive socio-economic analysis is conducted for the Arcachon Bay, wherein the primary economic activities are identified and characterized. Specifically, this analysis delineates their interrelationships with each other and with the natural ecosystem.

Subsequently, the impacts are assessed utilizing the eco-morphodynamic model established in Task 2.1. This facilitates the identification of climatic signals and critical thresholds (tipping points) concerning key coastal parameters. To elaborate, the integrated eco-morpho model of the Arcachon Bay (developed in Task 2.1) is employed to project long-term variations in physical metrics, including erosion/deposition rates and sediment volume near harbor entrances. Moreover, various climatic scenarios are considered, and these physical metrics are quantified across multiple plausible future scenarios.

Finally, the interplay between each economic activity and the model-derived physical metrics is examined to gauge the sensitivity of different ecosystem service sectors to climate impacts.

### 5.2 Socio-economic analysis

#### 5.2.1 General situation

The Arcachon Bay lies along the southwest coast of France, situated within the Nouvelle-Aquitaine region, covering an expanse of 150 km<sup>2</sup>. Positioned at the southwestern extremity, it opens to the sea between Cap Ferret and Arcachon. Upon analyzing the land cover across the Arcachon Bay territory (as illustrated in the subsequent figure 1), it becomes evident that within the initial 200 meters from the coastline (excluding

wetlands), artificial zones constitute approximately 75%, while forests and semi-natural areas account for roughly 20%, and agricultural lands occupy around 5%.

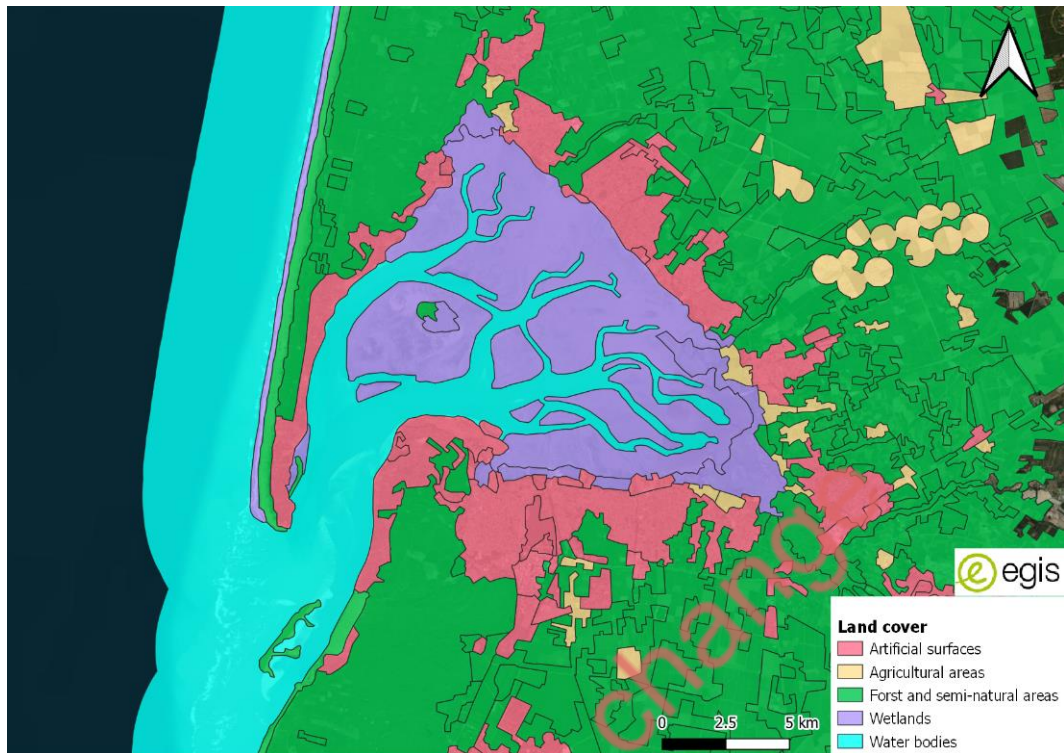


Figure 5.1. Land cover around the Bay (Corine Land Cover)

## 5.2.2 Port activities

### 5.2.2.1 Professional and non-professional fishery

The professional and non-professional fishing activities can be delineated and quantified as follows:

- As of 2014, the Bay accommodated approximately 400 professional fishermen (IUCN France, 2014).
- The harbor of Arcachon hosts over 110 fishing vessels and annually trades 2600 tons of fish (geoimage.cnes.fr). Extrapolating from the revenue rate of the Gironde estuary, as reported by IUCN France (IUCN France, 2014) at €11,500 per ton, this translates to €23 million solely for Arcachon.
- It is crucial to emphasize that fishing in the Bay is subject to regulation by public authorities, with prohibitions enforced near the Birds island, at Humeyre, and in the vicinity of the oyster farms.

The main impacts of professional and non-professional fishing activities on the different ecosystem services provided by *Zostera* seagrass are:

- On ESS water quality and ESS food provisioning: Fishery operations contribute to a significant number of navigation activities, exerting a widespread influence on the biosphere through noise pollution (impacting ecosystem service of food provisioning) and the introduction of hazardous substances (affecting water quality and subsequently, food provisioning). Navigation activities are linked to the concentration of irgarol in the water. Moreover, irgarol imposes constraints on specific phytoplankton populations and contributes to the deterioration of seagrass beds by disrupting photosynthesis processes (IUCN France, 2014), (Auby I. et al., 2011).
- Direct impact on seagrass growth: Potential uprooting/crushing of seagrass (less predominant effect due to regulations).

■

As well, the influence of ecosystem services provided by *Zostera* seagrass on professional and non-professional fishing activities are:

- Impact of ESS erosion on sedimentation in channel, and therefore on navigability is evident (Balle Beganton et al., 2015).
- Professional fishermen capture fishes that take food from the seagrass meadows. Therefore, the link with the ESS food provisioning is then noticeable (Balle Beganton et al., 2015), but difficult to assess.

#### 5.2.2.2 Dredging

To ensure good navigation operations, dredging activities are regularly planned at the harbor entrances within the Bay. Dredging activities in the Bay can be described as follows:

- Major dredging works are carried out roughly on a decadal basis for each channel entrance (Gironde.gouv.fr).
- Curing is done more regularly in specific limited areas: especially harbor entrances.
- The
- 
- Table **5.1** provides information on the dredged volumes for the period 2018-2023, estimated from 2 000 m<sup>3</sup> to 50 000 m<sup>3</sup>, for a cost of 15.8 €/m<sup>3</sup> to 60.3 €/m<sup>3</sup>, depending on the dredging method. An estimated cost of 50€ is calculated for 1m<sup>3</sup> of dredged material, accounting for all costs (tools, workers, before sediment treatment on land...). It corresponds to a mean cost of 1.5M€/yr on a 30 000 cubic meters dredged basis. No future trend for dredging is identified considering all the dependencies.

In recent years, dredging operations have been conducted at the harbors of Andernos-les-Bains, Arès, Gujan-Mestras, Lanton, Biganos, La Teste-De-Buch, and Arcachon, as reported on the Syndicat Mixte des Ports du Bassin d'Arcachon (SMPBA) website. Dredging is performed using either hydraulic dredge pumps or buckets, primarily for remedial purposes (see Fig. 5.2). Additionally, the SIBA reports an annual availability of 30,000 cubic meters of sediment.



*Figure 5.2. hydraulic dredge (left) and mechanical dredge (right) [SIBA]*





Figure 5.3. Location of the dredging works identified on the SMPBA website (SMPBA 2023)

Table 5.1. Data collected relative to dredging works for the period 2018-2023

City	Dredged volume (m3)	Year	Duration (month)	source	Cost (k€)	Cost /m3 (€/m3)
ANDERNOS	2000	2018	3	SMPBA- <a href="http://www.ecocitoyensdubassindarcachon.org">www.ecocitoyensdubassindarcachon.org</a>	-	-
GUJAN	15000	2018	3	<a href="http://SMPBA-gironde.gouv.fr">SMPBA-gironde.gouv.fr</a>	237	16
ANDERNOS	-	2019	2	SMPBA	-	-
LA TESTE	50000	2021	5	SMPBA	-	-
LANTON	10000	2021	1	SPMBA	261	26
LANTON	8000	2022	-	SMPBA	326	41
ARES	10000	2022	1	SMPBA	-	-
LANTON	5800	2023	-	SMPBA	350	60

It is noted that the dredged material is recycled. Ten sediment settling basins are present for sediment recycling, for a total capacity of 78 000 m3. These materials can be used for backfilling for sewage works, creation of forest tracks, topsoil for landscaping.



Figure 5.4. sediment settling basin (left) and their location (right) [SIBA]

The main impacts of dredging on the different ecosystem services provided by *Zostera* seagrass are :

- Impact on ESS water quality:
  - Dredging remobilizes sediment and therefore increases turbidity.
  - Tributyltin (TBT), an antifouling agent widely utilized in the past but banned since 1982, remains buried in the substrate and could potentially be released if the substrate is dredged too deeply (UICN France, 2014), leading to increased water pollution. TBT significantly impacts the biosphere, particularly affecting oysters. It is associated with mortality in bivalve larvae, reproductive disorders in certain gastropods, and shell malformations in oysters (IFREMER, 1997). Due to uncertainties regarding TBT concentration, substrate location, and dispersion, no quantification has been conducted.

Moreover, any dredging operation can potentially affect the surrounding environment, including habitat degradation, noise pollution, and the remobilization of other contaminants. The extent of these impacts varies depending on the type and scope of the dredging activity.

As well, the influence of ecosystem services provided by *Zostera* seagrass on dredging are:

- Impact of ESS erosion: Seagrass meadows contribute to increased sedimentation by slowing down the flow in their vicinity. Consequently, the necessity for dredging in the channels needs to be reevaluated.

## 5.2.3 Tourism and marine recreational activities

### 5.2.3.1 Pleasure boating and navigation

Pleasure boating and navigation in the Bay can be described as follows:

- Some navigation activities within the Bay are associated with fishing operations (as discussed earlier), while others pertain to recreational boating and tourism, such as shuttle services. It is estimated that approximately 12,000 boats traverse the Bay annually (UICN France, 2014).
- Shuttle boats traversing the Bay accommodate approximately 600,000 passengers annually, with up to 60 operations per day during the summer season (SIBA). These boats connect significant tourist destinations such as Arcachon/Moulleau-Cap Ferret and Arcachon-Andernos.
- Additionally, the Banc d'Arguin attracts around 250,000 visitors in July and August (located opposite the Dune du Pilat), making it one of the most popular tourist destinations within the Bay.

- Navigation represents 120 companies, 450 direct jobs and 127 M€ yearly revenue (SIBA, 2023).

The main impacts navigation and pleasure boating on the different ecosystem services provided by *Zostera* seagrass are:

- Impact on ESS water quality: In addition to fishing, navigation exerts a widespread influence on the biosphere through noise pollution and the introduction of hazardous substances.

As well, the influence of ecosystem services provided by *Zostera* seagrass on pleasure boating and navigation are:

- Impact of ESS erosion: Alterations in sedimentation levels within the channels will affect the draft. An adequate draft is essential for operations, particularly during low tide, as stated by SMPBA. This is not quantified.

### 5.2.3.2 Mooring

Mooring can be described and quantified as follows:

- In 2023, roughly 5000 moorings were available in the Bay, located mainly on the foreshore and in the river La Leyre (parc-marin-bassin-arcachon.fr, prefectorial decree, (Le Corre N. et al., 2015)). This figure has not changed significantly for the past 15 years (Fig. 5.5).
- Mooring is regulated: it is forbidden in *Zostera* areas.
- The areas dedicated to mooring are regularly dredged. This was the case for example in 2022 in Arès, for the place called "Trou de Tracasse" (SMPBA). Over a period of two months, dredging operations removed 10,000 cubic meters of sediment from both the channel and the mooring area.

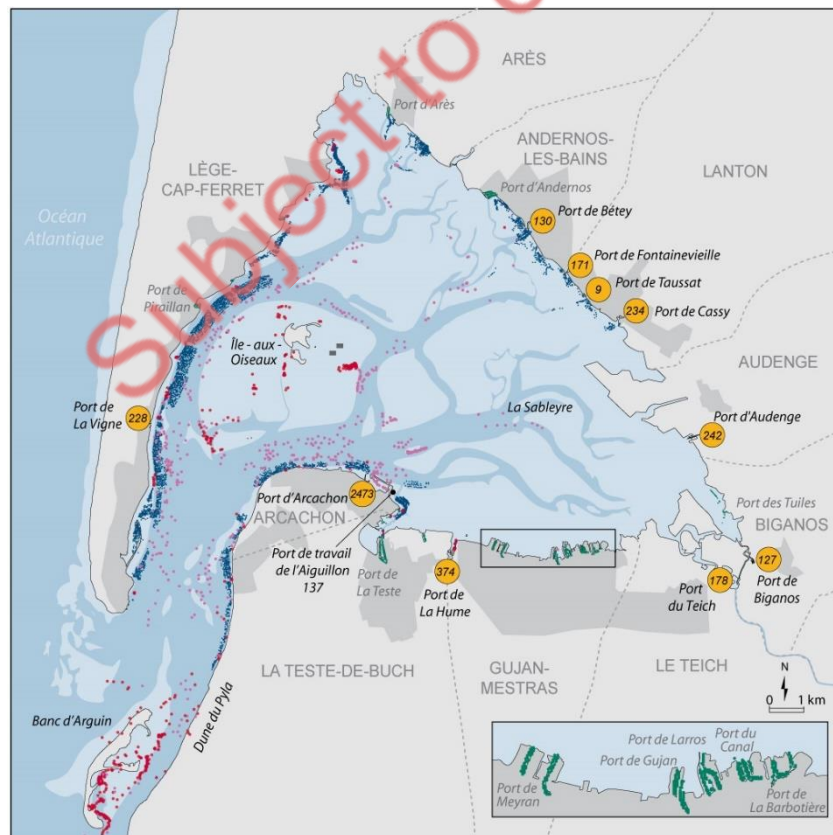


Figure 5.5. Location of moorings (mooring buoy in blue, anchor in red) observed in an afternoon in July 2008 (Le Corre N. et al., 2015)

The main impacts of mooring on the different ecosystem services provided by *Zostera* seagrass are:

- Mooring accounts for a significant portion of the boats navigating in the Bay, consequently influencing the ESS water quality as described before.

As well, the influence of ecosystem services provided by *Zostera* seagrass on mooring are:

- ESS flooding: Vegetation decreases both the flow and wave activity, thereby improving mooring conditions by reducing agitation.

#### 5.2.3.3 Residential and general tourism

Residential and general tourism activity in the Arcachon lagoon can be quantified as follows:

- In 2020, the population of the Bay of Arcachon was 138,983, compared to 127,286 in 2014, indicating a growth of 9.2% over 6 years (INSEE).
- During the summer, the population in the area swells to around 400,000, according to SIBA data.
- The Dune du Pilat attracts approximately 1 million tourists annually (Banzo et al., 2018).
- The newly adopted SCOT of 2023 imposes restrictions on new construction, prohibiting development outside already urbanized areas within the first 100 meters from the shoreline, except for public services or specific economic activities. Additionally, the plan outlines demographic evolution objectives, aiming for a growth rate of +1.30% per year until 2030, followed by +1% per year until 2040.
- In 2022, tourism in the Bay represented 760 M€ (SIBA, 2013).

The main impacts of tourism on ecosystem services provided by *Zostera* seagrass are on water quality:

- Population pressure affects water treatment management, with three water treatment plants located in the Bay (SIBA). This pressure can impact water quality, indirectly affecting environmental conditions necessary for the growth of seagrass and the overall biosphere.
- Increased nutrient runoff from human activities and sewage can lead to eutrophication (UICN France, 2014), potentially harming *Zostera* seagrass beds and reducing their ability to provide habitat and food for marine species.

On the other side, the positive influence of ecosystem services provided by *Zostera* seagrass on tourism can be clearly established:

- Healthy *Zostera* seagrass beds contribute to improved water clarity and quality, enhancing the aesthetic appeal of the Arcachon lagoon for tourists (ESS water quality).
- *Zostera* seagrass beds support a diverse array of marine life, including commercially important fish species, which can attract recreational fishermen and contribute to the local economy.
- The presence of thriving seagrass ecosystems can provide natural coastal protection, reducing erosion and safeguarding infrastructure and property, thus supporting the long-term sustainability of tourism and residential development in the area.
- ESS flooding: Potential coastline stabilization favored by seagrass meadows can help preventing coastal areas prone to flooding to be flooded.

#### 5.2.4 Oyster farming

Oyster farming in the Arcachon lagoon can be quantified as follows:

- The Bay of Arcachon hosts more than 300 oyster farming companies (Parc Marin).
- Oyster farming in the region provides employment for approximately 750 people on a permanent basis.
- The total area dedicated to oyster farms covers approximately 780 hectares.



- The oyster farming industry generates an annual revenue of €35 million and accounts for 8% of the French oyster production.

The main impacts of oyster farming on the ecosystem services provided by *Zostera* seagrass are:

- Oyster production relies heavily on water quality, which can be influenced by various factors including pollution and turbidity/sedimentation.
- Historically, the use of tributyltin (TBT) as an anti-fouling agent posed a threat to marine ecosystems, including *Zostera* seagrass beds, before its ban in 1982. Remobilization of TBT from subsoil deposits could potentially harm seagrass habitats and disrupt the ecosystem services they provide (UICN France, 2014).
- Sedimentation resulting from oyster farming activities can affect the light availability and sediment stability necessary for the growth and health of *Zostera* seagrass beds.

As well, the influence of ecosystem services provided by *Zostera* seagrass on oyster farming are clearly identified:

- *Zostera* seagrass beds play a crucial role in maintaining water quality by filtering pollutants and stabilizing sediments, thereby indirectly supporting the health and productivity of oyster farming operations.
- The presence of healthy *Zostera* seagrass habitats can enhance local biodiversity, providing important nursery and foraging grounds for various marine species that contribute to the ecological balance of the Bay of Arcachon.
- *Zostera* seagrass beds help to mitigate coastal erosion by trapping sediment and dampening wave energy, which can protect oyster farming infrastructure and ensure the long-term sustainability of the industry in the face of changing environmental conditions.

### 5.2.5 Conclusion

The socio-economic analysis conducted earlier is summarized in the table below, preceding the impact assessment in the subsequent section.

*Table 5.2. Summary of socio-economic analysis*

Activity	Estimated yearly economic significance	Main impacts of activity on ESS	Main impact of ESS on activity
<b>Fishing</b>	>23 M€ revenue	ESS Water quality ESS food provisioning	ESS erosion ESS food provisioning
<b>Dredging</b>	1.5M€ cost	ESS water quality	ESS erosion
<b>Boating and navigation</b>	127 M€ revenue	ESS water quality	ESS erosion
<b>Mooring</b>			
<b>Residential and tourism</b>	760 M€ revenue (200 M€ in touristic housing only)	ESS water quality	ESS water quality ESS flooding
<b>Oyster farming</b>	35M€ revenue	ESS water quality ESS erosion	ESS water quality ESS erosion

## 5.3 Impact assessment

### 5.3.1 Method

Following the above socio-economic description of the Arcachon Bay, numerical model results obtained using the eco-morphodynamic D-FM model are used to assess the impacts on the various socio-economic indicators associated to changing forcing conditions (climate scenarios).

The model and its characteristics in terms of physical and numerical considerations, forcings, extents, processes represented, etc. has been detailed in the previous deliverable D2.1. The coupled eco-morphodynamic model has been calibrated and validated for the period 2016-2019, representing correctly the trends and order of magnitude of the morphological changes that occurred. Two main models have been implemented:

- an eco-morpho-hydro model aiming at representing morphological changes and functioning with a morphological acceleration factor,
- an eco-wave-hydro model aiming at calculating water renewal time, plume dispersion, storm impacts, etc.

For this deliverable D2.2., the focus was on utilizing the first model to estimate the bio-physical indicators necessary for assessing damages in future scenarios. Additionally, preliminary findings from the second model are provided, which assess water renewal and flushing times.

The following sections are more specifically addressing the definition of the forcing conditions, the assessment of indicators in terms of sediment dynamics (mainly related to ESS erosion) and their sensitivity to changing climate conditions.

### 5.3.2 Current and climatic forcing conditions

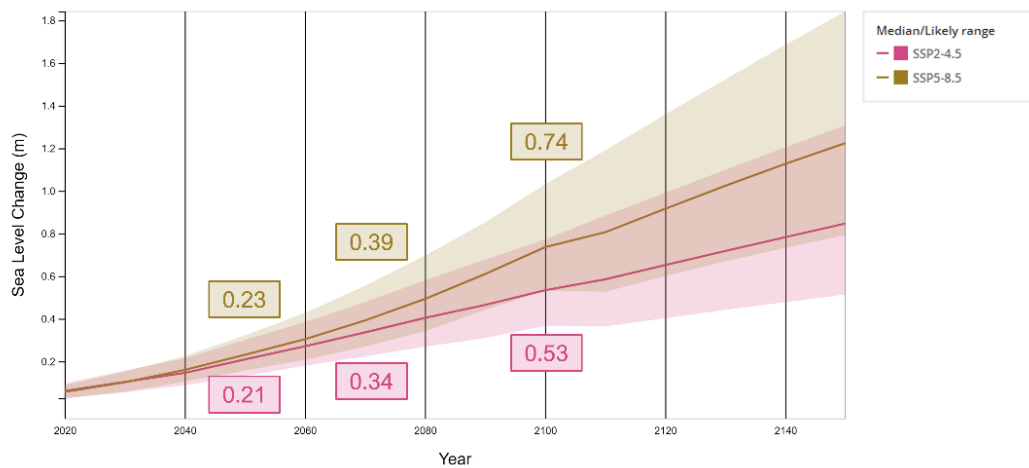
To align with the methodologies adopted in other pilot sites, the focus was placed on projecting future scenarios for the years 2050, 2070, and 2100. From a modeling standpoint, these future horizons involve translating changes in environmental forces (such as wind, waves, tide, etc.) and defining climate conditions based on global climate scenarios. Two global climate scenarios were chosen: "business-as-usual" SSP2-4.5 and "pessimistic" SSP5-8.5.

#### 5.3.2.1 Water levels

Anticipated rising sea levels are poised to directly influence the hydrodynamic circulation within the Arcachon Bay, thereby impacting water renewal, wave dynamics, and erosion/sedimentation patterns, consequently leading to morphological alterations within the bay.

Figure shows the regional projections of water level rise, as reported by IPCC AR6 for the North-European Atlantic coast, with projected sea level rises of 0.21 / 0.23, 0.34 / 0.39 and 0.53 / 0.79 m for the years 2050, 2070, and 2100 respectively, compared to the current level (mean 1995-2014) and for the two selected climate scenarios (SSP2-4.5 / SSP5-8.5).

## D2.2 Good practice criteria Multi-variable risk projections



Horizon \ Climate Scenario	SSP2-4.5	SSP5-8.5
2050	0.21	0.23
2070	0.34	0.39
2100	0.53	0.74

**Figure 5.6.** Sea level rise projections (m), median and likely range, for two climate scenarios: SSP2-4.5 and SSP5-8.5. Extracted from "<https://sealevel.nasa.gov>".

### 5.3.2.2 Wind

IPCC projections regarding wind magnitude are represented in Fig. 6.7, suggesting a decrease of the mean surface wind (-2.6% by 2100 for scenario SSP5-8.5).

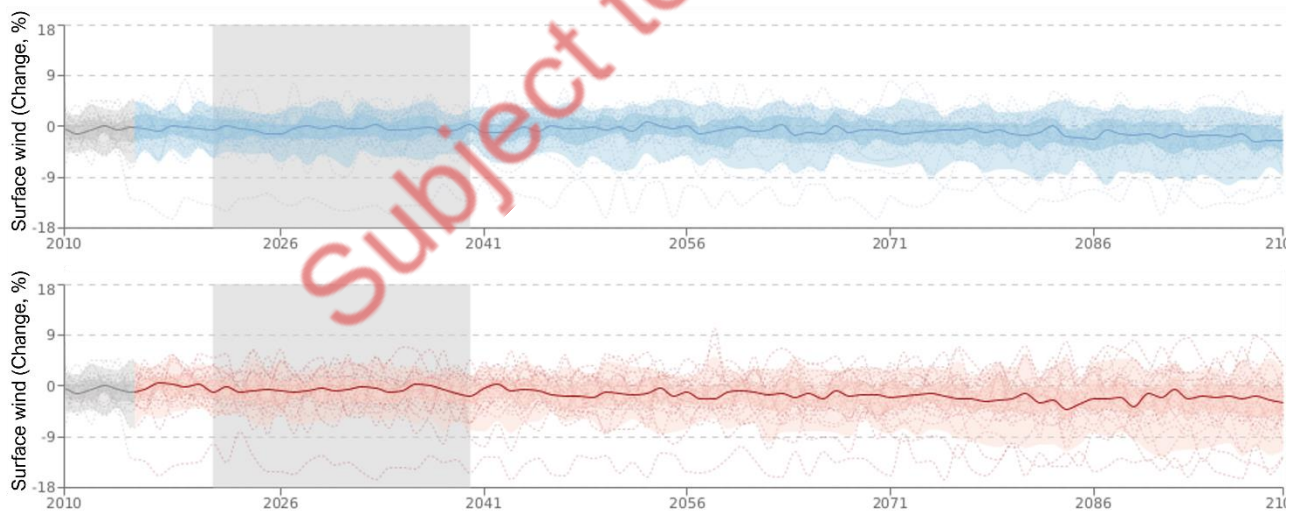


**Figure 5.7.** Surface wind projections (% of change). Ensemble mean (solid line) and confidence interval are represented for climate scenarios SSP2-4.5 (blue) and SSP5-8.5 (red).

Based on meteorological data collected from the Météo-France station situated in Cap Ferret, general projections can be derived through the analysis of trends observed over the past decades.

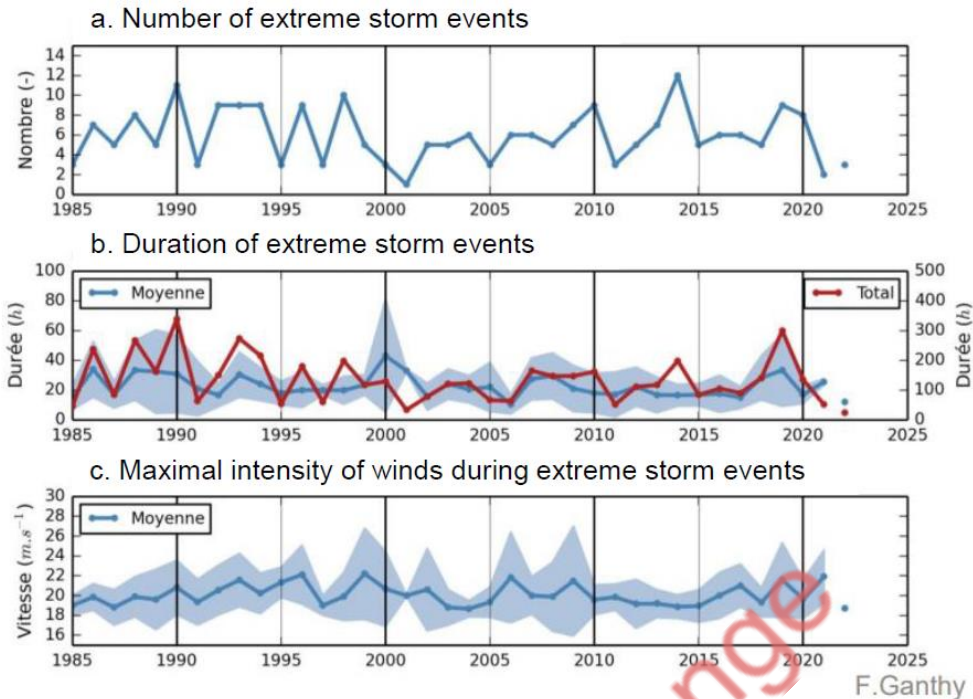


*Figure 5.8. Storm events analysis in term of number (a), duration (b) and intensity (c). From Ganthy F., Ifremer (personnal communication).*

After examining extreme wind events dating back to 1985, no significant trend in the frequency or duration of these events is evident. However, a minor uptick in the intensity of maximum wind speeds can be observed. Despite these observations, the extreme values utilized in the preceding deliverable D2.1 remain applicable for future climate scenarios.

#### 5.3.2.3 Waves

The analysis of meteorological data indicates a lack of discernible trends in storm events affecting the Arcachon Bay. Unlike offshore waves, which are typically impeded by the passes situated at the bay's entrance, Arcachon Bay experiences more pronounced impacts from changes in water levels and wind phenomena (Parisot et al., 2008). Consequently, for this study, the wave conditions for future scenarios are assumed to remain consistent with current conditions, as outlined in deliverable D2.1.

#### 5.3.2.4 Bathymetry

The coupled eco-morpho model has been validated using bathymetric surveys conducted in 2016 and 2019, demonstrating its capability to accurately assess morphological changes over a three-year period in this intricate coastal estuarine setting. However, this validation period is insufficient for predicting morphological changes over multiple decades. Forecasting long-term trends in morphological changes poses challenges and prompts inquiries into the existence and nature of morphological equilibrium. Nevertheless, attaining such equilibrium is elusive due to the constant evolution of external conditions (Dronkers 1986; Dam et al., 2016). The potential for reliable predictions in realistic environments remains uncertain (De Vriend et al. 1993; Haff 1996, 2013; Stive and Wang 2003; Dam et al. 2016).

In this context, various methodologies have been explored to evaluate morphological projections for the Bay, including considerations of tidal asymmetry (not reported here). However, due to the uncertainties inherent in these projections, a more straightforward approach has been adopted. The current methodology involves shorter simulations spanning a three-year period, utilizing a morphological acceleration factor. The initial bathymetry remains the same for each scenario, except for the inclusion of sea level rise (SLR). Subsequently,



the effects of varying SLR scenarios are examined after a three-year simulation period to assess various bio-physical indicators outlined in this study.

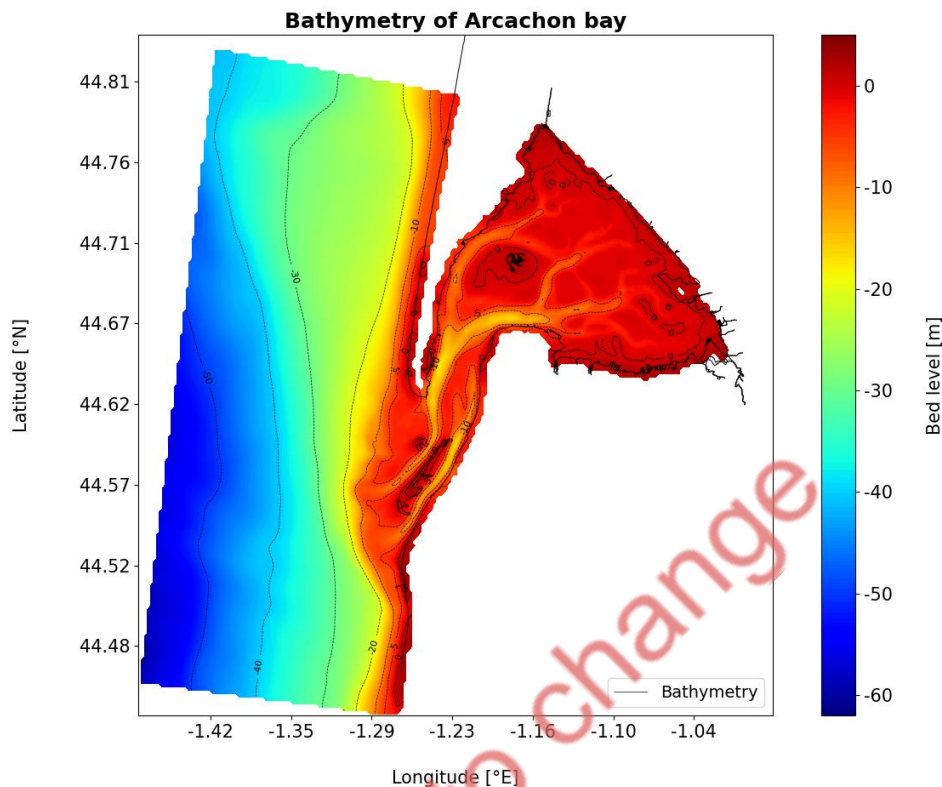


Figure 5.9. Initial bathymetry applied in the model (m with respect to current MSL).

### 5.3.3 Sediment dynamics

Seagrass meadows, acting as genuine ecological engineers in marine coastal regions, directly influence sediment dynamics. The influence of seagrass on sediment dynamics can be delineated across various aspects:

- Stabilization of the seabed within restored seagrass areas
- Alterations observed in the vicinity of existing seagrass zones
- Influence on channel morphology
- Impact on sediment grain size distribution
- Assessment of sedimentation patterns within port environments

Each of the aforementioned aspects is associated with quantifiable indicators that can be assessed using the sophisticated modeling tool. These indicators include erosion and sedimentation rates within seagrass areas, mudflats, and channels, as well as turbidity, water renewal time, sediment granulometry, and sedimentation around harbors.

Initially, the model incorporates the influence of seagrass on hydrodynamics, attenuating currents and waves as described in deliverable D2.1. Reduced currents in vegetated regions typically result in increased sedimentation within and around those areas. Consequently, higher vegetation density is expected to enhance currents within channels, leading to elevated flow velocities and subsequently, greater transport rates. Secondly, the vegetation module reduces bed shear stress and consequent sediment transport in vegetated zones, thereby stabilizing the seabed.

#### 5.3.3.1 Impact on seabed stabilization in seagrass areas

Seagrass plays a crucial role in capturing sediment from the water column, thereby reducing water turbidity. This dual effect promotes both the growth of seagrass and extends its depth range. As turbidity diminishes, light can penetrate deeper into the water column, facilitating seagrass growth at greater depths (Maxwell, P. et al., 2016). This dynamic creates a positive feedback loop that enhances seagrass growth.

#### 5.3.3.2 Impact in the vicinity of seagrass area

The presence of the seagrass meadow influences adjacent areas, particularly by altering hydrodynamic patterns (see deliverable D2.1).

We can examine three key aspects:

- The effect on salt marshes
- The impact on mooring capacity
- The influence on coastline stabilization

These aspects will be further elaborated upon without specific quantification at this stage.

##### **Impact on salt marshes**

Reeves et al. (2019) and Donatelli et al. (2018) show that salt marsh systems can be significantly influenced by the adjacent seagrass dynamics. Indeed, the amount of sediment delivered to the salt marshes are dependent of the state of the seagrass meadow, and this coupled evolution is on large time scales of decades to centuries. Seagrass meadows trap more sediment when prograding because of shear stress reduction, implying less suspended sediment available for deposition on the salt marshes. On the contrary, if vegetation on meadows dies, sediment is liberated and can go from the meadows to the salt marshes. Therefore, when salt marshes prograde, seagrass meadow tend to decline, and this interaction tends to be enhanced. Conversely, if seagrass meadows grow, salt marshes tend to decline, allowing for seagrass meadow progradation. This constitutes a positive feedback loop, which is especially pronounced when sediment is preserved within a relatively confined environment or back-barrier setting.

##### **Impact on mooring capacity**

The zones designated for mooring undergo regular dredging maintenance. If sedimentation decreases in the vicinity of seagrass areas, there may be a reduction in the need for dredging in mooring zones. Consequently, this could potentially increase mooring capacity, leading to positive effects on recreational boating and tourism. Furthermore, seagrass meadows tend to diminish current velocities, which could result in reduced agitation in mooring areas and potentially extend their operational timeframe.

##### **Impact on coastline stabilization**

Potential change in wave height and direction, as well as currents, can induce a change in longshore transport. Therefore, the extent of coastline retreat may vary depending on the orientation of the coastline and the alterations in environmental conditions.

Seagrass meadows help reducing wave agitation (Dinu et al., 2013). Deriving the change in wave energy from the change in wave height allows to estimate the change in longshore transport. For example, on the study case of a part of the southern Romanian coast conducted with SWAN model, a reduction of 5% in wave height has led to a 12% decrease in longshore transport. This is especially influenced by the extent of the vegetation meadow (and its proximity to the coastline), the wave climate and the local bathymetry.

#### 5.3.3.3 Impact on sediment size

Seagrass meadows, when dense, captures fine material by reducing turbulence and increasing deposition. Therefore, sediment distribution in high-density seagrass meadows tends to become muddier. However, in

low-density seagrass meadows, turbulence increases at the edges of the meadows putting small sediment in suspension and then increasing the mean sediment size (Maxwell, P. et al., 2016).

**Table 5.2.** Mudfraction change (%) between the beginning and the end of the run (3 years simulation) for current (reference) and future horizons. Location of each area considered (red) on following maps.

SSP5-8.5					
Future horizon		2020	2050	2070	2100
Areas around harbors	Ares	16.30	15.80	15.23	15.28
	Andernos	12.47	13.07	12.99	13.42
	Gujan	15.18	15.54	14.92	13.96
	La Teste	18.37	19.04	17.89	15.15
Mudflats		6.48	6.56	6.21	6.42
Bottom of the Bay		5.48	5.62	5.02	5.01

The figure consists of six maps of the Gironde estuary, arranged in two rows of three. The top row shows the locations of Ares, Andernos, and Gujan. The bottom row shows the locations of Mudflats, La Teste, and Bottom of the Bay. Red areas on the maps indicate the locations of the study areas.

The evolution of the mud fraction for a 3-years period has been simulated, for different areas, and different horizons. The modelling results (Table 5.3) support the increase of mud fraction for the bottom part of the Bay and the mudflats, in line with historic observations (Cognat, 2019). Concerning the evolution around harbor entrances, except for Ares, the mud fraction is predicted to increase quicker in 2050 and slower in 2070 and 2100, than in the current state. In Ares, the difference between the beginning and the end of the run decreases at each horizon with SLR increase.

A trend is difficult to predict with those results, as changes between horizons are insignificant. However, it seems that higher mean sea level reduces the deposition of mud in the vicinity of harbors. The evolution for mudflat is stable and no real impact of SLR is noticeable.

#### 5.3.3.4 Erosion/sedimentation of channels

The impact on sedimentation within the channel is analyzed for both primary and secondary channels. Considering the model configuration and assumptions, only channels wider than 200 meters are taken into consideration. These channels are highlighted in blue on the "Mudflat" map provided in Table 5.2.

The variation in sedimentation across different scenarios is determined by comparing the bathymetric changes from the beginning to the end of the three-year simulation period. This difference allows for the assessment of the percentage increase or decrease in sedimentation, as well as an estimation of the corresponding volume change.

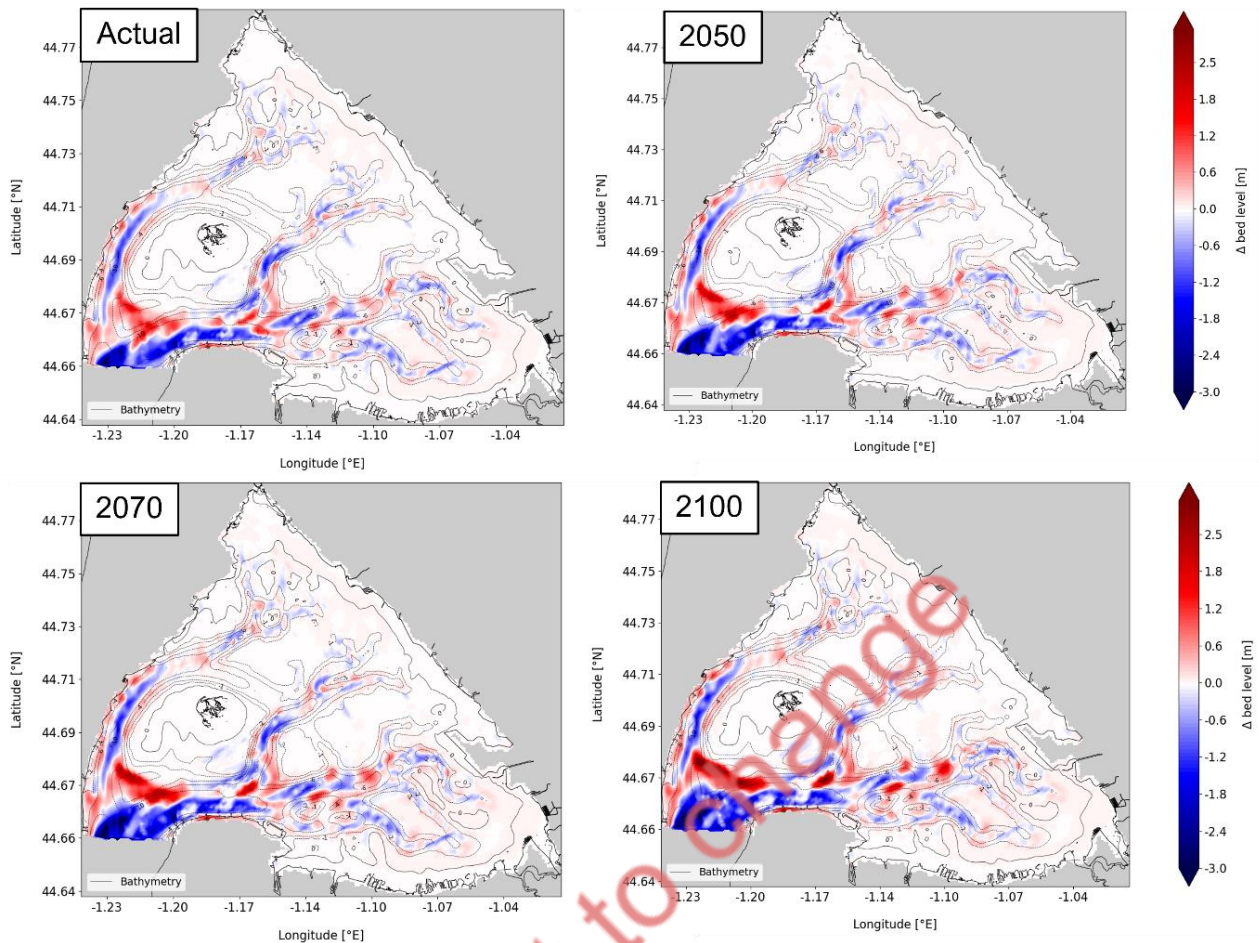


Figure 5.10. Morphological changes (m), calculated over 3 years for future horizons and corresponding SLR.

The morphological changes simulated over three years for the various targeted horizons reveal consistent trends (Fig. 5.10). These trends indicate erosion in the channel east of Arcachon, sedimentation in the southwestern portion of Ile aux Oiseaux, and noticeable erosion/sedimentation patterns within the main and secondary channels. Sedimentation is also observed on the mudflats near the river mouth of La Leyre. Across the entire bay, the average bed evolution rates for channels are -3.1, -3.6, -3.9, and -4.4 cm per year for the current state, 2050, 2070, and 2100 respectively. For mudflats (see Table 6-3, "Mudflats"), rates of +0.4, +0.5, +0.6, and +0.7 cm per year are recorded. Regarding the secondary channel situated at the highest part of the bay, the mean bed evolution rates are -2.0, -1.9, -1.9, and -1.1 cm/year for the current, 2050, 2070, and 2100 horizons respectively.

In summary, with an increase in sea level rise (SLR), erosion and sedimentation rates become more pronounced, and the areas affected by erosion or sedimentation remain comparable to those in the current situation.

#### 5.3.3.5 Impact on modification of draft

The decrease in sedimentation within the channel (particularly post-dredging) results in an augmentation of the draft, which can prove advantageous, particularly during low tide. This connection and its implications for various uses have been recognized by SMPBA.

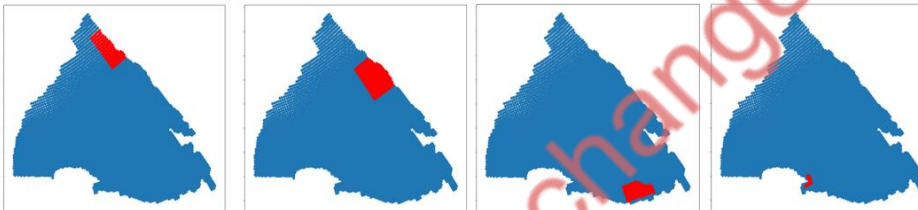


### 5.3.3.6 Sedimentation in the vicinity of ports

Following the global overview detailed in section 5.3.3.3, a more thorough analysis of the Bay's innermost part has been conducted to forecast potential changes associated with dredging requirements near harbor entrances. The subsequent Table 6.4 displays the outcomes in terms of sediment deposition volume (expressed as a relative difference over a three-year period in percentage) for areas situated near four harbor entrances.

*Table 5.4. Relative difference over 3 years (%) in term of volume deposited for areas around harbors entrances for current, 2050, 2070 and 2100 horizons.*

SSP5-8.5				
Horizons	2020	2050	2070	2100
Ares	1.04%	1.13%	1.20%	1.32%
Andernos	0.82%	0.84%	0.86%	0.84%
Gujan	1.74%	1.85%	1.94%	2.08%
La Teste	0.56%	0.57%	0.53%	0.44%

Ares
Andernos
Gujan
La Teste

The change in deposited volume around harbors remains relatively constant, with a peak of +0.3% observed for Gujan between the year 2100 and the current situation. Within the chosen areas, no notable influence of sea level rise (SLR) could be identified, and the deposited volume is not anticipated to decrease with SLR.

### 5.3.4 Water quality

Seagrass meadows play a significant role in influencing the water quality within the Bay, contributing to changes in suspended sediment concentration, according to Arias (2022). Studies by Pelisson (2019) and Arias (2022) employing modeling approaches have indicated that current levels of suspended sediment concentration are 2 to 10 times higher compared to concentrations prior to the regression of seagrass. This section examines water renewal by studying the overall renewal time of the Bay and the dispersion of potential pollutants originating from harbors under future climate conditions.

#### 5.3.4.1 Water renewal

The study of water renewal in Arcachon Bay relies on the calculation of flushing time using the model. According to Plus et al. (2009), flushing time is defined as the duration required for a significant portion of a water parcel to be replaced by water originating from outside the lagoon boundaries. In this study, a passive tracer is introduced with a theoretical concentration set at 1.0 (or 100%) throughout the Bay. The time taken for the tracer concentration to decrease below 37% of the initial concentration (i.e.,  $e^{-1}$ ) is noted, representing a threshold for the replacement of the water parcel. Employing this approach, Plus et al. (2009) calculated a water flushing time in the bay as 18.9 days under current conditions. By applying similar forcings (i.e., tidal currents and excluding wind waves and Leyre flow), our model yields flushing times of 20.0, 19.6, 19.6, and 19.2 days for current, 2050, 2070, and 2100 conditions, respectively. The difference between

computed water flushing times may be associated to the influence of vegetation on hydrodynamics, that is incorporated in our modelling approach.

Flushing time calculations are also conducted in proximity to harbor zones (Fig. 5.11). The objective is to evaluate the potential rate of water renewal around these potentially contaminated regions. These renewal times are assessed across various climate scenarios to comprehend the potential impact of sea level rise (SLR). It is observed that increasing water levels generally result in a quicker pace of water renewal, indicated by a faster decline in tracer concentration. The disparities between scenarios are more noticeable for Gujan, Lanton, and Ares. For instance, at Gujan harbor, tracer concentration reaches zero on day 4 for the 2100 scenario, while it takes less than 10 days to reach zero in the current situation.

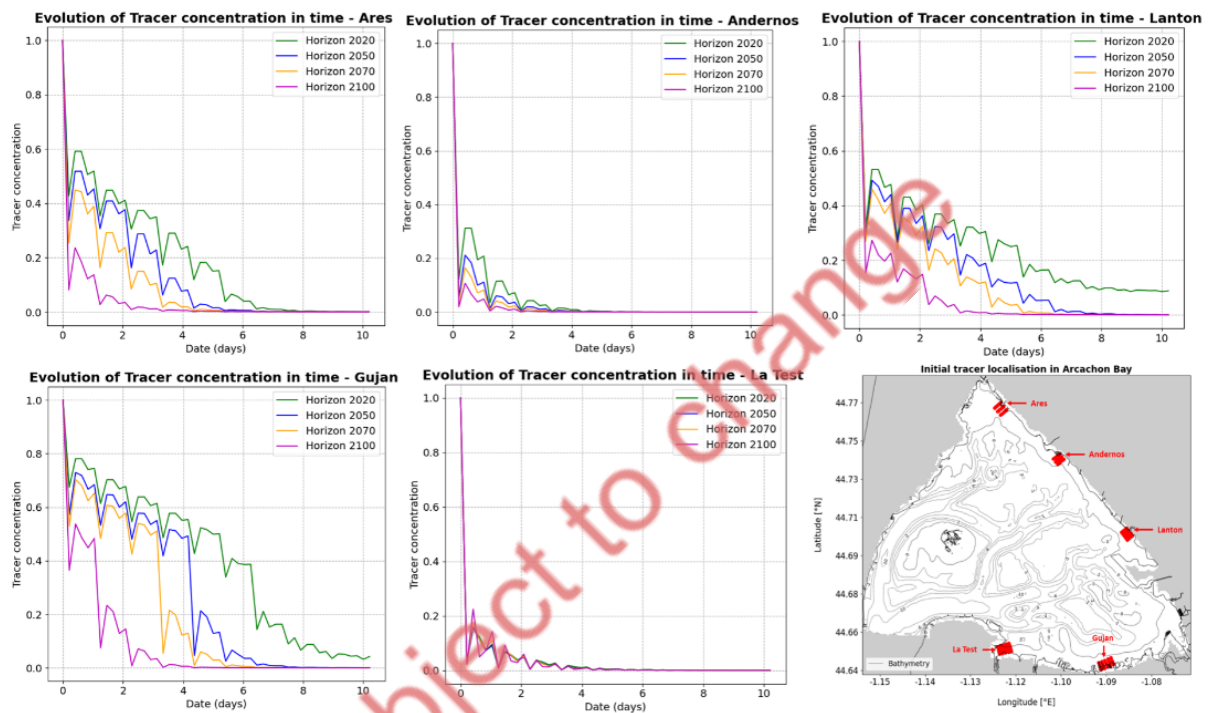


Figure 5.11. Evolution of tracer concentration (1 initially) for 5 harbors and 4 horizons over 10 days of simulation.

## 5.4 Sensitivity of ESS to climate forcing and multi-impact chains

Further below, each subsection focuses on a specific ecosystem service (ESS) potentially provided by the seagrass meadow. The interactions depicted in the sketches between various processes (represented as boxes) are elaborated upon, with processes being described and, if possible, quantified using the model or literature as previously outlined. Uncertainties and further questions arising from the study are also addressed. Processes may be interconnected between different ESS, and if so, this is indicated.

While there is a particular emphasis on ESS erosion, the impact of various climate forcing on the ESS water quality is also depicted based on an understanding of the system, although specific links have not been quantified.

### 5.4.1 Sediment management

The ESS Erosion facilitated by seagrass is a complex and multifaceted mechanism. Seagrass meadows exert influence on sedimentation, impacting sediment size, seabed stabilization within seagrass meadows, in areas

adjacent to seagrass, and within channels. The assessment of impacts conducted in section 5.3 enables the evaluation of the sensitivity of these impacts to changing climatic conditions.

As mentioned previously, while the impact of vegetation has not yet been fully assessed (as it will be in Task2.3), there is a climate change sensitivity regarding channel filling and sedimentation in mudflat zones. Channel erosion increases with higher sea level rise (SLR) across the entire bay, although establishing a trend at the bay's innermost part is more challenging. This directly affects dredging requirements and changes in draft, impacting navigation-related activities, as illustrated in the diagram (Fig. 5.12). Changes in navigation duration (for pleasure boating, tourism, and fishing) and direct costs associated with dredging operations are affected. The diagram underscores the indirect impacts on seagrasses through water quality deterioration (potential remobilization of TBT and increased presence of toxic substances as navigation intensifies).

Currently, within the innermost part of the bay, SLR does not appear to significantly affect sedimentation. Therefore, vegetation restoration could prove beneficial in influencing dredging needs near harbor entrances. The link between changes in sedimentation and alterations in navigation duration has been noted by SMPBA. For instance, in 2021 at La Teste-De-Buch, dredging of 50,000 cubic meters of sediment resulted in fishing professionals and pleasure boaters experiencing an increase of 1.5 to 2 hours of navigation time around low tide. It can be inferred that reduced sedimentation, leading to increased draft, allows for longer navigation operations, thereby generating positive economic impacts. Specifically, an increase in draft could benefit pleasure boating, tourism, and fishing activities.

With higher SLR, sedimentation on mudflats is anticipated to surpass current levels. This could impact coastline stabilization by increasing sediment deposition near the coast, as elucidated in the impact assessment section. Consequently, the intrusion of seawater may be affected, establishing a connection with flood control and impacting land cover and tourism.

The summarized diagram outlining the impacts of ESS erosion facilitated by seagrass is provided below:

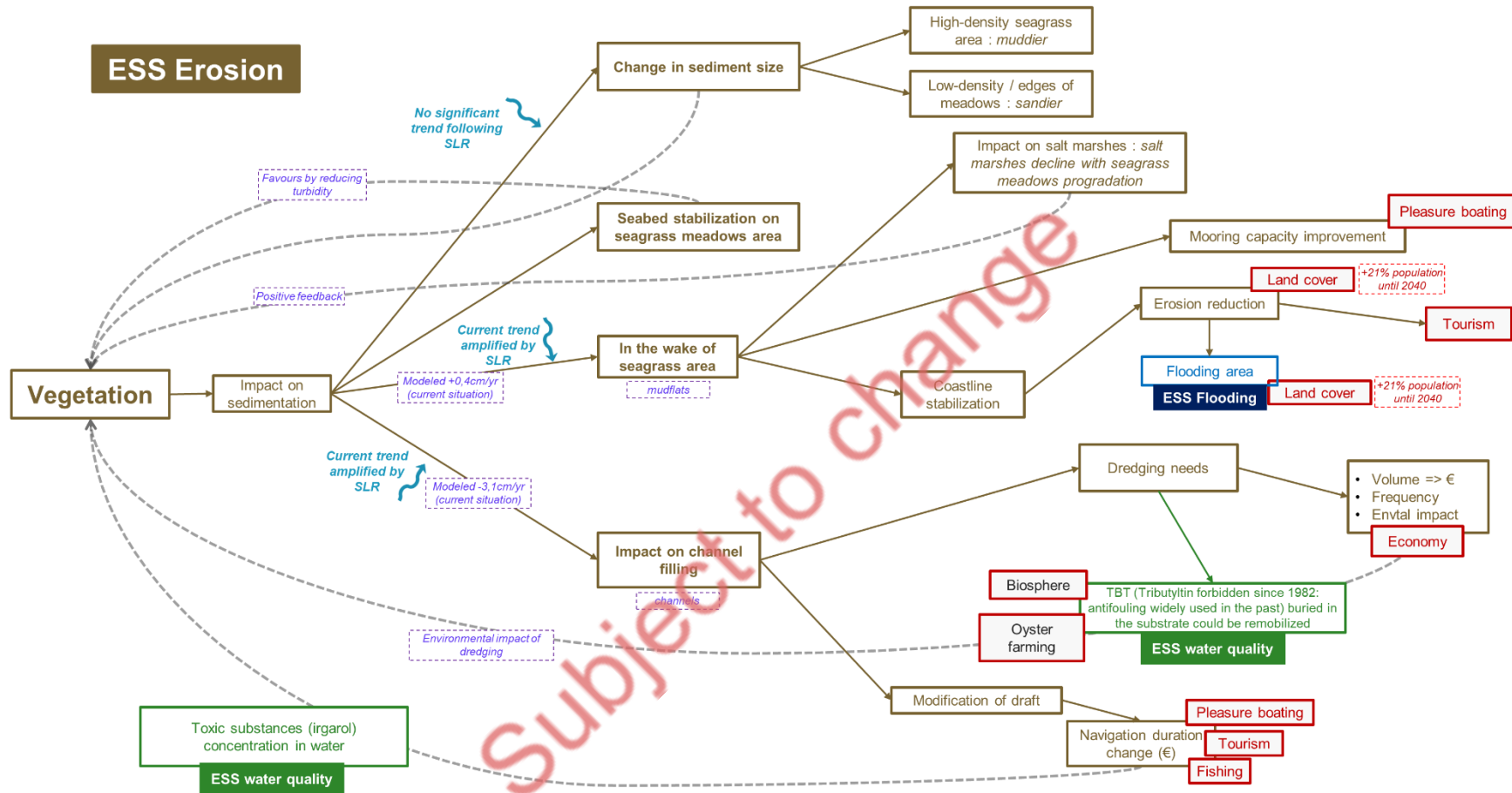


Figure 5.12. Multi-impact chain and climate sensitivity for ESS erosion.



#### 5.4.2 Water quality

The impact of climate change on the ESS water quality provided by seagrass meadows manifests in alterations to renewal times in the Bay. It has been modelled that renewal time for the whole Bay is expected to decrease by 4% until 2100. The renewal time for areas close to harbors is also expected to decrease when already important in the current situation: it would be divided by 3 until 2100 for Arès, Lanton, and Gujan, due to sea-level-rise.

Numerous feedback mechanisms are also highlighted in the literature:

- *Zostera* seagrasses possess the ability to absorb toxic substances (such as irgarol), thereby aiding in reducing their concentrations in the water (UICN France, 2014). Irgarol is particularly associated with navigation activities (fishing, tourism, pleasure boating), and an increase in irgarol concentration can lead to a restriction of phytoplankton populations.
- *Zostera* contributes to the natural regulation of nitrogen concentrations originating from wastewater (UICN France, 2014), via eutrophication.
- High-density seagrass, especially in sheltered environments, absorbs more ammonium, thereby reducing toxicity and promoting seagrass growth, thus establishing a positive feedback loop (Maxwell, P. et al., 2016).
- Another positive feedback loop is associated with sediment trapping: *Zostera* limits the suspension of fine particles, thereby enhancing water transparency.
- Nevertheless, negative feedback mechanisms are also identified in the literature (Maxwell, P. et al., 2016). One such mechanism is sediment sulfide toxicity: high-density seagrass traps organic matter, which decomposes and releases sulfide, impairing seagrass growth. This mechanism becomes more pronounced with higher temperatures.
- Additionally, photosynthesis leads to elevated pH levels, which inhibit seagrass growth in sheltered environments.

As evidenced by the impact assessment, changes in climate forcing will impact the renewal time of chemicals and pollutants. The synthetic diagram linking ESS water quality and socio-economic impacts is depicted below:

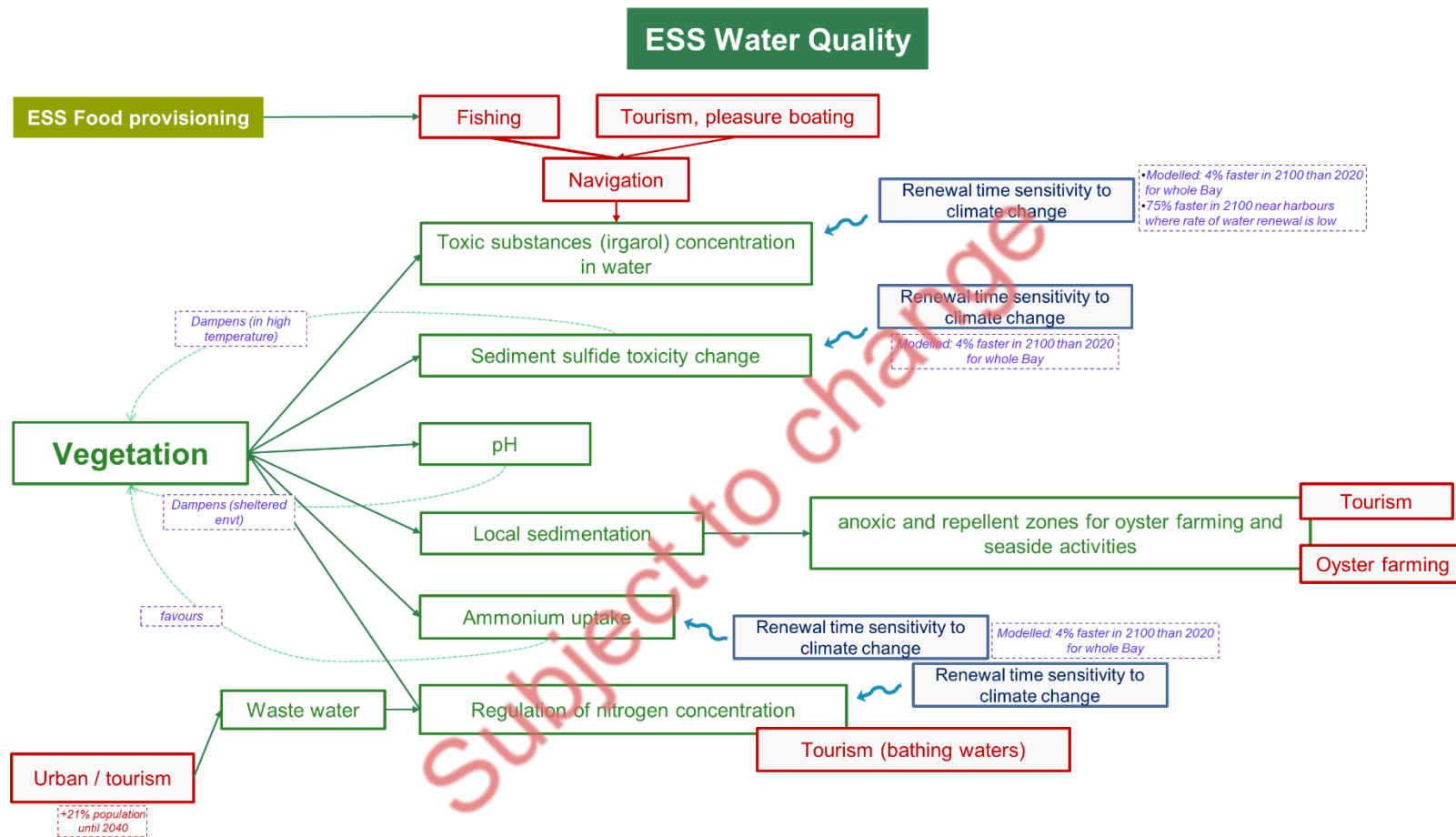


Figure 5.13. multi-impact chain and climate sensitivity for ESS water quality

## 5.5 Conclusion

The aim of the current deliverable is to assess the projections of ecosystem-services (ESS) provided by seagrass meadows within the Arcachon Bay for different future horizons: 2050, 2070 and 2100. In particular, this study characterizes the socio-economic consequences related to enduring morphological shifts under diverse climatic circumstances, achieved through a modeling approach.

After a comprehensive socio-economic analysis, the main economic activities have been identified. The impacts are then assessed using the eco-morphodynamic model. When possible, the quantification of bio-physical indicators needed for assessing sensitivity of ESS to climate forcings is presented. In the last section, the interplay between each economic activity and the model-derived physical metrics is examined. This work led to the conception of multi-impact chains for the main ESS aimed: Sediment management and Water quality.

In conclusion, the modeling tool helped to assess some trends for sediment management, linked with SLR. With higher SLR, sedimentation on mudflats is anticipated to increase, with a consequence on flood control. However, the erosion of channels, connecting harbors to the Bay, could benefit pleasure boating, tourism and fishing activities. SLR, and morphological changes associated, have a noticeable effect on water renewal times. Modeling results show an increase in water renewal, leading to an improved water quality in the Bay.

This modular approach we developed helps to estimate the risk reduction from ESS as a function of projection time horizon, and enables the future introduction of restoration scenarios to be executed in Task 2.3.

Subject to change

## 6 Multi-risk projections and climate warnings with ESS in Sicily Lagoon Pilot (UC)

The University of Catania (UNICT) leads the research activities related to the evaluation of the effectiveness of a range of coastal restoration measures within the REST-COAST Sicily pilot site: the Cuba-Longarini coastal lagoon system, belonging to the Natura 2000 site of the Coastal Wetlands of the South East of Sicily. One of the main risk to which the region is subject is twofold: a flooding and erosion threat to the village of Granelli, built over the dune-belt in between the lagoons and the sea; and the anthropic pressures on the lagoon biodiversity, induced by human activities in the surrounding area (intensive agriculture and tourism, mostly), which led to a reduction in both extension and quality of the local habitats and water resources. In collaboration with the local managers of the site, UNICT is assessing a range of solutions to both improve biodiversity value, by protecting the environment, and increase the provision of ecosystem services related to flooding and erosion risk mitigation. Presently, two solutions, additional to the ones currently carried out as pro-biodiversity measures (i.e. construction of artificial islands within the lagoons and new hydraulic connections between the different areas of the two lagoons), are investigated, (i) a revegetation of the dunebelt in between the Granelli village and the beach, (ii) an extension of the present seagrass meadow in front of the Granelli coast. The performance assessment of these solutions is pursued by means of numerical modelling, aimed to evaluate the response of the system to extreme events, under present and climate change conditions, therefore including impact of sea level rise as well as modification of the wave climate. Performance of the solutions is assessed by computing efficiency indicators based on reduction of flooded areas and shoreline erosion.

### 6.1 Case study

The "Pantani della Sicilia Sud-Orientale" (South-East of Sicily lagoons, Fig. 6.1a) is a saline lagoon and wetland system in close connection with the adjacent coastal environment. The area hosts important breeding populations of rare and endangered species, representing a crucial migration hot-spot for bird species along the central Mediterranean migration flyway. Due to its naturalistic and biodiversity value, these region is included in international environmental protection frameworks (RAMSAR, Natura 2000), Special Protection Areas and regional nature reserves.

The Cuba-Longarini lagoons is the largest complex of wetlands in the area (Fig. 6.1b), covering an area of approximately 240 ha. They are separated from the sea by a narrow coastal fringe, consisting of a dunestrip and a sandy beach, and are intermittently connected to the sea by a small estuary channel, depending on the actual lagoon water level. The lagoons are characterized by shallow waters, with depth generally smaller than one meter.

The construction of the small town of Granelli in the 1970s, over the narrow fringe between the sea and the lagoons, has led to a reduction of hydraulic connectivity between the wetlands and the sea, alongside the degradation of the coastal dunebelt, over which the urbanized area is built. As a consequence, the area is subject to flooding due to intense runoffs from the lagoon side, and from wave storms from the side.



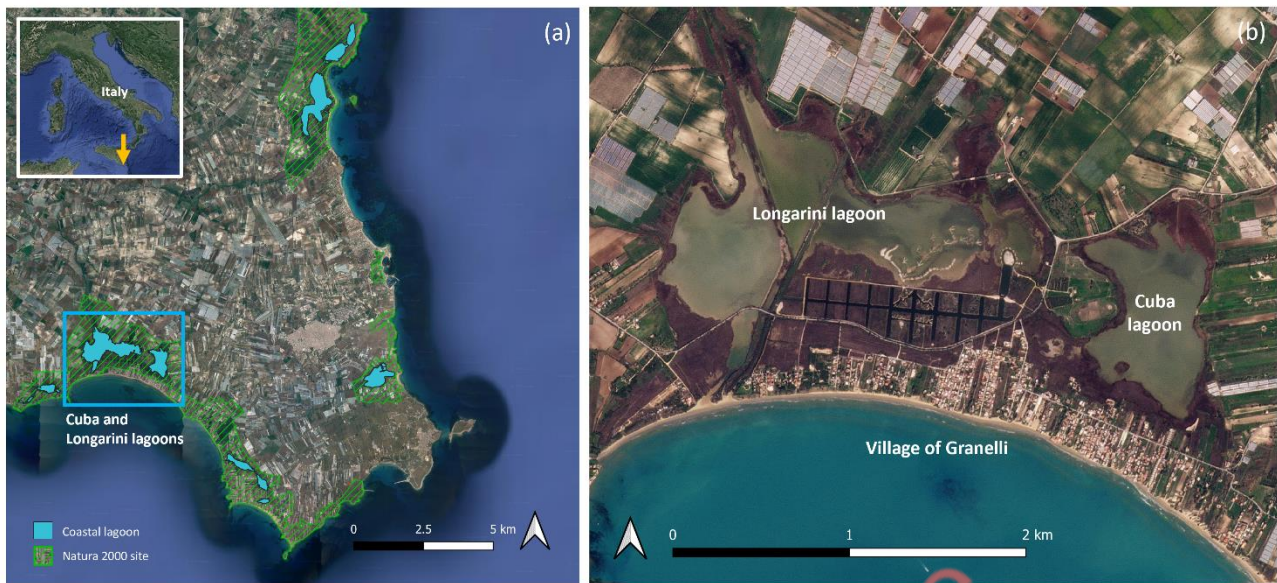


*Figure 6.1. a) Aerial view of the lagoons of the South-East of Sicily. b) aerial view of the Sicily lagoon pilot site area: the Cuba-Longarini lagoons.*

With the aim to mitigate coastal risk and restore biodiversity value, a range of Nature-based Solutions (NBSs) are investigated considering a current state (with actual active restoration measures) and proposed additional restoration measures. Indeed, as previously mentioned, the town of Granelli was built over a coastal dune strip, with consequences on the reduction of the sediment fluxes and the natural protection capabilities of the environment. A full dune reconstruction would rather be feasible due to the narrow space remaining in between the beach and the urbanized area. Instead, a revegetation to stabilize the dune and improve wave dissipation capabilities of the system could be envisaged. The chosen species is the endemic *Ammophila arenaria*, which is already marginally present on-site. The proposed intervention entails expanding the dune habitat by an area of about 4.3ha, stretching along the shoreline for a length of 3.3 km and extending across a width of 13 m (average). Furthermore, a replantation of the seagrass meadow in front of the town is also investigated. Specifically, an extension of the existing meadow of *Posidonia oceanica*, which is a protected marine plant, is designed to evaluate its capabilities to dissipate wave energy and reduce storm-induced erosion. The designed replantation of the seagrass extends for 104 ha, distributed around the existing meadow (7.7ha).

## 6.2 Materials and methods

In order to assess the performance of the solutions, a SWAN+XBeach modelling chain is setup. In the present chapter, the input data, the model setup and the pursued simulations are described.

### 6.2.1 Input data description

#### 6.2.1.1. Topographic and beach data

In order to build the SWAN numerical grid, bathymetric contours were taken from nautical charts (Istituto Idrografico della Marina, 2019). In order to build the Xbeach numerical grid, a Digital Elevation Model (DEM) of the study area was obtained from the Regional Geographic Information System of Sicilia Region. The DEM was recovered through LiDAR flights in 2013 and has an horizontal resolution of 2x2 m and vertical resolution

of 0.01 m. The DEM was combined with bathymetric data obtained through a multi-beam survey, previously carried out by the University of Catania, that covered the entire nearshore part of the domain in 2019. The dataset is integrated with data obtained by means of satellite images, drone data and field surveys, to include small artificial islands and channels built in 2023 to improve biodiversity value of the site.

The shoreline was obtained through PlanetScope satellite imagery (having 3x3 m resolution) by tracking the wet/dry boundary. Elevations from DEM, bathymetry and shoreline position were combined to assign elevation at the XBeach grid nodes through linear interpolation. The beach is made up by fine sand, with  $d_{50}=0.27\text{mm}$ , estimated based on several field samples collected at the Granelli beach.

### 6.2.1.2. Marine climate and sea level rise data

Present wave conditions were obtained from the MEDSEA MULTIYEAR WAV 006 012 reanalysis dataset (Korres et al., 2021) provided by the Copernicus Marine Service. The dataset spans the years 1993-2022 and includes hourly time series of marine climate, with a spatial resolution  $4.66 \times 4.66 \text{ km}$ .

Climate change projected wave conditions were taken from Ocean surface wave time series for the European coast from 1976 to 2100 derived from climate projections dataset (Caires et al., 2020). The dataset provides hourly time series on the marine wave climate derived from ocean surface wave parameters calculated across a European-wide domain. The ocean surface wave fields are generated through ECMWF's Wave Model (SAW), driven by surface wind and incorporating considerations for ice coverage at polar latitudes based on IPCC AR5 climate projections. The year timespan of the dataset is 2041-2100, with hourly temporal resolution and a spatial resolution of  $30 \times 30 \text{ km}$ .

The dataset includes projected wave conditions for two IPCC AR5 Representative Concentration Pathway (RCP) scenarios: one aligns with a more optimistic emission trajectory, wherein emissions begin to decline beyond 2040 (RCP4.5), and the other represents a pessimistic scenario where emissions persistently increase throughout the century, often referred to as the business-as-usual scenario (RCP8.5).

For both present and future projection datasets, significant wave height  $H_s$ , peak period  $T_p$  and mean wave direction  $\theta$  were extracted for present, RCP4.5 and RCP8.5 scenarios. The data were extracted in the correspondence of the grid point closest to our model offshore boundary (latitude  $36.69^\circ\text{N}$ , longitude  $15.00^\circ\text{E}$  - EPSG 32633).

The categorization of events based on their  $H_s$  and  $\theta$  was also carried out to identify the prevailing direction and the direction associated with the most energetic sea states. This analysis involved subdividing the directional sector from which waves originate into eight sub-sectors. Considering the geographical fetch of the site under investigation, the directional sector for wave propagation spans from  $150^\circ\text{N}$  to  $270^\circ\text{N}$ , covering a total width of  $120^\circ$ . Therefore, the whole sector was subdivided into eight sub-sectors, each spanning  $15^\circ$  (Fig. 6.2).

For each sub-sector, an extreme value analysis was conducted to obtain  $H_s$  associated with storms with given return period  $T_r$ . In order to be consistent among the present and future scenarios, the extreme value analysis was conducted considering the same length of for the time window of analysis. For the historical timeseries the time window corresponds to the actual extension of the dataset time series, namely 1993-2022 (present condition). For the RCP scenarios two year windows were considered instead, namely the 2041-2070 and the 2071-2100. Thus doing, the extreme value analysis is carried out considering a dataset 30 years long, for each scenario.

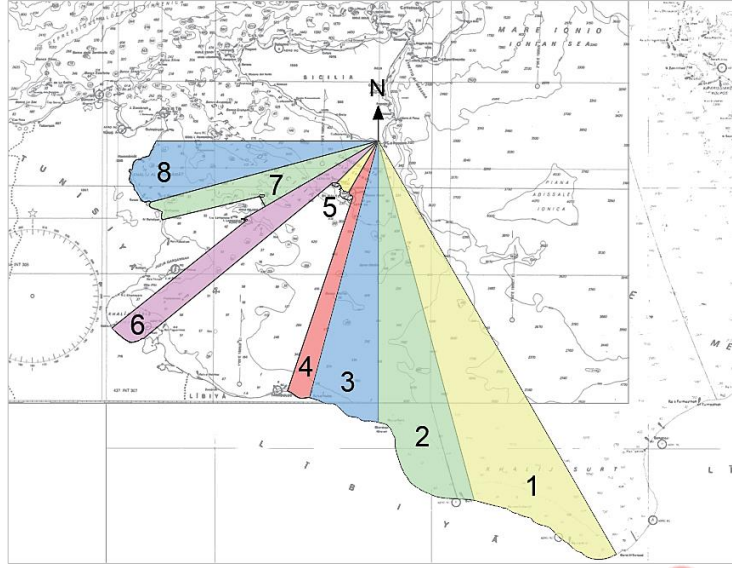


*Figure 6.2. Geographical fetch and wave directional sub-sectors.*

Extreme value analysis was conducted as follows. First, a Peak-Over Threshold method was used to identify peaks associated with storms within the extracted  $H_s$  timeseries, given an  $H_s$  threshold of 2.0 m and a minimum temporal distance between independent events equal to 12 hours (Boccotti, 2004). Then, a range of probability distributions (Weibull, Gumbel, LogNormal and Generalised Pareto) were tested against the storm  $H_s$  timeseries to check which one best-fits with the sample. The goodness-of-fit was tested by means of the Kolmogorov-Smirnov test. The Generalised Pareto distribution was identified as the best-fitting one for the extreme values of  $H_s$  for each one of the directional sub-sectors.

Finally, for each subsector  $H_s$  value for a return period  $T_r$  of 5, 50, 100 years was extracted from the adapted Pareto distribution. From a preliminary analysis of both the storms per each subsector and the geographical fetch, it was noted that a predominant occurrence of events came from the western directions. Consequently, the subsequent analysis was focused on the eighth subsector corresponding to the West ( $\theta = 262.5^\circ\text{N}$ ).

Concerning the peak period, the following site-specific correlations between  $T_p$  and  $H_s$  were defined by applying the least squares method to the available datasets:

$$T_p = 6.6301H_s^{0.2593} \quad (6.1)$$

$$T_p = 6.3327H_s^{0.2867} \quad (6.2)$$

$$T_p = 6.3224H_s^{0.2892} \quad (6.3)$$

for present, RCP4.5 and RCP8.5 scenarios, respectively.

Sea level rise projections based on IPCC AR6 for the years 2020-2100 were obtained from the NASA Sea Level Change projection tool at the closest geographical coordinates to our site (latitude  $36.00^\circ$  and longitude

14.00°). In IPCC AR6, the RCP scenarios have been replaced with Socioeconomic Pathways (SSP). Since there is no direct one-to-one correspondence between specific RCP and SSP scenarios, a combination of RCP and SSP scenarios can be chosen depending on the projected storyline to be investigated. Since considerations about future socio-economic projections at our study case are not available, we decided to combine RCP and SSP scenarios based on the same radiative forcing value. Therefore, wave conditions for RCP4.5 scenarios were matched with sea level rise projections for SSP2-4.5 scenario (radiative forcing equal to 4.5 W/m<sup>2</sup>). Similarly, data projected for RCP8.5 wave scenarios are associated with sea level rise corresponding to SSP5-8.5 scenario (radiative forcing equal to 8.5 W/m<sup>2</sup>). The sea level rise projection is the one corresponding to the last year of the examined year window, i.e. 2070 and 2100, for the 2041-2070 and 2071-2100 windows respectively.

In the end, we investigated 5 climatic scenarios, a present scenario (SP) based on the analysis of the historical re-analysis dataset, two climate change projection scenarios associated with a radiative forcings equal to 4.5 W/m<sup>2</sup> with 2070 and 2100 time horizons (S4.5-2070 and S4.5-2100 respectively), and two scenarios for radiative forcing equal to 8.5 W/m<sup>2</sup> scenarios (S8.5-2070 and S8.5-2100).

Considering the abovementioned, a range of hydrodynamic scenarios were investigated, based on combination of sea level rise and wave conditions at different return period (Table 6.1).

*Table 6.1. Present and future hydrodynamic scenarios investigated for the Sicily pilot site.*

Return Period [years]	Climatic scenario	Year window	HS [m]	TP [s]	SLR [m]
5	Present (SP)	1993 - 2022	4.26	9.65	0.00
	S4.5-2070	2041 - 2070	5.68	10.42	0.37
	S4.5-2100	2071 - 2100	5.16	10.14	0.57
	S8.5-2070	2041 - 2070	5.22	10.20	0.48
	S8.5-2100	2071 - 2100	5.48	10.34	0.78
50	Present (SP)	1993 - 2022	5.61	10.37	0.00
	S4.5-2070	2041 - 2070	8.06	11.52	0.37
	S4.5-2100	2071 - 2100	7.21	11.16	0.57
	S8.5-2070	2041 - 2070	6.67	10.95	0.48
	S8.5-2100	2071 - 2100	8.36	11.68	0.78
100	Present (SP)	1993 - 2022	6.01	10.56	0.00
	S4.5-2070	2041 - 2070	8.70	11.77	0.37
	S4.5-2100	2071 - 2100	7.75	11.39	0.57
	S8.5-2070	2041 - 2070	6.97	11.09	0.48
	S8.5-2100	2071 - 2100	9.18	12.00	0.78

#### 6.2.1.3. Vegetation data

The XBeach model allows to simulate the wave dissipation due to the presence of vegetation. To do so, characteristics of vegetation and spatial distribution of the vegetation must be given as input to the model. The spatial distribution of vegetation was obtained by EUNIS2019 habitat maps (Chytrý et al., 2020) integrated with field surveys.



### 6.2.2 Modelling setup

The SWAN computational domain extends for 2068 km<sup>2</sup>, encompassing approximately 90 km of coastline (Fig. 6.3a). The numerical grid consists of 17141 nodes. The unstructured grid resolution (i.e. distance between nodes) is variable and bathymetry-dependent. For depths greater than 100 m, the elements have a side of 1 km. For depths between 100 m and 30 m, the size gradually changes from 1 km to 400 m. For depth less than 30 m, the elements maintain a size of 400 m. A higher resolution (100 m) was adopted in the proximity of the XBeach domain.

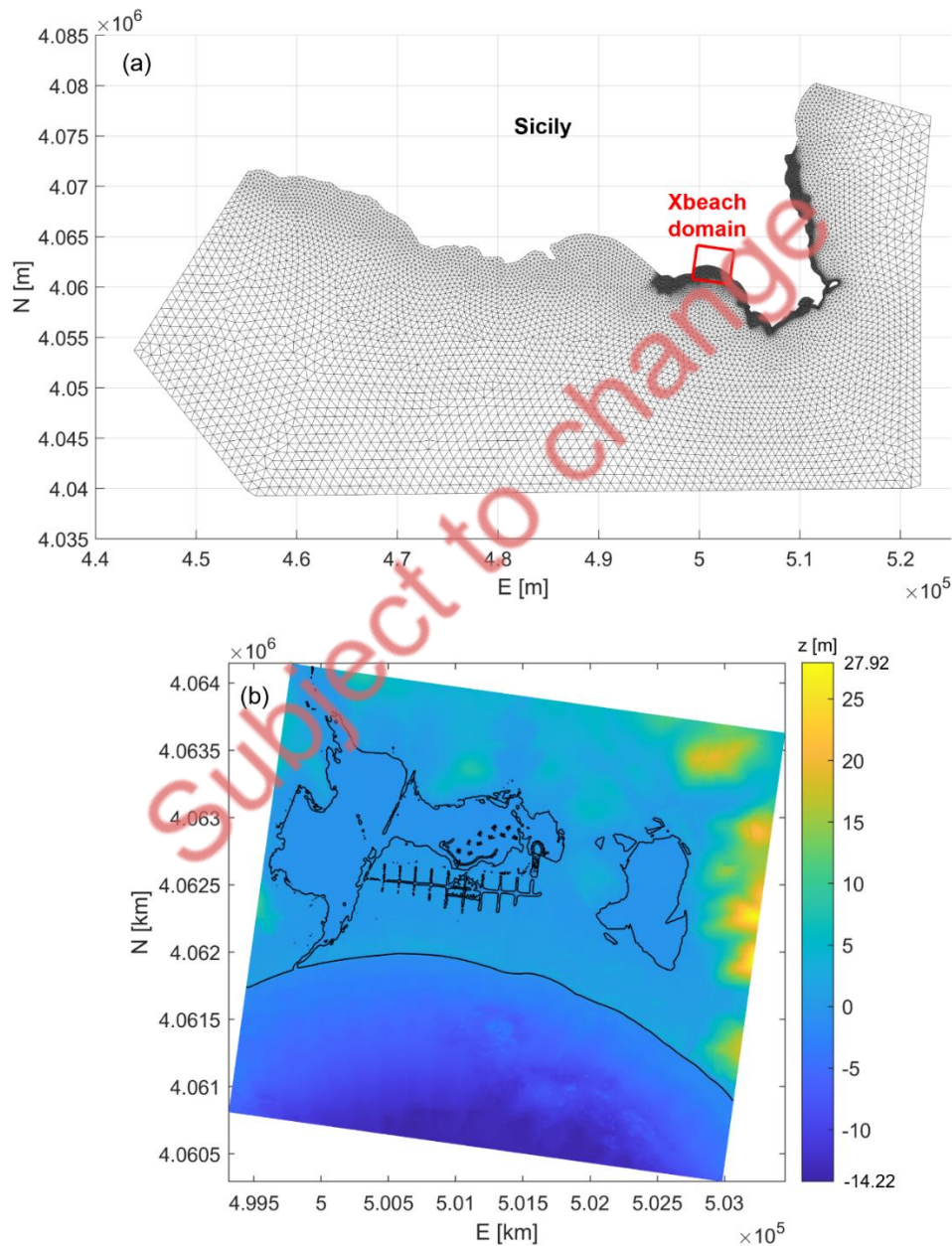


**Figure 6.3.** a) SWAN numerical grid. The red rectangle shows the nested Xbeach domain. b) XBeach numerical grid with associated elevation values in color scale.

The XBeach computational domain (Figure 6.3b) is nested into the SWAN domain and consists of a 3.36 km cross-shore and 3.69 km long-shore tile, consisting of a total surface of 12398 km<sup>2</sup>, enclosing the Cuba-Longarini lagoon system, Granelli town and beach. A structured grid with variable resolution was built within the domain, ranging 2.5 - 10 m cross-shore and 5 - 10 m longshore. The grid is made up by 1150 (cross-shore) x 544 (long-shore) cells, for a total of 625,600 nodes. To each cell node, an elevation value is associated based on the topographical data mentioned in Section 6.2.1.

The XBeach model allows to simulate wave dissipation due to presence of vegetation by implementing a dissipative term in the short-wave action balance equation (Holthuijsen et al, 1989):

$$\frac{\partial A}{\partial t} + \frac{\partial c_x A}{\partial x} + \frac{\partial c_y A}{\partial y} + \frac{\partial c_\theta A}{\partial \theta} = - \frac{D_b + D_f + D_v}{\sigma} \quad (6.4)$$

where  $A$  is the wave action,  $c_x$ ,  $c_y$  and  $c_\theta$  are the propagation speeds in the  $x$ -,  $y$ - and  $\theta$ - domains respectively,  $D_b$  is the wave energy dissipated by breaking,  $D_f$  is the wave energy dissipated by bottom friction,  $\sigma$  is the wave angular frequency and

$$D_v = \sum_{i=1}^{n_{sec}} D_{v,i} \quad (6.5)$$

is the wave energy dissipated by vegetation, where  $n_{sec}$  is the number of vegetation vertical sections and  $D_{v,i}$  is the short-wave energy dissipation due to the vegetation layer  $i$

$$D_{v,i} = \frac{1}{2\sqrt{\pi}} \rho \widetilde{C}_d b_v N_v \left( \frac{kg}{2\sigma} \right)^3 \frac{(\sinh^3 k\alpha_i h - \sinh^3 k\alpha_{i-1} h) + 3(\sinh k\alpha_i h - \sinh k\alpha_{i-1} h)}{3k \cosh^3 kh} H_{rms}^3 \quad (6.6)$$

where  $\widetilde{C}_d$  is the drag coefficient,  $\rho$  is the water density,  $b_v$  is the vegetation stem diameter,  $N_v$  is the number of vegetation stems per m<sup>2</sup>,  $k$  is the wave number,  $h$  is the water level,  $\alpha_i$  is the relative vegetation height for layer  $i$  (Suzuki et al., 2012; van Rooijen et al., 2015)

For each habitat within the study area, a representative vegetation species is assigned based on a cross-comparison between EUNIS habitat mapping and field surveys. The pertinent characteristics of the vegetation, such as the number of vertical sections ( $n_v$ ), vertical section height ( $\alpha h$ ), drag coefficient ( $\widetilde{C}_d$ ), stem diameter ( $b_v$ ), and vegetation density ( $N$ ) were sourced from relevant literature (Knutson et al., 1982; Garzon et al., 2019; Fernández-Montblanc et al., 2020; van Loon-Steensma et al., 2016) and local expert approach. The specific values employed in the study are presented in Table 6.2. Vegetation maps for current state (including already performed restoration), dune revegetation, and seagrass revegetation used in Xbeach are shown in Fig. 6.4a,b, and c respectively.

Table 6.2. Vegetation characteristics associated with EUNIS habitat codes

Species	Associated habitat (EUNIS code)	nsec	$\alpha h$ [m]	$\tilde{C}_d$ [-]	bv [m]	Nv
<i>Ammophila arenaria</i>	Shifting coastal dunes (N14)	1	1	0.7	0.0025	260
<i>Spartina alterniflora</i>	Coastal saltmarshes and saline reedbeds (MA25)	1	0.625	1	0.003	400
<i>Phragmites australis</i>	Reedbeds normally without free-standing water (Q51)	2	0.25	0.86	0.006	110
			2	0.86	0.026	110
<i>Posidonia oceanica</i>	Biocenosis of <i>Posidonia oceanica</i> (MB252)	1	0.50	1	0.01	280

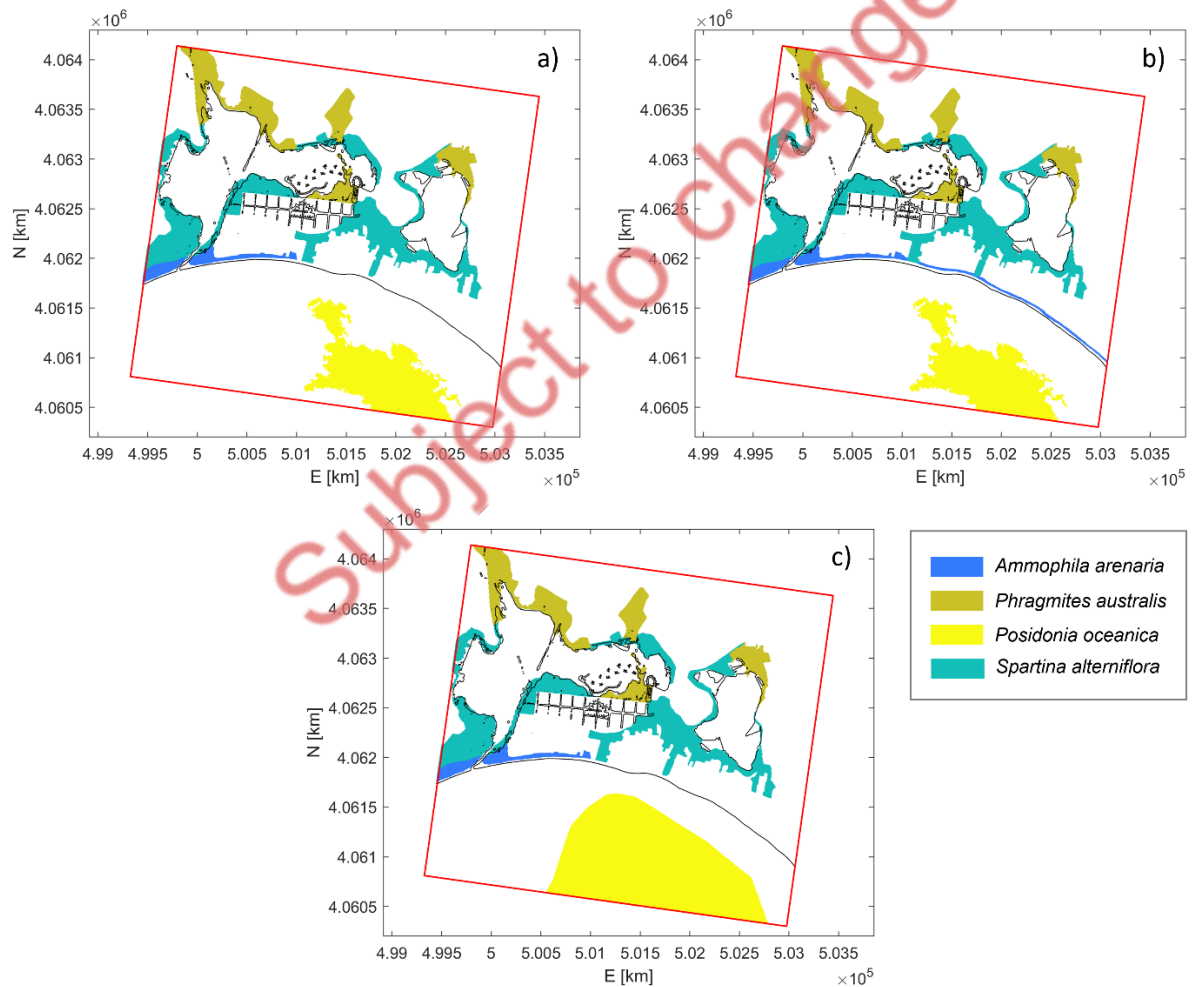


Figure 6.4. Vegetation maps used as inputs in Xbeach for: (a) current state, (b) dune revegetation, (c), seagrass revegetation.

### 6.2.3 Model validation

The model validation is carried out for both SWAN and XBeach, to evaluate hydrodynamic and morphodynamic accuracy of the modelling chain. The model is validated considering a real storm event occurred from 21st of April 2022 06:00 UTM+1 to 22nd April 2022 07:00 UTM+1. The storm lasted 25 hours and reached a  $H_s$  at the peak of the storm equal to 4.19 m, measured in the correspondence of a wave buoy, installed by the University of Catania in front of the beach of Granelly in the framework of the INTERREG Italia-Malta Project NEWS. The storm was chosen because its energy was high enough to produce a significant modification of the shoreline, which was clearly detectable from PlanetScope satellite images. Therefore, the shoreline on the 19th of April 2022 was taken as the initial one.

The storm is propagated by the SWAN-Xbeach modelling chain, then the estimated post-storm coastline is compared with the one measured from the first clear available satellite image following the storm, corresponding to the 4th of May 2022. No other storms occurred between the end of the chosen storm event and the 4th of May

In particular, hourly wave data from 20th of April 2022 00:00 UTM+1 to 25th of April 2022 00:00 UTM+1 (120 hours) were extracted from MEDSEA MULTIYEAR WAV 006 012 reanalysis dataset. Data are extracted in the correspondence of the reanalysis model grid point closest to the SWAN offshore boundary (36.4792 lat, 15.0000 lon). Then, each hourly seastate was simulated, for a total of 120 SWAN simulations. Fig. 6.5 shows the significant wave height measured by the wave buoy (blue line) and the model prediction (black dots).

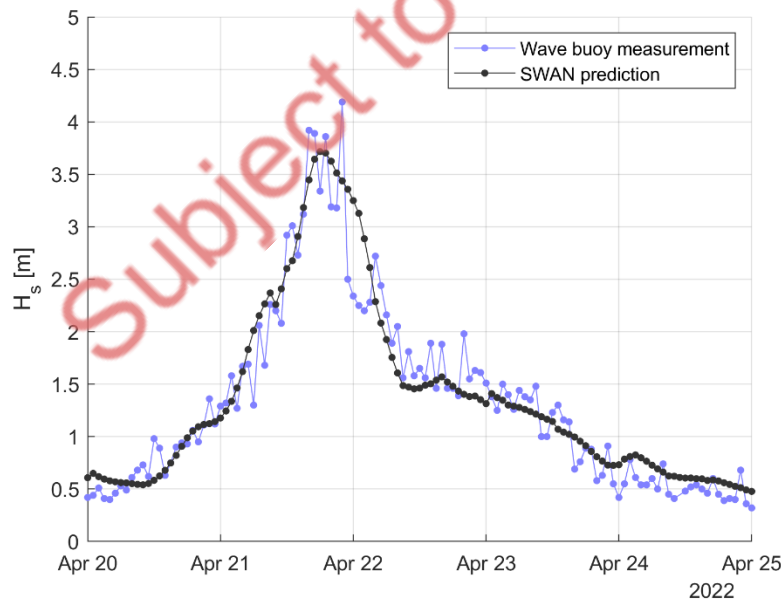


**Figure 6.5.** Significant wave height of the storm used for validation of the model, measured by local wave buoy (blue) and SWAN prediction at the grid node closest to buoy position (black).

To assess SWAN model prediction performance, the following metrics are computed:

$$B = \frac{1}{N} \sum_{i=1}^N (H_{s,mod,i} - H_{s,obs,i}) \quad (6.7)$$



where  $B$  stands for Bias, and it is an indicator of the tendency of the model to over- or under-predict observed values,  $N$  is the number of samples, and  $H_{s,obs,i}$  and  $H_{s,mod,i}$  are the  $i$ -th observed and modelled significant wave heights respectively;

$$RMSE = \sqrt{\frac{1}{N} \sum_{i=1}^N (H_{s,obs,i} - H_{s,mod,i})^2} \quad (6.8)$$

where  $RMSE$  stands for root-mean square error and it is a dimensional metric to quantify accuracy of the model to reproduce observed values, and

$$WSS = 1 - \frac{\sum_{i=1}^N (H_{s,obs,i} - H_{s,mod,i})^2}{\sum_{i=1}^N (|H_{s,mod,i} - \langle H_{s,obs} \rangle| + |H_{s,obs,i} - \langle H_{s,obs} \rangle|)^2} \quad (6.9)$$

where WSS is the Willmott Skill Score, also known as Willmott agreement index (Willmott, 1981), which is a nondimensionalized indicator of the agreement between predicted and observed values, ranging from 0 (complete disagreement) to 1 (perfect agreement).

Bias resulted equal to 0.02 m, resulting in the model not having a strong tendency to over- or under-estimate observed values. RMSE resulted equal to 0.37 m, whereas WSS is equal to 0.95, showing a highly satisfactory agreement between model and measured values.

In the following, the validation of the capabilities of XBeach to correctly predict storm morphodynamics is illustrated. Preliminarily, it should be recalled that XBeach allows to decouple hydrodynamic and morphodynamic time by means of morphodynamic acceleration. In other words, morphological changes can be accelerated by a certain morphodynamic factor (up to 10), by keeping the same duration of the hydrodynamic event. Given the above, the following procedure is carried out:

- (i) Five sea states have been chosen from the selected storm, with each sea state being 5 hours apart from the next one.
- (ii) Five runs have been performed to simulate the above mentioned five sea states, with XBeach simulating 0.5 hours of hydrodynamic time and 5 hours of morphodynamic time, with a morphodynamic acceleration factor equal to 10.
- (iii) After the first simulation is run (simulating sea state no.1), the final bed elevation of simulation n.1 is extracted and given as a bed elevation input to simulation no.2 (simulating sea states no.2).
- (iv) The procedure is repeated up to simulation no. 5.
- (v) The location of the computed shoreline after simulation no. 5 (sea state no.5), corresponding to 25 hours after the beginning of the storm, is extracted and compared with the post-storm coastline obtained from satellite image after the storm, corresponding to the 4th of May 2022.

Fig. 6.6 shows the sea-states generated in XBeach with the abovementioned methodology.

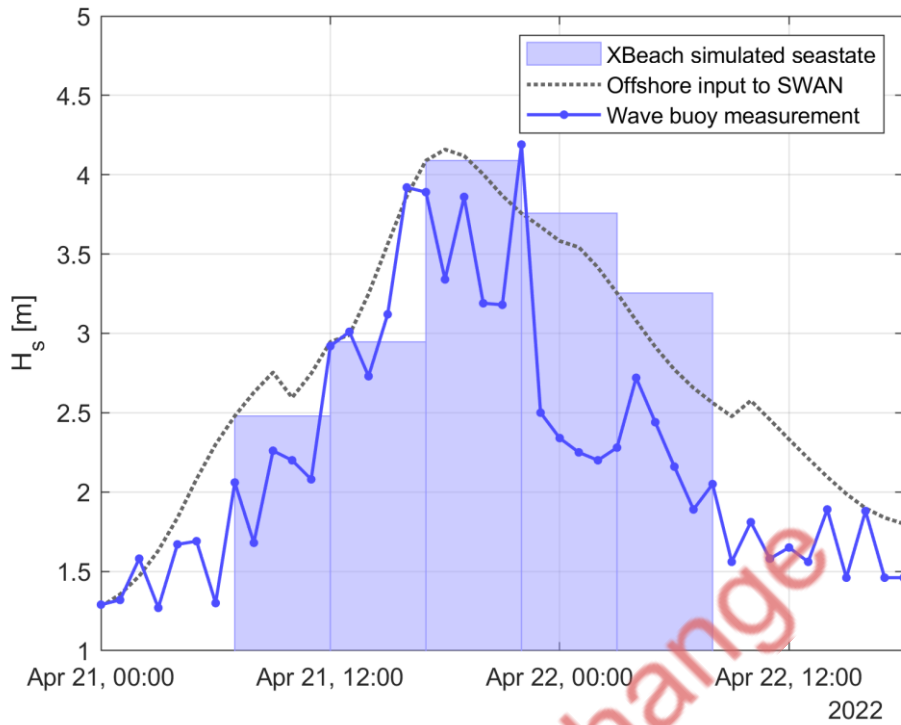


Figure 6.6. Storm seastates generated for validation

Fig. 6.7 shows the pre-storm (blue line), post-storm (green line) shorelines obtained from satellite imagery and post-storm shoreline predicted by the model (red line). To evaluate the performance of the model setup in reproducing correctly storm morphodynamics of the site, the post-storm shoreline obtained from satellite imagery is compared with the one resulted from the model simulations. In order to quantify the comparison, 30 transects orthogonal to the pre-storm shoreline are considered. For each transect, the distance between observed pre-storm and observed ( $d_{obs}$ ) and modelled ( $d_{mod}$ ) post-storm shorelines is measured. To assess prediction skill of the model, the following metrics are computed

$$B = \frac{1}{N} \sum_{i=1}^N (d_{mod,i} - d_{obs,i}) \quad (6.10)$$

where  $B$  stands for Bias,  $N$  is the number of samples, and  $d_{mod,i}$  and  $d_{obs,i}$  are the  $i$ -th observed and modelled significant wave heights respectively; and the RMSE

$$RMSE = \sqrt{\frac{1}{N} \sum_{i=1}^N (d_{mod,i} - d_{obs,i})^2} \quad (6.11)$$

Bias resulted equal to 0.91 m, i.e. 6.7% of the average beach observed retreat at each transect (14.28 m), revealing only a minor tendency of the modelled shoreline to retreat, i.e. over-predicting erosion, whereas RMSE resulted equal to 2.55 m.

Moreover, the Brier Skill Score, or BSS (Sutherland, 2004) is computed. The BSS is a commonly used score in coastal modelling to validate morphodynamic modelling by comparing modelled and observed post-storm

beach profiles with a pre-storm baseline. In this application, since data pre- (nor post-) storm observations of beach profiles are not available, BSS is applied to shoreline change. BSS is calculated according to the Murphy-Epstein decomposition (Murphy and Epstein, 1989):

$$BSS = \frac{\alpha - \beta - \gamma + \varepsilon}{1 + \varepsilon} \quad (6.12)$$

where

$$\alpha = r^2 \quad (6.13)$$

$$\beta = \left( r - \frac{\sigma_{d,mod}}{\sigma_{d,obs}} \right)^2 \quad (6.14)$$

$$\gamma = \left( \frac{\langle d_{mod} \rangle - \langle d_{obs} \rangle}{\sigma_{d,obs}} \right)^2 \quad (6.15)$$

$$\varepsilon = \left( \frac{\langle d_{obs} \rangle}{\sigma_{d,obs}} \right)^2 \quad (6.16)$$

where  $r$  is the correlation coefficient between  $d_{obs}$  and  $d_{mod}$ ,  $\sigma_{d,obs}$  and  $\sigma_{d,mod}$  indicate the standard deviation of  $d_{obs}$  and  $d_{mod}$  respectively, and angular brackets denote the mean of a set of observations/predictions. Perfect modelling would lead to  $\alpha = 1$ ,  $\beta = 0$  and  $\gamma = 0$ , and therefore to a BSS = 1. Results from our model give  $\alpha = 0.79$ ,  $\beta = 0.09$  and  $\gamma = 0.04$ , leading to a BSS equal to 0.97, therefore resulting in an excellent satisfactory shoreline change prediction skill of our model.

Largest discrepancies were observed in the proximity of the lagoon-sea channel, up to 6.42 m at transect V3. This is due to the inherent morphological dynamic of the estuarine region, which is also influenced by the river discharges, which are not integrated in the model yet. In any case, since the focus of the present study is to assess the capability of the NBS to reduce erosion and flooding risk in the city area, their influence on the evolution of the estuarine mouth is presently not taken into account in the investigation.

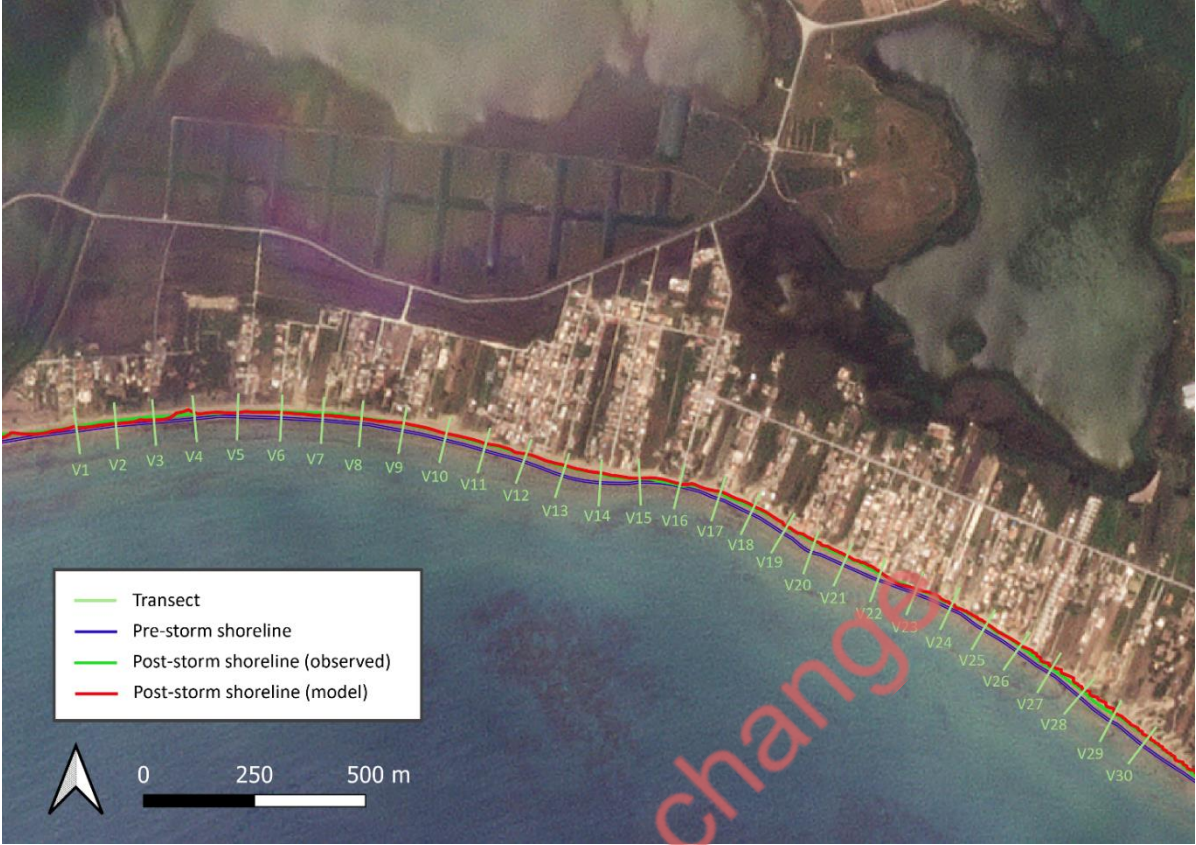


*Figure 6.7. Pre-storm (blue line), post-storm (green line) shorelines obtained from satellite imagery and post-storm shoreline predicted by our model (red line). The figure shows the position of the 30 transects along which shoreline observed and predicted shoreline retreat is computed.*



### 6.2.4 Simulations

Table 6.2 shows the plan of the numerical simulations, which have been obtained by combining all hydrodynamic scenarios, and the three restoration scenarios (current state, dune revegetation, seagrass revegetation).

## 6.3 Performance of the Nature-Based solutions under different climate scenarios

In the present section, results from the simulations are shown and performance of the investigated Nature-based Solutions to reduce coastal hazard is evaluated by means of simple efficiency indicators. To assess the performance of the solution to reduce flooding risk, efficiency of flooding reduction  $E_f$  is evaluated:

$$E_f = \frac{A_{f,CS} - A_{f,NbS}}{A_{f,CS}} \cdot 100 \quad (6.17)$$

where  $A_{f,CS}$  is the flooded area due to inundation in current state conditions (no new NbS, other than lagoon islands and channels, that are intended for biodiversity and water quality improvement, but have negligible impact on coastal risk reduction),  $A_{f,NbS}$  is the flooded area due to wave storm considering an NbS option (dune revegetation or seagrass revegetation). An efficiency indicator for flooding reduction for the city area  $E_{fc}$  is also computed, which is calculated analogously to  $E_f$ , but including the flooded areas due to inundation in the city area only.

Fig. 6.8 shows the inundation map for an present scenario (SP, SLR = 0.000 m), current state (no NBS), with 100 years Tr storm conditions ( $H_s = 6.01$  m,  $T_p = 10.56$  s).

The figure shows the maximum water levels  $z_{w,max}$  reached during the simulation due to wave storm. A significant inundation of the low-lying area in the proximity of the Longarini lagoon discharge channel is observed on the left side of the map. The city area (bounded by the gray line) appears to be not significantly affected by inundation, with limited water levels mainly in the western part of the city, close to the Longarini discharge channel, and inbetween the two central city blocks, which however hosts a plain land lot which can presently absorb the flooding. The total flooded area is 0.229 km<sup>2</sup>, whereas the city flooded area is 0.019 km<sup>2</sup>.

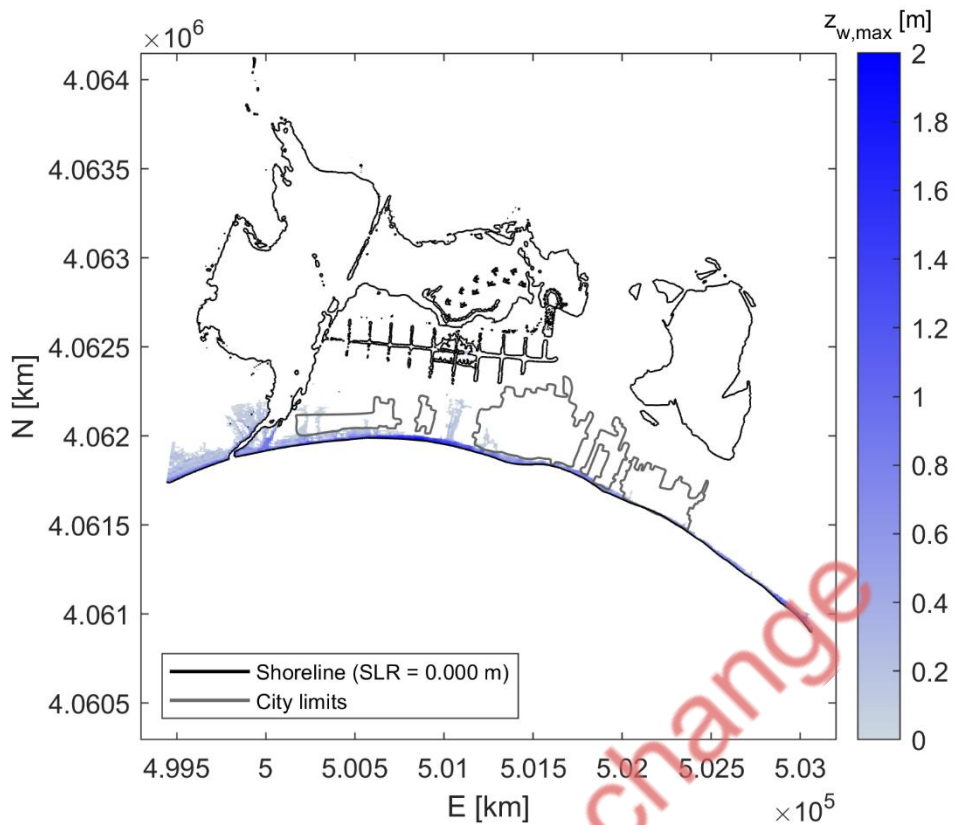
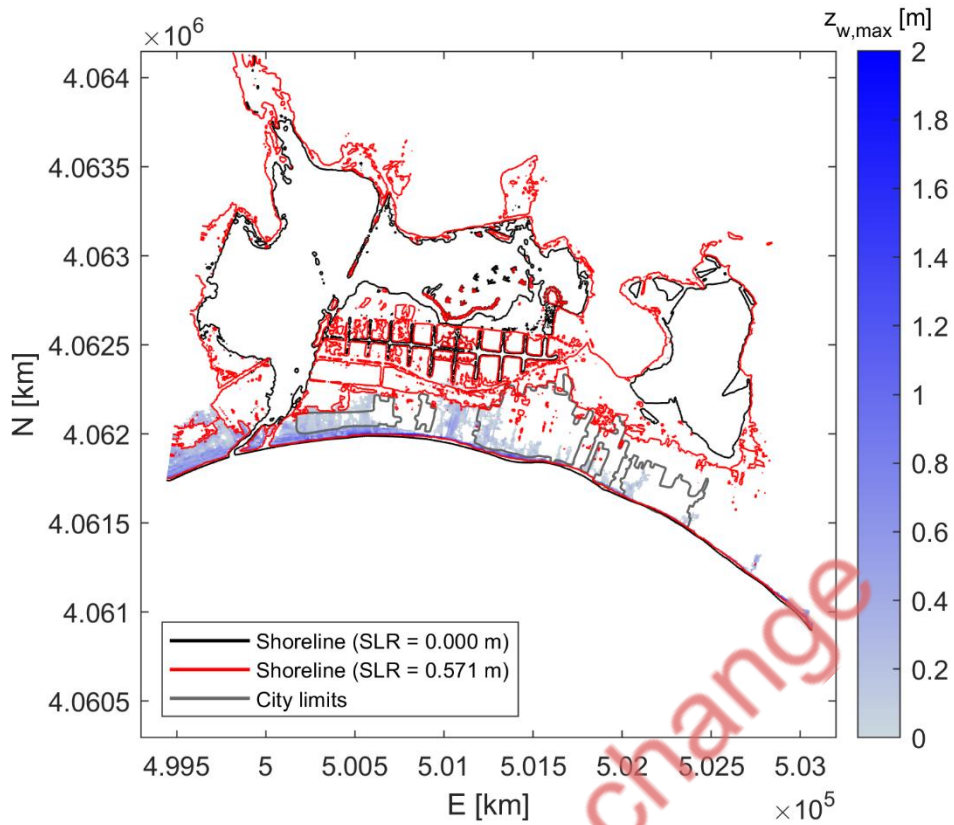


Figure 6.8. Inundation map for present scenario (SP),  $T_r = 100$  years, current state,  $H_s = 6.01$  m,  $T_p = 10.56$  s,  $SLR = 0.000$  m.

Fig. 6.9 shows the S45-2100 simulation, current state, for 100 years  $T_r$  storm wave conditions ( $H_s = 7.75$  m,  $T_p = 11.39$  s) and  $SLR = 0.571$  m.

The increase in sea level leads to significant extension of the area covered by the two lagoons, leading to an opening of a second channel to the Longarini lagoon area. Low-lying land lots between city and lagoons, now lie below the mean sea level, with some of them hydraulically connected with the lagoons. In this scenario, the inundated area significantly increases reaching  $0.361$  km<sup>2</sup> over the whole investigated domain and  $0.095$  km<sup>2</sup> within the city area (23% of the total city area). Furthermore, the city area results to be threatened by the increase of the lagoon water level.



**Figure 6.9.** Inundation map for simulation S4.5-2100 ( $T_r = 100$  years) scenario, current state,  $H_s = 7.75$  m,  $T_p = 11.39$  s,  $SLR = 0.369$  m

Fig. 6.10 shows the inundation maps, with a zoom on the city area, for simulated scenario S4.5-2100 with 100 years  $T_r$  storm wave conditions ( $H_s = 7.75$  m,  $T_p = 11.39$  s) and  $SLR = 0.571$  m, for current state (subpanel 6.8a), dune revegetation (subpanel 6.9b), subpanel (6.9c). From the comparison between the subpanels, the two interventions both reduce flooded areas due to waves, especially in the eastern part of the domain reaching a flooding reduction efficiency for the whole investigated domain  $E_f$  of 10.05% and 22.09% for dune revegetation and seagrass revegetation respectively. The eastern city blocks are the ones that benefit the most from the flooding reduction in the city, with  $E_{fc}$  of 20.45% and 52.57% for dune revegetation and seagrass revegetation respectively.

Table 6.3. Plan of simulations

id	Tr [years]	Restoration scenario	Climatic scenario	HS [m]	TP [s]	SLR [m]
1	5	Current state (no NbS)	Present (SP)	4.26	9.65	0.00
2			S4.5-2070	5.68	10.42	0.37
3			S4.5-2100	5.16	10.14	0.57
4			S8.5-2070	5.22	10.20	0.48
5			S8.5-2100	5.48	10.34	0.78
6	5	Dune revegetation	Present (SP)	4.26	9.65	0.00
7			S4.5-2070	5.68	10.42	0.37
8			S4.5-2100	5.16	10.14	0.57
9			S8.5-2070	5.22	10.20	0.48
10			S8.5-2100	5.48	10.34	0.78
11	5	Seagrass revegetation	Present (SP)	4.26	9.65	0.00
12			S4.5-2070	5.68	10.42	0.37
13			S4.5-2100	5.16	10.14	0.57
14			S8.5-2070	5.22	10.20	0.48
15			S8.5-2100	5.48	10.34	0.78
16	50	Current state (no NbS)	Present (SP)	5.61	10.37	0.00
17			S4.5-2070	8.06	11.52	0.37
18			S4.5-2100	7.21	11.16	0.57
19			S8.5-2070	6.67	10.95	0.48
20			S8.5-2100	8.36	11.68	0.78
21	50	Dune revegetation	Present (SP)	5.61	10.37	0.00
22			S4.5-2070	8.06	11.52	0.37
23			S4.5-2100	7.21	11.16	0.57
24			S8.5-2070	6.67	10.95	0.48
25			S8.5-2100	8.36	11.68	0.78
26	50	Seagrass revegetation	Present (SP)	5.61	10.37	0.00
27			S4.5-2070	8.06	11.52	0.37
28			S4.5-2100	7.21	11.16	0.57
29			S8.5-2070	6.67	10.95	0.48
30			S8.5-2100	8.36	11.68	0.78
31	100	Current state (no NbS)	Present (SP)	6.01	10.56	0.00
32			S4.5-2070	8.70	11.77	0.37
33			S4.5-2100	7.75	11.39	0.57
34			S8.5-2070	6.97	11.09	0.48
35			S8.5-2100	9.18	12.00	0.78
36	100	Dune revegetation	Present (SP)	6.01	10.56	0.00
37			S4.5-2070	8.70	11.77	0.37
38			S4.5-2100	7.75	11.39	0.57
39			S8.5-2070	6.97	11.09	0.48
40			S8.5-2100	9.18	12.00	0.78
41	100	Seagrass revegetation	Present (SP)	6.01	10.56	0.00
42			S4.5-2070	8.70	11.77	0.37
43			S4.5-2100	7.75	11.39	0.57
44			S8.5-2070	6.97	11.09	0.48
45			S8.5-2100	9.18	12.00	0.78

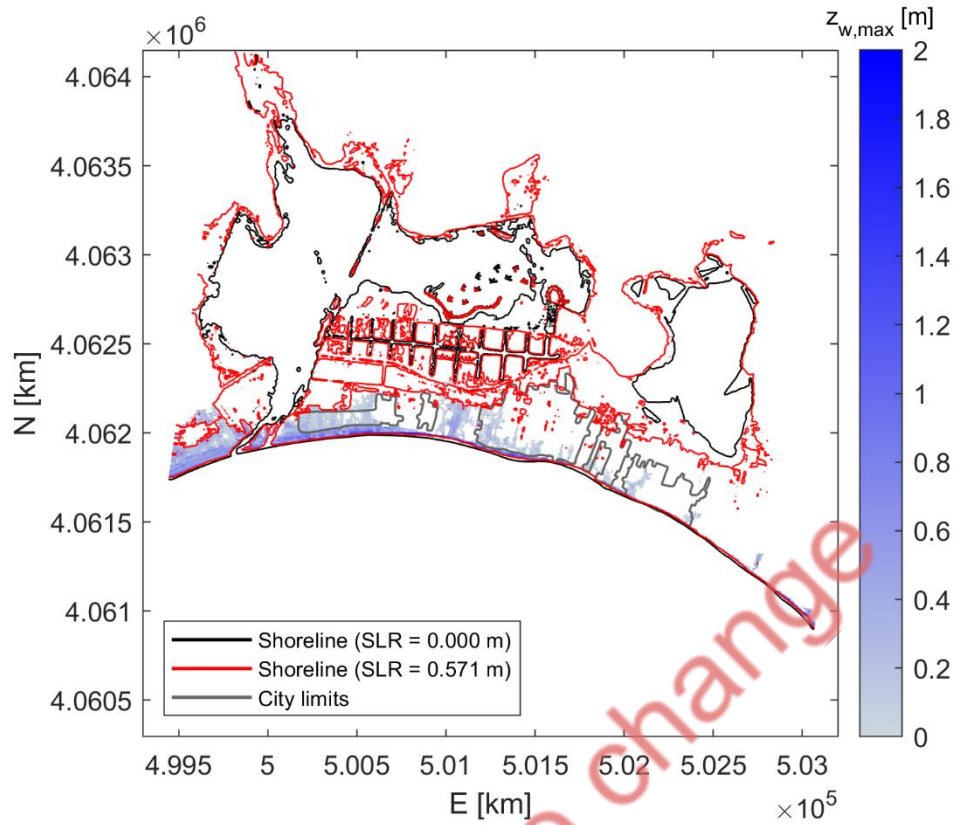


**Figure 6.10.** Inundation map for simulation S4.5-2100 ( $Tr = 100$  years) scenario, current state,  $H_s = 7.75$  m,  $T_p = 11.39$  s,  $SLR = 0.369$  m



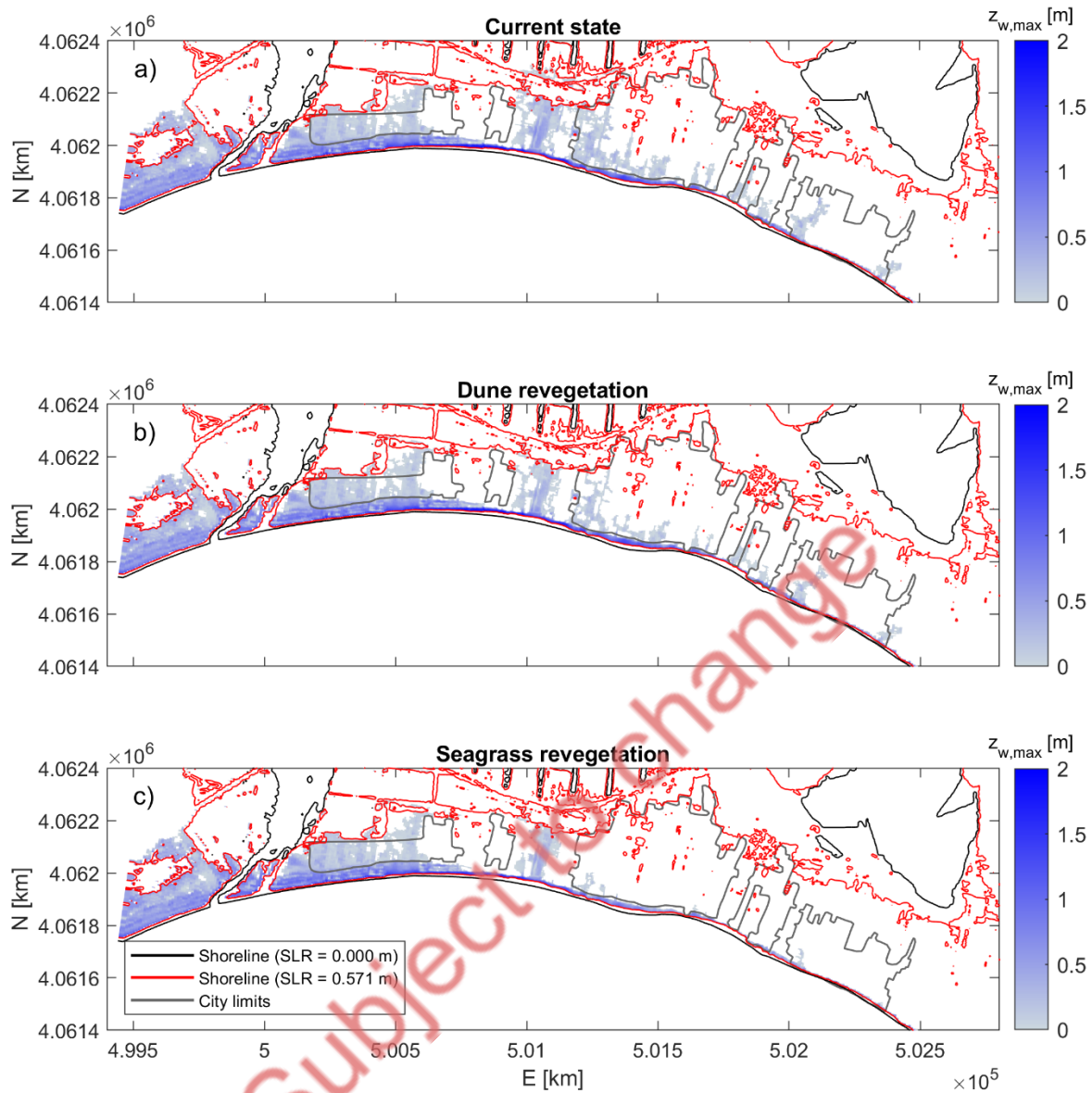


**Figure 6.11.** Inundation maps for simulation scenario S4.5-2100,  $Tr = 100$  years ( $H_s = 7.75$  m,  $T_p = 11.39$  s,  $SLR = 0.369$  m): a) current state, b) dune revegetation, c) seagrass revegetation.

To provide an overall view of the efficiency of the investigated NbS, the bar plot in Fig. 6.11a illustrates the flooded areas due to inundation in the city area for all the simulations with  $Tr = 100$  years. Fig. 6.11a reveals that the most severe scenario in terms of flooded city areas is the S8.5-2100, with 0.238 km<sup>2</sup> of flooded area, 59% of the city area. In all the investigated scenarios, the proposed NBS contribute to reduction of inundated areas, with flooding reduction efficiency indicator ranging from 11 to 24% for dune revegetation and from 51% to 57% for seagrass revegetation (Figure 6.11b).

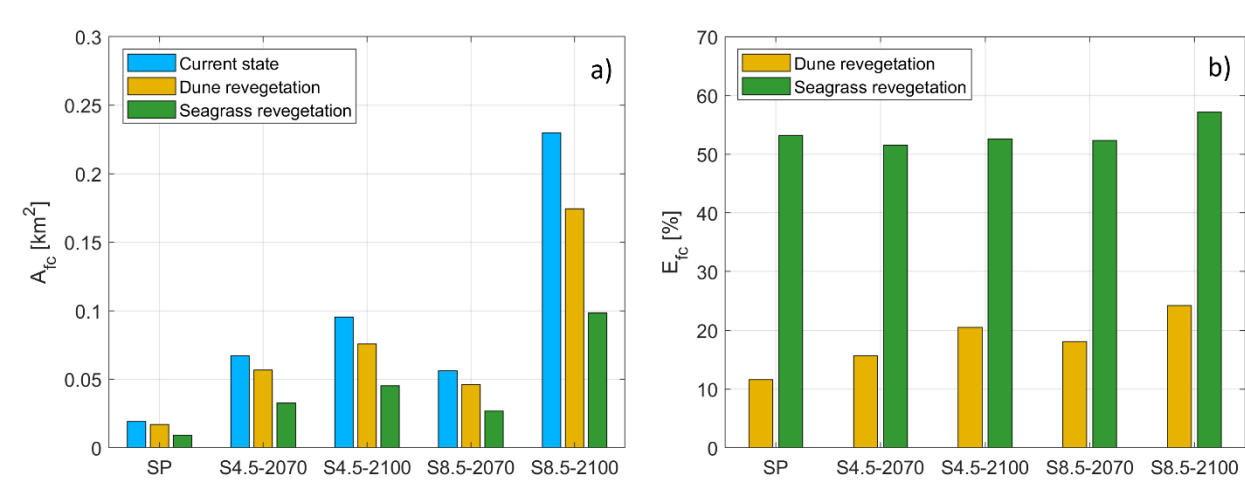


Figure 6.12. a) Flooded areas due to wave storm ( $T_r = 100$  years) in the city area; b) Flooding reduction efficiency percentage due to proposed NBS

Concerning the capability of the NbS to reduce erosion due to wave storm, an erosion reduction efficiency indicator  $E_e$  is computed as:

$$E_e = \frac{d_{CS} - d_{NBS}}{d_{CS}} \cdot 100 \quad (6.18)$$

where  $d_{\_}$  is the distance between the shoreline position at time 0, to the position of the shoreline at the end of the simulation ( $t = 1800$  s). The distance is measured along a transect, specifically, three transects have been chosen and their position is depicted in Figure 6.12a (T1, T2, T3 in green). By means of this indicator, shoreline retreat is a positive value, whereas a shoreline advancement will result in a negative value. The subscript CS indicates a current state simulation, whereas NBS indicates a simulation with an implemented NBS. A preliminary analysis revealed that the dune revegetation intervention exerts a negligible influence on the shoreline position, therefore the performance in reducing erosion is investigated only for the seagrass revegetation.

Figure 6.13a shows shoreline change maps for S8.5-2070 climatic scenario, i.e. with  $H_s = 6.97$  m,  $T_p = 11.09$  and  $SLR = 0.476$  m ( $T_r = 100$  years), for current state. Figure 6.13b illustrates a close-up view of the region corresponding to the dark gray dashed rectangle in Figure 6.13a, whereas Figure 6.13c show the same close-up view but for a simulation with seagrass revegetation. Comparing the results in the subpanels b and c, the presence of the revegetated seagrass meadow mitigate the shoreline retreat due to the wave storm. The shoreline retreat for the current state  $d_{CS}$  at transect T2 is 3.61 m, whereas for the seagrass revegetation case  $d_{NBS}$  is 0.79 m; the erosion reduction efficiency indicator  $E_e$  is equal to 78.12%. Table 6.4 lists the  $d_{CS}$ ,  $d_{NBS}$  and  $E_e$  for all the hydrodynamic scenarios and for all the examined transects. The table reveals that the best performance is given by the seagrass revegetation at the transect T2, with  $E_e$  ranging between 80.00 and 91.76%. Similarly, in the correspondence of transect T3, nearby the eastern city block, the seagrass revegetation also mitigates shoreline retreat, with  $E_e$  ranging between 13.53 and 56.32%. A more complex dynamics is observed close to transect T1, with outcomes of advancements/retreats depending on the different scenarios. This is probably related by the morphodynamics at the estuarine channel.

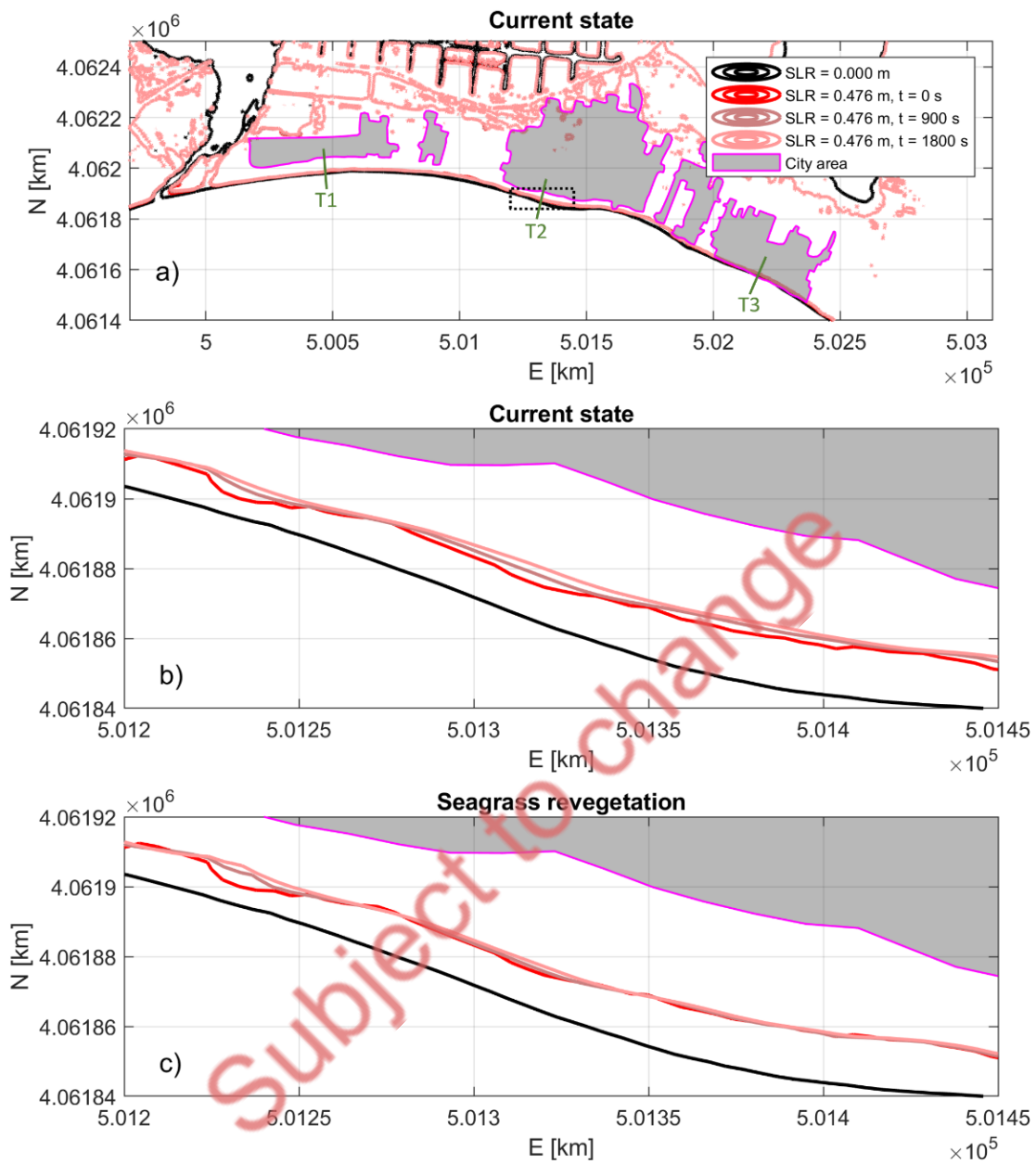


**Figure 6.13.** (a) Shoreline change for simulated scenario S8.5-2070 ( $T_r = 100$  years), current state (No NBS) (b) zoom in the city area (corresponding to the dashed rectangle in subpanel 6.9a); (c) same scenario but with seagrass revegetation NBS, zoom in the city area.

*Table 6.4. Shoreline change distances and erosion efficiency indicator obtained by the comparison of current state and seagrass revegetation simulations*

Scenario	Transect T1			Transect T2			Transect T3		
	dCS [m]	dNbS [m]	Ee [%]	dCS [m]	dNbS [m]	Ee [%]	dCS [m]	dNbS [m]	Ee [%]
SP	-2.99	-0.34	88.63	3.70	0.40	89.19	0.87	0.38	56.32
S4.5-2070	0.47	1.04	-121.28	4.51	0.61	86.70	2.77	1.44	48.01
S4.5-2100	1.96	1.95	0.51	3.64	0.30	91.76	3.42	2.94	13.53
S8.5-2070	1.69	1.97	-16.57	3.61	0.79	78.12	3.96	2.30	41.92
S8.5-2100	3.83	3.87	-1.04	3.90	0.78	80.00	2.85	1.43	49.82

## 6.4 Conclusions

To conclude, both the proposed additional Nature-based Solutions, specifically addressed to coastal risk reduction, seem to provide a notable contribution in mitigating both wave-induced coastal flooding and erosion in the urbanized area. However, the SLR projections, even for the less severe condition, foresee scenarios in which the area potentially occupied by the lagoon increases significantly and reaches the city area. This has also consequences for the biodiversity, as the sea level would eventually (i) deepen the water level in the lagoon, making it potentially unsuitable for some species of wading birds to prosper; (ii) submerge the artificial islands purposely made for birds to nest, and favour higher wave energy due to decreasing lagoon shallowness; (iii) increase saltwater exchange with the sea, which is not a biodiversity threat per se, but may have consequences for fresh groundwater quality in the surrounding area. Further studies will focus on including rain precipitations and river discharges due to extreme events, to include the full wetland dynamics and to assess consequences of compound floodings in present and projected scenarios.

## 7 Multi-risk projections and climate warnings with ESS in Foros Bay Pilot (BAS)

The Foros Bay is a part of the Burgas Bay, the largest Bulgarian bay. Together with adjacent low-laying wetland, it represents a biodiversity hotspot. The area is one of the most protected from wave action along the Bulgarian coast, and is a centrepiece for both unique natural diversity (landscape, habitat, and species) and human uses. The area is protected under the NATURA 2000 network (both Birds and Habitat) – BG0000271 Mandra-Poda; The Foros Bay is a part of an important place from ornithological point of view (“Mandra-Poda Complex”) and lays on the Via Pontica bird migratory route.

Several dramatic changes have occurred on the bay and its watershed area since 1920. Previously, the coastal area bordering the bay was a wetland almost completely covered with hygrophytes and hydrophytes; there were sand dunes and a dry land never had been flooded by the nearby lake that was used as vineyards. Subsequently, a part of the swamp was dried out to gain land for city development transforming it into settling (stabilization) basins and damming part of Mandra Lake to serve the oil refinery (Birdlife International, 2002).

The area is an important centre for community engagement into environmental protection – there is a visiting centre for bird watching. Also, educational programmes for volunteers and children were developed. Being the most wave protected part of the coast with a sandy bottom, the area offers suitable conditions for wave-sensitive species (such as seagrasses and other submerged aquatic plants) to accommodate and persist. The spatial distribution of the soft-bottom vegetation is limited by high turbidity and macroalgae mats that cover a part of the bottom. The habitats are vulnerable to both marine and land-based activities (point and diffuse sources) or processes (river floods). The adjacent low-lying wetland is also vulnerable to river floods and, despite of being less wave exposed, to coastal floods and erosion associated with extreme hydrometeorological events. Moreover, the expected climate impact would result in the coastal environment change; hence, flooding and erosion hazards due to sea level rise would cause even more severe consequences.

### 7.1 Study framework

Methodology framework in use is designed to reveal the impact of extreme events on the pilot and in particular to elucidate the mitigating role of vegetation. More precisely, the seagrass effect on damping of system energy and subsequent resilience increase to coastal erosion and flooding were investigated. To this end, we applied the event approach by considering three design events with return periods of 20, 50 and 100 years. The study framework is schematised in Fig.7.1.

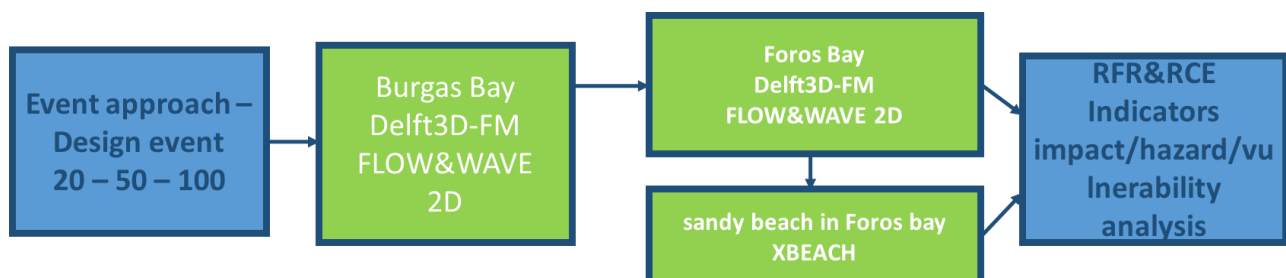


Figure 7.1. Schematization of the study framework



## 7.2 Data

### 7.2.1 Bathymetry & Topography

Different data types were used to generate a composite terrain model of Burgas Bay and Foros Bay. The wide Burgas Bay was mapped with a multibeam sonar in 2022. During 2023, additional bathymetric data for Foros Bay with a resolution of 3 m/cell size were obtained. For depths between 4 and 25 m, a seabed model with 7 m/cell size resolution was compiled. In the shallowest part of the Foros Bay, in 2023, bathymetric surveys were carried out using a boat mounted single-beam echo sounder. As a result, the entire Uzungeren Lake was mapped. The shallows were mapped by unmanned aerial photogrammetry, which also provides topography data. The UAS provided higher resolution data for the composite model allowing generation very high resolution digital surface model (20 cm/pix).

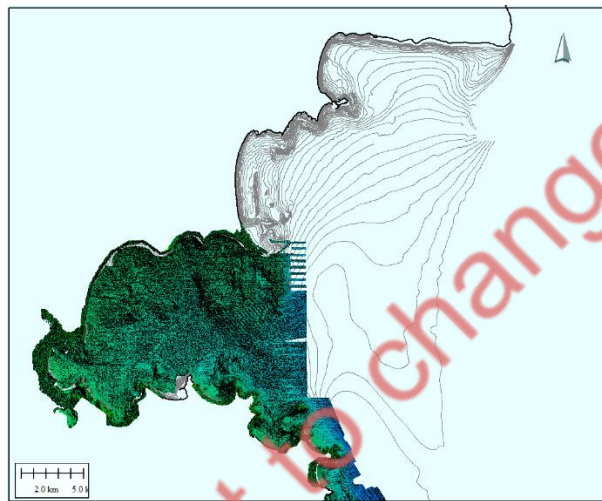


Figure 7.2. Bathymetry and topography compiled datasets used in the study

### 7.2.2 Waves and surge

Datasets for waves, currents and surge level used in the study can be described as follows:

- Wave properties extracted from the wave hindcast covering the period 1980 – 2020 (Valchev et al., 2010; Valchev et al., 2012) in order to reproduce recent past to present conditions (Fig.7.3)
- Surge level coming from Copernicus Climate Change Service as boundary conditions for the Foros Bay domain

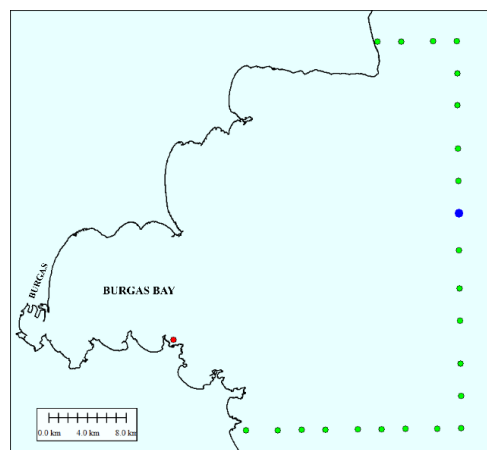


Figure 7.3. Location of points for which wave and wind properties were extracted from a hindcast dataset

### 7.2.3 Bottom sediments

The bottom sediments in Foros Bay, including the inner part of the bay and the entrance to the Usungeren Lake were surveyed in January 2023. The granulometry of a total of 13 samples were analyzed. According to the Wentworth classification, sediment type varies with depth decrease from fine sand through very coarse silt to very fine silt. D50 varies between 157 and 6  $\mu\text{m}$ . Additional data available in IO-BAS gathered in 2022 show that the bottom sediments in the deeper parts of the Foros bay and Port of Burgas water area are presented mostly silts including also medium sands and clays. D50 varies between 245 and 0.03  $\mu\text{m}$ . The locations of bottom sediment samples are presented in Fig.7.4.



Figure 7.4. Location of bottom sediment samples collected for the needs of REST-COAST Project (red dots) and those of supplementary samples (green dots).

### 7.2.4 Vegetation

The Foros Bay accommodates soft-bottom vegetation with a total area of 39 ha. The dominant species is the seagrass *Zostera noltei*, *Hornemann* but other aquatic species are also present, e.g. *Zannichellia palustris* L. and *Stuckenia pectinata* (L.) Börner, macroalgae - *Ulva* sp., *Ceramium* sp., *Cladophora coelothrix* Kützinger etc. The distribution of seagrass meadows is shown in Fig.7.5. The envisioned areas of seagrass restoration are also included in the figure.



Figure 7.5. Location of the seagrass meadow present in Foros Bay (light green polygon A) and the envisioned area of seagrass restoration (dark green polygons B and C)

### 7.3 Models and methods

Methodology framework was designed to reveal the impact of extreme events on the pilot and in particular to define the energy attenuation role of vegetation. Therefore, the event approach was employed by reconstructing three design events with return periods of 20, 50 and 100 years. Hydrodynamic conditions in terms of waves, currents, surge and winds corresponding to the recent past and present were obtained by means of probabilistic analysis of available data.

#### 7.3.1 Design of extreme hydrometeorological events

In order to design a realistic extreme event, first, peak over threshold (POT) analysis was used to identify the individual coastal storms applying a threshold of 2 m for significant wave height, which were exceeded for a time-span longer than 18 hours considering (Valchev et al., 2016). Thus, a total of 215 events were identified, each represented by significant wave height maxima ( $H_s$ ) with associated values of peak wave period ( $T_p$ ), wave direction, event duration as well as wind speed maxima ( $V_{max}$ ) during the event.

Furthermore, Extreme Value Analysis (EVA) was applied to calculate return values of design properties relevant for selected return periods serving as boundary conditions for Burgas Bay Delft3D-FM model. Time series for all points located along the open boundaries of Burgas Bay Delft3D-FM domain were statistically analysed (Fig. 7.3). It was found that significant wave height, peak wave period and wind speed behave in a similar manner following the growth, developed and decay phase of the event. All events were driven by winds with direction turning from NNW to ESE in the course of event, with an average of  $42.2^\circ\text{N}$  (NE). The results from EVA application are shown in Table. 7.1.

*Table. 7.1. Return values of wave properties and wind speed for selected design events*

TR	$H_s$ , m	$T_p$ , s	$V_{max}$ , m/s
TR020	8.4	10.9	20.9
TR050	10.5	11.4	21.6
TR100	12.5	11.8	22.0

Results reported in Valchev et al. (2012) were used to determine the event duration, wave and wind direction behaviour for the storm event prototype. Thus, the event duration was set to 110 hours, with duration of growth phase - 17 hours, developed phase - 55 hours and decay phase - 38 hours.

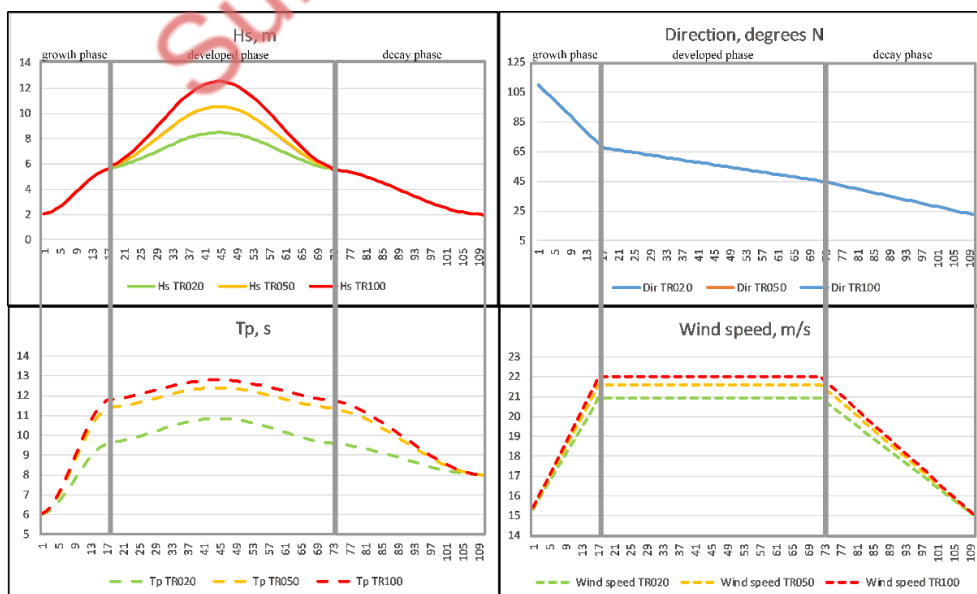


*Figure 7.6. Extreme events' pattern for selected return periods*

The waves and wind direction was set to vary in the event course: from ESE to ENE during the growth, from ENE to NE during the developed sea and from NE to NNE during the decay. The time series of  $H_s$  and  $T_p$  were calculated for each storm phase using the formula  $s = S \sin(\pi \frac{t}{T_d})^2$ , where  $S$  is the property maximum,  $T_d$  - event duration,  $t$  - time. The overall extreme event's pattern for selected return periods is shown in Fig.7.6. Such time series were constructed for each boundary point according to the local statistics.

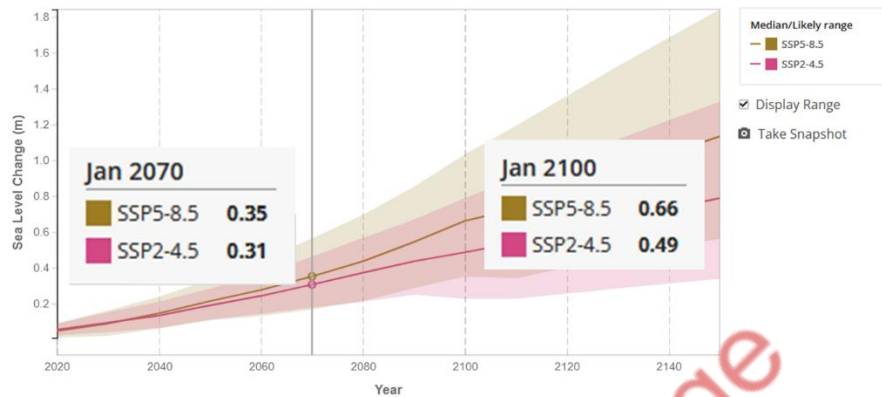


Figure 7.7. Sea level rise scenarios and projections (<https://sealevel.nasa.gov/ipcc-ar6-sea-level-projection-tool>)

The future conditions were addressed by making use of existing climate scenarios, more specifically middle and high-end ones RCP4.5 (SSP2-4.5) and RCP8.5 (SSP5-8.5). Considered projections were 2070 and 2100. According to predictions of IPCC AR6 (2023) sea level rise for Burgas would vary between 0.31 and 0.66 cm, according to the corresponding scenarios and projections (Fig.7.7). Surges relevant for Burgas were taken from Copernicus climate change services (<https://cds.climate.copernicus.eu/>). The values used are presented in Table 7.2.

Table 7.2. Return values of future surge level and for selected design events

TR	Surge, m	
	RCP4.5	RCP8.5
TR025	0.603	0.640
TR050	0.653	0.700
TR100	0.702	0.757

As for waves, a recent study concludes that the projected changes in the mean wave properties in middle future are more significant under RCP8.5. Moreover, possible effects seem to be more pronounced with respect to the extreme wave heights: 100-year return period growth is 5% for the western and 25% for the eastern Black Sea (Islek et al., 2022). Therefore, we hypothesized that there will be no change in the future wave conditions; the more so, our recent past to present estimates tend to exceed the projected values provided by Copernicus climate change services (<https://cds.climate.copernicus.eu/>).

### 7.3.2 Modelling system

The modelling system consists of two Delft3D-FM domains – Burgas Bay and Foros Bay. Additionally, XBeach model was implemented on a domain comprising a low-laying coastal stretch represented by a sandy beach and adjacent underwater area located within the Foros bay. All elements of the system are coupled offline (Fig.7.8).

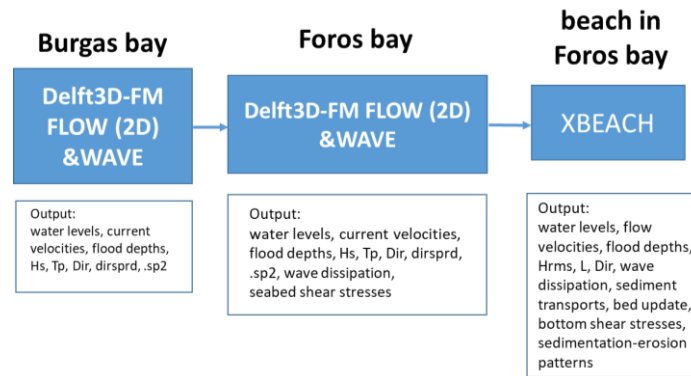


Figure 7.8. Modelling system scheme

The Burgas Bay Delft3D-FM domain (Fig.7.9) was implemented by online coupling of flow and wave processes. The flow module uses unstructured grid with spatial resolution varying from 500m at the offshore boundary to 20 m for the shallower than 20 m depths. The grid consists of 537276 cells. The wave module uses regular grid with horizontal resolution of 100 m. The model resolution is high enough to allow for a very good representation of the hydrodynamics and wave dynamics within the coastal area of complex bathymetry.

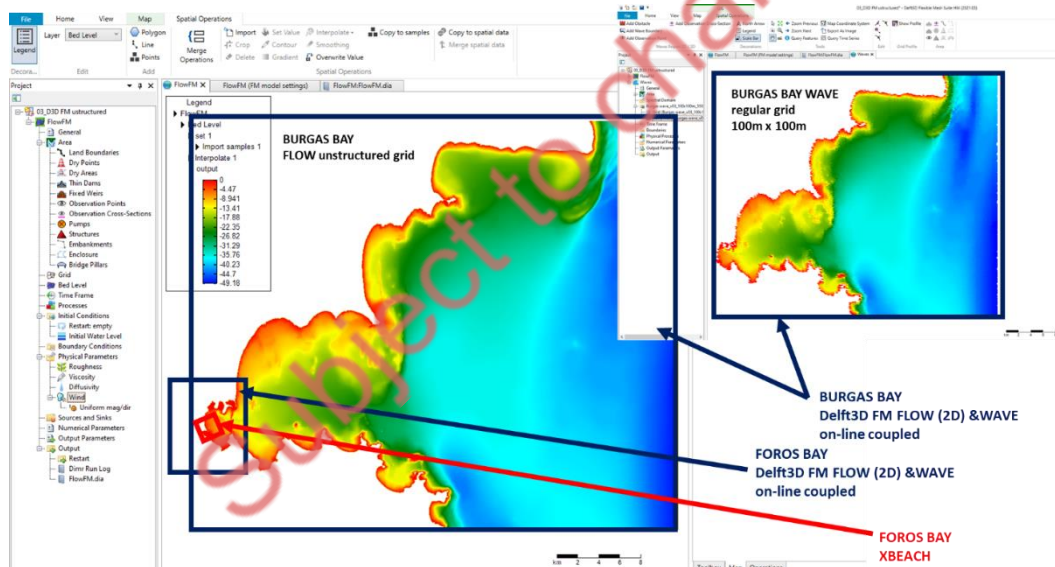
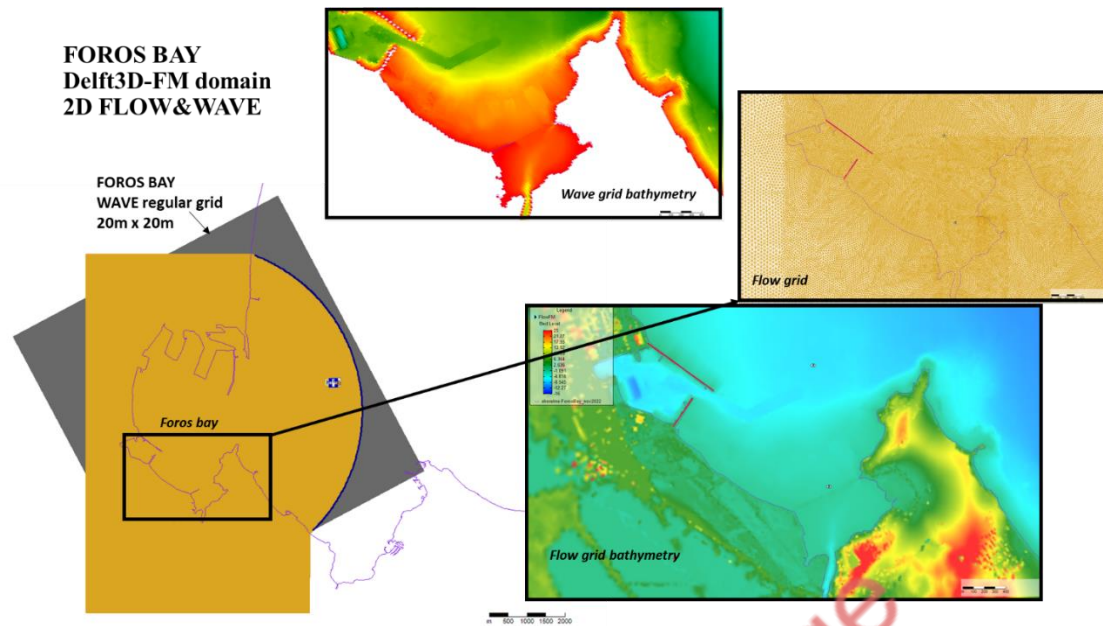


Figure 7.9. Burgas Bay Delft3D-FM FLOW&amp;WAVE domain and location of the other elements of the modelling chain

The Foros Bay Delft3D-FM domain is of higher spatial resolution and covers Burgas port infrastructures, the Poda protected area and Uzungeren Lake within Foros Bay as well as surrounding low-laying area and the located nearby Port of Burgas (Fig.7.10). The flow module is set on unstructured grid with cell sizes varying from 50 m at the offshore boundary to 20 m in the nearshore part of the grid. The wave grid is regular with spatial resolution of 20 m. The flow grid consists of 83237 cells, while the wave grid comprises 157156 cells. The offshore boundary conditions for the flow grid consist of water levels. The wave module boundary points are located at every grid node at the offshore boundary.





**Figure 7.10.** Foros Bay Delft3D-FM domain setup. Unstructured flow grid and regular wave grid (left). Water depths (wave module) and bathymetry (flow module) and a fragment of the unstructured flow grid (right). The offshore boundary conditions points (water levels) for the flow grid are depicted by blue dots (left).

The presence of seagrasses into the model domain was implemented into the model as area trachytopes, using the formula of Baptist (2005). The formulae require following input parameters: vegetation height ( $h_v$ ), density ( $n$ ), drag coefficient ( $C_D$ ) and alluvial bed roughness ( $C_b$ ). The values applied in the model set-up are summarized in Table 7.3.

**Table 7.3.** Input parameters used for seagrasses implementation into the model

$h_v$ [m]	$n$	$C_D$ [-]	$C_b$
0.3	6.5	1.8	62

Two polygons of seagrass meadows corresponding to present and restored areas are shown in Fig.7.11. The situation of the area planned for seagrass restoration was selected considering the depth limitation posed to the community spread. Thus, the offshore boundary was restrained to the 6 m depth contour. The simulations performed are listed in Table 7.4.

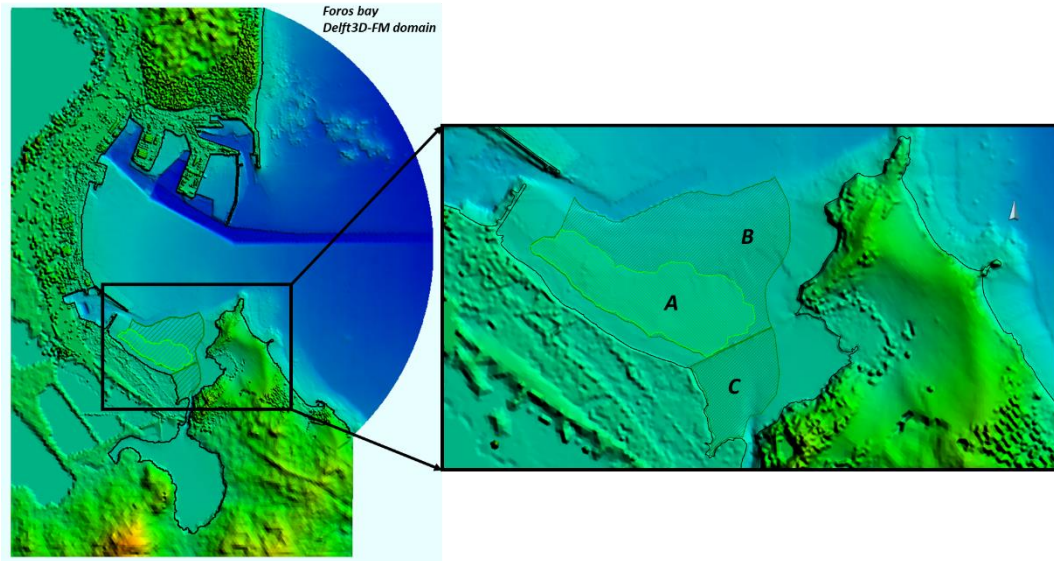


**Figure 7.11.** Location of the seagrass meadows within Foros Bay Delft3D-FM domain existing to present delineated by light green polygon (A) and the planned area of seagrass restoration delineated by dark green polygons (B and C)

**Table 7.4.** Simulations overview for Foros Bay domain (P – present, R – restored)

Alternative	SLR	Waves	Surges	Vegetation	No. of simulations
A0 (Baseline)	-	WAV_P	SS_P	VEG_P	3
A1	-	WAV_P	SS_P	VEG_R	3
A2 (Do nothing)	SLR_4.5 (2H)	WAV_P	SS_4.5	VEG_P	6
A3 (Do nothing)	SLR_8.5 (2H)	WAV_P	SS_8.5	VEG_P	6
A4	SLR_4.5 (2H)	WAV_P	SS_4.5	VEG_R	6
A5	SLR_8.5 (2H)	WAV_P	SS_8.5	VEG_R	6

The 2DH morphodynamic model XBeach (Roelvink et al., 2009) is implemented at the south-western part of the Foros Bay (Fig.7.12). The domain is limited landward by the international road E87 and covers a coastal stretch presented by low-laying area, a part of natural protected area Poda with maximum elevation of 6m. It includes a narrow subaerial beach, together with the bottom slope up to 7m depth. The grid is regular non-equidistant with varying cell sizes cross-shore – from 14m to 2m at the middle of the grid – and regular 5m-resolution along-shore, resulting in 151145 nodes. The model was run in surfbeat mode using cyclic lateral boundary and bedfriction manning coefficients map with value of 0.02 for the bottom slope and 0.04 for the terrestrial part of the domain. The model is fed by hourly wave parameters and water levels at the offshore boundary coming from the Foros Bay Delft3D-FM model output. Waves at the boundary are expressed as JONSWAP spectra through the wave parameters  $H_s$ ,  $T_p$ , wave direction, directional spreading, as the random seed for waves in the model is set to 0 for comparison purposes. The morphological acceleration factor (morfac) is set to 10, the sediments are homogeneous with  $D_{50}$  of 0.0001m and  $D_{90}$  of 0.0002m.

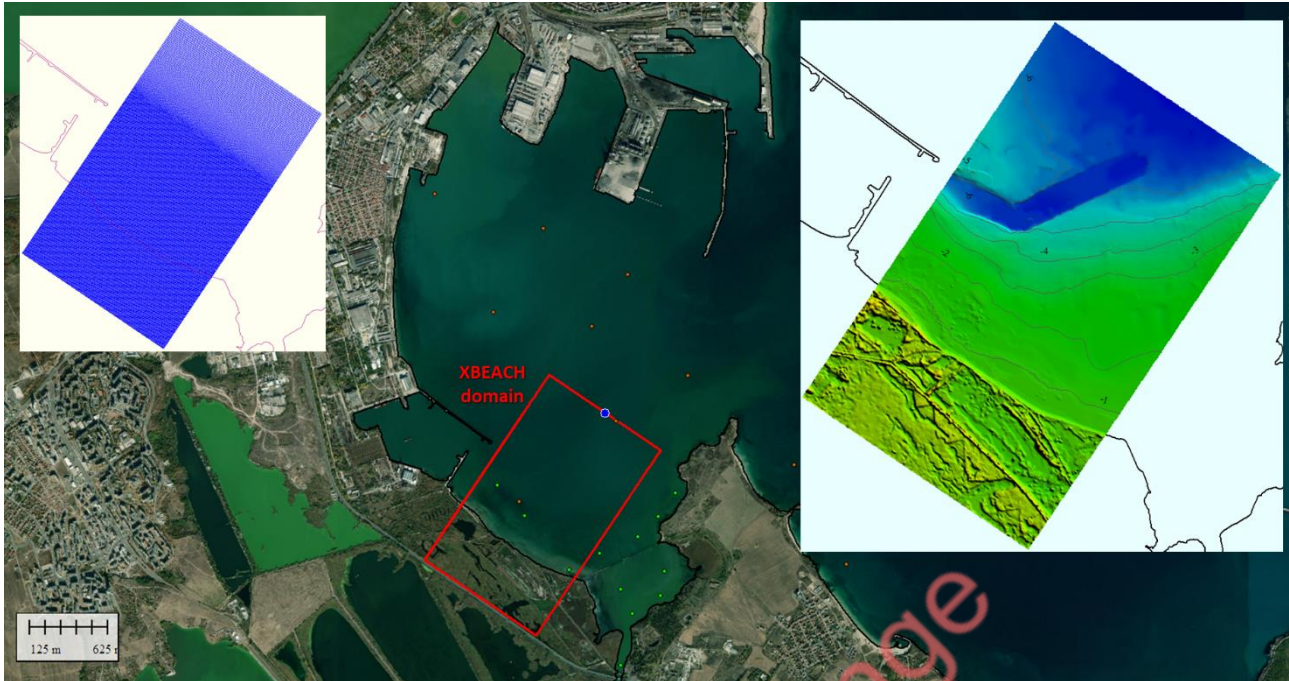


**Figure 7.12.** Location of XBeach model domain within Foros Bay delineated by red line (left) and bathymetry of the domain (right). The blue dot at the XBeach boundary allocates the output model location of Foros Bay Delft3D-FM model used for XBeach boundary conditions

The seagrass meadows – both existing to present and planned for restoration – are incorporated into the model using the vegetation module of XBeach (Van Rooijen et al., 2015). It was set up with following parameters: vegetation stem diameter of 0.005m, vegetation density – 130/sq.m, and vegetation height of 0.30m. The spatial coverage of two variants of seagrass patches within the domain are presented using grid map files (Fig.7.13). The simulations performed are listed in Table 7.5.

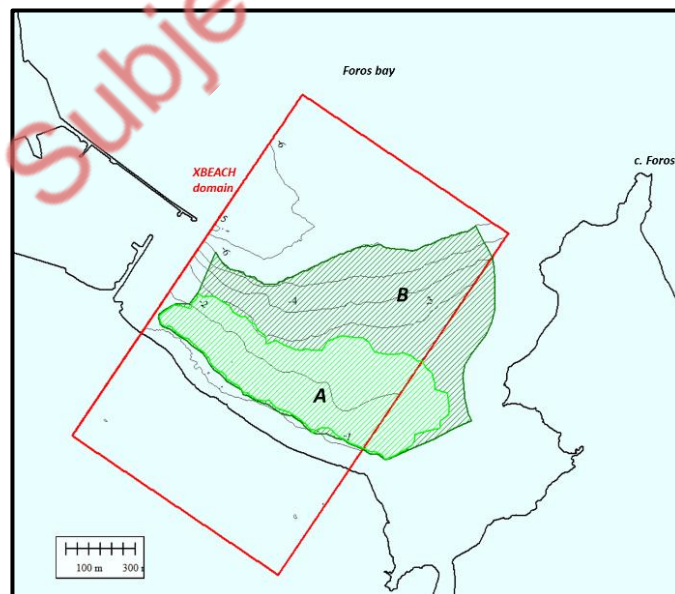


**Figure 7.13.** Distribution of seagrasses into the XBeach domain (red polygon). The seagrass meadow existing to present is delineated by light green polygon (A) and the planned area of seagrass restoration is delineated by dark green polygon (B).

*Table 7.5. Simulations overview for Foros Bay beach (P – present, R – restored)*

Alternative	SLR	Waves	Surges	Vegetation	No. of simulations
A0 (Baseline)	-	WAV_P	SS_P	VEG_P	3
A1	-	WAV_P	SS_P	VEG_NO	3
A2	-	WAV_P	SS_P	VEG_R	3
A2 (Do nothing)	SLR_4.5 (2H)	WAV_P	SS_4.5	VEG_P	6
A3 (Do nothing)	SLR_8.5 (2H)	WAV_P	SS_8.5	VEG_P	6
A5	SLR_4.5 (2H)	WAV_P	SS_4.5	VEG_NO	6
A6	SLR_8.5 (2H)	WAV_P	SS_8.5	VEG_NO	6
A7	SLR_4.5 (2H)	WAV_P	SS_4.5	VEG_R	6
A8	SLR_8.5 (2H)	WAV_P	SS_8.5	VEG_R	6

### 7.3.3 Ecosystem Services (ESS) assessment

For both present and future conditions two ecosystem services were assessed – Reduction of Flood Risk (RFR) and Reduction of Coastal Erosion. The indicators are based on result of the hydrodynamic and morphodynamic modelling described above. The RFR assessment is using model results of Foros Bay Delft3D-FM FLOW&WAVE model, while the RCE is using the results from XBeach model domain. The RFR indicator is flooded area (sq.km) calculated for the Foros Bay and the surrounding wetland solely, with a threshold of 1cm of water layer thickness. Two indicators are employed for RCE analysis – eroded volumes and eroded areas – calculated for the entire model domain. The erosion area are outlined using a threshold of 1cm sediment layer thickness.

## 7.4 Results and discussion

### 7.4.1 Hydrodynamic modelling

Analysis of the preliminary model results showed that restored seagrasses do not have a noticeable impact on the flow and wave pattern and the overall energy reduction in the system in comparison with the contribution of the existing meadow. Therefore, we decided to conduct model studies without any seagrasses as a baseline in order to prove their ESS.

The overall model results show that the prevailing flow pattern does not change significantly for all modelled conditions. A reduction of flow velocities is observed which is very well pronounced over the area of both present and restored seagrass in particular for lower energy conditions (TR020 design event) (Fig.7.14). However, this effect decays with the increase of energy input of the system accompanied by the sea level rise for both climate change scenarios into consideration.

The general circulation pattern during extreme events shows presence of a large anticyclonic eddy, which follows the coastal contour from cape Foros through the inner part of the bay. This facilitates the channeling of polluted and highly eutrophicated waters into the seagrass area. In calm hydrometeorological conditions, the reverse flow is observed (e.g. in Fig.7.5), i.e. discharge of these waters from the interior of the bay past c. Foros to open waters. For that reason, the narrow coastal strip along the eastern side of the bay is not suitable for seagrass restoration because the probability of their survival is very low, both in strong and weak conditions.



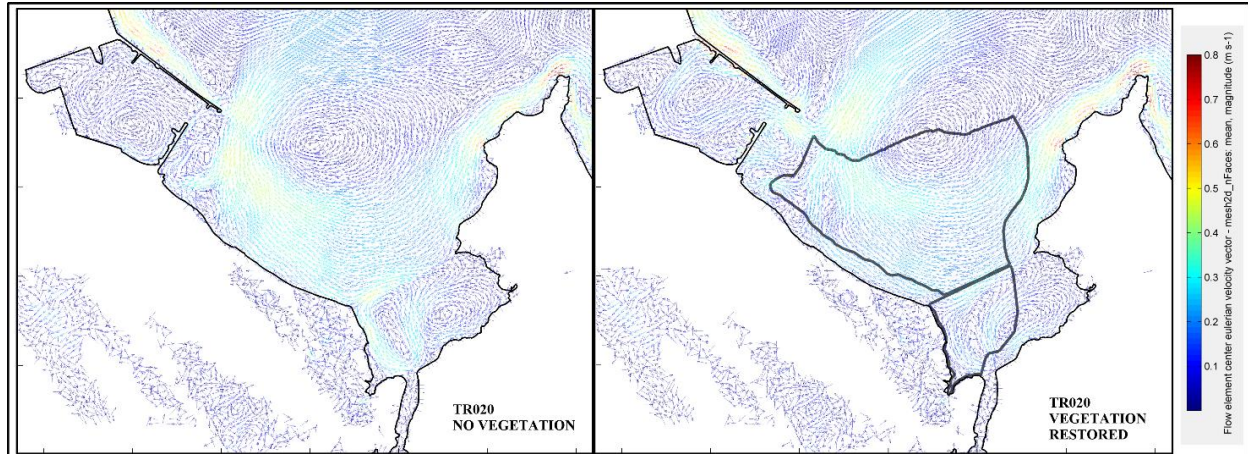


**Figure 7.14.** Flow pattern calculated for TR020 design event (present climate conditions) for the case of no vegetation (left) and in presence of existing and restored seagrass meadows

Concerning the waves, the model results show a decrease of significant wave height over the area occupied by seagrasses, which is more pronounced in the shallower part of the meadow, as well as in the inner bay. This is corroborated by the wave energy dissipation (Fig.7.15). Similarly to the flow behaviour, this effect vanishes with the increase of energy input in the system.

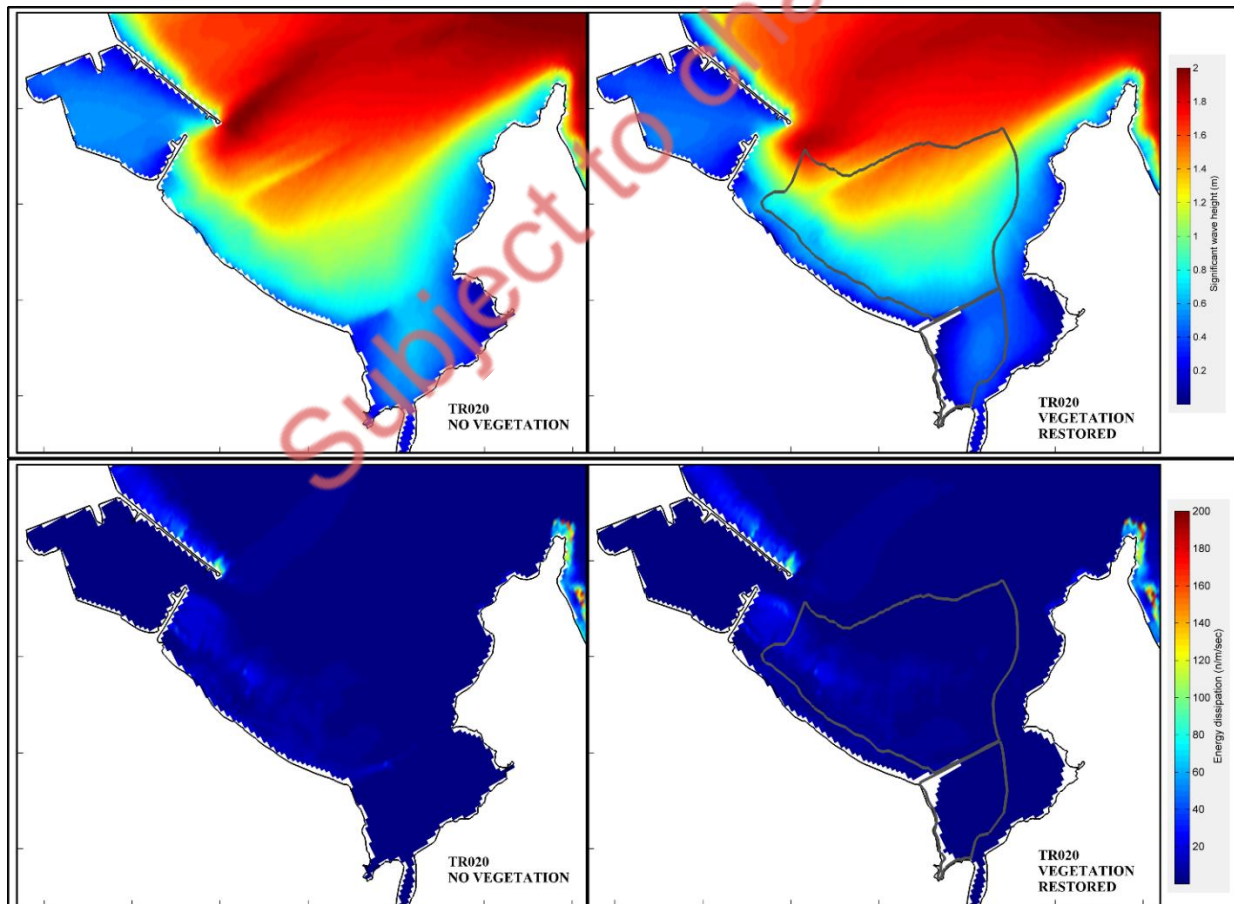


**Figure 7.15.** Significant wave height (upper panel) and wave energy dissipation (lower panel) for TR020 design event (present climate conditions) for the case of no vegetation (left) and in presence of existing and restored seagrass meadows



The model results for present climate conditions show that part of Poda protected area, as well as the narrow strip along the coastline including Usungeren Lake, Poda swamp and small parts of the settling basins of the oil refinery are flooded for all return periods. With the rise of sea level and surges due to climate change, the flooded areas increase significantly covering the larger part of Poda protected area and the whole settling basins behind the wetland (Fig.7.16). The same applies for the low-laying areas situated in the eastern coast of the bay. The analysis of the entire set of simulations show that the seagrasses have insignificant effect on reduction of flooding.

Flood areas for all design events concerning present conditions and two considered horizons of RCP4.5 and RCP8.5 are presented in Table 7.5. The percentage of flood increase with respect to TR020 present conditions shows that there is a slight increase of flood area for the rest of design events (6-8%) due to the wave action and surge. However, the flood area increases drastically for selected climate scenarios and projections as the percentage varies between 62% (RCP4.5 H2070) and 84% (RCP8.5 H2100) owing to the sea level rise.

*Table 7.5. Flood areas [sq. km] for all design events concerning present conditions and two considered horizons of RCP4.5 and RCP8.5. Right panel presents the percentage of flood increase due to climate change with respect to present conditions*

Return period	Flood areas [sq. km]					Percentage of flood increase with respect to TR020 present conditions				
	Present climate conditions	RCP4.5 H2070	RCP4.5 H2100	RCP8.5 H2070	RCP8.5 H2100	Present climate conditions	RCP4.5 H2070	RCP4.5 H2100	RCP8.5 H2070	RCP8.5 H2100
<b>TR020</b>	0.996	1.611	1.724	1.643	1.802	100	162	173	165	181
<b>TR050</b>	1.054	1.640	1.753	1.666	1.814	106	165	176	167	182
<b>TR100</b>	1.074	1.662	1.765	1.687	1.832	108	167	177	169	184

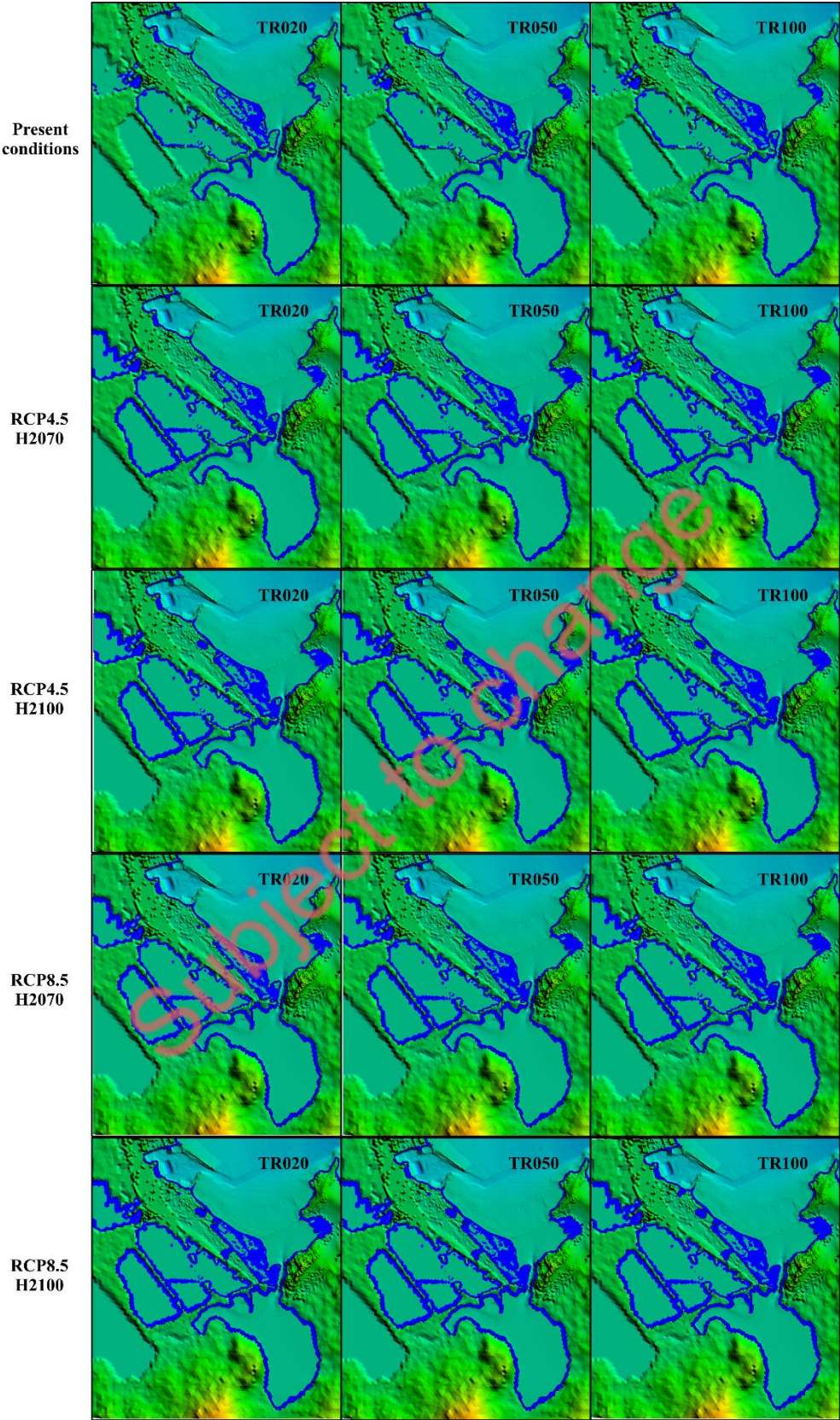


Figure 7.16. Flooded areas for considered return periods concerning present conditions and two considered horizons of RCP4.5 and RCP8.5

#### 7.4.2 Morphodynamic modelling

Similarly to hydrodynamic modelling strategy, model studies were conducted without any seagrasses as a baseline in order to prove their ESS. Further, two variants of seagrass distribution were modelled related to the existing and planned for restoration meadows.

Considering the results of all modelled simulations it can be stated that, the presence of seagrasses affect significantly the erosion-accumulation pattern (Fig.7.17 and 7.18). The most considerable erosion volumes are observed along the coastline while within the surf zone and wetland the intensity of erosion process decreases. Breaching and accumulation fans occur at coastline and wetland, while seaward in the surf zone, the morphodynamic pattern is marked by alternation of erosion-accumulation strips of a small layer thickness up to 5 cm expanding to 3 m depth. Erosion processes aggravate with the sea level rise as the area of interaction shifts towards the wetland.

In presence of seagrasses, their protection effect on the bottom slope is substantial for both present and future conditions, whereas on the coastline and wetland this effect is notable only for lower sea level. Concerning design event TR020, breaching takes place in case of 0.49m (RCP4.5 H2100) and 0.66m (RCP8.5 H2100) sea level rise. In former case, the seagrasses manage to prevent occurrence of coastline breaching located in the middle of modelled area in case of (Fig.7.17), which is not observed in the latter. Concerning design event TR050, the situation is similar but in both cases the seagrasses cannot cope with reduction of erosion processes. Concerning design event TR100, the breaching of the coastline occurs already in H070 (sea level 0.31m) for both climate change scenarios. In presence of seagrasses, the erosion subsides for above mentioned cases but fails in case of H2100 for both scenarios (Fig.7.18). The effect of the restored seagrass meadow is discernible only on the bottom slope affecting considerably the erosion area.

Subject to change

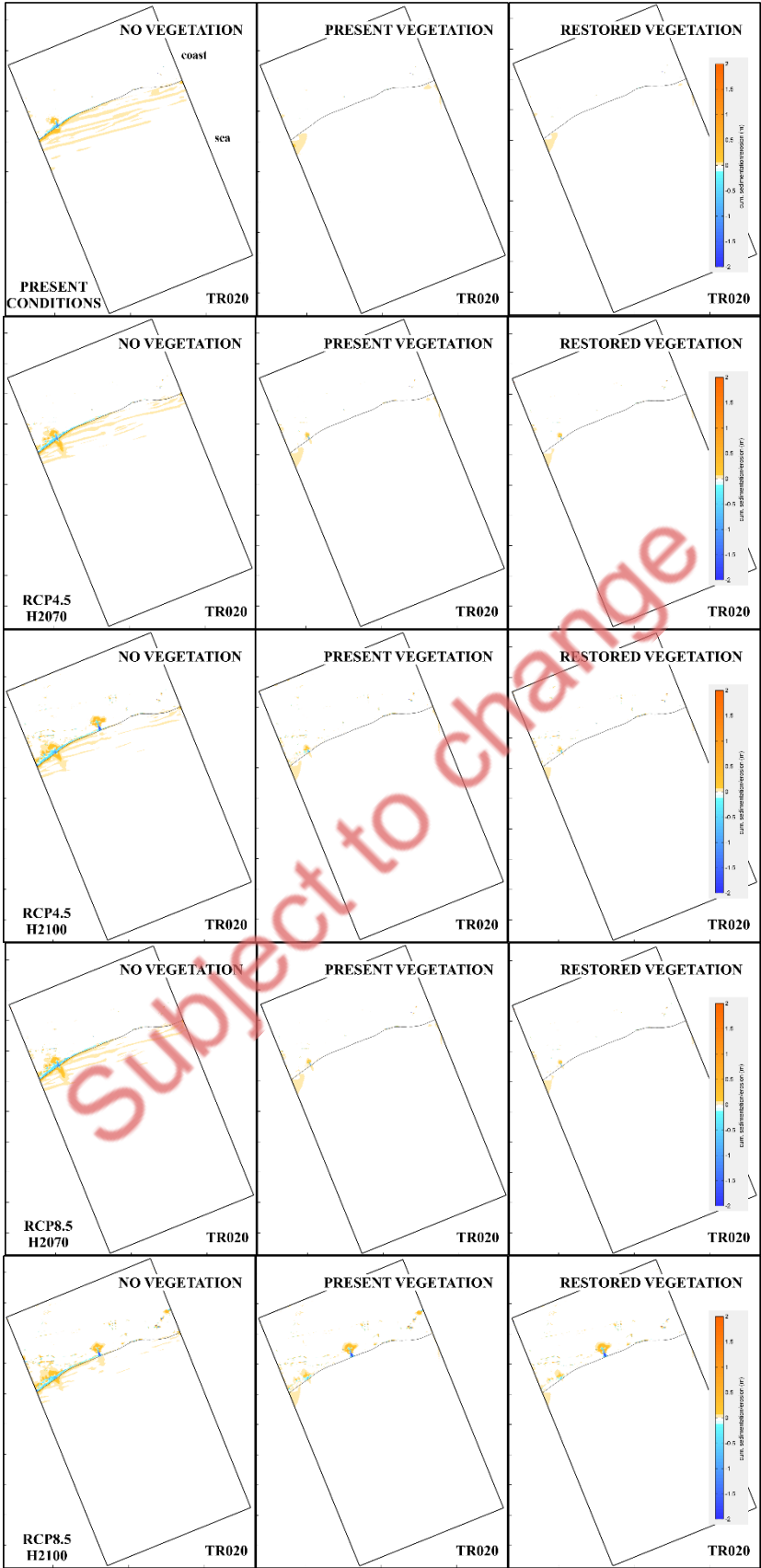


Figure 7.17. Sedimentation – erosion patterns calculated for TR020 storm event for present climate conditions and future climate change under RCP4.5 and RCP8.5, horizons 2070 and 2100



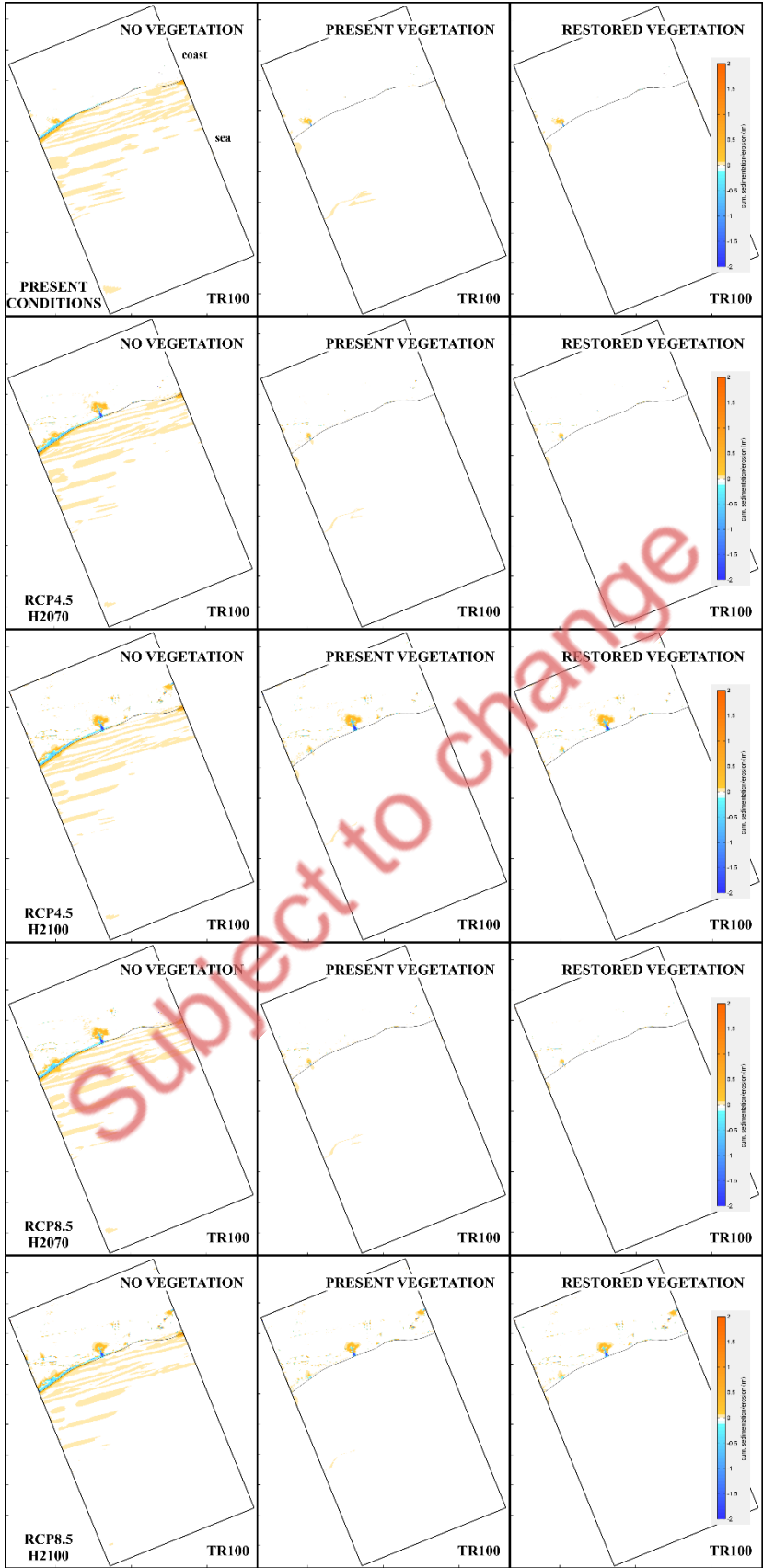


Figure 7.18. Sedimentation – erosion patterns calculated for TR100 storm event for present climate conditions and future climate change under RCP4.5 and RCP8.5, horizons 2070 and 2100



### 7.4.3 Assessment of ecosystem services

Two ecosystem services were assessed – Reduction of Flood Risk (RFR) and Reduction of Coastal Erosion (RCE) – for both present and future conditions.

Flood area (in sq.km) was employed as indicator for RFR ESS assessment, which was calculated for the Foros Bay and the surrounding wetland solely. Flood areas concerning present conditions and two considered horizons of RCP4.5 and RCP8.5 for all design events are presented in Fig.7.19. The flood area increases drastically for selected climate scenarios and projections owing to the sea level rise. The percentage varies between 62% (RCP4.5 H2070) and 84% (RCP8.5 H2100). The result implies that the seagrass presence has insignificant effect on reduction of flooding risk. Hence, this ESS is not relevant for the case of Foros pilot since the rising level is the main source of flooding, which seagrasses could not possibly influence on. The differences due to the direct wave impact and surges are similar and vary within a small range of 3-8% of the flood area as the difference decreases with sea level growth for future scenarios. Moreover, this behaviour is reproduced for all climate change conditions into consideration.

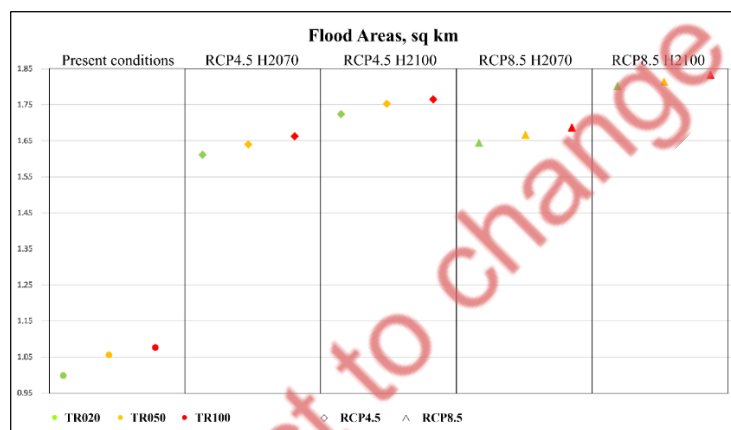


Figure 7.19. Flood areas concerning present conditions and two considered horizons of RCP4.5 and RCP8.5 calculated for all design events

As for the analysis of RCE ESS, two indicators were employed – eroded volumes and eroded areas – which were calculated for the entire XBeach model domain. Erosion volumes and area for cases of no vegetation, present and planned for restoration concerning present conditions and two considered horizons of RCP4.5 and RCP8.5 calculated for all design events are presented in Fig.7.20 and Fig.7.21, respectively.

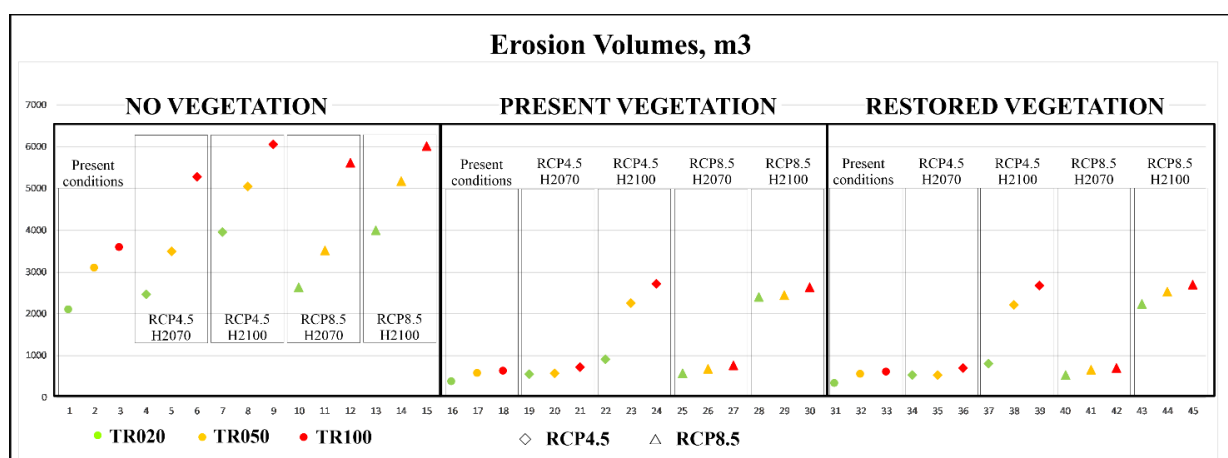


Figure 7.20. Erosion volumes for cases of no vegetation, present and planned for restoration concerning present conditions and two considered horizons of RCP4.5 and RCP8.5 calculated for all design events

In case of no vegetation, the erosion volumes are in the range 2000 - 6000 m<sup>3</sup>. In presence of seagrasses, the erosion volumes decrease substantially by 1.7 to 7.9 times, as they are below 1000 m<sup>3</sup> for all cases except for RCP4.5 H100 (TR050 and TR100) and RCP8.5 H100 (all return periods). The contribution of the restored seagrass meadow over the present vegetation is estimated to be 5% on the average as the maximum one 11.4% is calculated for case of TR020 RCP4.5 H2100 (Fig.7.20).

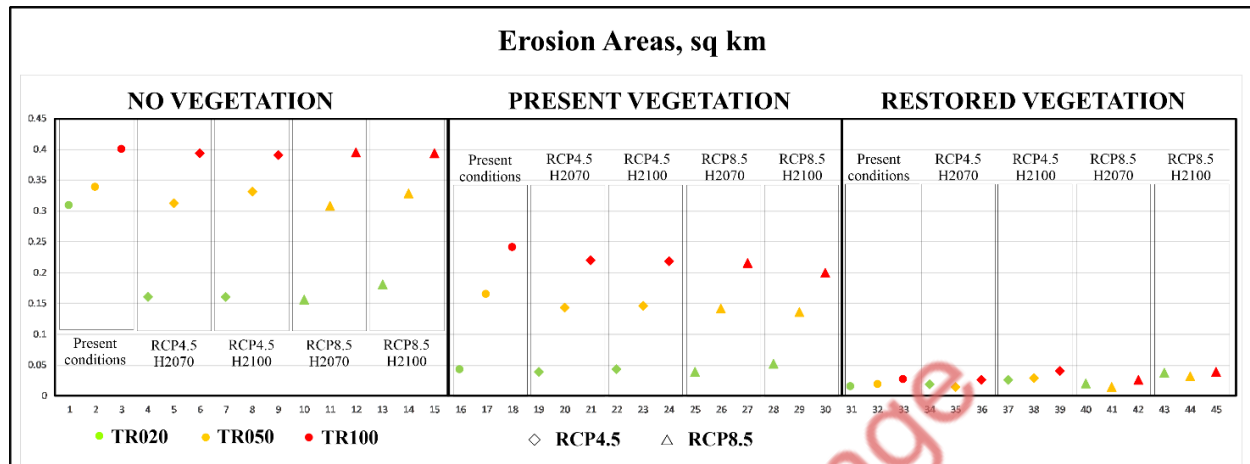


Figure 7.21. Erosion area for cases of no vegetation, present and planned for restoration concerning present conditions and two considered horizons of RCP4.5 and RCP8.5 calculated for all design events

The behaviour of erosion area indicator shows slightly different trend. It displays the increasing contribution of seagrasses, as the ecosystem service is most valued considering the impact of restored vegetation (Fig.7.21). It should be reminded that this indicator includes also erosion areas of very thin eroded layer since the imposed threshold is set to 1cm sediment layer thickness.

In absence of vegetation, the areas affected by erosion vary between 0.16 and 0.40 sq. km. The existing vegetation contributes to the erosion mitigation by decreasing of the affected area by 1.7 – 7.4 times, whilst the contribution of restored meadows appears to be even more impacting – effected areas decrease by 4.8 – 21.6 times. The contribution of restored seagrass meadow over the present vegetation is estimated to be 72% on the average as the maximum one 90% is calculated for case of TR050 RCP4.5 H2070 (Fig.7.21).

The overall results suggest that the tipping point for contribution of ecosystem services towards reduction of erosion lies between climate change scenarios RCP8.5 H2070 and RCP4.5 H2100 with the major role of sea level rise within the range 0.35-0.49m.

## 7.5 Conclusions

The presented study reveals the impact of extreme events in combination with climate change projections of sea level rise on the Foros pilot and in particular estimates the ecosystem services of existing and planned for restoration seagrass vegetation. It is based on the results of hydrodynamic and morphodynamic modelling performed using Delft3D-FM FLOW&WAVE and XBeach models. The event approach was applied by considering three design events with return periods of 20, 50 and 100 years. The future conditions were addressed by making use of existing climate scenarios, more specifically middle and high-end ones RCP4.5 (SSP2-4.5) and RCP8.5 (SSP5-8.5). Considered projections were 2070 and 2100.

The hydrodynamic model results show that the prevailing flow pattern does not change significantly for all modelled conditions. A reduction of flow velocities is observed, which is very well pronounced over the area of both present and restored seagrass in particular for lower energy conditions. However, this effect decays

with the increase of energy input of the system accompanied by the sea level rise for both climate change scenarios into consideration. Concerning the waves, a decrease of significant wave height over the area occupied by seagrasses was observed, which is more pronounced in the shallower part of the meadow, as well as in the inner bay corroborated by the wave energy dissipation pattern. Similarly to the flow behaviour, this effect vanishes with the increase of energy input in the system.

For both present and future conditions two ecosystem services were assessed – Reduction of Flood Risk (RFR) and Reduction of Coastal Erosion. The RFR indicator is flooded area (sq.km) while two indicators are employed for RCE analysis are eroded volumes and eroded areas. It is very important which indicator would be considered as more indicative, because the analysis depends on the targeted process and would lead to different valuation of ESS.

Concerning present conditions, the flood area indicator shows a slight increase of 6-8% for TR050 and TR100 compared to TR020 due to the wave action and surge. However, the flood area increases drastically for the selected climate scenarios and projections as the percentage varies between 62% (RCP4.5 H2070) and 84% (RCP8.5 H2100) mainly due to the sea level rise. The result implies that the seagrass presence has insignificant effect on reduction of flooding risk. Hence, this ESS is not relevant for the case of Foros pilot since the rising level is the main source of flooding, which seagrasses could not possibly influence on.

With respect to the RCE, it can be concluded that the presence of seagrasses affect significantly the erosion-accumulation pattern. The most considerable erosion volumes are observed along the coastline while within the surf zone and wetland the intensity of erosion process decreases. In case of no vegetation, the erosion volumes are in the range 2000 - 6000 m<sup>3</sup>, while in presence of seagrasses, they decrease substantially by 1.7 to 7.9 times. The contribution of the restored seagrass meadow over the present vegetation is estimated to be 5% on the average as the maximum one 11.4% is calculated for case of TR020 RCP4.5 H2100.

On the other hand, the erosion area indicator displays the increasing contribution of seagrasses with respect to the case of no vegetation, as the ecosystem service is most valued considering the impact of restored seagrass meadows. In absence of vegetation, the areas affected by erosion vary between 0.16 and 0.40 sq. km. The existing vegetation contributes to the erosion mitigation by decreasing of the affected area by 1.7 – 7.4 times, whilst the contribution of restored meadows appears to be even more impacting – effected areas decrease by 4.8 – 21.6 times. The contribution of restored seagrass meadow over the present vegetation is estimated to be 72% on the average as the maximum one 90% is calculated for case of TR050 RCP4.5 H2070.

The overall results suggest that the tipping point for contribution of ecosystem services towards reduction of erosion lies between climate change scenarios RCP8.5 H2070 and RCP4.5 H2100 with the major role of sea level rise within the range 0.35-0.49m.

## 8 Multi-risk projections and climate warnings with ESS in Vistula Lagoon (IBW)

### 8.1 General setting

Vistula Lagoon has a very mild wave climate due to its shallow bed (ca. 2.5m on average). Wind driven storm surges can be very high, in the range of 1.5m. However, the artificial island, see Fig. 8.1, is intended to easily absorb such events, because serving as safe haven for birds, it will remain uninhabited and occasional inundations are viewed as natural phenomenon for a meadow.



*Figure 8.1. Location of artificial island – study site in the Polish part of Vistula Lagoon: source – public domain, adapted by G. Różyński*

### 8.2 Sea level rise

High end IPCC sea level rise predictions along the Polish coast, located at the southernmost part of the Baltic Sea Baltic, are in the range of 0.7 – 0.9 m by the end of 21st Century, incl. the glacial isostatic adjustment. It will impact the western corner of the Lagoon - depression pertaining to Vistula Lagoon River Delta – cf. Fig. 8.1. This vast issue is beyond the REST-COAST project – dikes securing the delta are being refurbished now and will have to be elevated further to secure future safety and ensure sustainable farming in the delta. As these ventures are entirely outside REST-COAST, IBW does not plan any studies related to remediation of sea level rise aftermaths in the delta. Moreover, the barrier separating the Lagoon from the Baltic Sea is one of the most robust entities along the Polish coast and its breaching is very unlikely, also in case of the highest seawater levels. This issue is also beyond the scope of the studied pilot site.



The resistance of the artificial island to sea level rise is explained in Fig. 8.2. We can see the just constructed rim encompassing the area which is currently being filled by sediment dredged during construction of the passage through Vistula Lagoon barrier and the navigational channel through the Lagoon to the harbor of Elbląg – this harbor is intended to be reinvigorated by provision of independent passage to it through the Polish part of Vistula Lagoon. The rim is very massive and consists of two rows of sheet piles, topped with stone armor to resist huge forces exerted by ice fields, which are still encountered in winter month despite climate change. The island's interior will be maintained artificially as meadow to provide optimum habitat for birds hatching in such environment – natural succession of vegetation leading to gradual colonization of the island by shrubs and trees will therefore be halted by periodic mowing after the hatching season (mid of July).



*Figure 8.2. The rim of artificial island, Sept. 2023: source - REST-COAST*

### 8.3 Hydrodynamic forcings

Hydrodynamic simulations were executed to evaluate the change of wave and current fields in the Lagoon after construction of the island. The DELFT3D package was used for this purpose. The location of the island was selected to minimize those changes having also in mind minimum disturbances to wildlife in the Lagoon. Fig. 8.3 shows an exemplary simulation for NE wave approach and the wind speed of 10 m/s. The NE direction corresponds to the longest fetch in Vistula Lagoon. It indicates very low impacts – the primary reason for it is the shallow seabed, significantly limiting wave parameters. Moreover, as was just mentioned, the area is fetch-limited, even for the longer axis of the Lagoon, running from SW to NE.



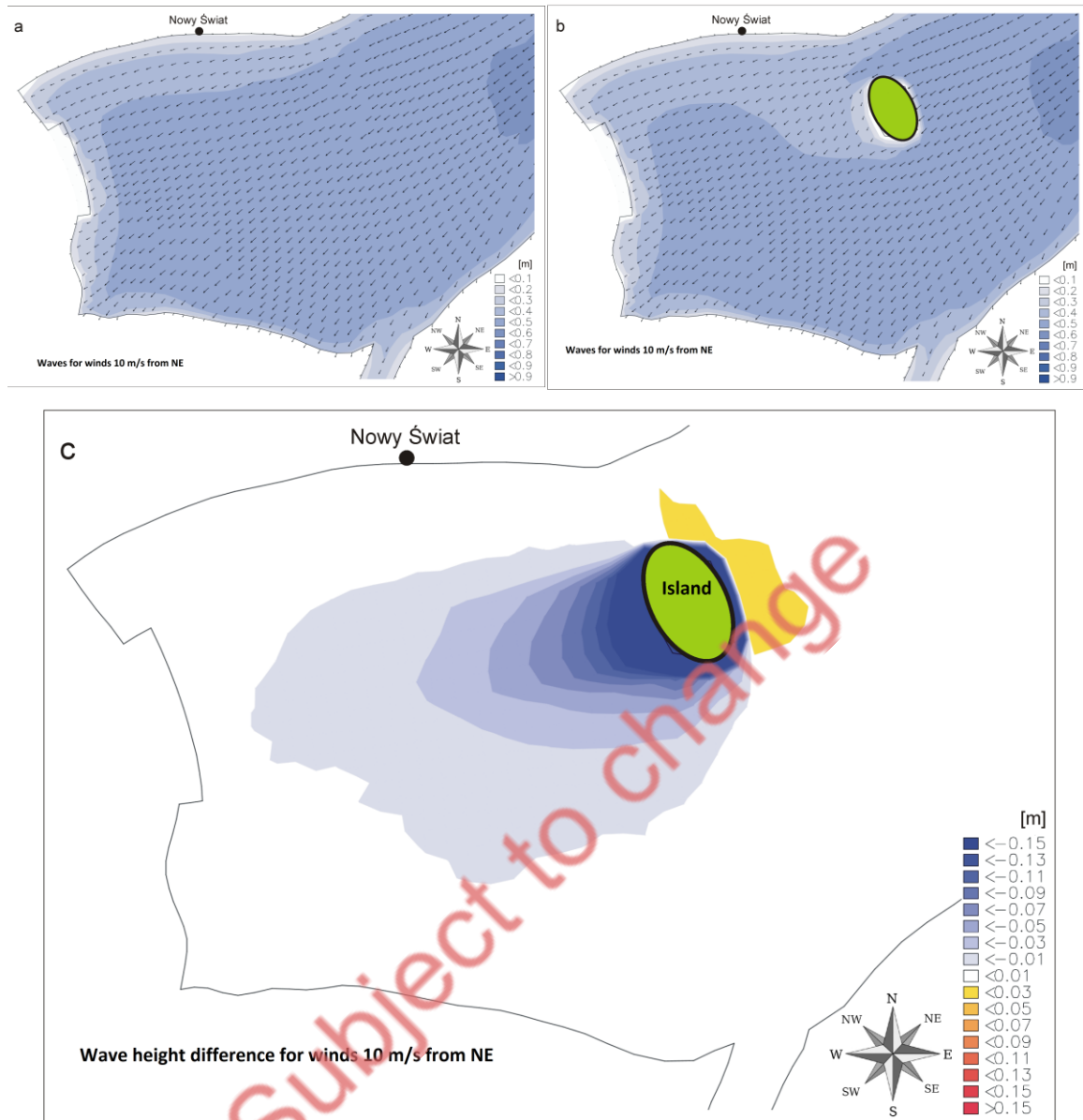


**Figure 8.3.** Wave heights for wind  $v = 10$  m/s from NE: (a) without artificial island, (b) with the island, (c) differences in wave height: source – IBW PAN

## 8.4 Conclusions

This pilot site is primarily aimed at biodiversity restoration and conservation of birds deemed important elements of the local ecosystem. Vistula Lagoon is both NATURA 2000 area for both birds (PLB280010) and habitats (PLH280007). This explains the efforts aimed at biodiversity restoration. Simultaneously, one of key characteristics of the Lagoon is its almost perfect sheltering from climate change consequences, apart from its south western corner, which is entirely outside the REST-COAST project. Therefore, climate change consequences are of secondary importance at the study site, since occasional inundations of the island are deemed natural at seaside meadows.

## 9 Integrated conclusions

The aim of the current deliverable is to assess the projections of ecosystem-services (ESS) provided by effective coastal restoration, combining sediment management (e.g. dunes reconstruction) with reconstruction of salt marsh and seagrass meadows within different REST\_COAST pilot sites. The main conclusions for the more advanced Pilots (in terms of restoration) and under future horizons are summarized in what follows.

Restoration of **salt marshes** for ESS in Wadden Sea and Venice Lagoon:

- In **Wadden Sea**, results indicated that NBS has significant impacts on hydrodynamics, sediment transport and morphological changes. Variation of water levels within the salt marsh area showed that NBS delayed rising and falling of water levels, and the latter is prominent. Therefore, it can be generally expected to have more sedimentation as there is more time for settling of sediments. However, this process depends on the storm severity as well as the locations within the salt marsh area. Furthermore, it was found that the sediment transport outside the salt marsh area decreases, particularly along the salt marsh edge. Bed evolution significantly decreased within the salt marsh area, resulting in low volume of sediments from erosion and sedimentation depending on the severity of a storm event. During storm events, salt marsh area supplied sediment into Ley Bay causing erosion therein, which remarkably decreased in the application of NBS. These preliminary results clearly indicate that the selected NBS, application of salt marsh, is a potential agent for coastal protection, which enables the resistance against the adverse impacts during storm events.
- In **Venice Lagoon** the restoration intervention manifests its influence on hydrodynamics through changes in currents, particularly during the flooding phase. Sea level experiences a slight adjustment, typically within the range of  $\pm 1\text{cm}$ , primarily attributed to the constrained water flow caused by the presence of salt marshes. Concerning the wave climate, the investigation of the projections suggests minimal alterations in wave conditions towards the end of the century. When examining the inclusion of restoration intervention, higher waves are more effectively attenuated by the restoration intervention. The placement of salt marshes emerges as a critical factor, with those close to deeper channels inducing significant increases in significant wave height (SWH) and currents. Notably, the western part of the northern group of salt marshes and the area between the two southernmost salt marshes present the lowest currents in the REST configuration. In addition, the southern group is identified as affected by wave reduction.

Restoration of **seagrass meadows** for ESS in Foros Bay and Arcachon Bay:

- In the **Foros Bay**, a reduction of flow velocities is observed, which is very well pronounced over the area of both present and restored seagrass in particular for lower energy conditions. However, this effect decays with the increase of energy input of the system accompanied by the sea level rise for both climate change scenarios into consideration. Concerning the waves, a decrease of significant wave height over the area occupied by seagrasses was observed, which is more pronounced in the shallower part of the meadow, as well as in the inner bay corroborated by the wave energy dissipation pattern. Similarly, to the flow behavior, this effect vanishes with the increase of energy input in the system. On the other hand, the result implies that the seagrass presence has insignificant effect on reduction of flooding risk. Hence, this ESS is not relevant for the case of Foros pilot since the rising level is the main source of flooding, which seagrasses could not possibly influence on. Finally, it can be concluded that the presence of seagrasses affects significantly the erosion-accumulation pattern. The most considerable erosion volumes are observed along the coastline

while within the surf zone and wetland the intensity of erosion process decreases. And the erosion area indicator displays the increasing contribution of seagrasses with respect to the case of no vegetation, as the ecosystem service is most valued considering the impact of restored seagrass meadows.

- The **Arcachon Bay** restoration links socio-economic characteristics with enduring morphological shifts under diverse climatic circumstances. After a comprehensive socio-economic analysis, the main economic activities have been identified. The impacts are then assessed using the eco-morphodynamic model. When possible, the quantification of bio-physical indicators needed for assessing sensitivity of ESS to climate forcings is presented. In the last section, the interplay between each economic activity and the model-derived physical metrics is examined. This work led to the conception of multi-impact chains for the main ESS aimed: Sediment management and Water quality. In conclusion, the modeling tool helped to assess some trends for sediment management, linked with SLR. With higher SLR, sedimentation on mudflats is anticipated to increase, with a consequence on flood control. However, the erosion of channels, connecting harbors to the Bay, could benefit pleasure boating, tourism and fishing activities. SLR, and morphological changes associated, have a noticeable effect on water renewal times. Modeling results show an increase in water renewal, leading to an improved water quality in the Bay. This modular approach we developed helps to estimate the risk reduction from ESS as a function of projection time horizon, and enables the future introduction of restoration scenarios to be executed in Task 2.3.

Restoration by **effective sediment management** for ESS in Sicily Lagoon, Vistula lagoon and Ebro Delta:

- In **Sicily Lagoon** both proposed additional NBS (dune reconstruction and revegetation to stabilize the dune), seem to provide a notable contribution in mitigating both wave-induced coastal flooding and erosion in the urbanized area. However, the SLR projections, even for the less severe condition, foresee scenarios in which the area potentially occupied by the lagoon increases significantly and reaches the city area. This has also consequences for the biodiversity, as the sea level would eventually (i) deepen the water level in the lagoon, making it potentially unsuitable for some species of wading birds to prosper; (ii) submerge the artificial islands purposely made for birds to nest, and favour higher wave energy due to decreasing lagoon shallowness; (iii) increase saltwater exchange with the sea, which is not a biodiversity threat per se, but may have consequences for fresh groundwater quality in the surrounding area.
- **Vistula lagoon** site is primarily aimed at biodiversity restoration and conservation of birds deemed important elements of the local ecosystem. Vistula Lagoon is both NATURA 2000 area for both birds (PLB280010) and habitats (PLH280007). This explains the efforts aimed at biodiversity restoration. Simultaneously, one of key characteristics of the Lagoon is its almost perfect sheltering from climate change consequences, apart from its south western corner, which is entirely outside the REST-COAST project. Therefore, climate change consequences are of secondary importance at the study site, since occasional inundations of the island are deemed natural at seaside meadows.
- For the lower river course, feeding the Ebro Delta site, the projected reductions in mean annual flow will dramatically reduce the sediment transport capacity of the **Ebro River** under natural conditions, due to the nonlinearity of the sediment transport rating curve. The impact of such reductions on the potential sediment transport capacity of the Ebro River under altered conditions will depend on how the Ebro River is managed in the future. The projected reductions suggest a future mean annual flow between 12 km<sup>3</sup>/yr and 13.5 km<sup>3</sup>/yr. The potential sediment transport capacity for the natural regime is expected to be reduced to between 10 Mton/yr and 17 Mton/yr. If the potential sediment

transport under altered conditions was similarly reduced, it would fall to a range between 3.5 km<sup>3</sup>/yr and 5 km<sup>3</sup>/yr and some carrying capacity would still remain in the river. However, if current abstractions of 6 km<sup>3</sup>/yr were maintained in the future, available flow would be reduced to 6 km<sup>3</sup>/yr to 7.5 km<sup>3</sup>/yr, which represent a larger reduction than that of natural flow. Therefore, it is very likely that the potential for sediment transport under altered conditions will be reduced more than that under natural conditions.

- For the coastal dynamics, a new approach to beach nourishment seems to be the best strategy, with alternating dunes being the most efficient mitigation action to protect the **Ebro delta beaches** from erosion and flooding damages. Nevertheless, this has to be put in a long-term view where alternating dunes and coastal bays and lagoons provide more resilient protection for several reasons. First, the simulations show that within future projections, the efficiency gap is reduced until at the end alternating dunes perform better even better than classical nourishment. Besides, classical nourishment has a huge associated problem when planned as long-term action derived from the littoral sediment transport. This effect produces a known loss of sediment through time, being necessary to re-nourish the area to maintain its effectiveness. The continuous dune has been used during the last decades in different tests and although it reduces short term hazards, the constant action of waves reduced durability and increases carbon footprint at the long-term. Also, the continuous dune is very weak against consecutive events for the same reason. Instead, the embryonic alternating dune system is a more stable strategy since the waves hit the front dunes and the back ones are maintained intact, increasing their efficiency through time. The best strategy then would be to use alternating dune and reconstruct the front dunes if necessary and even create some small nourishments to help the structure. These small nourishments have been proved to be more ecological and stable than big nourishments. Even so, when simulating future horizons with the worst climate change scenarios, the mitigation actions required continuous maintenance for a sustained protection from the combined effect of the SLR and wave/surge storms.

## References

- Alberti, T., Anzidei, M., Faranda, D., Vecchio, A., Favaro, M., & Papa, A. (2023). Dynamical diagnostic of extreme events in Venice lagoon and their mitigation with the MoSE.
- Anderson, R.S.(2002) Modeling the tor-dotted crests, bedrock edges, and parabolic profiles of high alpine surfaces of the Wind River Range, Wyoming. *Geomorphology* 46, 35–58.
- Auby I., Bost C.A., and Budzinski H. (2011). Régression des herbiers de zostères dans le Bassin d’Arcachon : état des lieux et recherche des causes. Rapport Ifremer RST/LER/AR/11.007, 195p.
- Arias A. (2022). Modélisation des interactions macrophytes-dynamique sédimentaire : Application aux herbiers de zostères du Bassin d’Arcachon et à leur régression récente. MSc manuscript, Université de Bordeaux, Ifremer, 52p.
- Ballé-Béganton J., J. Herry, M. Philippe, R. Pasco, B. Angst, M. Urien, D. Bailly, M. Cassé (2015). Les services écosystémiques en soutien à la gestion des herbiers de zostères du golfe du Morbihan. Projet Interreg IVA Manche VALMER, 14p.
- Banzo M., C. Cazals et V. André-Lamat (2018). Le bassin d’Arcachon entre attractivité et protection. *Sud-Ouest européen*, 45, 13-24.
- Baptist, M., 2005. Modelling floodplain biogeomorphology, PhD Dissertation, TU Delft library, <http://resolver.tudelft.nl/uuid:b2739720-e2f6-40e2-b55f-1560f434cbee>.
- Baptist, M. J., Van Der Wal, J. T., Folmer, E. O., Gräwe, U., & Elschot, K. (2019). An ecotope map of the trilateral Wadden Sea. *Journal of Sea Research*, 152, 101761.
- Batalla R.J., Vericat D. (2011) Hydrology and Sediment Transport. The Ebro River Basin. Handbook of Environmental Chemistry 13, 21–46, D. Barcelo and M. Petrovic (eds.)
- Benedet, L., Dobrochinski, J. P. F., Walstra, D. J. R., Klein, A. H. F., & Ranasinghe, R. W. M. R. J. B. (2016). A morphological modeling study to compare different methods of wave climate schematization and evaluate strategies to reduce erosion losses from a beach nourishment project. *Coastal engineering*, 112, 69-86.
- Bladé, E., Cea, L., Corestein, G., Escolano, E., Puertas, J., Vázquez-Cendón, E., Dolz, J., Coll, A. (2014) Iber: Herramienta de simulación numérica del flujo en ríos. *Rev. Int. Métodos Numér. Cálculo. Diseño Ing.*, 30, 1–10.
- Boucher J.-M., Delteril J.-P., Manaud F., Maurer D. and Trut G. (1997). Étude intégrée du bassin d’Arcachon. Rapport Ifremer, Brest, France, 129p.
- Bouma, H., De Jong, D.J., Twisk, F., Wolfstein, K., 2005. A Dutch Ecotope System for Coastal Waters (ZES.1). Middelburg, report RIKZ/2005.024. English version June 2006.
- Caires, S., & Yan, K. (2020). Ocean surface wave time series for the European coast from 1976 to 2100 derived from climate projections. Copernicus Climate Change Service (C3S) Climate Data Store (CDS).
- Cea, L., Puertas, J., Vázquez-Cendón, M.E. (2007) Depth Averaged Modelling of Turbulent Shallow Water Flow



- with Wet-Dry Fronts. *Arch. Comput. Methods Eng.*, 14, 303–341.
- Chen, W., Staneva, J., Jacob, B., Sanchez-Artus, X. and Wurpts, A., What-If Nature-Based Storm Buffers on Mitigating Coastal Erosion. *Science of the Total Environment* (under review) Available at SSRN 4463184.
- Church J. A., Clark P. U., Cazenave A., Gregory J. M., Jevrejeva S., Levermann A., et al. (2013). "Sea level change'," in *Climate change 2013: The physical science basis. contribution of working group I to the fifth assessment report of the intergovernmental panel on climate change*. Eds. Stocker T. F., Qin D., Plattner G.-K. (Cambridge; New)
- Chytrý, M., Tichý, L., Hennekens, S. M., Knollová, I., Janssen, J. A., Rodwell, J. S., ... & Schaminée, J. H. (2020). EUNIS Habitat Classification: Expert system, characteristic species combinations and distribution maps of European habitats. *Applied Vegetation Science*, 23(4), 648-675.
- Cognat M. (2019). Rôles des facteurs environnementaux et des interactions biomorphodynamiques sur l'évolution spatio-temporelle des herbiers de zostères dans une lagune mésotidale. PhD thesis, Université de Bordeaux.
- Colosimo, I., van Maren, D. S., de Vet, P. L. M., Winterwerp, J. C., and Van Prooijen, B. C., 2023. Winds of opportunity: The effects of wind on intertidal flat accretion. *Geomorphology*, 108840. doi.org/10.1016/j.geomorph.2023.108840
- Coles, S., 2009. An introduction to statistical modeling of extreme values. 3. print., Springer series in statistics. Springer: London, United Kingdom.
- Dam, G., M. van der Wegen, R. J. Labeur, and D. Roelvink (2016). Modeling centuries of estuarine morphodynamics in the Western Scheldt estuary. *Geophys. Res. Lett.*, 43, 3839-3847.
- Dean, R. G., & Yoo, C. H. (1992). Beach-nourishment performance predictions. *Journal of waterway, port, coastal, and ocean engineering*, 118(6), 567-586.
- Delft3D, 2023. Delft3D-Flow User Manual: Delft3D-FLOW User Manual (deltares.nl), p. 252-261 and 627-630.
- De Vriend, H. J., M. Capobianco, T. Chesher, H. E. de Swart, B. Latteux, and M. J. F. Stive (1993). Approaches to long-term modelling of coastal morphology: A review. *Coast. Eng.*, 21(1-3), 225–269.
- Dinu I., Monclus i Bori A., Gràcia V., Garcia-Leon M., Lin-Ye J., Stanica A. and Sanchez-Arcilla A. (2023). Assessing the coastal protection role of seagrass meadows along a barrier beach, southern Romanian coast. *Journal of Sea Research*, 191, 102329.
- Dissanayake, P. and Wurpts, A., 2013. Modelling an anthropogenic effect of a tidal basin evolution applying tidal and wave boundary forcing: Ley Bay, East Frisian Wadden Sea, *Coastal Engineering* 82, 9-24.
- Dissanayake, P., Wurpts, A., Winter, C., 2019. Storm Classification and the Investigation of Impacts on Beach/Dune. In: Goseberg, Nils; Schlurmann, Torsten (Hg.): *Coastal Structures 2019*. Karlsruhe: Bundesanstalt für Wasserbau. S. 632-641. [https://doi.org/10.18451/978-3-939230-64-9\\_063](https://doi.org/10.18451/978-3-939230-64-9_063).
- Dolch, T., Folmer, E. O., Frederiksen, M. S., Herlyn, M., van Katwijk, M. M., Kolbe, K., ... Westerbeek, E. P. (2017). Seagrass. In *The Wadden Sea Quality Status Report*
- Donatelli C., Ganju N. K., Fagherazzi S. and Leonardi N. (2018). Seagrass Impact on Sediment Exchange Between Tidal Flats and Salt Marsh, and The Sediment Budget of Shallow Bays. *Geophysical Research Letters*,

45(10), 4933-4943.

Dronkers, J. (1986). Tidal asymmetry and estuarine morphology. *Neth. J. Sea Res.*, 20(2/3), 117–131.

Elias, E., Alonso, A.C., van Maren, B. (2021). Morfologische veranderingen Eems-Dollard en Groninger Wad. Deltares report 11203742-000-ZKS-0003

Elmilady, H., van der Wegen, M., Roelvink, D., & van der Spek, A. (2020). Morphodynamic evolution of a fringing sandy shoal: From tidal levees to sea level rise. *Journal of Geophysical Research: Earth Surface*, 125, e2019JF005397. <https://doi.org/10.1029/2019JF005397>

Esselink, P., van Duin, W.E., Bunje, J., Cremer, J., Folmer, E.O., Frikke, J., Glahn, M., de Groot, A.V., Hecker, N., Hellwig, U., Jensen, K., Körber, P., Petersen, J., Stock, M., 2017. Salt marshes, In: Wadden Sea Quality Status Report 2017. Eds: Kloepper, S. et al., Common Wadden Sea Secretariat, Wilhelmshaven, Germany. Last updated 21.12.2017.

Faranda, D., Ginesta, M., Alberti, T., Coppola, E., & Anzidei, M. (2023). Attributing Venice Acqua Alta events to a changing climate and evaluating the efficacy of MoSE adaptation strategy. *npj climate and atmospheric science*, 6(1), 181.

Fernández-Montblanc, T., Duo, E., & Ciavola, P. (2020). Dune reconstruction and revegetation as a potential measure to decrease coastal erosion and flooding under extreme storm conditions. *Ocean & Coastal Management*, 188, 105075.

Garner, G. G., T. Hermans, R. E. Kopp, A. B. A. Slangen, T. L. Edwards, A. Levermann, S. Nowicki, M. D. Palmer, C. Smith, B. Fox-Kemper, H. T. Hewitt, C. Xiao, G. Aðalgeirsdóttir, S. S. Drijfhout, T. L. Edwards, N. R. Golledge, M. Hemer, R. E. Kopp, G. Krinner, A. Mix, D. Notz, S. Nowicki, I. S. Nurhati, L. Ruiz, J-B. Sallée, Y. Yu, L. Hua, T. Palmer, B. Pearson, 2021. IPCC AR6 Sea-Level Rise Projections. Version 20210809. PO.DAAC, CA, USA. Dataset accessed [2023-11-26] at <https://podaac.jpl.nasa.gov/announcements/2021-08-09-Sea-level-projections-from-the-IPCC-6th-Assessment-Report>.

Garzon, J. L., Miesse, T., & Ferreira, C. M. (2019). Field-based numerical model investigation of wave propagation across marshes in the Chesapeake Bay under storm conditions. *Coastal Engineering*, 146, 32-46.

Golledge N. R. (2020). Long-term projections of sea-level rise from ice sheets. *Wiley Interdiscip. Reviews: Climate Change* 11 (2), e634. doi: 10.1002/wcc.634

Gorría, H. (1877) Desecación de las marismas y terrenos pantanosos denominados de Los Alfaques. Tech. Rep., Ministerio de Agricultura. Madrid

Gracia, V., García, M., Grifoll, M., & Sánchez-Arcilla, A. (2013). Breaching of a barrier under extreme events. The role of morphodynamic simulations. *Journal of Coastal Research*, (65), 951-956.

Grases, A., Gracia, V., García-León, M., Lin-ye, J., & Sierra, J. P. (2020). Coastal flooding and erosion under a changing climate: implications at a low-lying coast (Ebro Delta). *Water*, 12(2), 346.

Haff, P. K. (1996), Limitations on predictive modeling in geomorphology, in *The Scientific Nature of Geomorphology*. Edited by B. Rhoads and C. Thorn, pp. 337-358, Wiley, New York.

Haff, P. K. (2013), Prediction in geology versus prediction in engineering, *Geol. Soc. Am. Spec. Pap.*, 502, doi:10.1130/2013.2502(06).

- Hargrove, W. W., Hoffman, F. M., & Hessburg, P. F. (2006). Mapcurves: a quantitative method for comparing categorical maps. *Journal of Geographical Systems*, 8, 187-208.
- Hausfather, Z., & Peters, G. P. (2020). RCP8. 5 is a problematic scenario for near-term emissions. *Proceedings of the National Academy of Sciences*, 117(45), 27791-27792.
- Hersbach, H., Bell, B., Berrisford, P., Hirahara, S., Horányi, A., Muñoz-Sabater, J., ... & Thépaut, J. N. (2020). The ERA5 global reanalysis. *Quarterly Journal of the Royal Meteorological Society*, 146(730), 1999-2049.
- Holthuijsen, L. H., Booij, N., & Herbers, T. H. C. (1989). A prediction model for stationary, short-crested waves in shallow water with ambient currents. *Coastal engineering*, 13(1), 23-54.
- Houser, C., Hapke, C., & Hamilton, S. (2008). Controls on coastal dune morphology, shoreline erosion and barrier island response to extreme storms. *Geomorphology*, 100(3-4), 223-240.
- Houwing, E. J., Tanczos, I.C., Kroon, A., De Vries, M.B., 2000. Interaction of submerged vegetation, hydrodynamics and turbidity; analysis of field and laboratory studies, Conference Proc. INTERCOH2000.
- Ibáñez C., Prat N., Canicio A. (1996) Changes in the hydrology and sediment transport produced by large dams on the lower Ebro river and its estuary. *Regulated Rivers: Research and Management*, 12, 51-62.
- Islek, F., Yüksel, Y. and Sahin. C. 2022. Evaluation of regional climate models and future wave characteristics in an enclosed sea: A case study of the Black Sea. *Ocean Engineering*, Volume 262, 112220, ISSN 0029-8018, <https://doi.org/10.1016/j.oceaneng.2022.112220>
- IPCC SIXTH ASSESSMENT REPORT (AR6) "CLIMATE CHANGE 2023" (<https://www.ipcc.ch/report/ar1/wg1/sea-level-rise/>), 2023
- Jacob, B., Dolch, T., Wurpts, A., & Staneva, J. (2023). Evaluation of seagrass as a nature-based solution for coastal protection in the German Wadden Sea. *Ocean Dynamics*, 73(11), 699-727
- Istituto Idrografico della Marina (2019), Nautical charts, Panels 20-21, Genova.
- Janowski, L., Madricardo, F., Fogarin, S., Kruss, A., Molinaroli, E., Kubowicz-Grajewska, A., & Tegowski, J. (2020). Spatial and temporal changes of tidal inlet using object-based image analysis of multibeam echosounder measurements: A case from the Lagoon of Venice, Italy. *Remote Sensing*, 12(13), 2117.
- Jiménez, José A., and Agustín Sánchez-Arcilla. (2004). "A long-term (decadal scale) evolution model for microtidal barrier systems." *Coastal Engineering* 51.8-9: 749-764.
- Kaiser, R.; Knaack, H.; Miani, M.; Niemeyer, H.D., 2010. Examination of Climate Change adaptation strategies for Coastal Protection. In: MCKEE SMITH, J. and LYNETT, P. (ed.): *Proceedings of the 32nd International Conference on Coastal Engineering*, 2010, Shanghai. <http://journals.tdl.org/icce/index.php/icce/issue/view/154/showToc>
- Kaspar, F., Niermann, D., Borsche, M., Fiedler, S., Keller, J., Potthast, R., Rösch, T., Spanghel, T., and Tinz, B.: Regional atmospheric reanalysis activities at Deutscher Wetterdienst: review of evaluation results and application examples with a focus on renewable energy, *Adv. Sci. Res.*, 17, 115-128. <https://doi.org/10.5194/asr-17-115-2020>, 2020
- Knutson, P. L., Brochu, R. A., Seelig, W. N., & Inskeep, M. (1982). Wave damping in *Spartina alterniflora* marshes. *Wetlands*, 2, 87-104.

- Korres, G., Ravdas, M., & Zacharioudaki, A. (2019). Mediterranean sea waves analysis and forecast (CMEMS MED-Waves).
- Kriegler, F. J. (1969). Preprocessing transformations and their effects on multispectral recognition. In Proceedings of the Sixth International Symposium on Remote Sensing of Environment (pp. 97-131).
- Lang A., Mikolajewicz U. (2020). Rising extreme sea levels in the German bight under enhanced CO<sub>2</sub> levels: A regionalised large ensemble approach for the north Sea. *Clim Dyn* 55, 1829–1842. doi: 10.1007/s00382-020-05357-5
- Le Corre N., Le Berre S., Peuziat I., Brigand L. and Courtel J. (2015). Approche des espaces de la pratique nautique par l'analyse de la fréquentation : l'exemple du bassin de navigation arcachonnais. *VertigO*, vol. 15(3), online.
- Lesser, G., Roelvink, J.A., Van Kester, J.A.T.M., Stelling, G.S., 2004. Development and validation of a three-dimensional morphological model. *Coastal Engineering*, 51, 883–915.
- Management Plan of Protected Area "Poda" for the period from 2002 - 2010", Birdlife International, 2002
- Mathis M., Mikolajewicz U. (2020). The impact of meltwater discharge from the Greenland ice sheet on the Atlantic nutrient supply to the northwest European shelf. *Ocean Sci.* 16 (1), 167–193. doi: 10.5194/os-16-167-2020
- Mascioli, F., Piattelli, V., Cerrone, F., Gasprino, D., Kunde, T., Miccadei, E., 2021. Feasibility of objective seabed mapping techniques in a coastal tidal environment (Wadden Sea, Germany), *Geosciences*, 11(2), 49.
- Maxwell, P. J. S. Eklof, M. M. van Katwijk, K. R. O'Brien, M. de la Torre-Castro, C. Boström, et al. (2016). The fundamental role of ecological feedback mechanisms for the adaptive management of seagrass ecosystems - a review. *Biological Reviews*, pp. 0-0.
- Mayer, A., & Silver, W. L. (2022). The climate change mitigation potential of annual grasslands under future climates. *Ecological Applications*, 32(8), e2705.
- Mendoza, E. T., Jimenez, J. A., & Mateo, J. (2011). A coastal storms intensity scale for the Catalan sea (NW Mediterranean). *Natural Hazards and Earth System Sciences*, 11(9), 2453-2462.
- Mikolajewicz U., Sein D. V., Jacob D., König T., Podzun R., Semmler T. (2005). Simulating Arctic sea ice variability with a coupled regional atmosphere-ocean-sea ice model. *Meteorologische Z.* 14 (6), 793–800. doi: 10.1127/0941-2948/2005/0083
- Mudd, S.M., Furbish, D.J. (2004) Influence of chemical denudation on hillslope morphology. *J. Geophys. Res. Earth Surf.*, 109. doi:10.1029/2003JF000087.
- Murphy, A. H., & Epstein, E. S. (1989). Skill scores and correlation coefficients in model verification. *Monthly weather review*, 117(3), 572-582.
- Nepf, H. M., & Vivoni, E. R. (2000). Flow structure in depth-limited, vegetated flow. *Journal of Geophysical Research: Oceans*, 105(C12), 28547-28557.
- Niemeyer, H. D., Berkenbrink, C., Ritzmann, A., Knaack, H., Wurpts, A., Kaiser, R., 2014. Evaluation of Coastal Protection Strategies in Respect of Climate Change Impacts. In: *Die Küste* 81. Karlsruhe: Bundesanstalt für

Wasserbau. S. 565-577.

Nguyen, H. M., Bryan, K. R., Zhou, Z., & Pilditch, C. A. (2022). Modeling the effects of aerial temperature and exposure period on intertidal mudflat profiles. *Continental Shelf Research*, 245, 104802.

Oberrecht, D., 2020. Development of a numerical modeling approach for large-scale fluid mud flow in estuarine environments. Hannover: Gottfried Wilhelm Leibniz Universität, Diss., 2020, xvi, 118 S. DOI: <https://doi.org/10.15488/10488>

Palmer M. D., Gregory J. M., Bagge M., Calvert D., Hagedoorn J. M., Howard T., et al. (2020). Exploring the drivers of global and local sea-level change over the 21st century and beyond. *Earth's Future* 8, e2019EF001413. doi: 10.1029/2019EF001413

Palmer M., Howard T., Tinker J., Lowe J., Bricheno L., Calvert D., et al. (2018). UKCP18 marine report. Met Office Hadley Centre, Exeter, United Kingdom, 133pp.

Paola, C., Voller, V.R. (2005) A generalized Exner equation for sediment mass balance. *J. Geophys. Res. Earth Surf.*, 110. doi:10.1029/2004JF000274.

Parisot J.-P., J. Diet-Davancens, A. Sottolichio, E. Crosland, C. Drillon, and R. Verney (2008). Modélisation des agitations dans le bassin d'Arcachon. *Xèmes Journées Sophia Antipolis*, pages 435-444.

Pein, J., Staneva, J., Mayer, B., Palmer, M. D., & Schrum, C. (2023). A framework for estuarine future sea-level scenarios: Response of the industrialised Elbe estuary to projected mean sea level rise and internal variability. *Frontiers in Marine Science*, 10, 1102485.

Pelisson C. (2019). Modélisation de la dynamique sédimentaire dans le Bassin d'Arcachon en lien avec la dynamique temporelle des herbiers de zostères. MSc manuscript, Université Bretagne-Sud, Ifremer, 50p.

Plus M., Dumas F., Stanisière J.-Y. and Maurer D. (2009). Hydrodynamic characterization of the Arcachon Bay, using model-derived descriptors. *Continental Shelf Research* 29, 1008-1013.

Pries, A. J., Miller, D. L., & Branch, L. C. (2008). Identification of structural and spatial features that influence storm-related dune erosion along a barrier-island ecosystem in the Gulf of Mexico. *Journal of Coastal Research*, (24), 168-175.

Reeves I. R. B., L. J. Moore, E. B. Goldstein, A. B. Murray, J. A. Carr et al. (2019). Impacts of Seagrass Dynamics on the Coupled Long-Term Evolution of Barrier-Marsh-Bay Systems. *JGR Biogeosciences*, 125(2), e2019JG005416.

Rodríguez-Santalla, I., & Navarro, N. (2021). Main threats in Mediterranean coastal wetlands. The Ebro Delta case. *Journal of Marine Science and Engineering*, 9(11), 1190.

Roelvink, D., Reniers, A., Van Dongeren, A. P., De Vries, J. V. T., McCall, R., & Lescinski, J. (2009). Modelling storm impacts on beaches, dunes and barrier islands. *Coastal engineering*, 56(11-12), 1133-1152

Roland A, Zhang YJ, Wang HV, et al (2012). A fully coupled 3D wave-current interaction model on unstructured grids. *Journal of Geophysical Research: Oceans* 117(C11). <https://doi.org/10.1029/2012JC007952>

Santillán, D., Cueto-Felgueroso, L., Sordo-Ward, A., Garrote, L. (2020) Influence of Erodible Beds on Shallow Water Hydrodynamics during Flood Events. *Water*, 12, 3340, doi:10.3390/w12123340



- de Schipper, M. A., Ludka, B. C., Raubenheimer, B., Luijendijk, A. P., & Schlacher, T. A. (2021). Beach nourishment has complex implications for the future of sandy shores. *Nature Reviews Earth & Environment*, 2(1), 70-84.
- Scheel, F. (2017). Memo Input Reduction Tool - Description and User Manual. Deltares memo 1221439-000-HYE-0004.  
[https://svn.oss.deltares.nl/repos/openearthtools/trunk/matlab/applications/tools/input\\_reduction\\_tool/Description\\_and\\_user\\_manual\\_input\\_reduction\\_tool.pdf](https://svn.oss.deltares.nl/repos/openearthtools/trunk/matlab/applications/tools/input_reduction_tool/Description_and_user_manual_input_reduction_tool.pdf)
- Schrijvershof, R. A., van Maren, D. S., Torfs, P. J., & Hoitink, A. J. F. (2023). A Synthetic Spring-Neap Tidal Cycle for Long-Term Morphodynamic Models. *Journal of Geophysical Research: Earth Surface*, 128(3), e2022JF006799.
- Shields, A. (1936). Anwendung der Aehnlichkeitsmechanik und der Turbulenzforschung auf die Geschiebebewegung. Mitteilung der Preussischen Versuchsanstalt für Wasserbau und Schiffbau, Heft 26, Berlin.
- SIBA (2013). Recueil de données tourisme sur le Bassin d'Arcachon. Online documentation, 17p., consulted in December 2023.
- SIBA (2023). Recueil de données touristiques, Bassin d'Arcachon. Bassin d'Arcachon, un monde à part. Région Nouvelle Aquitaine, updated in June 2023, 30p.
- Soulsby, R.L., Whitehouse, R.J.S. (1997) Threshold of Sediment Motion in Coastal Environments. Pacific Coasts and Ports '97: Proceedings of the 13th Australasian Coastal and Ocean Engineering Conference and the 6th Australasian Port and Harbour Conference, Volume 1
- Stive, M. J. F., and Z. B. Wang (2003). Morphodynamic modeling of tidal basins and coastal inlets, in *Advances in Coastal Modeling*. Elsevier Oceanogr. Ser., vol. 67, edited by V. C. Lakhan, pp. 367-392, Elsevier, Amsterdam.
- Sutherland, J., Peet, A. H., & Soulsby, R. (2004) Evaluating the performance of morphological models. *Coastal engineering*, 51(8-9), 917-939.
- Suzuki, T., Hu, Z., Kumada, K., Phan, L. K., & Zijlema, M. (2019). Non-hydrostatic modeling of drag, inertia and porous effects in wave propagation over dense vegetation fields. *Coastal Engineering*, 149, 49-64.
- Suzuki, T., Zijlema, M., Burger, B., Meijer, M. C., & Narayan, S. (2012). Wave dissipation by vegetation with layer schematization in SWAN. *Coastal Engineering*, 59(1), 64-71.
- Tagliapietra, D., Baldan, D., Barausse, A., Buosi, A., Curiel, D., Guarneri, I., Pessa, G., Rismondo, A., Sfriso, A., Smania, D., & Volpi Ghirardini, A. (2018). *Protecting and restoring the salt marshes and seagrasses in the lagoon of Venice*. <http://journal.um-surabaya.ac.id/index.php/JKM/article/view/2203>
- Tanino, Y., & Nepf, H. M. (2008). Laboratory investigation of mean drag in a random array of rigid, emergent cylinders. *Journal of Hydraulic Engineering*, 134(1), 34-41.
- Tena A., Batalla R.J., Vericat D., Lopez-Tarazón J.A. (2011) Suspended sediment dynamics in a large regulated river over a 10-year period (the lower Ebro, NE Iberian Peninsula). *Geomorphology*, 125, 73–84.
- UICN France (2014). Panorama des services écologiques fournis par les écosystèmes français - étude de cas : les écosystèmes marins et côtiers d'Aquitaine. Paris, France, 48p.

- Van Leer, B. (1979) Towards the Ultimate Conservative Difference Scheme, V. A Second Order Sequel to Godunov's Method. *J. Comput. Phys.*, 32, 101–136.
- Van Loon-Steensma, J. M., Hu, Z., & Slim, P. A. (2016). Modelled impact of vegetation heterogeneity and salt-marsh zonation on wave damping. *Journal of Coastal Research*, 32(2), 241-252.
- Van Maren, D. S., Oost, A. P., Wang, Z. B., & Vos, P. C. (2016). The effect of land reclamations and sediment extraction on the suspended sediment concentration in the Ems Estuary. *Marine Geology*, 376, 147-157.
- Van Maren, D. S., van Kessel, T., Cronin, K., & Sittoni, L. (2015). The impact of channel deepening and dredging on estuarine sediment concentration. *Continental Shelf Research*, 95, 1-14.
- Vanoni V. A., Brooks N. H. (1957) Laboratory studies of the roughness and suspended load of alluvial streams. Sedimentation Laboratory, California Institute of Technology, Pasadena, Calif.
- Van Rijn, L.C. (1984a) Sediment Transport, Part I: Bed Load Transport. *J. Hydraul. Eng.*, 110, 1431–1456.
- Van Rijn, L.C. (1984b) Sediment Transport, Part II: Suspended Load Transport. *J. Hydraul. Eng.*, 110, 1613–1641.
- Van Rijn, L.C. (1987). Mathematical modelling of morphological processes in the case of suspended sediment transport. Delft: Delft Hydraulics Communications #382.
- Van Rooijen, A. A., Van Thiel de Vries, J. S. M., McCall, R. T., Van Dongeren, A. R., Roelvink, J. A., & Reniers, A. J. H. M. (2015, June). Modeling of wave attenuation by vegetation with XBeach. In E-proceedings 36th IAHR World Congress (pp. 1-7).
- Valchev N., E. Trifonova, N. Andreeva. 2012. Past and recent trends in the western Black Sea storminess, *Nat. Hazards Earth Syst. Sci.*, 12, 961–977, 2012, doi:10.5194/nhess-12-961-2012
- Valchev, N, N. Andreeva, P. Eftimova, B. Prodanov, I. Kotsev, Assessment of vulnerability to storm induced flood hazard along diverse coastline settings, 3rd European Conf. on Flood Risk Manag. FLOODrisk 2016, E3S Web of Conferences 7 10002, 2016 (URL: <DOI: 10.1051/e3sconf/20160710002>).
- Vuik, V. (2017). POV Waddenzeedijken; effectiviteit voorlanden HR - Stabiliteit van vegetatie. HKV memo PR3365.30.
- Winterwerp, J. C., Zhou, Z., Battista, G., Van Kessel, T., Jagers, H. R. A., Van Maren, D. S., & Van Der Wegen, M., 2018. Efficient consolidation model for morphodynamic simulations in low-SPM environments. *Journal of Hydraulic Engineering*, 144(8), 04018055.
- WMO, 2008. Guide to Meteorological Instruments and Methods of Observation, No. 8. CWOP-WMO8.pdf (weather.gov)
- York: Cambridge University Press), 1137–1216. Available at:  
[http://www.climatechange2013.org/images/report/WG1AR5\\_Chapter13\\_FINAL.pdf](http://www.climatechange2013.org/images/report/WG1AR5_Chapter13_FINAL.pdf).
- Zijl, F., Groenenboom, J., Laan, S. & Zijlker, T. (2022). DCSM-FM 100m: a sixth-generation model for the NW European Shelf: 2022 release. Deltares rapport 11208054-004-ZKS-0002.
- Zhang Y, Ye F, Stanev E et al (2016) Seamless cross-scale modelling with SCHISM. *Ocean Modelling* 102. <https://doi.org/10.1016/j.ocemod.2016.05.002>